

ELECTROCATALYSIS IN SOLID ACID FUEL CELLS

Thesis by

Mary WC Louie

In Partial Fulfillment of the Requirements

for the degree of

Doctor of Philosophy



California Institute of Technology

Pasadena, California

2011

(Defended May 20, 2011)

© 2011

Mary WC Louie

All Rights Reserved

Acknowledgements

This work would not have been possible without financial support from the National Science Foundation (NSF), DMR-0906543, and from the Caltech Center for the Science and Engineering of Materials, an NSF Materials Research Science and Engineering Center (DMR-0520565). Additional funding has been provided by the Gordon and Betty Moore Foundation (via the Caltech Center for Sustainable Energy Research) and by the Department of Defense Multidisciplinary University Research Initiative (W911NF-07-1-0410) administered by the Army Research Office. I have been fortunate enough to be supported by the NSF Graduate Research Fellowship Program, the Baker Hughes Scholarship from the Society of Women Engineers, and the Ludo Frevel Crystallography Scholarship from the International Center for Diffraction Data.

I am grateful to my thesis advisor, Professor Sossina Haile, who has been a wonderful mentor both professionally and personally. She works tirelessly to provide all the resources her group members need to be productive, and all the while, her office door is always open and her patience, endless. I have always left her office with more clarity than when I entered. For these reasons, I owe a great portion of graduate career to Sossina.

I thank Professor Adrian Hightower, scientist and kickboxer extraordinaire, for our valuable discussions, scientific and nonscientific alike. His boundless enthusiasm and optimism have made the endless hours of AFM troubleshooting in his sub-basement laboratory more bearable.

I thank my thesis committee members, Professors Kaushik Bhattacharya, Konstantinos Giapis and William Goddard. Professor Bhattacharya first exposed me to the theory of martensite in ME260, and since then, I have had a good deal of fun pondering the implications of crystallographic compatibility on solid acid compounds. I have also shared many projects with Professor Giapis, including microplasmas and electrosprays. I thank him for the advice and support he has given me throughout the years. I would also like to acknowledge Professor David Goodwin for his time as a member of my candidacy committee.

There are many individuals to whom I owe my gratitude for their contributions to my research at Caltech. I am grateful to Calum Chisholm for our exchanges about anything and everything related to solid acid fuel cells and for his enthusiasm and energy. I thank Yoshihiro Yamazaki for our discussions on hydrogen transport and for letting me “borrow” his textbooks. Ayako Ikeda has been an invaluable resource; I thank her for the information she provides me regarding the stability of solid acid compounds. For the AFM work, Brian Sayers and Shijie Wu assisted a great deal with troubleshooting and instrumentation. I also would like to acknowledge Mikhail Kislitsyn for his work on the structural and thermal characterization of CRDP compounds, as well as Diana Smirnova and Manuj Swaroop who worked on initial twinning calculations for CDP in ME260.

There are many others I would like to thank for help along the way. Kenji Sasaki was my mentor when I first arrive in the Haile group, not to mention the first to explore the complexities of electrocatalysis in solid acid systems. Jeff Snyder exposed me to the world of lab equipment on eBay and kept me on my toes with his excited and loud utterances in the hallway. Eric Toberer not only gave me much needed advice over the

years but also made our office fun. I am grateful to David Boyd for discussions and help with oxygen plasmas and Raman spectroscopy, Yong Hao for point electrode calculations, and Ali Saramat for our collaboration on nanoparticle synthesis. Peter Babilo never hesitated to offer a confused first-year student a helping hand in the lab. Nick Brunelli was a patient teacher; I am grateful to him for our many discussions early in my graduate career. I cannot thank William Chueh and Wei Lai enough for their many, *many* (somewhat underappreciated) hours spent writing LabVIEW programs from which the Haile group benefits on a daily basis. I would also like to acknowledge the hard work of the undergraduate students who have worked with me over the years: Tewodros Mamo, Helen Telila, Lauren Baranowski, Sarah Howell, and Xiuyuan Li.

The Haile lab is great group to work with; every member has always been ready to lend a hand to others. I also cannot forget the supportive staff on campus, including Rosie Sanchez, Kathy Bubash, Fenton Harvey, Fran Matzen, Irene Loera, Mike Vondrus, Mike Roy, Rick Gerhart and Rick Germond.

I owe a great deal to individuals who have shaped my career and have been, and still are, mentors to me. As an undergraduate student at Berkeley, I was fortunate to have befriended Jessica Preciado who is truly an inspiring individual; if not for her, I probably would not have gone to graduate school. I must also thank my first research mentor, Andy Malec, who put up with the many blunders of a novice in the laboratory and who patiently taught me how to count the number of hydrogen in organic compounds (or, at the time, what looked to me like “random zig-zags”). Loddie Foose never ceases to offer

me advice; at times, I think she knows me better than I do. And finally, Lisa Cowan is a dear friend, without whom I would not have survived my early years here.

I consider myself lucky to have entered Caltech with a great chemical engineering class; they managed to make my first year of classes and exams, I dare say, fun. In particular, Yvonne Chen, Diana Smirnova, and Havala Pye have become my good friends. I will miss our girls' game nights, not to mention repeatedly losing to Yvonne in bowling. Also, Diana kept me sane with our long runs and long conversations. Yvonne was my roommate for almost three years and is like a sister to me; to this day, she lends her patient ear for my ramblings.

I was fortunate enough to befriend many wonderful individuals: Puneet Chhabra, Glenn Garrett, Amy Fu, Peter Agbo, Arthur Chan, Eric Olmon, Chethana Kulkarni, Andrew Metcalf, and Nick Heinz. I also have not forgotten Alem and Hanu who always manage to put a smile on my face.

My husband, William, has been supportive and ever so patient with me. I thank him and his family for their love and support. Last but most definitely not least, I thank my family. My parents are the only reason why I have enjoyed the opportunities that they have only dreamt of; I still do not know how to express my appreciation of the sacrifices they have made. Also, Carrie, my "twin" sister and partner in crime (not to mention Dr. Louie No. 1), who despite being only one year older, was always the first to venture into the unknown when we were growing up. She has paved the way for me; she is and will always be my older, wiser sister.

Abstract

Solid state electrochemical reactions play a crucial role in many energy conversion devices, yet the pathways of many reactions remain unknown. The elusiveness of the reaction mechanisms is due, in part, to the complexity of electrochemical reactions; because electrochemical reactions require the interaction of many species (e.g., ions, electrons, and adsorbates) across multiple phases (e.g., electrolyte, catalyst, and gas phases), elucidation of the reaction pathway can quickly become complicated. In this work, we develop and utilize model catalyst | electrolyte systems, that is, structures of reduced complexity, to study electrode reactions in solid acid fuel cells which operate at intermediate temperatures of ~ 250 °C. We employ AC impedance spectroscopy to explore the reaction pathway for hydrogen electro-oxidation over Pt thin films sputter-deposited atop the proton-conducting solid acid electrolyte CsH_2PO_4 . We observed that hydrogen electro-oxidation occurs by diffusion of hydrogen through Pt, taking advantage of the entire Pt | CsH_2PO_4 interfacial area rather than being confined to the triple-phase sites. This insight opens up new avenues for developing high performance electrodes with low Pt loadings by eliminating the requirement that Pt-based electrodes be comprised of high triple-phase site densities long considered to be critical for Pt electrocatalysis. Indeed, even for flat, planar electrodes of very thin Pt films, we obtained a Pt utilization that is significantly higher than in typical composite electrodes.

We also demonstrate the efficacy of a new tool for probing the spatial heterogeneity of electrochemical reactions at the metal | electrolyte interface. We characterized oxygen electro-reduction kinetics at the nanoscale Pt | CsHSO_4 interface at ~ 150 °C using conducting atomic force microscopy in conjunction with cyclic

voltammetry and AC impedance spectroscopy. Not only did we find the electrochemical activity for oxygen electro-reduction to vary dramatically across the electrolyte surface but the current-voltage data, when analyzed in the Butler-Volmer framework, exhibited a strong counter-correlation between two key kinetic parameters, the exchange coefficient and exchange current. Specifically, the exchange current spanned five orders of magnitude while the exchange coefficient ranged between 0.1 and 0.6. Such a correlation has not been observed before and points to the power of atomic force microscopy for electrochemical characterization at electrolyte | metal | gas boundaries in general.

As reduction in microstructural complexity is a key advantage in model electrode | electrolyte systems, we also sought to understand the bulk properties of solid acid compounds, specifically, the relationship between microstructure and the superprotonic phase transition, the latter of which lends solid acid compounds their high proton conductivities at intermediate temperatures. We found a correlation between phase transformation hysteresis and crystallographic compatibility of the high- and low-temperature phases of the $\text{Cs}_{1-x}\text{Rb}_x\text{H}_2\text{PO}_4$ solid solution series. Therefore, it is to be expected that hysteresis, and therefore microcrack formation, can be minimized during phase transformation via the principle of crystallographic compatibility. This is confirmed in single crystals of CsHSO_4 , which was found to have higher crystallographic compatibility, lower hysteresis, and significantly fewer microcracks formed during phase transition compared to CsH_2PO_4 . The apparent applicability of the theory of crystallographic compatibility implies a new tool for identifying solid acid compounds with suitable microstructures for fuel cell application and for model electrode | electrolyte systems.

Table of Contents

Chapter 1 Introduction.....	1
1.1 Overview.....	1
1.2 Fuel Cells	1
1.2.1 Fuel Cell Basics.....	2
1.2.2 Overpotentials in Fuel Cells.....	4
1.2.3 Component Requirements.....	6
1.2.4 Types of Fuel Cells	8
1.3 Solid Acid Fuel Cells	10
1.3.1 Solid Acid Compounds	10
1.3.2 CsH_2PO_4 as an Electrolyte: Benefits and Challenges.....	13
1.3.3 Solid Acid Fuel Cell Performance.....	16
1.4 Electrode Reactions in Solid Acid Fuel Cells.....	17
1.4.1 Hydrogen Electro-oxidation and Oxygen Electro-reduction	17
1.4.2 Electrochemical Reaction Pathways	18
Chapter 2 Experimental Methods.....	22
2.1 AC Impedance Spectroscopy	22
2.1.1 Basic Principles.....	22
2.1.2 Data Analysis: Equivalent Circuit Models.....	26
2.1.3 Data Analysis: Physical Models.....	32
2.1.4 Experimental Corrections	34
2.2 Potential Sweep (DC) Methods	35
2.3 AC vs. DC Measurements.....	37

2.4	Scanning Probe Microscopy for Electrochemistry	38
2.4.1	<i>Atomic Force Microscopy</i>	39
2.4.2	<i>Electrical Atomic Force Microscopy</i>	42
2.5	Cell Geometries for Probing Solid State Electrochemistry	43
2.5.1	<i>Symmetric vs. Asymmetric Gas Environments</i>	43
2.5.2	<i>Electrode Symmetry and Geometry</i>	46
2.5.3	<i>Electrode Microstructure</i>	50
2.6	Solid Acid Compounds for Electrode Studies: Challenges	51
2.6.1	<i>Water Solubility</i>	51
2.6.2	<i>Mechanical Properties</i>	52
2.6.3	<i>Superprotonic Phase Transition</i>	52
2.6.4	<i>Thermal and Chemical Stability</i>	54
Chapter 3	Hydrogen Electro-oxidation over Thin Film Pt Electrodes	55
3.1	Introduction	56
3.2	Experimental	57
3.2.1	<i>Sample Preparation</i>	57
3.2.2	<i>Characterization</i>	58
3.3	Results and Discussion	61
3.3.1	<i>Film Morphology and Structure</i>	61
3.3.2	<i>Impedance Response: Effect of Platinum Film Dimension</i>	65
3.3.3	<i>Impedance Response: Impact of Gold Overlayers</i>	70
3.3.4	<i>Diffusion Analysis</i>	71
3.3.5	<i>Ultra-thin Platinum Films</i>	74
3.4	Implications for Electrode Design	76
3.5	Summary	79

Chapter 4	Oxygen Electro-reduction at Nano-Pt CsHSO₄.....	80
4.1	Introduction.....	82
4.2	Experimental.....	85
4.2.1	<i>Half-cell Fabrication</i>	85
4.2.2	<i>Experimental Conditions</i>	86
4.2.3	<i>Measurement Conditions</i>	87
4.2.4	<i>Data Analysis</i>	88
4.3	Results and Discussion	89
4.3.1	<i>Cyclic Voltammetry</i>	89
4.3.2	<i>Impedance Spectroscopy</i>	92
4.3.3	<i>Analysis of Oxygen Electro-reduction Kinetics</i>	96
4.3.4	<i>Heterogeneity of Electrochemical Kinetics</i>	100
4.4	Summary	105
Chapter 5	Phase Transformation Hysteresis in Solid Acid Compounds.....	107
5.1	Introduction.....	109
5.2	Theory of Crystallographic Compatibility.....	111
5.3	Experimental.....	116
5.3.1	<i>Synthesis and Fabrication</i>	116
5.3.2	<i>Characterization</i>	117
5.3.3	<i>Determination of Eigenvalues</i>	119
5.4	Results and Discussion: Cs _{1-x} Rb _x H ₂ PO ₄	119
5.4.1	<i>Phase and Chemical Characterization</i>	119
5.4.2	<i>Conductivity and Phase Transformation Hysteresis</i>	123
5.4.3	<i>Eigenvalues and Correlation to Hysteresis</i>	126

5.5	Results and Discussion: Microstructure of CsH_2PO_4 and CsHSO_4	128
5.5.1	<i>Microcrack Formation</i>	128
5.5.2	<i>Microstructure of Single-crystal Surfaces</i>	130
5.5.3	<i>In situ Imaging of CsHSO_4</i>	134
5.6	Summary and Outlook	138
Appendix A Derivations		141
A.1	Kinetics of Electrode Reactions: Butler-Volmer Equation	141
A.2	Finite-Length Warburg with Reversible Bounds	146
A.3	Reaction Mechanism	152
A.3.1	<i>Hydrogen Adsorption as a Rate-Limiting Step</i>	154
A.3.2	<i>Hydrogen Absorption as a Rate-Limiting Step</i>	155
A.3.3	<i>Hydrogen Diffusion as a Rate-Limiting Step</i>	156
A.3.4	<i>Charge Transfer as a Rate-Limiting Step</i>	157
Appendix B Reactivity of Candidate Electrocatalysts with CsH_2PO_4		158
B.1	Motivation	158
B.2	Experimental	160
B.2.1	<i>Sample Preparation and Heat Treatment</i>	160
B.2.2	<i>Characterization</i>	160
B.3	Results and Discussion	160
Appendix C Platinum Thin Film Anodes		164
C.1	Experimental Setup	164
C.2	Platinum Film Quality	165

C.2.1	<i>Before and After Electrochemical Characterization</i>	165
C.2.2	<i>Film Structure and Impedance Response of Sub-5 nm Films</i>	168
C.2.3	<i>Mechanical Integrity: 375 nm vs. Sub-8 nm Films</i>	172
C.2.4	<i>Effect of Mechanical Pressure from Current Collector</i>	175
C.3	Non-electrode Impedance Responses	177
C.3.1	<i>Origin of Spurious Electrical Effects</i>	177
C.3.2	<i>Appearance of Constriction Effect</i>	178
C.3.3	<i>Evidence of Constriction Effect</i>	180
C.4	Layered Pt-Au Film Electrodes	183
C.5	Electrolyte Effects: $\text{Cs}_{0.25}\text{Rb}_{0.75}\text{H}_2\text{PO}_4$ vs. CsH_2PO_4	188
C.5.1	<i>150 nm Platinum Films</i>	189
C.5.2	<i>7.5 nm Platinum Films</i>	191
C.6	Effect of Environmental Parameters	193
C.7	Role of the Superprotonic Phase Transition in Electrode Kinetics	199
C.7.1	<i>Temperature Dependence</i>	199
C.7.2	<i>Platinum Film Geometry Dependence</i>	201
C.7.3	<i>Temperature Cycling and Crack Formation</i>	202
Appendix D	Hydrogen Electro-oxidation over Palladium Thin Films	207
D.1	Experimental	207
D.2	Results and Discussion	209
D.2.1	<i>Palladium Film Characteristics</i>	209
D.2.2	<i>Characteristics of Impedance Spectra</i>	214
D.2.3	<i>Effect of Palladium Film Geometry</i>	216
D.2.4	<i>Effect of Environmental Parameters</i>	217
D.2.5	<i>Impedance Response of Layered Pt-Au Film Electrodes</i>	220

D.2.6	<i>10 nm Palladium Films</i>	221
D.2.7	<i>Comparison to Platinum</i>	222
D.3	Summary	223
D.4	Recommendations for Future Studies	224
Appendix E	Nickel Thin Films	225
Appendix F	Pt CsHSO₄ by Atomic Force Microscopy	229
F.1	Experimental Details	229
F.1.1	<i>Instrumentation and Setup</i>	229
F.1.2	<i>Sample Heating</i>	230
F.2	Data Analysis	232
F.2.1	<i>Open- and Short-Circuit Corrections</i>	232
F.2.2	<i>Measurement Stability</i>	236
F.2.3	<i>Analysis of Cyclic Voltammograms</i>	238
F.2.4	<i>Effect of Force on Electrochemical Measurements</i>	239
F.3	Nano-Pt CsHSO ₄ vs. Wire-Pt CsH ₂ PO ₄	240
F.4	Platinum Oxide Reduction at Pt CsHSO ₄	242
F.4.1	<i>Experimental</i>	242
F.4.2	<i>Results and Discussion</i>	243
F.5	Oxygen Electro-Reduction at Pt Single-crystal CsHSO ₄	246
F.5.1	<i>Experimental</i>	246
F.5.2	<i>Results and Discussion</i>	249
Appendix G	Pt Ba_{3-x}K_xH_x(PO₄)₂ by Atomic Force Microscopy	254
G.1	Introduction	254
G.2	Experimental	255

G.3	Results and Discussion	257
G.3.1	$Ba_{3-x}K_xH_x(PO_4)_2$ Characteristics	257
G.3.2	Fabrication of Microscale $Ba_{3-x}K_xH_x(PO_4)_2$ Half-cells	258
G.3.3	Oxygen Electro-reduction at $Pt Ba_{3-x}K_xH_x(PO_4)_2$	261
G.3.4	Troubleshooting.....	264
G.4	Recommendations for Future Studies	266
Appendix H	$Pd CsHSO_4$ by Atomic Force Microscopy	268
H.1	Experimental	268
H.2	Results and Discussion	269
H.2.1	Oxygen Electro-reduction	269
H.2.2	Transient Behavior of $Pd CsHSO_4$	274
H.2.3	Palladium Oxidation	276
H.2.4	Stability of $Pd CsHSO_4$	277
H.3	Summary	278
Appendix I	Crystallographic Compatibility in $Cs_{1-x}Rb_xH_2PO_4$	280
I.1	Visualization of the Cubic-to-Monoclinic Transformation in CsH_2PO_4	280
I.2	Calculation of Transformation Matrix	282
I.3	Calculation of Compatible Variant Pairs: Twinning Modes.....	283
I.4	Calculation of the Austenite-Martensite Interface	285
I.5	Results for CsH_2PO_4	287
Appendix J	Microstructure of Solid Acid Compounds: Supplemental.....	292
J.1	Additional Images	292
Appendix K	$Pt CsH_2PO_4 Au$ as a Mixed Potential Hydrogen Sensor	294
K.1	Introduction.....	294
K.2	Mixed Potential Effect	295

K.3	Experimental	297
K.4	Results and Discussion	298
<i>K.4.1</i>	<i>Sensor Response</i>	298
<i>K.4.2</i>	<i>Variability in the Sensor Response</i>	303
K.5	Summary and Recommendations	304
References	305

List of Figures

Figure 1.1	Schematic of a fuel cell based on a proton-conducting electrolyte	3
Figure 1.2	Fuel cell polarization curve and overpotentials.	5
Figure 1.3	Schematic of a typical composite electrode.....	8
Figure 1.4	Arrhenius plot of proton conductivity showing the superprotonic phase transition of select solid acid compounds	11
Figure 1.5	Superprotonic phase transition in CsH_2PO_4 : Proton conductivity and corresponding unit cells.	12
Figure 1.6	Proton conduction mechanism in CsH_2PO_4	13
Figure 1.7	Cartoon of triple-phase boundary pathways.	19
Figure 1.8	Comparison of triple-phase and two-phase boundary pathways	21
Figure 2.1	Basics of AC impedance	25
Figure 2.2	Nyquist representation of impedance response.....	25
Figure 2.3	Depiction of ion movement due to an alternating electric field.....	26
Figure 2.4	Impedance spectrum for three serial RC sub-circuits and comparison of RQ and RC response.....	30
Figure 2.5	Equivalent circuit for three serial electrochemical	31
Figure 2.6	Schematic for Warburg diffusion.....	33
Figure 2.7	Potential profile for cyclic voltammetry	36
Figure 2.8	Cyclic voltammograms for some common circuit elements.....	37
Figure 2.9	Atomic force microscope probes: tip and cantilever description	40
Figure 2.10	Operation of atomic force microscopy.	41
Figure 2.11	Asymmetric and symmetric gas configurations for electrode studies	45

Figure 2.12	Electrode geometries for solid state electrochemical measurements.....	48
Figure 2.13	Requirements of asymmetric electrode geometries	49
Figure 2.14	Different electrode microstructures for a catalyst-electrolyte system	51
Figure 2.15	Fuel cell open-circuit voltage with temperature cycling.....	53
Figure 3.1	XRD pattern of Pt film on a CsH_2PO_4 substrate.....	61
Figure 3.2	Representative SEM micrographs of Pt films.....	63
Figure 3.3	Schematic of the Pt CsH_2PO_4 Pt system	63
Figure 3.4	SEM micrographs of Pt grain size for various film thicknesses.....	64
Figure 3.5	XRD patterns showing correlation of grain size with Pt film thickness...	65
Figure 3.6	Impedance spectra for Pt film electrodes of different thicknesses	66
Figure 3.7	Plots of Pt film electrode resistance as a function of film geometry	68
Figure 3.8	Dependence of $p\text{H}_2$ reaction order and activation energy on film thickness.....	69
Figure 3.9	Schematic of the Au Pt CsH_2PO_4 Pt Au cell	71
Figure 3.10	Impedance spectra: Au Pt CsH_2PO_4 Pt Au vs. Pt CsH_2PO_4 Pt	71
Figure 3.11	Extracted hydrogen diffusivity as a function of film	74
Figure 3.12	Area-normalized electrode resistance of Pt films as function of thickness.....	76
Figure 4.1	Schematic of nano-electrode setup using an atomic force microscope	83
Figure 4.2	Cyclic voltammograms: Au CsHSO_4 vs. Pt CsHSO_4	90
Figure 4.3	AC impedance spectra for Pt CsHSO_4 as a function of overpotential	93
Figure 4.4	Impedance spectra for Pt CsHSO_4 at -1.0 and -0.9 V	93
Figure 4.5	Resistance of Pt CsHSO_4 as a function of overpotential.....	96

Figure 4.6	Tafel plot for Pt CsHSO ₄	98
Figure 4.7	Image of typical CsHSO ₄ surface by SEM and AFM.....	101
Figure 4.8	Tafel plots and extracted i_0 and α values as a function of position	103
Figure 4.9	Semi-log plot of i_0 as a function of α , showing correlation	103
Figure 5.1	Schematic of austenite-to-martensite transformation for CsH ₂ PO ₄	113
Figure 5.2	Room temperature XRD patterns of Cs _{1-x} Rb _x H ₂ PO ₄	120
Figure 5.3	XRD patterns for CsH ₂ PO ₄ as a function of temperature	122
Figure 5.4	Thermal expansion of CsH ₂ PO ₄ : lattice parameters and cell volume.....	122
Figure 5.5	Temperature dependence of the proton conductivity of CsH ₂ PO ₄	124
Figure 5.6	Reproducibility of Cs _{1-x} Rb _x H ₂ PO ₄ upon repeated temperature cycling.	124
Figure 5.7	Phase transition temperature and hysteresis width as functions of Rb content.....	126
Figure 5.8	Middle eigenvalue, λ_2 , as a function of Rb content, and hysteresis width as a function of λ_2	127
Figure 5.9	SEM images of cracks in CsH ₂ PO ₄ and CsHSO ₄ after heat treatment...	129
Figure 5.10	Optical clarity of CsH ₂ PO ₄ and CsHSO ₄ crystals after heat treatment...	129
Figure 5.11	SEM images of polished CsH ₂ PO ₄ crystal before and after heat treatment.	131
Figure 5.12	SEM images of fractured CsH ₂ PO ₄ crystal before and after heat treatment	131
Figure 5.13	SEM images of fractured CsH ₂ PO ₄ crystal after heat treatment.....	131
Figure 5.14	SEM images of as-grown CsHSO ₄ crystal before and after heat treatment.	132

Figure 5.15	SEM images of polished CsHSO_4 crystal before and after heat treatment.	133
Figure 5.16	Topography of fractured CsHSO_4 crystal at elevated temperatures	135
Figure 5.17	Topography of fractured CsHSO_4 crystal as function of temperature....	137
Figure 5.18	Plot of phase transition hysteresis as a function of middle eigenvalue and volume change for three classes of solid acid compounds.	140
Figure A.1	Effect of potential on free energy profiles for charge transfer reaction..	143
Figure A.2	Effect of exchange current on the current-overpotential behavior.	145
Figure A.3	Warburg diffusion: schematic of diffusion of species through a film	147
Figure A.4	Two-phase boundary pathway for hydrogen electro-oxidation.	153
Figure B.1	Plot of Gibbs free energy for metal oxide formation at 240 °C in air for various metal oxides.....	159
Figure B.2	Plot of Gibbs free energy of select metal carbides and nitrides in air at 240 °C.....	163
Figure C.1	Drawing of test station for symmetric cell measurements.....	165
Figure C.2	SEM micrographs of 375 nm Pt films on top of CsH_2PO_4 before and after electrochemical characterization.	166
Figure C.3	SEM micrographs of 75 nm Pt films on top of CsH_2PO_4 before and after electrochemical characterization	167
Figure C.4	SEM micrographs of 7.5 nm Pt films on top of CsH_2PO_4 before and after electrochemical characterization.	167
Figure C.5	SEM micrographs of 7.5, 22.5, 37.5 and 52.5 nm Pt films on top of CsH_2PO_4 after electrochemical characterization.	168

Figure C.6	SEM micrographs of sub-5 nm thin Pt films before and after electrochemical characterization.....	170
Figure C.7	Nyquist spectra for 1.5, 3, and 4.5 nm thick Pt films and the corresponding area-normalized electrode resistances in comparison to thicker films	171
Figure C.8	SEM micrographs of the undersides of as-deposited 4.5 and 7.5 nm Pt films	174
Figure C.9	SEM micrographs of the undersides of as-deposited 1.5, 3, and 4.5 nm Pt films.....	174
Figure C.10	Cross-section image showing delamination of an intact 375 nm Pt film from CsH_2PO_4	174
Figure C.11	SEM micrographs of a 375 nm Pt film deposited onto CsH_2PO_4 , after electrochemical testing, showing buckling	175
Figure C.12	Pt film quality, after electrochemical characterization, as a function of film thickness and mechanical pressure applied to the cell	176
Figure C.13	The constriction effect: ion movement at various frequencies.	178
Figure C.14	Impedance spectra: Solartron 1250 vs. 1260 FRA.	180
Figure C.15	Representative impedance spectra for a Pt CsH_2PO_4 Pt showing no effect of $p\text{H}_2$ on ohmic offset and high frequency arc.	182
Figure C.16	Temperature dependence of the ohmic offset and the width of the high frequency arc.....	183
Figure C.17	Impedance response of Pt-Au layered thin film electrode system.....	185
Figure C.18	Impedance spectra of a Au CsH_2PO_4 Au symmetric cell.....	188
Figure C.19	Nyquist plot for 150 nm Pt films on CsH_2PO_4 and $\text{Cs}_{0.25}\text{Rb}_{0.75}\text{H}_2\text{PO}_4$ electrolytes	190

Figure C.20	Nyquist plots for 7.5 nm Pt films on CsH_2PO_4 and $\text{Cs}_{0.25}\text{Rb}_{0.75}\text{H}_2\text{PO}_4$ electrolytes	193
Figure C.21	$p\text{H}_2$ and $p\text{H}_2\text{O}$ dependence plots for Pt CsH_2PO_4 Pt (75 nm).	196
Figure C.22	$p\text{H}_2$ and $p\text{H}_2\text{O}$ dependence plots for Pt CsH_2PO_4 Pt (7.5 nm).	196
Figure C.23	Arrhenius behavior of Pt CsH_2PO_4 Pt (75 nm)	198
Figure C.24	Arrhenius behavior of Pt CsH_2PO_4 Pt (7.5 nm)	198
Figure C.25	Pt CsH_2PO_4 Pt across the phase transition: plot of cell temperature and resistance as functions of time, and corresponding Arrhenius plot.	200
Figure C.26	Dependence of electrode resistance on film geometry below the phase transition temperature	202
Figure C.27	Effect of the superprotonic phase transition on cracking in polycrystalline CsH_2PO_4 discs, with application of mechanical pressure	203
Figure C.28	The effect of the superprotonic phase transition on cracking in polycrystalline CsH_2PO_4 discs <i>without</i> application of mechanical pressure applied	204
Figure C.29	Impedance spectra for Pt CsH_2PO_4 Pt symmetric cells (7.5 and 150 nm Pt) before and after a cool-heat cycle through the phase transition.	206
Figure C.30	Effect of thermal cycling on the impedance response of Pt CsH_2PO_4 Pt symmetric cell.....	206
Figure D.1	XRD pattern of 100 nm Pd films on top of CsH_2PO_4 before and after electrochemical characterization.....	210
Figure D.2	SEM images of the cross sections of Pd CsH_2PO_4 Pd cells.	210
Figure D.3	SEM micrographs of 10 nm Pd films deposited on top of CsH_2PO_4 before and after electrochemical characterization	211

Figure D.4	SEM micrographs of 100 nm Pd films deposited on top of CsH_2PO_4 before and after electrochemical characterization	212
Figure D.5	SEM micrographs of 100 nm Pd films deposited on top of CsH_2PO_4 : lateral variation in film structure.....	213
Figure D.6	Impedance spectrum for a Pd CsH_2PO_4 Pd cell (100 nm Pd films)	214
Figure D.7	Equivalent circuit model for the Pd CsH_2PO_4 Pd symmetric cell.	215
Figure D.8	Select impedance spectra for 100, 200, and 300 nm thick Pd films	216
Figure D.9	Plots of the electrode resistances as functions of film diameter.	217
Figure D.10	Plots of the area-normalized electrode resistances as functions of film thickness.....	217
Figure D.11	Representative plots for extracting $p\text{H}_2$ reaction order and activation energy.....	218
Figure D.12	Impedance spectra for the Pd-Au thin film system: Pd CsH_2PO_4 , Au Pd CsH_2PO_4 , and Pd Au CsH_2PO_4	221
Figure D.13	Impedance spectra for Pd CsH_2PO_4 Pd cell (10 nm Pd films).	222
Figure E.1	SEM micrographs of Ni films deposited on top of CsH_2PO_4 before and after electrochemical characterization.....	226
Figure E.2	Images of 100 nm Ni films after heat treatment compared to those after electrochemical characterization	227
Figure E.3	XRD patterns of 100 nm Ni films on top CsH_2PO_4 before and after testing.....	228
Figure E.4	XRD patterns of as-deposited 400 nm Ni films on top CsH_2PO_4 fabricated by thermal evaporation and by sputter deposition.	228
Figure F.1	Photographs of experimental setup for electrochemical AFM.	230
Figure F.2	Schematic of the CsHSO_4 cell configurations for AFM.	231

Figure F.3	Analysis of the temperature gradient across CsHSO ₄ in AFM.....	232
Figure F.4	Illustration of how stray capacitance affects two arbitrary processes.....	233
Figure F.5	Open-circuit impedance response as a function of the current range selected in instrumentation	234
Figure F.6	Representative Nyquist and Bode-Bode plots before and after open- circuit correction.	235
Figure F.7	Short-circuit measurement for a Pt-coated AFM probe in contact with Au foil	236
Figure F.8	AFM image of a CsHSO ₄ surface: effect of thermal drift	237
Figure F.9	Measurement stability: two impedance spectra collected with frequency sweeps in opposite directions.....	238
Figure F.10	Cyclic voltammograms for Pt CsHSO ₄ at various scan rates and the corresponding α values	239
Figure F.11	Effect of force and of probe withdrawal/reapproach on cyclic voltammograms for Pt CsHSO ₄	240
Figure F.12	i_0 - α correlation: Pt CsHSO ₄ vs. Pt CsH ₂ PO ₄	242
Figure F.13	Pt oxide reduction peak as a function of chemical and electrochemical oxidation time	245
Figure F.14	Pt oxide reduction peak voltage, current and area as a function of chemical and electrochemical oxidation time.....	246
Figure F.15	Cyclic voltammograms for a Pt probe in contact with as-grown CsHSO ₄ single-crystal surface.....	248
Figure F.16	Cyclic voltammograms for a Pt probe in contact with single-crystal CsHSO ₄ , contaminated with acidic solution.....	249
Figure F.17	Cyclic voltammogram and Nyquist spectra for Pt probe in contact with fractured CsHSO ₄ crystal.....	250

Figure F.18	Tafel plots for Pt fractured CsHSO ₄ and i_0 - α correlation.....	251
Figure F.19	AFM topography image of a single-crystal CsHSO ₄ surface	253
Figure F.20	AFM images of CsHSO ₄ crystal surfaces showing damage caused by probe	253
Figure G.1	Schematic of experimental setup for electrochemical AFM measurements of Ba _{3-x} K _x H _x (PO ₄) ₂ electrolytes.....	257
Figure G.2	SEM images: Ba _{3-x} K _x H _x (PO ₄) ₂ powder vs. CsHSO ₄ powder	258
Figure G.3	SEM images of Ba _{3-x} K _x H _x (PO ₄) ₂ platelets on a Pt-coated Si wafer.....	259
Figure G.4	SEM images showing wafer-to-wafer transfer of Ba _{3-x} K _x H _x (PO ₄) ₂ platelets	261
Figure G.5	Electrochemical AFM measurements at Pt Ba _{3-x} K _x H _x (PO ₄) ₂ and corresponding cyclic voltammograms	262
Figure G.6	Cyclic voltammograms for Pt Ba _{3-x} K _x H _x (PO ₄) ₂ obtained by wafer-to-wafer platelet transfer	263
Figure G.7	Short-circuit measurements on Pt-coated silicon wafer.....	264
Figure G.8	Raman spectrum for Ba _{3-x} K _x H _x (PO ₄) ₂ platelets deposited on Si wafer .	266
Figure H.1	Cyclic voltammograms and impedance spectra for nano-Pd CsHSO ₄ .	270
Figure H.2	Electrode resistances plotted as functions of overpotential, and Tafel plot for the Pd CsHSO ₄ system	272
Figure H.3	Variation of Tafel plot with position across a CsHSO ₄ surface.....	273
Figure H.4	i_0 - α correlation: Pd CsHSO ₄ vs. Pt CsHSO ₄	273
Figure H.5	Polycrystalline CsHSO ₄ damaged by AFM probe.....	274
Figure H.6	Transient features in the cyclic voltammograms of Pd CsHSO ₄	275
Figure H.7	Behavior of reduction peaks in Pd CsHSO ₄ as a function of chemical and electrochemical oxidation time	277

Figure H.8	Spatial (and time) dependence of Pd CsHSO ₄ response	278
Figure I.1	Visualization of the phase transformation in CsH ₂ PO ₄	281
Figure I.2	Schematic of parallel twins separating two alternating variants.....	284
Figure I.3	Schematic of the interface between austenite and two variants of martensite.....	286
Figure J.1	SEM images of CsH ₂ PO ₄ crystal before and after heat treatment	292
Figure J.2	SEM images of a polished CsH ₂ PO ₄ crystal after heat treatment.....	292
Figure J.3	Twins in CsHSO ₄ : SEM image after heat treatment and AFM image at superprotonic conditions.	293
Figure K.1	Schematic polarization curves for determining mixed potentials in Au CsH ₂ PO ₄ Pt hydrogen sensor	296
Figure K.2	Plot of open-circuit voltage as a function of time for a Pt CsH ₂ PO ₄ Au sensor at 235 °C for various <i>p</i> H ₂	299
Figure K.3	Mixed potential response of Pt CsH ₂ PO ₄ Au sensor at 235 °C plotted against <i>p</i> H ₂	300
Figure K.4	Schematic showing how mass transport effects can result in a large change in mixed potential for a small change in gas composition..	301
Figure K.5	Mixed potential response of multiple Pt CsH ₂ PO ₄ Au sensors at 235 °C plotted against <i>p</i> H ₂	302
Figure K.6	Plot of open-circuit voltage as a function of time for a Pt CsH ₂ PO ₄ Au sensor at 235 °C for various <i>p</i> H ₂	302

List of Tables

Table 1.1	Common fuel cell types and their primary characteristics	9
Table 2.1	Impedance response of frequently encountered circuit elements.....	27
Table 2.2	Impedance response of frequently encountered sub-circuits.....	28
Table 2.3	Impedance response for bounded and unbounded Warburg diffusion.....	33
Table 3.1	Experimentally-determined parameters for hydrogen transport in Pt	74
Table 3.2	Comparison of platinum-based anodes for solid acid fuel	79
Table 4.1	Conducting AFM probes employed in this study	88
Table 5.1	Lattice parameters and chemical compositions for $\text{Cs}_{1-x}\text{Rb}_x\text{H}_2\text{PO}_4$	120
Table 5.2	Thermal expansion parameters for CsH_2PO_4	123
Table B.1	Reactivity of CsH_2PO_4 with metal oxides at 150 °C and 240 °C.....	162
Table B.2	Reactivity of CsH_2PO_4 with metal nitrides and carbides at 240 °C.....	163
Table C.1	Summary of parameters extracted from the low frequency arc generated by addition of Au films to the Pt CsH_2PO_4	186
Table C.2	Comparison of fitted parameters for 150 nm Pt films on CsH_2PO_4 and $\text{Cs}_{0.25}\text{Rb}_{0.75}\text{H}_2\text{PO}_4$	191
Table C.3	Comparison of fitted parameters for 7.5 nm Pt films on CsH_2PO_4 and $\text{Cs}_{0.25}\text{Rb}_{0.75}\text{H}_2\text{PO}_4$	193
Table C.4	$p\text{H}_2$ and $p\text{H}_2\text{O}$ dependences of electrolyte-related processes.....	194
Table D.1	Pd thin films: area-normalized resistance, $p\text{H}_2$ and $p\text{H}_2\text{O}$ reaction order and activation energy.....	218
Table H.1	AFM probes employed for comparing Pd CsHSO_4 and Pt CsHSO_4	269
Table I.1	Lattice parameters and atomic positions for monoclinic CsH_2PO_4	281
Table I.2	Lattice parameters and atomic positions for cubic CsH_2PO_4	281
Table I.3	Twelve martensite variants for transformation of CsH_2PO_4	288

Table I.4	Allowed twinning modes of CsH_2PO_4 martensite.....	289
Table I.5	CsH_2PO_4 martensite variant pairs that can form an interface with the austenite phase.....	290

List of Acronyms

ACIS	alternating current impedance spectroscopy
AFC	alkali fuel cell
AFM	atomic force microscopy
BKHP	barium potassium hydrogen phosphate, $\text{Ba}_{3-x}\text{K}_x\text{H}_x(\text{PO}_4)_2$
CDP	cesium dihydrogen phosphate, CsH_2PO_4
CHS	cesium hydrogen sulfate, CsHSO_4
CRDPn	cesium rubidium dihydrogen phosphate, $\text{Cs}_{1-x}\text{Rb}_x\text{H}_2\text{PO}_4$, where $n = 100x$
CV	cyclic voltammetry
dFLW	distributed finite-length Warburg
EDS	energy dispersive spectroscopy
FRA	frequency response analyzer
MCFC	molten carbonate fuel cell
OCV	open-circuit voltage
PAFC	phosphoric acid fuel cell
RMS	root mean square
SAFC	solid acid fuel cell
PEMFC	polymer electrolyte membrane or proton exchange membrane fuel cell
SEM	scanning electron microscopy
SOFC	solid oxide fuel cell
XRD	X-ray diffraction

Chapter 1 Introduction

1.1 Overview

Solid acid fuel cells (SAFCs) based on CsH_2PO_4 electrolyte membranes have the unique advantage of operating at warm temperatures near 250 °C. They were first demonstrated in the laboratory in 2004¹ and today have been scaled to stacks of 1.4 kW.² Despite the rapid development of SAFCs, durability and cost, both of which pertain to the performance of the electrodes, are the key challenges which must be overcome in order for SAFCs to become technologically relevant.³ Thus, the overall objective of this work is to gain a fundamental understanding of electrochemical pathways in SAFCs using model electrode systems and newly developed characterization tools.

In this chapter, we present a brief introduction of fuel cells and, in particular, the current status of SAFCs. We describe the basics of electrocatalysis in solid state electrochemical systems and how an improved understanding of electrochemical reaction kinetics can drastically advance the SAFC technology.

1.2 Fuel Cells

The need for clean, reliable and secure energy is one of the most important challenges of this century. As such, many technologies are being pursued to address this challenge. Among these, fuel cells stand to play a significant role in any renewable energy cycle because they can efficiently convert fuels to electricity. Fuel cells are devices that combine the advantages of both combustion engines and batteries. Like

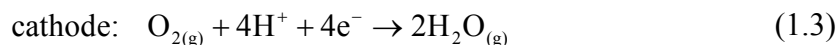
combustion engines, they intake fuel continuously without a need to recharge, but like batteries, they convert chemical energy directly to electricity. Consequently, fuel cells can operate with higher efficiencies and lower emissions of greenhouse gases per unit of fuel input compared to combustion engines which are limited by the Carnot efficiency. Furthermore, they have no moving parts so they are silent during operation and have the potential to operate with longer lifetimes. Finally, it has been shown that fuel cells can be scaled up to large sizes without loss in power density. Due to these advantages, fuel cells have been pursued for decades for both mobile and stationary power generation.

1.2.1 Fuel Cell Basics

A simple schematic of a fuel cell, based on a proton-conducting electrolyte, is shown in Figure 1.1. For a fuel cell operating on hydrogen as the fuel and oxygen as oxidant, the driving force for conversion of energy is the Gibbs free energy of the reaction,



The direct reaction of hydrogen and oxygen gases cannot occur because a gas-impermeable membrane separates the two reactants. In order to utilize the energy stored in the chemical bonds, electrochemical reactions occur at the electrodes and the resulting ions (protons in this case) are transported through the electrolyte membrane, with concurrent electron transport through an external circuit to do useful work. Specifically, at the anode, hydrogen is electrochemically oxidized to protons and electrons, while at the cathode, oxygen is electrochemically reduced to form water. The half-cell reactions for a proton-conducting electrolyte are:



The two half-cell reactions, (1.2) and (1.3), sum to the net reaction (1.1). The standard Gibbs free energy of the reaction, $\Delta G_{\text{rxn}}^\circ$, as written in Equation (1.1), is -483 kJ mol^{-1} at 25°C , where the superscript “o” refers to standard conditions of 1 atm of the reactants and products.

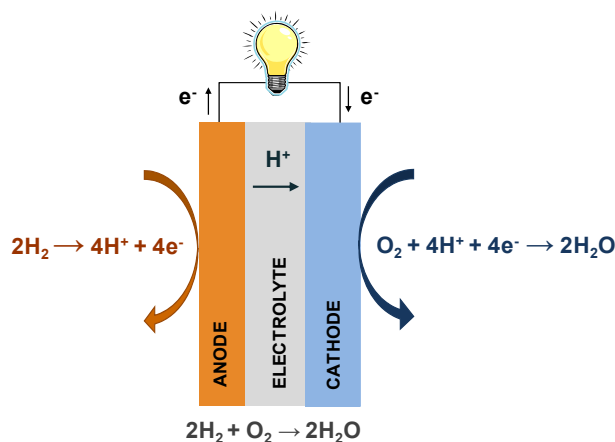


Figure 1.1 A simple schematic of a fuel cell based on a proton-conducting electrolyte membrane.

This chemical potential driving force for water formation, $\Delta G_{\text{rxn}}^\circ$, can be related to the electrochemical potential via the relation

$$E^\circ(T) = -\frac{\Delta G_{\text{rxn}}^\circ(T)}{nF} \quad (1.4)$$

where E° is the standard Nernst potential of the fuel cell (or the theoretical open-circuit voltage), n denotes the number of electrons transferred in the reaction (e.g., $n = 4$ in this case), and F is the Faraday constant ($96,485 \text{ C mol}^{-1}$). The standard Nernst potential corresponding to Equations (1.1)–(1.3) can be computed to be 1.25 V . To compute the Nernst potential at more realistic conditions, one can readily show that

$$E_{eq}(T) = E^\circ(T) - \frac{RT}{nF} \ln \frac{p_{H_2O}^{2(c)}}{p_{H_2}^{2(a)} p_{O_2}^{(c)}} \quad (1.5)$$

where E_{eq} is the equilibrium/theoretical Nernst potential, p_i is the partial pressure of species i at the anode (a) or cathode (c), and R and T have their usual meanings. Values for $\Delta G_{rxn}^\circ(T)$ are tabulated for various reactions (or can be computed from the formation energies for the reactants and products).

1.2.2 Overpotentials in Fuel Cells

Fuel cells are evaluated by their power output, and therefore it is desirable to maintain a high cell voltage under large current loads. However, the voltage across a fuel cell during operation is less than that predicted by the Nernst voltage because of irreversible losses as current is drawn from the cell. Figure 1.2 is a schematic of representative polarization and power density curves and depicts the four common sources of voltage losses, or overpotentials. The overpotential, η_i , is best described as a drop in voltage (from equilibrium) which is used to drive a specific process. The cell voltage at any current density, j , can be expressed as

$$E(j) = E_{eq} - \eta_L - \eta_{act} - \eta_{iR} - \eta_D \quad (1.6)$$

η_L is the voltage loss due to gas leaks across the electrolyte or partial electronic conductivity of the electrolyte. η_{act} is the activation overpotential due to slow kinetics at the electrodes, that is, the driving force required to push reactions over its activation barrier. η_{iR} is the overpotential due to ohmic resistances, primarily from ion transport through the electrolyte, and is characterized by a linear regime in the polarization curve. At high currents, a drop in the cell voltage is characteristic of mass transport losses, η_D ,

for example, due to the depletion of reactants at the electrodes faster than they can be supplied. The ultimate goal is to minimize all the overpotentials and shift the polarization curve toward E_{eq} .

The relative contribution of each overpotential in Equation (1.6) and how it varies with current density depend on the fuel cell type and the materials used therein. For example, low-temperature fuel cells typically have large activation overpotentials while high temperature fuel cells such as SOFCs have a larger contribution from ohmic loss and cross-over.

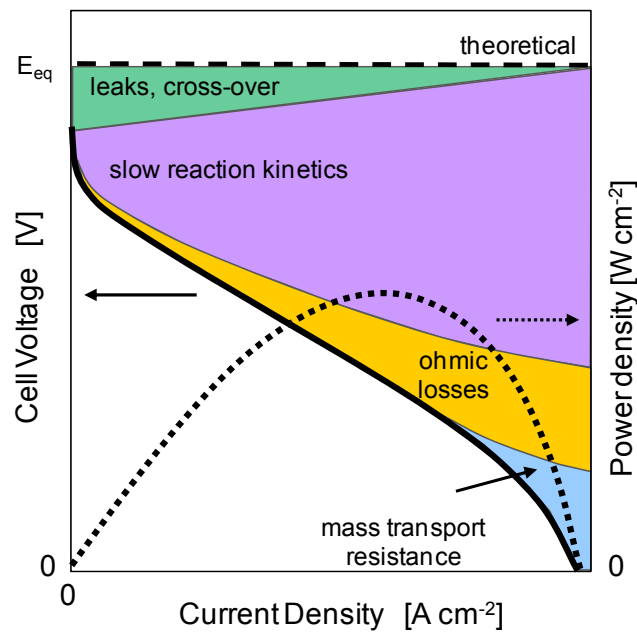


Figure 1.2 Schematic of a fuel cell polarization curve, with contributions of various overpotentials as indicated by the shaded regions. The power density (dotted line) is the product of the cell voltage and current density.

1.2.3 Component Requirements

In order to maintain a sufficiently high power density, or a sufficiently high cell voltage, for a given current density (Figure 1.2), it is necessary to minimize overpotentials. Cross-over effects can be reduced by an appropriate choice of the electrolyte material, specifically one with minimal-to-no electronic conductivity, and by optimizing its fabrication so as to obtain high density membranes with low porosity. Proper sealing of the anode and cathode chambers is also required.

The thickness of the membrane should be reduced so as to minimize the total voltage loss due to ion conduction since

$$\eta_{iR} = jR = j \frac{L}{\sigma_H} \quad (1.7)$$

where L is the membrane thickness and σ_H is the proton conductivity. In cases where the electrolyte membrane must be very thin, the cell is fabricated to be electrode-supported, meaning that either the anode or cathode is fabricated to be the structural support of the assembly.

The activation overpotential is related to the rate at which the half-cell reactions can occur at the electrodes and is often expressed as

$$\eta_{act} \approx \frac{RT}{\alpha nF} \ln \left(\frac{j}{j_0} \right) \quad (1.8)$$

where j_0 is the exchange current density which flows under zero overpotential, and α is termed the exchange coefficient, an indicator of the electrochemical activity under non-equilibrium conditions (i.e., at non-zero overpotentials). Equation (1.8) describes how much voltage is required to attain a specific electrochemical current flow at the electrodes. If the activity of the electrode is high, less driving force, or overpotential, is

required to attain sufficient currents. From the equation, one can see that larger values of j_0 and α are desirable for lowering η_{act} . The exchange current density, which is usually normalized by the macroscopic electrode area, can be improved by increasing the number of active sites per electrode area or by improving the intrinsic activity of the electrode. On the other hand, the exchange coefficient is geometry-independent and can only be affected by changing material properties. The derivation of Equation (1.8) is detailed in Appendix A.1.

The requirements for electrodes are arguably more demanding than those for the electrolyte membrane. Because electrochemical reactions involve gas phase species, electrons and ions, electrodes are required to transport each of these species. That is, to minimize activation losses, η_{act} , electrodes must not only be catalytically active, as discussed in the previous paragraph, but must also transport participating electrons and ions to and from active sites. Furthermore, they must have sufficient porosity to reduce mass transport losses, η_D . More often than not, one material cannot satisfy all of these requirements, so a porous composite of electrolyte and (metal) catalyst particles is typically employed as the electrode (Figure 1.3). Typically, the electrolyte and catalyst are pure ion- and electron-conductors, respectively, and thus the locations at which these two solid phases come together to meet the gas phase are critical; the site at which these three phases meet is termed the triple-phase boundary (TPB). Thus, the ideal electrode structure requires interconnected ionic, electronic and gas pathways while maximizing the number of triple-phase boundary sites. Any catalyst or electrolyte particle that is isolated from its own network will not contribute to the total electrochemical current.

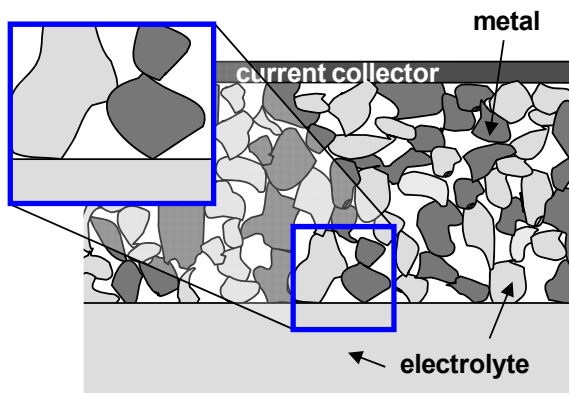


Figure 1.3 Schematic of a typical composite electrode comprised of electrolyte and catalyst/electronically-conducting particles in a porous network. Enlargement shows a triple-phase boundary site, with the electrolyte particle connected to the electrolyte membrane and the metal/catalyst particle connected to a neighboring particle (and out to the current collector).

1.2.4 Types of Fuel Cells

Several different types of fuel cells, with operating temperatures ranging from room temperature up to as high as 1000 °C, are being actively pursued today. The operating temperature of a fuel cell is dictated by that required to attain sufficiently high ionic conductivity in the electrolyte, and thus, different fuel cell types are distinguished by their electrolytes. Table 1.1 shows a brief summary of the common fuel cells and their general characteristics. A good overview of the different types of fuel cells can be found in a review article by Carrette et al.⁴ A more thorough reference is a text book by Larminie and Dicks.⁵

Table 1.1 Common types of fuel cells and their primary characteristics.^{4, 5}

Fuel Cell Type	Oper. Temp. [°C]	Electrolyte	Mobile Ion	Fuel
PEMFC polymer electrolyte membrane fuel cell proton exchange membrane fuel cell	70–110	sulfonated polymers	H ₃ O ⁺	H ₂ CH ₃ OH
AFC alkali fuel cell	100–250	(Na,K)OH _(aq)	OH [−]	H ₂
PAFC phosphoric acid fuel cell	150–220	H ₃ PO ₄	H ⁺	H ₂
MCFC molten carbonate fuel cell	500–700	(Na,K) ₂ CO ₃	CO ₃ ^{2−}	hydrocarbons CO
SOFC solid oxide fuel cells	700–1000	(Zr,Y)O _{2−δ}	O ^{2−}	hydrocarbons CO

In general, operation at high temperatures improves fuel flexibility, reducing reliance on hydrogen gas as the primary fuel, and increases the efficiency of fuel cells due to faster reaction kinetics at the electrodes. However, at temperatures close to 1000 °C, material compatibility between supporting components becomes a problem, and repeated thermal cycling is often not possible. Consequently, high temperature fuel cells, such as solid oxide fuel cells (SOFCs) and molten carbonate fuel cells (MCFCs), are typically employed for stationary power generation. At lower temperatures, rapid thermal cycling is possible, as indicated by the demonstration of fuel cell vehicles based on polymer electrolyte membrane fuel cells (PEMFCs), but operation with sufficient power output requires the use of expensive catalysts such as platinum. At intermediate temperatures, the benefits of both improved reaction kinetics and ease of thermal cycling are retained; however, fuel cells operating at these temperatures are based on corrosive liquid electrolytes. While liquid electrolytes have the benefit of high ionic conductivities, they also can cause the dissolution of catalysts, resulting in reduced activity.

Consequently, substantial effort in the fuel cell community has been directed towards lowering the temperature of operation of SOFCs to 400–600 °C (called intermediate temperature solid oxide fuel cells, ITSOFCs) via the research and development of electrolyte and electrode materials with sufficient ionic conductivities and electrocatalytic activities at lower temperatures. A recently discovered class of fuel cells which operate in this preferred intermediate temperature range is solid acid fuel cells, the subject of this work.

1.3 Solid Acid Fuel Cells

1.3.1 Solid Acid Compounds

A relatively new addition to the fuel cell community is the solid acid fuel cell (SAFC), first demonstrated in 2001 and operable at warm temperatures of 100–300 °C, depending on the solid acid electrolyte. Solid acid compounds have physical and chemical similarities to normal salts and normal acids; they dissolve in water like common salts but are able to donate acidic protons like typical acids. Common stoichiometries are MHXO_4 , MH_2XO_4 and $\text{M}_3\text{H}(\text{XO}_4)_2$ where M can be Cs, Rb, K, Na, and even NH_4 , and X can be P, S, Se, and As. Typical room temperature structures of solid acids consist of hydrogen-bonded XO_4 groups, with the dimensionality of the hydrogen bonding network being dictated by the $\text{H}:\text{XO}_4$ ratio. On heating to warm temperatures of $\sim 100\text{--}300$ °C, a subset of these compounds undergo a phase transition to a high temperature disordered phase at which the proton conductivity is increased by several orders of magnitude. Since discovery of this phenomenon for CsHSO_4 and

CsHSeO_4 in 1982,⁶ the so-called superprotonic transition has been identified in additional solid acid compounds, such as $\text{Rb}_3\text{H}(\text{SeO}_4)_2$,⁷ $(\text{NH}_4)_3\text{H}(\text{SO}_4)_2$,⁸ $\text{Cs}_2(\text{HSO}_4)(\text{H}_2\text{PO}_4)$,⁹ CsH_2PO_4 ,¹⁰ and even $\text{CsHPO}_3\text{H}^{11}$ (Figure 1.4).

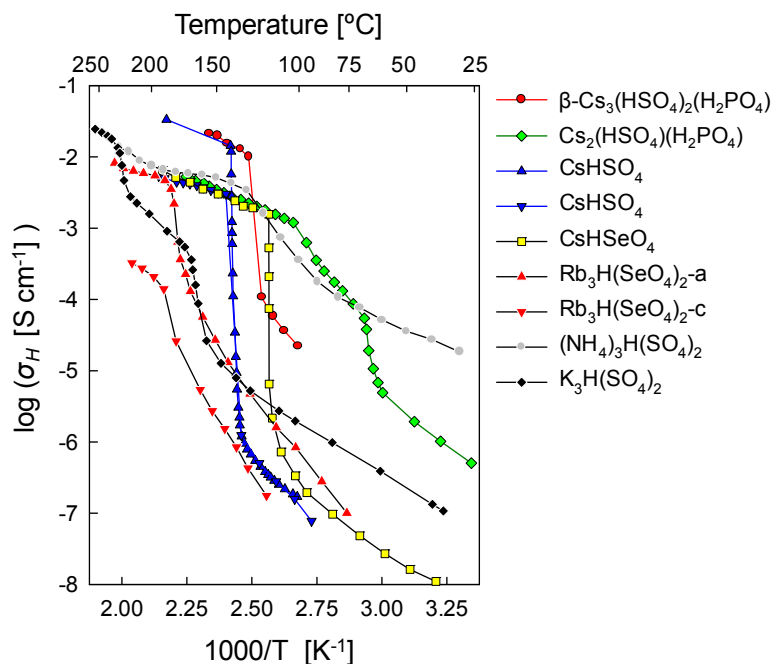


Figure 1.4 The proton conductivity, σ_{H} , of several solid acid compounds observed to exhibit a superprotonic phase transition, after Haile et al.¹² and references therein.

Presently, among the solid acid compounds known to have a superprotonic phase transformation, CsH_2PO_4 is the most promising as a fuel cell electrolyte.^{3, 10} On heating, CsH_2PO_4 undergoes a monoclinic-to-cubic phase transition at $\sim 228^\circ\text{C}$ at which the proton conductivity jumps by almost four orders of magnitude to $> 10^{-2} \text{ S cm}^{-1}$ (Figure 1.5a). The monoclinic structure (Figure 1.5b) is comprised of phosphate groups linked in chains by double-minima hydrogen bonds, charge balanced by Cs cations. On heating, the structure transforms to a CsCl-type cubic structure with Cs at the corners and a phosphate group at the center. The phosphate group is often represented (as in Figure

1.5b) as equally occupying six symmetrically-equivalent crystallographic positions, and in essence, is rapidly rotating, enabling proton transfer between neighboring phosphate groups (Figure 1.6). Despite the disorder in structural oxygen, X-ray diffraction patterns of the superprotonic phase reveal sharp diffraction peaks due to the fixed positions of the cesium and phosphorus atoms in the lattice.

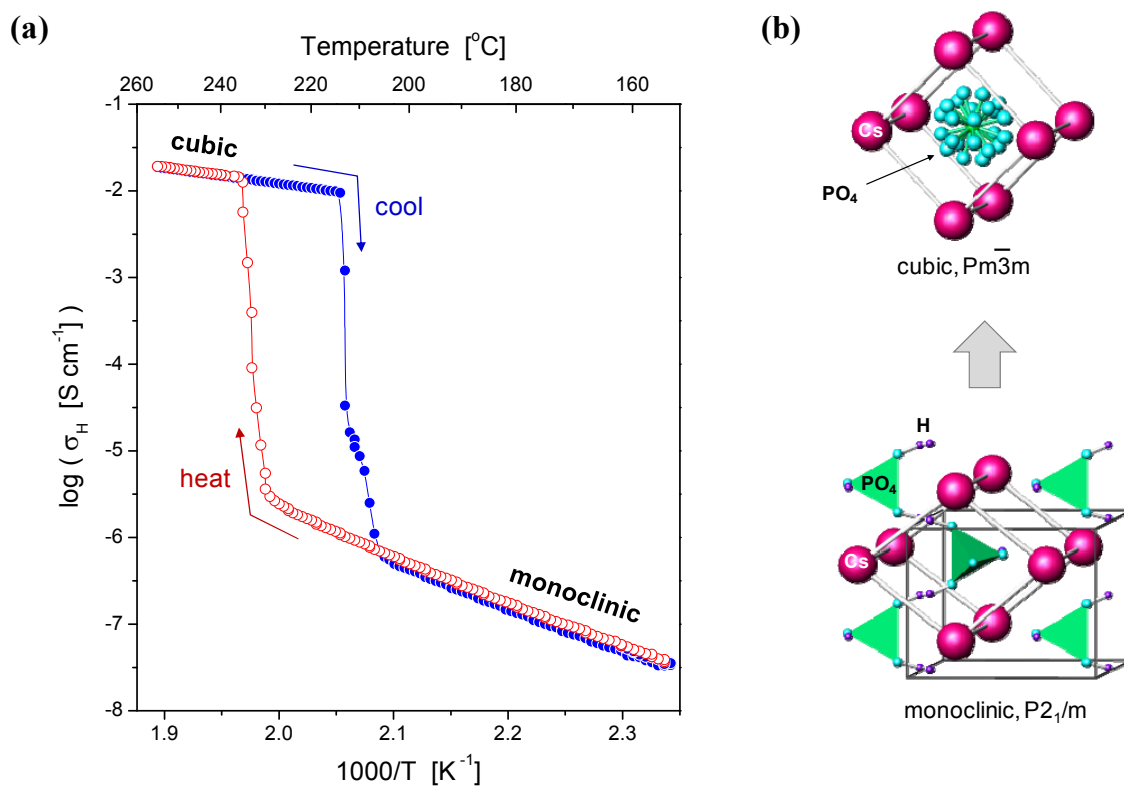


Figure 1.5 Superprotonic phase transition in CsH_2PO_4 : (a) Plot of proton conductivity as a function of temperature, on heating and cooling, in flowing N_2 with ~ 0.4 atm H_2O , (b) Unit cells of monoclinic and cubic phases, the latter with high disorder in oxygen (PO_4) and hydrogen (not shown).

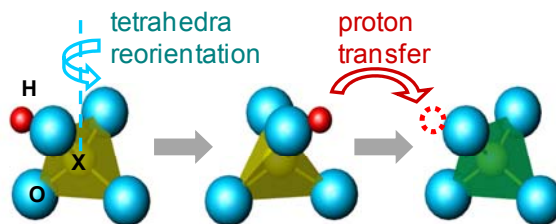


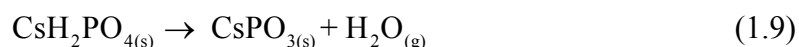
Figure 1.6 Schematic of the proton conduction mechanism in CsH_2PO_4 .¹³

1.3.2 CsH_2PO_4 as an Electrolyte: Benefits and Challenges

Solid state electrolytes which facilitate anhydrous proton transport hold great promise for fuel cell applications. SAFCs operate at temperatures near 250 °C using truly solid electrolytes that exhibit remarkably high, liquid-like proton conductivities. They retain the benefits of the “warm” operating temperatures while avoiding challenges associated with corrosive liquid electrolytes. The absence of corrosive liquids and the lower operating temperatures, compared to SOFCs, means that auxiliary components can be fabricated from relatively inexpensive stainless steel. The higher operating temperature of SAFCs, compared to PEMFCs, suggests higher fuel flexibility and the potential to eliminate costly precious metal catalysts in the electrodes. Equally important, solid acid electrolytes are true proton conductors and do not rely on a water molecules as carriers to transport protons, as is the case with polymer membranes. Because polymer membranes must remain sufficiently hydrated to maintain adequate proton conductivities, they require operation below 100 °C and the use of complex water management systems to maintain sufficient hydration near the anode while minimizing flooding at the cathode.⁴ SAFCs do not require such water management systems and can operate well beyond 100 °C. The absence of water in the membrane also means that SAFCs can

operate with methanol as a fuel with virtually none of the cross-over observed with polymer membranes.^{3, 4, 14}

Although CsH_2PO_4 provides many advantages as an intermediate fuel cell electrolyte, it has some challenges of its own. CsH_2PO_4 reaches its superprotonic phase at relatively high temperatures, compared to other solid acid compounds, most of which transform at temperatures below 150 °C (Figure 1.4); at the higher operating temperatures for CsH_2PO_4 , dehydration has a greater tendency to occur via the reaction



Therefore, a sufficient water vapor pressure must be supplied in the fuel and oxidant streams to suppress the dehydration process. A thorough study of the phase stability for CsH_2PO_4 has been carried out^{15, 16} and serves as a guide for stable operating conditions. For example, a minimum water partial pressure of ~ 0.15 atm is required for reliable operation at 250 °C. Under sufficient water partial pressures, one can observe the proton conductivity behavior (like that shown in Figure 1.5a) to be reproducible over many temperature cycles.

While solid acid compounds have tendency to dehydrate at elevated temperatures, they are readily soluble in liquid water. This is less of a concern during operation due to operating temperatures well above 100 °C; however, during on-off cycling, humid reactant/product gases must be purged out of the system to avoid condensation.

A final challenge with solid acid compounds is related to their interesting mechanical properties. While solid acid compounds are relatively brittle in the low conductivity phase, they are highly plastic in the superprotonic phase, as has been reported specifically for CsHSO_4 and CsH_2PO_4 .^{3, 17–20} This has implications during fuel

cell operation because sealing of the anode and cathode chambers are done so by the application of pressure which can cause irreversible deformation of the electrolyte over the course of operation. Avoiding this problem is not extremely difficult. It has been reported, in the case of CsH_2PO_4 , that the strain rate can be reduced by a factor of five by adding ~ 10 wt% of $2\text{ }\mu\text{m}$ SiO_2 particles, with only a 20% drop in the proton conductivity at fuel cell operating temperatures.³

The challenges associated with CsH_2PO_4 as an electrolyte are not insurmountable by any means. CsH_2PO_4 remains, at present, the ideal electrolyte for SAFCs. Nevertheless, the search for additional application-relevant solid acid proton conductors is ongoing. Among the solid acid compounds known to undergo a superprotonic phase transition, almost all are based on sulfates and selenates which are unstable under the reducing conditions of the anode, reacting with H_2 to form H_2S or H_2Se .²¹ Of the phosphate-based compounds possible, only that with Cs (the largest of the alkali metal cations) exhibits the superprotonic phase transition. A recently identified phosphite compound, CsHPO_3H ,¹¹ which exhibits a relatively low phase transition temperature of $\sim 140\text{ }^\circ\text{C}$, has not been pursued extensively due to expectations that it would be unstable at oxidizing conditions, although related compounds show some promise as fuel cell electrolytes.^{22,23} Superprotonic solid acid compounds are a relatively unexplored class of materials with a rich chemistry that has not yet been fully exploited. As demonstrated in the recent report of a water-insoluble, superprotonic, barium-potassium compound²⁴, there is much room for the discovery and development of additional application-relevant proton conductors.

1.3.3 Solid Acid Fuel Cell Performance

Solid acid fuel cells based on CsH_2PO_4 as an electrolyte membrane, operating on humidified H_2 and O_2 , have been demonstrated in literature to have peak power densities as high as 400 mW cm^{-2} at 248°C .²⁵ This demonstration was based on thin $25\text{--}36 \mu\text{m}$ CsH_2PO_4 membranes and composite electrodes comprised of a mixture of nanoparticulate Pt, carbon-supported Pt, and micron-scale CsH_2PO_4 particles. Despite the high Pt loadings used, $\sim 8 \text{ mg cm}^{-2}$ for each electrode, large activation overpotentials at the electrodes were found to limit the overall performance.¹⁰

Substantial progress has been made since the first demonstration of CsH_2PO_4 -based SAFCs in 2004. SAFCs based on Pt- CsH_2PO_4 composite electrodes readily operate with 180 mW cm^{-2} peak power densities at $\sim 250^\circ\text{C}$ and degrade negligibly over several hundred hours of continuous operation.³ Moreover, the power densities have been demonstrated to be scalable to 20-cell stacks, with each cell comprised of a $50 \mu\text{m}$ CsH_2PO_4 membrane and a total (anode + cathode) Pt loading of 4 mg cm^{-2} . SAFCs have also demonstrated resistance to poisoning by impurities in the fuel stream, thus improving fuel flexibility by lowering the cleanup requirements of reformed fuels. Specifically, a tolerance to H_2S , NH_3 , CH_3OH , CH_4 , C_3H_8 and CO at 100 ppm, 100 ppm, 5%, 5%, 3%, and 20%, respectively, have been reported.³

Although significant progress in SAFC development has been made, they are not yet competitive with those of conventional polymer and solid oxide fuel cells, primarily due to high activation overpotential losses at the electrodes. While it has been possible to fabricate thin electrolyte membranes to improve overall fuel cell performance, achieving electrodes with high activity or competitive platinum loadings remains a challenge. The

current Pt loadings of 4 mg cm^{-2} is over an order of magnitude higher than loadings of $\sim 0.1 \text{ mg cm}^{-2}$ in PEMFC electrodes.²⁶ This is not necessarily surprising since the electrode requirements for SAFCs are in a class of their own, and the tools/processes required to optimize the electrode microstructure are still under development. Advancement of SAFCs requires the design of new electrode structures with improved performance and the development of new materials with high activity under SAFC operating conditions. Much of this work is presently under investigation, both by fabrication of high performing electrode structures^{27, 28} and by fundamental mechanistic studies of electrocatalysis, discussed in this work.

1.4 Electrode Reactions in Solid Acid Fuel Cells

1.4.1 Hydrogen Electro-oxidation and Oxygen Electro-reduction

For a majority of fuel cells, the kinetics of oxygen electro-reduction is much slower than that of hydrogen oxidation. In the case of PEMFCs, the exchange current density, j_0 in Equation (1.8), for hydrogen oxidation is typically five to six orders of magnitude greater than that for oxygen reduction.^{26, 29} There is some consensus on the hydrogen oxidation mechanism on Pt; specifically, hydrogen dissociatively adsorbs onto Pt and the resulting hydrogen is oxidized to protons and electrons, with dissociative adsorption being rate limiting.²⁶ On the other hand, oxygen reduction is considerably more complex. The oxygen reduction reaction, being a four electron transfer reaction, has at least four intermediate transfer steps. The reduction mechanism requires the dissociation of a strong O-O double bond and is further complicated by the formation of

stable adsorbed intermediates such as M-O and M-OH (where M = metal catalyst).²⁶ These are a few reasons why the mechanism of oxygen reduction has not yet been fully elucidated even though it has been studied in the fuel cell community for decades. It is unclear how much information from the PEMFC literature can be translated to SAFCs due to their different operating temperatures and environmental conditions (i.e., presence of liquid water).

In the case of SAFCs, it has been shown that the electrode resistance at the cathode is roughly two orders of magnitude larger than at the anode.¹⁰ To a first approximation, this activity difference between the anode and cathode is less drastic than that observed in PEMFCs. Thus, while most of the focus in the PEMFC community has been to improve electrocatalysis at the cathode, SAFCs stand to gain from improving the performance (and lowering the cost) of both the anode and cathode.

1.4.2 Electrochemical Reaction Pathways

Elucidation of reaction kinetics at the electrodes can provide valuable information that can be used to rationally design electrode structures and/or screen for new catalysts. However, reaction pathways for virtually every type of fuel cell remain elusive. Like heterogeneous catalysis, electrochemical catalysis relies on the intimate contact of a solid phase (catalyst) with a liquid or gas medium. However, electrocatalysis is notably more complicated because carrying out reactions that involve gas phase species, electrons and ions requires the presence of materials that can transport each of these species. Figure 1.7 shows some possible mechanisms for hydrogen oxidation and oxygen reduction via the triple-phase boundary pathway. From Figure 1.7, the complexity of the oxygen reduction mechanism is apparent simply from entertaining the number of possible reaction steps

that can occur compared to hydrogen oxidation. In the case of hydrogen oxidation, hydrogen gas can adsorb (or dissociatively adsorb) directly onto the triple-phase site and undergo charge transfer, or, it can adsorb on the catalyst at some distance away in which case the adsorbed hydrogen must diffuse across the metal surface to be oxidized into protons and electrons at the triple-phase boundary. In the case of oxygen reduction, direct adsorption of O_2 and desorption of H_2O (Figure 1.7b) is the simplest pathway possible, but many other pathways are possible. For example, oxygen can adsorb as neutral (or partially reduced) species onto the metal catalyst before diffusing to the TPB site to be (further) reduced by incoming electrons and protons (Figure 1.7c). In yet another scenario, protons can be reduced to neutral hydrogen which then diffuses to the adsorbed oxygen species (Figure 1.7d). The rate at which each of these possible reaction steps can occur (if at all) depends on material properties (catalyst activity, ionic or electrical conductivity, solid or liquid), characteristics of the species (surface diffusion coefficients, bond strengths), electrode structure (number and identity of active sites) and also environmental conditions (temperature, gas environment, and partial pressure).

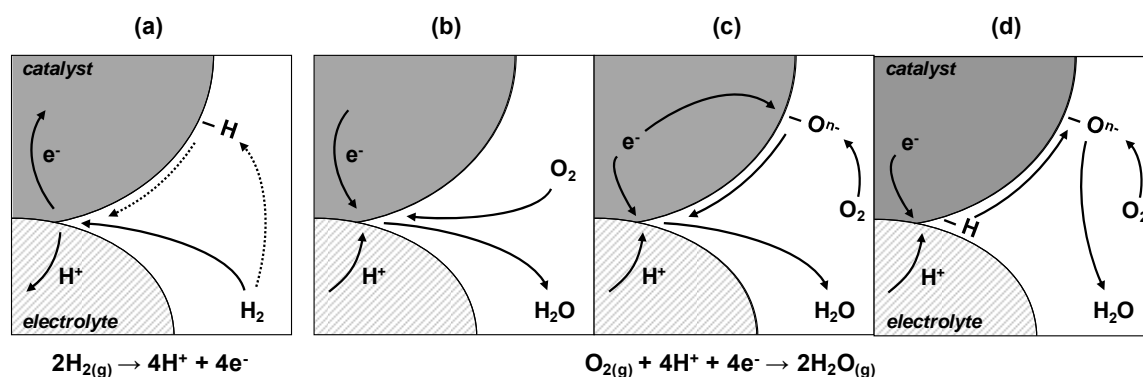


Figure 1.7 Simplified cartoon of some possible triple-phase boundary pathways in (a) hydrogen electro-oxidation and (b–d) oxygen electro-reduction.

Depending on the characteristics of the materials, it is entirely possible that the triple-phase boundary pathway is not relevant at all. While there are many systems in which the triple-phase boundary pathway is preferred, there are also a number of electrode systems which catalyze electrochemical reactions via a two-phase boundary pathway. This case can occur for electrodes which have both ionic and electronic conductivity, for example, cerium oxide and some perovskite oxides,³⁰ both of which are materials of interest for SOFCs. Many BCC and FCC metals, particularly palladium, are known to have a finite solubility of atomic hydrogen and therefore can transport both electrons and neutral species.³¹ We present a (simple) schematic (Figure 1.8) for the latter case, comparing the triple-phase and two-phase boundary pathways for a metal catalyst in contact with a proton conductor. One can immediately see that, if the hydrogen can be transported through the metal, the active area is increased significantly, from a region confined near the TPB (Figure 1.8a) to the entire metal | electrolyte interfacial area. Whether a given electrode | electrolyte system catalyzes an electrochemical reaction via the triple-phase or two-phase pathway can have significant consequences in electrode design. In the case of an electrochemical reaction confined to TPB sites, a logical route would be to use catalyst nanoparticles to maximize the number of such sites (Figure 1.3), whereas a reaction occurring via the two-phase boundary pathway calls for maximizing the electrode | electrolyte interface.

It is clear that identification of the rate-limiting steps in electrochemical reactions is crucial to the advancement of SAFCs. Because the SAFC is the solid state system to operate at low-to-intermediate temperatures, there is a scarcity of electrochemical

information the catalyst-solid acid system. In this work, we present our efforts to develop and employ novel tools to elucidate the reaction pathways in solid acid fuel cell systems.

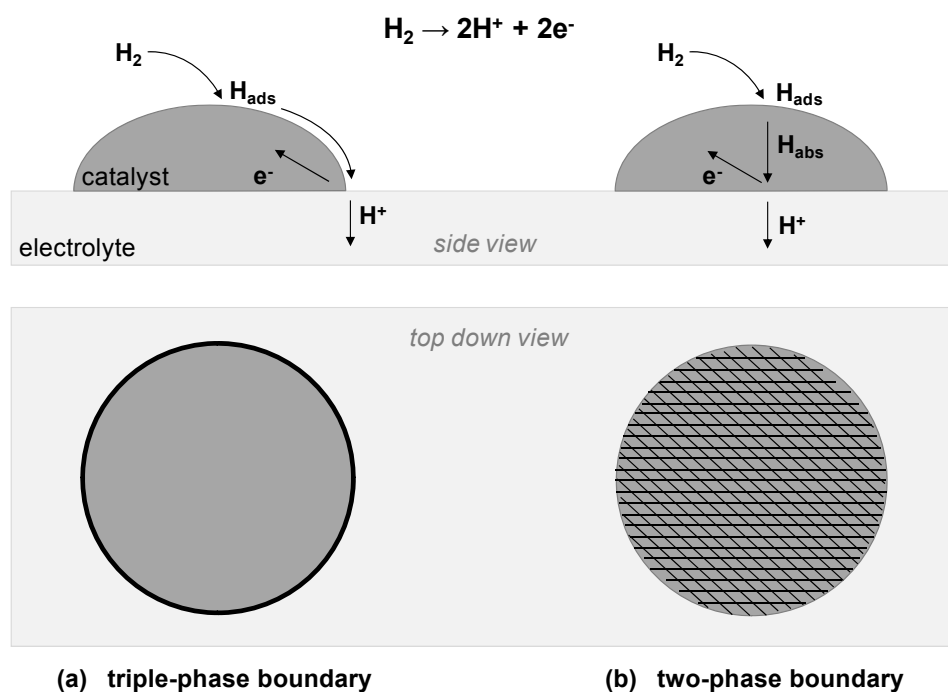


Figure 1.8 Comparison of triple-phase and two-phase boundary pathways for a metal catalyst in contact with a proton-conducting electrolyte.

Chapter 2 Experimental Methods

2.1 AC Impedance Spectroscopy

2.1.1 Basic Principles

Alternating current impedance spectroscopy (ACIS) is a powerful technique for characterizing a wide variety of electrochemical systems which undergo a great number of microscopic processes when stimulated with an electric field. The net current flowing through the system depends on the properties of the materials under investigation as well as the interfaces present. Processes occurring within the electrolyte, e.g., in the crystal lattice or across grain boundaries, as well as at electrode|electrolyte interfaces often occur with different characteristic timescales. ACIS holds the potential to distinguish between such electrochemical processes and determine the contribution of individual electrode or electrolyte processes which often elude DC techniques.^{32–34}

In a typical AC impedance measurement, a low amplitude sinusoidal voltage perturbation is applied to the system of interest and the resulting current measured, or vice versa (Figure 2.1a). The effectiveness of ACIS lies in the application of a small signal perturbation of various frequencies. Each frequency stimulates a specific electrochemical response that depends on the behavior of charged species undergoing various processes, each with its own characteristic timescale. The input signal, $V(t)$, is described by the complex time-dependent wave function

$$V(t) = V_0 e^{j\omega t} \quad (2.1)$$

where V_0 is the amplitude, ω is the angular frequency ($2\pi f$), and $j = \sqrt{-1}$. For a signal small enough to probe a linear regime of the current-voltage characteristics of the system, the current response generated by this potential stimulus is sinusoidal with the same angular frequency and shifted by the phase angle, θ (Figure 2.1b). The current output, $I(t)$, can be expressed as

$$I(t) = I_0 e^{j(\omega t + \theta)} \quad (2.2)$$

where I_0 is the amplitude of the output current signal. The impedance can be written as

$$Z(\omega) = \frac{V(t)}{I(t)} = |Z| e^{-j\theta} \quad (2.3)$$

or

$$Z(\omega) = |Z| \cos \theta - j|Z| \sin \theta = Z_R - jZ_I \quad (2.4)$$

where $Z_R = |Z| \cos \theta$ and $Z_I = |Z| \sin \theta$ are the real and imaginary parts of the impedance, respectively, and $|Z|$ is the impedance modulus. A particularly useful representation of impedance spectra is the Nyquist plot, which is a plot of the impedance in the complex plane, $-Z_I$ against Z_R , both of which are parametric functions of frequency (Figure 2.2). In the Nyquist representation, electrochemical processes occurring with sufficiently different characteristic timescales (typically at least two orders of magnitude apart) are represented by separate arcs along the real axis, and the resistance associated with each arc is represented by the width of the arc on the real axis. Other common representations of impedance data are Bode-Bode plots, Figure 2.3(b–c), which are plots of $|Z|$ and θ as functions of frequency, computed using the relations

$$|Z(\omega)| = \sqrt{Z_R^2 + Z_I^2} \quad (2.5)$$

$$\theta = \tan^{-1} \left(\frac{Z_I}{Z_R} \right) \quad (2.6)$$

Bode-Bode plots, although less commonly used for data presentation than Nyquist plots, are all the same employed for analysis of data. The existence of a phase shift between input voltage and output current, Figure 2.1b, (or in other words, an imaginary component in the impedance response) is a consequence of time-dependent nature of capacitive processes occurring in the system, for example, the dielectric properties of the bulk electrolyte, or the charging of interfaces. Figure 2.3 is a simple schematic illustrating how an alternating potential affects the movement of a charge species at different perturbation frequencies and the spectral features generated as a consequence of interactions between the charged species and its environment. At infinitely high frequencies, the charged species in the system samples an infinitely small distance in the bulk of the electrolyte; as such, the resistance is zero. At finite but high frequencies, the species can traverse further and interact with the bulk lattice, yielding a finite impedance. As the frequency is further lowered, interaction with grain boundaries, followed by electrode | electrolyte interfaces, occurs. For each of these processes, the corresponding arc in the spectrum describes resistive and capacitive behavior of that process. At infinitely low frequencies, all transient processes have reached steady state; the impedance of the system corresponds to the resistance of all the processes in the system, equivalent to that measured under DC conditions. Grain bulk and grain interior processes typically have characteristic frequencies that are relatively high and therefore yield arcs that are well-separated from electrode arcs. It should be noted that while only one

electrode arc is shown in Figure 2.2, it is possible and even common to observe multiple electrode arcs.

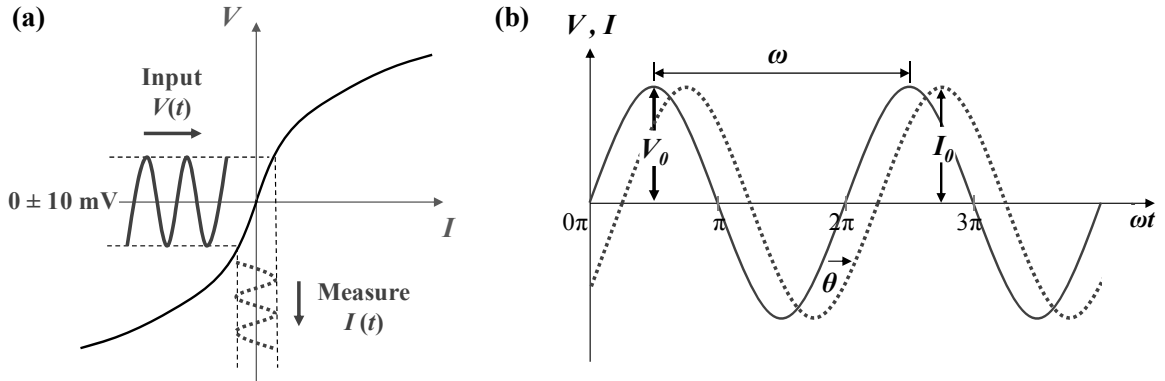


Figure 2.1 Basics of ACIS: (a) Depiction of an alternating voltage source and current response in relation to a generic polarization curve and (b) the relationship between input voltage and output current.

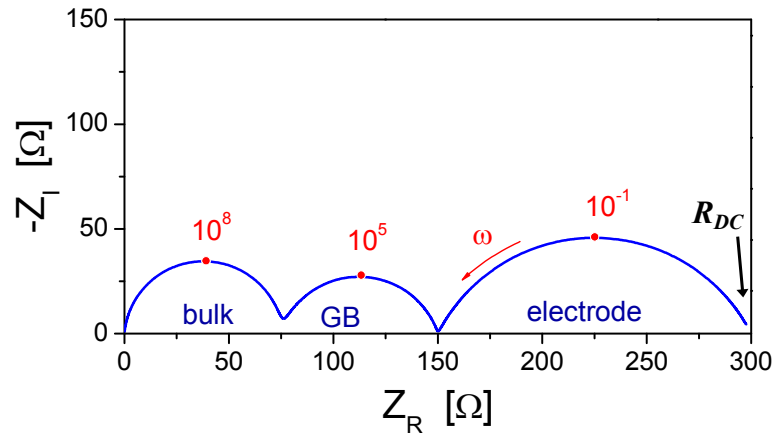


Figure 2.2 Simulated impedance spectrum, in a Nyquist representation, for a generic electrochemical system showing arcs for electrolyte processes (bulk and grain boundary, GB) and electrode processes. At low frequencies, the impedance approaches the DC limit (R_{DC}), that is, the slope of the polarization curve, Figure 2.1a.

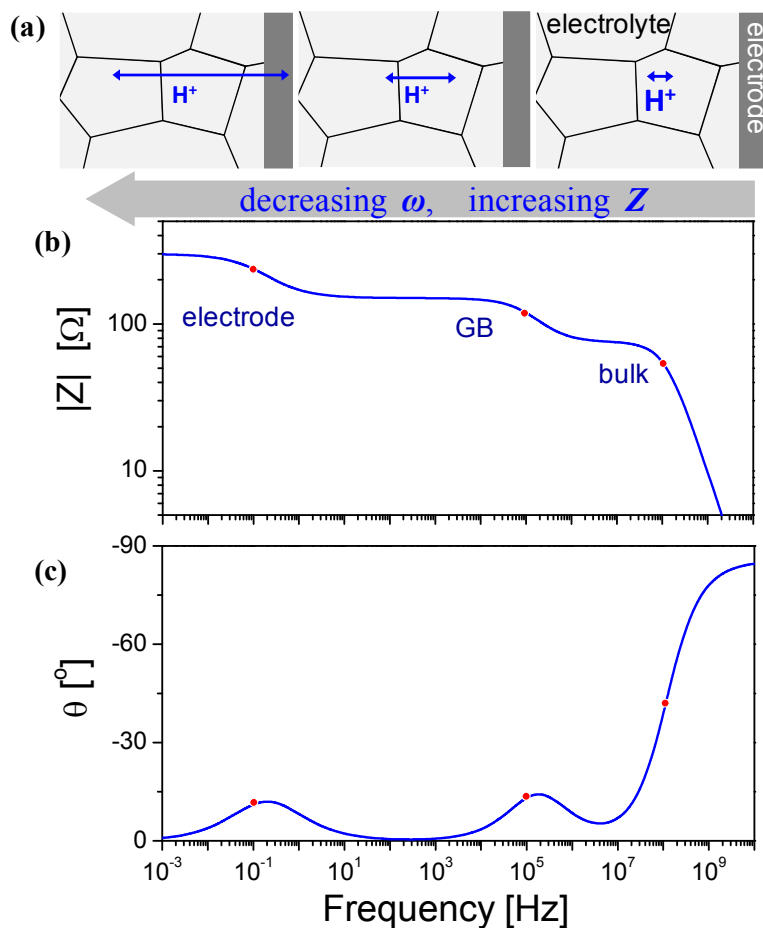


Figure 2.3 A simple cartoon depicting the movement of a proton under a perturbed electric field at various frequencies and how it gives rise to the shape of $|Z|$ and θ in the Bode-Bode plots. By convention, data are plotted as a function of f rather than ω .

2.1.2 Data Analysis: Equivalent Circuit Models

Because the fundamental principles that govern charge are similar between electrons and ions, it is possible to use electrical circuits to represent processes occurring in electrochemical systems. Table 2.1 shows some common circuit elements and their impedance responses. To analyze electrochemical data, one can build a circuit models comprised of a combination of discrete circuit elements.

Table 2.1 Impedance response of frequently encountered circuit elements.

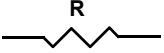

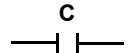
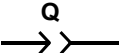
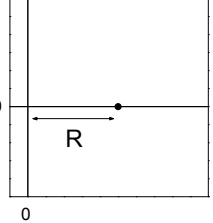
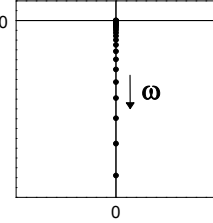
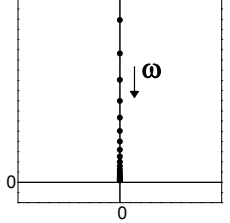
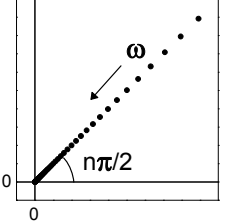
	(a)	(b)	(c)	(d)
Circuit				
Impedance $Z(\omega)$	R	$j\omega L$	$\frac{1}{j\omega C}$	$\frac{1}{C_Q(j\omega)^n}$
Nyquist plot $(-Z_I \text{ vs. } Z_R)$				

Table 2.2 shows the impedance response for several commonly used electrical sub-circuits. One particular sub-circuit frequently employed for data analysis is comprised of a resistor and capacitor in parallel, denoted here as RC. The RC sub-circuit generates a perfect semi-circle on the Nyquist plot with the center of the semi-circle lying on the real axis (Table 2.2a). The impedance of the RC circuit can be computed readily from their individual elements.

$$Z_{RC}(\omega) = \left(\frac{1}{R} + j\omega C \right)^{-1} = \frac{R}{1 + \omega^2 C^2 R^2} - j \frac{\omega C R^2}{1 + \omega^2 C^2 R^2} \quad (2.7)$$

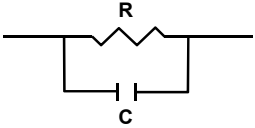
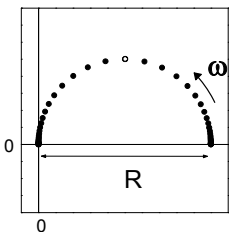
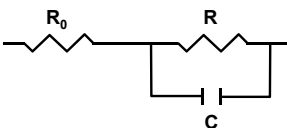
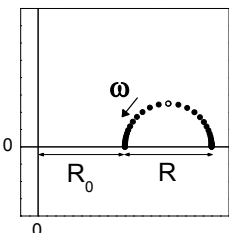
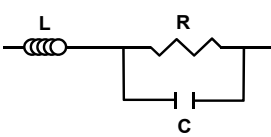
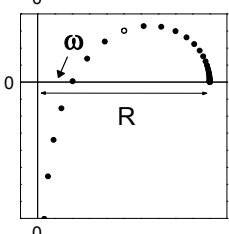
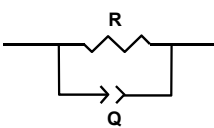
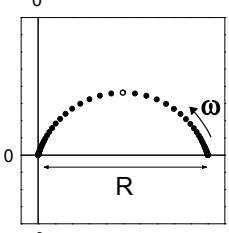
The width of the arc corresponds to resistance, R , and the capacitance, C , can be determined using the relation

$$\omega_0 = \frac{1}{\tau_0} = \frac{1}{RC} \quad (2.8)$$

where ω_0 is the characteristic frequency, located at the apex of the semi-circle (Table 2.2a), and τ_0 is the characteristic timescale. It can be shown that multiple such sub-circuits, constructed in series, will yield separate arcs in the spectrum, provided that the

characteristic frequencies are sufficiently different from one another, as illustrated in Figure 2.4a for three parallel RC sub-circuits in series. The resistances and the characteristic frequencies of each process can be extracted directly from the plot, and the corresponding capacitances can be computed using Equation (2.8). Table 2.2 shows several additional useful sub-circuits, for example, the R-RC (resistor in series with RC), which results in an offset of the arc from the origin along the real axis (Table 2.2b).

Table 2.2 Impedance response of frequently encountered sub-circuits. The unfilled data marker in each plot corresponds to the characteristic frequency, ω_0 .

Circuit	Impedance $Z(\omega)$	Nyquist plot ($-Z_I$ vs. Z_R)
(a) 	$\frac{R}{1 + \omega^2 C^2 R^2} - j \frac{\omega C R^2}{1 + \omega^2 C^2 R^2}$	
(b) 	$R_0 + \frac{R}{1 + \omega^2 C^2 R^2} - j \frac{\omega C R^2}{1 + \omega^2 C^2 R^2}$	
(c) 	$\frac{R}{1 + \omega^2 C^2 R^2} - j \omega \frac{R^2 C - \omega^2 C^2 R^2 L - L}{1 + \omega^2 C^2 R^2}$	
(d) 	$\left(\frac{1}{R} + Y(j\omega)^n \right)^{-1}$	

Of note is the L-RC circuit (inductor in series with RC) since this is commonly observed in experimental systems. In electrochemical measurements, electrical leads attached to (or in series with) the sample of interest can behavior like inductors. Because the impedance of an inductor increases with frequency ($Z_L = j\omega L$), the contribution of inductance is greater at higher frequencies at which the cell impedance (described by RC in this case) can often be “pulled” below the real axis (Table 2.2c). Such an effect may not only mask the true resistance (which is higher than the experimentally observed arc width) but also shift the characteristic frequency from the apparent apex of the arc.

In practice, impedance arcs are rarely perfect semi-circles but, rather, are slightly depressed. Graphically, this means that the arc can be visualized as a portion of a circle whose center lies below the real axis (Table 2.2d). This experimental observation has been treated by introducing an empirical circuit element, called the constant phase element, denoted as Q. The impedance response of the constant phase element is

$$Z_Q = \frac{1}{Y(j\omega)^n} \quad (2.9)$$

where Y is a constant and $0 \leq n \leq 1$. The constant phase element can be thought of as having resistive and capacitive character; Equation (2.9) corresponds to a capacitor with capacitance Y when $n = 1$, and a resistor with resistance Y^{-1} when $n = 0$. Like the RC circuit, the RQ circuit generates an arc in the Nyquist plot, but for $n < 1$, the arc appears depressed (Figure 2.4b). It can be shown that the characteristic frequency, ω_{Q0} , and equivalent capacitance, C_{equiv} , of the RQ sub-circuit are

$$\omega_{Q0} = \left(\frac{1}{RY} \right)^{1/n} \quad (2.10)$$

and

$$C_{equiv} = Y^n R^{\frac{1}{n}-1} \quad (2.11)$$

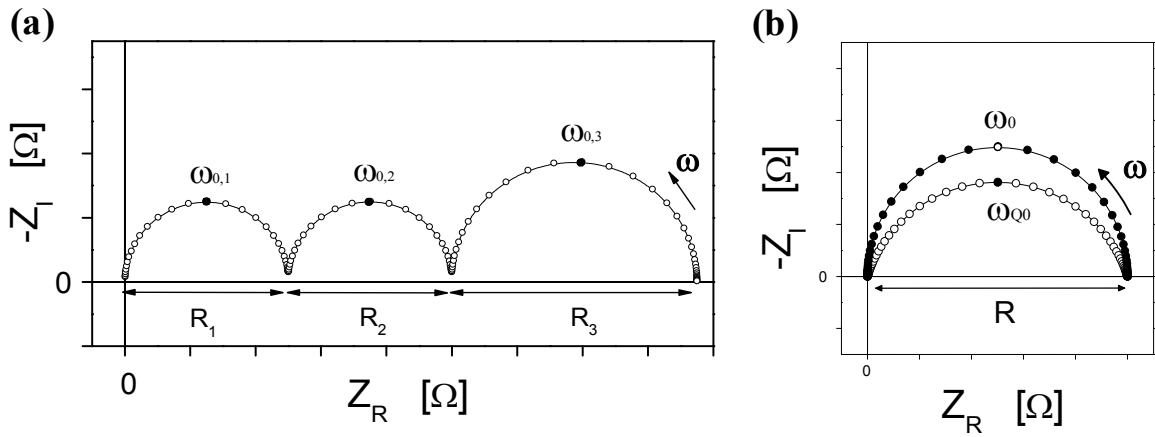


Figure 2.4 Impedance spectrum for (a) three serial RC sub-circuits with resistances and (b) a single RQ circuit plotted alongside a RC circuit.

Although the physical origin of a depressed arc in the impedance spectrum has not been fully established, there are some indications that surface roughness or spatial heterogeneities at interfaces are key factors.^{34, 35} That is, heterogeneities at an interface results in a dispersion of characteristic frequencies of a process and the spreading, or depression, of the resulting arc. This explanation is consistent with typical n values of 0.95 and 0.75–0.85 for bulk and grain boundary processes, respectively; such values for n reflect the structural variety of grain boundary types as well as the expectation that ion transport across grain boundaries is more readily affected by impurities than bulk transport. The behavior of the electrode response varies widely and depends heavily on

the electrode structure and the nature of the processes probed, however, n values as low as 0.6 are not uncommon.^{36–40} Thus the Nyquist plot shown in Figure 2.2 can be represented by an equivalent circuit comprised of three RQ sub-circuits (Figure 2.5), with n values below 1.

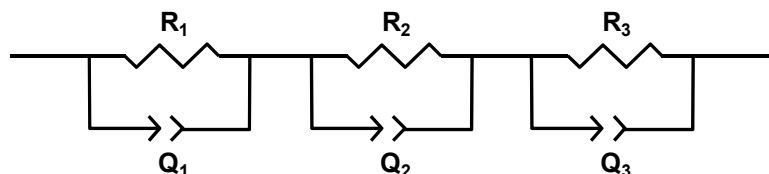


Figure 2.5 Equivalent circuit for describing three electrochemical processes occurring in series, such as those for grain interior, grain boundary, and electrode, shown in Figure 2.2.

While ion transport through the bulk of an electrolyte material, i.e., through grain interior and grain boundaries, is relatively straightforward to analyze, electrode processes are much more complicated because multiple parallel and serial pathways can be operative (Figure 1.7) and generate an ambiguous impedance response comprised of multiple arcs in the Nyquist plot (unlike the simplified single-arc electrode response shown Figure 2.2). In the absence of a physical model derived from appropriate transport equations and/or kinetic expressions, equivalent circuits are tremendously useful for analyzing impedance spectra and extracting parameters of interest. However, a given electrode response can be described by multiple equivalent circuits, each comprised of a discrete set of circuit elements in a specific configuration, and thus the choice of an equivalent circuit for analyzing data is not unique. Consequently, while equivalent circuits are extremely useful for preliminary analysis and the extraction of relevant kinetic parameters, it is not possible, without additional information about the system, to determine how these parameters relate to the physical processes of interest.

2.1.3 Data Analysis: Physical Models

There are several frequently used circuit elements which are based on physical processes. We present here the elements based on the Warburg impedance which describes an electrode process that is rate-limited by the diffusion of a reactant species to (or a product species from) the site at which an electrochemical step occurs. Consider the process shown in Figure 2.6, in which an uncharged species, R, diffuses from an interface at $x = L$ through some medium to an interface at $x = 0$ at which it undergoes a charge transfer reaction. (The medium in which R diffuses is one that is not affected by an electric field.) The Warburg impedances (Table 2.3) can be derived from Fick's second law,

$$\frac{\partial c_R}{\partial t} = D \frac{\partial^2 c_R}{\partial x^2} \quad (2.12)$$

where c_R is the concentration of species R, and D is the diffusion coefficient of R in the medium/electrolyte. In the simplest cases (as are presented here), it is assumed that charge transfer at $x = 0$ is infinitely fast such that the impedance response for the electrochemical step occurring at $x = 0$ is governed by the diffusion of R and the interfacial processes at $x = L$ at which R is supplied. Each spectrum shown in Table 2.3 is obtained by solving Equation (2.12), under a small perturbation about the equilibrium concentration, for different boundary conditions (also indicated in the table). Derivation of the Warburg impedance expressions in Table 2.3 can be found in the textbook by Orazem and Tribollet.³³ Note that the solutions to Equation (2.12) yield $n = 0.5$, but in practice, n is often allowed to vary freely during fitting of impedance data to provide an indication of non-idealities in the system.

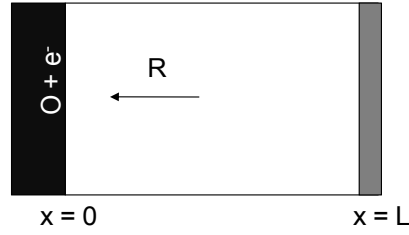


Figure 2.6 Schematic for the diffusion of R from an interface at $x = L$ to undergo charge transfer, $R \rightleftharpoons O + e^-$, at $x = 0$.

Table 2.3 Warburg impedance: solutions to Fick's second law for diffusion of an uncharged species, R. $\tau = L^2/D$ is the characteristic timescale of the diffusion process.

	(a)	(b)	(c)
	Infinite-length Warburg	Finite-length Warburg	Blocked Warburg
Circuit			
Impedance $Z(\omega)$ (where $\tau = L^2/D$)	$\frac{R_0}{(j\omega\tau)^n}$	$R_0 \frac{\tanh[(j\omega\tau)^n]}{(j\omega\tau)^n}$	$R_0 \frac{\coth[(j\omega\tau)^n]}{(j\omega\tau)^n}$
Nyquist plot ($-Z_I$ vs. Z_R)			
boundary conditions			
at $x = 0$	reversible/ fast charge transfer	reversible/ fast charge transfer	reversible/ fast charge transfer
at $x = L$	$L = \infty$, unbounded	reversible/ fast supply of R	irreversible/ slow supply of R

A characteristic feature of Warburg diffusion is a straight line, with a phase angle close to 45° , in the Nyquist plot at high frequencies. In the case of unbounded diffusion for which the boundary at $x = L$ is infinitely far away (Table 2.3a), the solution to

Equation (2.12) has the same form as the constant phase element, Equation (2.9) for $n \approx 0.5$, that is, the response approaches zero impedance at high frequencies and an infinitely large impedance at low frequencies. This is consistent with unbounded diffusion, since at zero frequency, the diffusion length (and therefore, the effective resistance) is infinitely large. In the case of bounded diffusion, i.e., $L \neq \infty$, and reversible boundary conditions, the impedance reaches a finite impedance at zero frequency (Table 2.3b) while retaining a similar linear response at high frequencies, giving it the characteristic half-teardrop shape (derivation shown in Appendix A.2). On the other hand, when diffusion is irreversibly bounded at $x = L$ (Table 2.3c), a linear regime is still evident at high frequencies, but the impedance increases suddenly at lower frequencies because the supply of the diffusing species is blocked at $x = L$.

It must be noted, again, that the use of any circuit is not unique and additional supporting evidence is required before employing any particular circuit element. In this particular case, the observation of a half-teardrop shape alone is not sufficient evidence of a process rate-limited by diffusion. For example, two (or more) electrode processes which have similar characteristic frequencies can manifest themselves as a single arc with a half-teardrop shape.

2.1.4 *Experimental Corrections*

Depending on the specific measurement of interest, it may be necessary to perform corrections to experimental data. If a high-frequency process is of interest, it is common to account for the inevitable inductance of the instrumentation by adding an inductor in series to the total circuit (assuming that inductance has been confirmed to be the culprit), as in Table 2.2c, or by applying a short-circuit correction. In the latter case,

the electrical leads are connected together, or shorted, the impedance response measured at the same frequency points as used in the experiment, and the experimental data adjusted by subtracting the short correction measurement which is typically comprised of the resistance of the electrical leads and inductance of the system (wires and instrument). This option is available in some instruments for convenience, although a user-applied correction is relatively straightforward. Similarly, “open” corrections are also available; in this case, the sample is removed and the impedance response measured. Such a correction is particularly useful for samples which have small capacitances (as is the case for electrochemical AFM measurements, Chapter 4).

2.2 Potential Sweep (DC) Methods

Potential sweep voltammetry is a versatile technique for probing both transient and steady-state processes in electrochemical systems and is commonly used to examine processes such as adsorption/desorption or charging/discharging. In linear sweep voltammetry, the voltage is varied linearly with time at a defined rate from an initial voltage, V_1 , to some final voltage, V_2 , and the current response is measured. Data are typically presented as plots of the measured current as a function of the applied voltage. The simplest response one can obtain is at infinitely slow scan rates; in this case, the current measured contains no transient information. At non-zero scan rates, transient processes surface as peaks, that is, currents in excess of the steady-state (Faradaic) current. The position, size, and shape of the peak can provide a great deal of information about the process, such as the amount of charge passed or the kinetics of the process.⁴¹ Using linear sweep voltammetry, one can capture the behavior of the system over a

voltage range of interest and vary the scan rate to gauge the relative kinetics of transient processes.

One can also extend the process by reversing the voltage ramp after reaching a specified voltage (Figure 2.7). This method, called cyclic voltammetry, is commonly employed, particularly in aqueous electrochemistry, and gives additional information about the reversibility of the processes in the system. The shape of the voltammogram generated depends on the processes that are occurring in the system (Faradaic and/or non-Faradaic), the degree of reversibility, the kinetics and the chosen sweep rate. Figure 2.8 shows cyclic voltammograms for some common electrical circuit elements and circuits although real electrochemical systems often generate much more complicated responses because the resistance and capacitance of the process (R and C in the circuits of Figure 2.8) can vary with voltage.

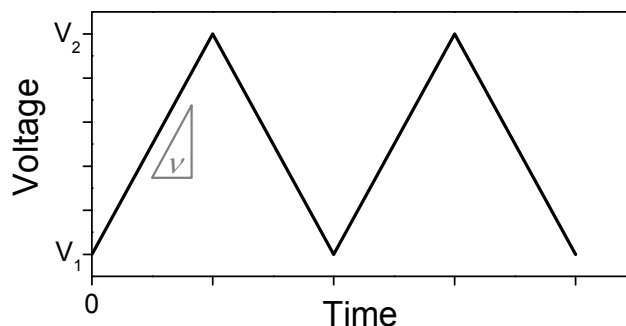


Figure 2.7 Example of a potential profile used in cyclic voltammetry for probing electrochemical processes occurring between V_1 and V_2 . Here, two cycles are shown. The scan rate, v , is the absolute value of the ramp rates.

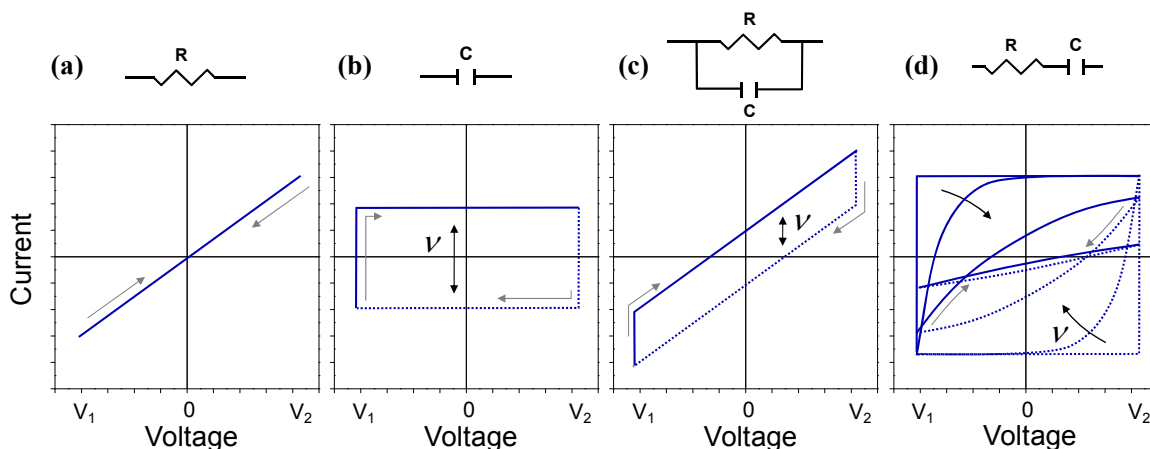


Figure 2.8 Schematic of cyclic voltammograms (one cycle) for a (a) resistor, (b) capacitor, (c) resistor in parallel with a capacitor, and (d) resistor in series with a capacitor. The scan rate is denote by ν .

Note that ohmic contributions can greatly affect the data quality, more so in sweep voltammetry techniques than ACIS. If the resistance of the electrolyte is large and dominates the total resistance, it can mask the electrochemical response of interest. In aqueous systems, the ohmic contribution can be minimized due to flexibility in the placement of electrodes, but in solid state systems, a high ohmic contribution cannot be avoided due to geometry constraints. It is, in principle, possible to manually subtract the ohmic contributions since the electrolyte conductivity is usually known, but if the electrolyte resistance is much higher than the electrode resistances, the correction may result in large errors.

2.3 AC vs. DC Measurements

The total resistance of the processes as measured by ACIS (real impedance at zero frequency) corresponds to the slope of the DC polarization curve, i.e., a sweep

voltammogram collected at zero scan rate (Figure 2.1a). Thus, one can extract the entire polarization curve by performing impedance measurements at a range of voltages. In such measurements, one obtains not only the slope of the polarization curve but also the electrochemical behavior of individual processes. Furthermore, given a particular electrode process, it is possible to relate key parameters obtained using AC and DC methods. The electrode impedance at zero bias can be related to the exchange current, i_0 , in the Butler-Volmer expression (Appendix A.1), which can be extracted from the polarization curve to describe the kinetics of the electrode process at equilibrium conditions,

$$R_0 = \frac{RT}{i_0 F} \quad (2.13)$$

where R_0 is the total electrode resistance and i_0 is the exchange current density.

2.4 Scanning Probe Microscopy for Electrochemistry

Scanning probe microscopy is a class of mapping techniques based on the interaction between a nanosized probe and a surface of interest. Among these are scanning tunneling microscopy and atomic force microscopy, the most well-known and among the first developed (in 1981 and 1986, respectively). As there are many extensive textbooks on scanning probe techniques, we will only briefly provide some background information on atomic force microscopy, used in this work, and its relevance in solid state electrochemical systems.

2.4.1 Atomic Force Microscopy

Atomic force microscopy (AFM) relies on the interaction force between a nanoscale probe and a surface. In the simplest terms, it operates by dragging a sharp tip across a surface while monitoring the tip's lateral and vertical position; if the size of the tip is smaller than the features on the surface, then one can obtain a well-resolved image of the topography of that surface. AFM tips today can be fabricated with radii below 5 nm, and one need not rely on mechanical contact between tip and sample in order to obtain an image. When a probe is brought close to the sample surface, the atoms on the very tip of the probe and atoms at the sample's surface exhibit various interaction forces depending on their separation distance (Figure 2.9a). These forces include but are not limited to van der Waals, capillary, electrostatic, and chemical forces and are frequently exploited for mapping surface properties.

AFM tips/probes are usually made from silicon or silicon nitride and vary in shape and size. A probe is usually comprised of a finely etched tip which extends from the apex of a pyramid/cone (Figure 2.9b); the latter, in turn is supported on a beam, commonly a rectangular or triangular cantilever which extends from a silicon chip (Figure 2.9c). The tip radius, cantilever dimensions, and material properties are all design parameters which dictate the imaging capabilities of the probe. Generally, the tip radius controls the image resolution, and the beam characteristics give the spring constant of the probe and therefore the range of forces that can be probed during measurement. The interaction force between the tip and sample, F , is related to the cantilever characteristics via the relation

$$F = k_{\text{cantilever}} \Delta x \quad (2.14)$$

where $k_{cantilever}$ is the spring constant of the probe and Δx is the deflection of the cantilever. Probes with spring constants ranging from 0.01 to 40 N m⁻¹ are available commercially; the choice of probe depends on the application and imaging mode of interest.

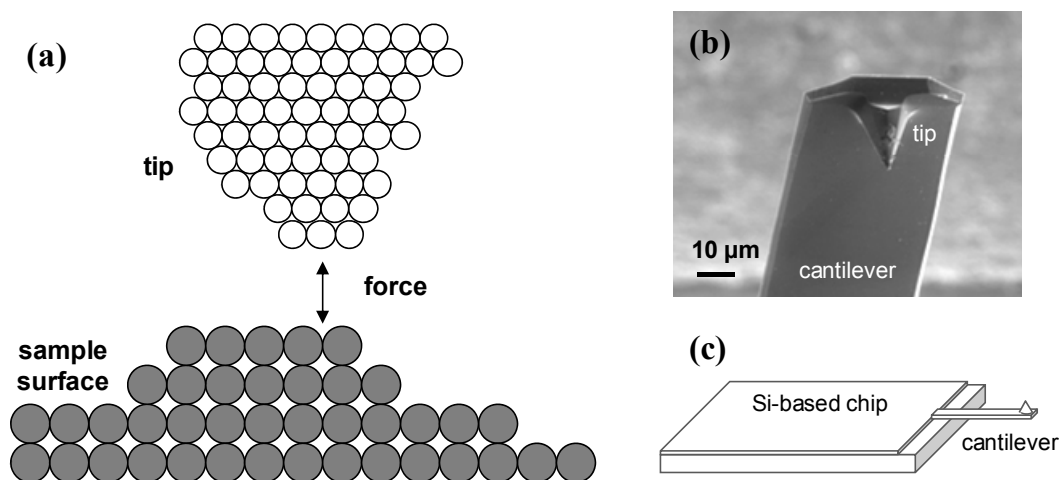


Figure 2.9 AFM probes: (a) interaction of tip and surface atoms, (b) SEM micrograph⁴² of a cantilever and (c) a sketch of a probe.

Although there are several different operating modes in AFM, we discuss only contact mode operation which is used in this study. For a more extensive review, the reader is referred to the textbook by Bonnell.⁴³ Contact mode imaging is typically carried out by maintaining a constant force between the sample and probe by moving either the sample or probe to control the separation distance between the two. The instrumentation required for an atomic force microscope is relatively simple compared to other high resolution imaging techniques such as electron microscopy (Figure 2.10). As the probe is rastered across the sample surface via a piezoelectric scanner, the deflection of the

cantilever is monitored by bouncing a laser signal off the top (reflective) surface of the cantilever. The reflected laser signal is measured by a four-quadrant photodiode detector, the signal from which is fed into the scanner to control the height of the sample to maintain a constant tip-sample separation/force. (Although the sample is being moved by the scanner in Figure 2.10, it is equally common to have the probe attached to the scanner and moved across an immobile sample.) The x - y - z movement of the piezoelectric is recorded to yield the final topography image. In order to perform a typical contact mode measurement, a desired force (or cantilever deflection) is specified by the user. Probes used for contact mode measurements are relatively compliant, with spring constants typically $0.1\text{--}1\text{ N m}^{-1}$ to minimize damage to the sample and tip.

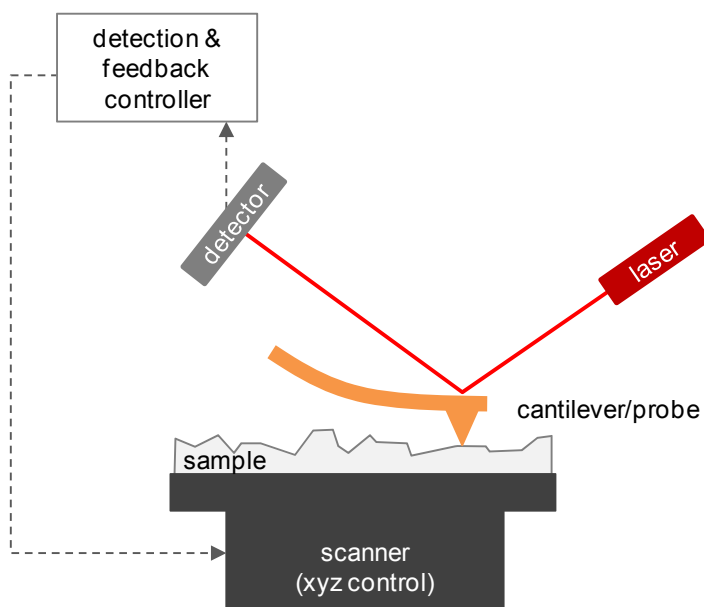


Figure 2.10 Operating principle of atomic force microscopy and basic components.

2.4.2 *Electrical Atomic Force Microscopy*

Electrical (or conducting) AFM is a technique in which a metal-coated AFM probe is used rather than an electrically insulated one. For electrical AFM, the system typically is operated in contact mode so that the probe is in physical contact with the sample surface. Given the proper instrumentation, the spatial variation of both topography and current can be recorded as the tip is rastered across a surface, and the local currents can be correlated to properties of the sample.

In this work, we extend such a technique to study materials which are ionic conductors. In this case, electrochemical reactions must occur at the probe | sample contact in order for current to pass. As such, the metal coating on the probe is one which is catalytically active, and the ionic conductor is fabricated with an active electrode at its underside to complete the circuit. Compared to conventional electrical AFM, measured currents can be significantly lower because the current is limited not only by the size of the probe but also the electrochemical activity of the probe | sample interface. Thus, a challenge of electrochemical AFM is its high system impedance, and thus great care must be taken to minimize spurious contributions to the electrochemical response. This includes reducing electrical and mechanical noise that causes fluctuations in the measured current and accounting for effects of stray capacitance.

Electrical AFM provides many advantages for exploring solid state electrochemical systems. The electrochemical activity of an ionic material at the nanoscale and its spatial heterogeneity can be readily explored. Not only this, AFM studies do not require vacuum, and, therefore, many materials can be examined under appropriate atmospheres and at elevated temperatures. Many metals/catalysts can be

examined readily by simply changing the coating on the AFM probe, and current collection from the nanoscale probe, by design of the microscope, is automatic. Finally, as discussed in the Section 2.5.2 below, the small size of the probe enables electrochemical studies at the metal|solid electrolyte interface, under bias, without contributions from the second electrode (at the opposing side of the electrolyte).

2.5 Cell Geometries for Probing Solid State Electrochemistry

The impedance response of real systems often contains arcs that are not sufficiently well-separated in frequency. In such cases, analysis of data to identify the origin of the various electrode arcs can become difficult, and fitting with models can generate large errors and unreliable results. In this section, we discuss sample geometries and environmental conditions, relevant for solid state systems, which can alleviate some of the challenges associated with probing electrode reaction mechanisms. If chosen correctly, a specific cell configuration can greatly reduce the complexity of the impedance response, for example, by eliminating arcs or deconvoluting the impedance spectrum.

2.5.1 Symmetric vs. Asymmetric Gas Environments

Although fuel cell measurements are, by definition, operated in asymmetric gas environments, that is, with oxidizing conditions at the cathode and reducing conditions at the anode (Figure 2.11a), such a configuration is not commonly employed for electrochemical studies in the laboratory. One of the reasons for this is the experimental difficulty of sealing the two chambers to separate the two gases and holding a

reproducible open-circuit voltage across the cell. Another reason is the possible ambiguity in identifying contributions from the anode and cathode which, in many cases, can be convoluted in the impedance response of the cell.

Symmetric cells are arguably the most widely used sample configuration for probing electrode properties of solid state fuel cell materials. In the symmetric cell configuration, identical electrodes are fabricated on both sides of the electrolyte membrane and placed in a uniform gas environment, either oxidizing or reducing, depending on the half-cell reaction of interest. In this configuration, unlike that for the fuel cell configuration, there exists no electrochemical potential gradient across the sample, so an electric field must be applied across the cell to induce an electrochemical response. Symmetric cell measurements are often studied near equilibrium conditions, that is, near the open-circuit voltage of zero, by using ACIS to apply a small perturbation about equilibrium. The resulting impedance response contains information about the resistance of the reaction of interest at equilibrium, that is, the slope of the polarization curve at 0 V. For example, for an electrode | electrolyte | electrode cell (with a proton-conducting electrolyte) in uniform hydrogen atmosphere, both the forward and reverse direction of $\text{H}_2 \rightleftharpoons 2\text{H}^+ + 2\text{e}^-$ at both electrodes are probed.

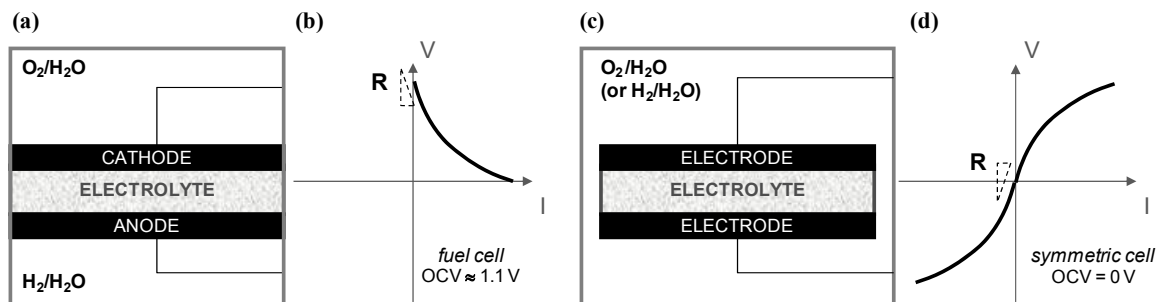


Figure 2.11 Schematics of and polarization curves for (a–b) fuel cell or asymmetric cell and (c–d) symmetric gas configuration. The total resistance measured at the open-circuit voltage corresponds to the slope of the polarization curve.

The relatively simple experimental setup required for symmetric cell studies makes it straightforward to gather a great deal of information about the electrode reactions. The main disadvantage of the symmetric cell configuration is the inability to probe a reaction under non-equilibrium conditions (i.e., away from the open-circuit voltage), which are considered more representative of the situation during fuel cell operation. Specifically, it is not useful to apply a non-zero net voltage across the cell; since the polarization curve for the symmetric cell is, itself, symmetric (Figure 2.11d), both hydrogen oxidation (occurring at one electrode) and proton reduction (occurring at the second electrode) will be occurring simultaneously. These two processes are rarely separable in the impedance spectrum, and, therefore, it is not easy to isolate the electrochemical response for the direction of interest, that is, hydrogen oxidation.

It should be noted there are no concerns with using symmetric cells for measuring the bulk properties (e.g., ionic conductivity) of the electrolyte; the electrolyte arc is usually well-separated from the electrode arc(s) and therefore can be identified easily. By the same argument, the choice of electrodes is not critical for bulk conductivity measurements since it does not impact ion conduction in the electrolyte.

2.5.2 Electrode Symmetry and Geometry

As mentioned in the previous section, it is not possible, with symmetric cell measurements, to extract the electrochemical response of a single electrode under a non-zero voltage. One might immediately suggest that the solution to this is to use a three-electrode configuration (Figure 2.12a), in which the current is passed between the working electrode and counter electrode, but the voltage is measured against a reference electrode. Such a configuration is commonly used in aqueous electrochemical systems. However, it has been shown that, in systems based on solid electrolytes, the placement of the electrodes can greatly affect the results and thus a small misalignment can influence the measured electrochemical response.^{44, 45}

Another way to extract the response of a single electrode, while still retaining the experimental convenience of the symmetric gas environments, is to change the characteristics of the two electrodes. During measurement, the voltage applied across a cell comprised of an electrolyte sandwiched between two electrodes (denoted by subscripts 1 and 2) is given by the expression

$$V_{tot} = IR_{tot} = V_{el} + I \left(\frac{\tilde{R}_1}{A_1} + \frac{\tilde{R}_2}{A_2} \right) \quad (2.15)$$

where V_{tot} is the total voltage drop across the cell, V_{el} is the voltage drop across the electrolyte, I is the current that passes through the cell and R_{tot} is the total resistance of the system, a portion of which comes from the electrode resistances, \tilde{R}_1 / A_1 and \tilde{R}_2 / A_2 . \tilde{R} denotes the area-normalized resistance in units of $\Omega \text{ cm}^2$ (i.e., inverse activity of the electrode), and A denotes the electrode area. Equation (2.15) can be rearranged to obtain

$$V_{tot} = V_{el} + V_1 \left[1 + \frac{\tilde{R}_2}{\tilde{R}_1} \left(\frac{A_1}{A_2} \right) \right] \quad (2.16)$$

For the symmetric cell case (Figure 2.11c), $A_1 = A_2$ and $\tilde{R}_1 = \tilde{R}_2$. Therefore,

$$V_{tot} = V_{el} + 2V_1 \quad (2.17)$$

showing that the voltage loss due to the electrodes are equally distributed between the two identical electrodes (i.e., $V_1 = V_2$).

From Equation (2.16), one can immediately see that the relative contributions of the two electrodes to the total voltage loss (overpotential) depends on their relative activities and areas. If $A_1 = A_2$ but $\tilde{R}_1 \gg \tilde{R}_2$ (Figure 2.12b), then

$$V_{tot} = V_{el} + V_1 \left[1 + \frac{\tilde{R}_2}{\tilde{R}_1} \right] \approx V_{el} + V_1 \quad (2.18)$$

and the voltage drop across the entire cell is only comprised of that from the electrolyte and from Electrode 1. To achieve this in the laboratory, Electrode 2 would need to be fabricated with much higher performance than Electrode 1. This can be done by either increasing the active site density of Electrode 2 or increasing the inherent activity of the electrode/catalyst. Note that the two electrodes need not be comprised of the same material; for example, one can use, for Electrode 2, a catalyst with much higher inherent activity. In practice, such an approach is not particularly useful because it is limited to the study of low-activity electrode materials.

A more straightforward route is to keep the electrode activities exactly the same, $\tilde{R}_1 = \tilde{R}_2$, but change the relative areas of the electrodes, $A_2 \ll A_1$ (Figure 2.12c). Equation (2.16) then yields

$$V_{tot} = V_{el} + V_1 \left[1 + \frac{A_1}{A_2} \right] \approx V_{el} + V_1 \quad (2.19)$$

In both Equations (2.18) and (2.19), the overall voltage drop is dominated by that across the electrolyte membrane and only one of the electrodes. The electrode with the higher absolute resistance, \tilde{R}_1 / A_1 (Electrode 1, in this example), becomes the working electrode because it dominates the total electrode response of the cell. The electrode with the lowest absolute resistance, i.e, higher activity and/or larger area, contributes negligibly to the total cell resistance and essentially behaves as a reversible, reference electrode. Thus, one can apply a voltage with respect to this reference electrode and probe electrochemical reactions at the working electrode under fuel cell relevant potentials. The ohmic electrolyte contribution can be easily separated from the electrode contribution via impedance spectroscopy.

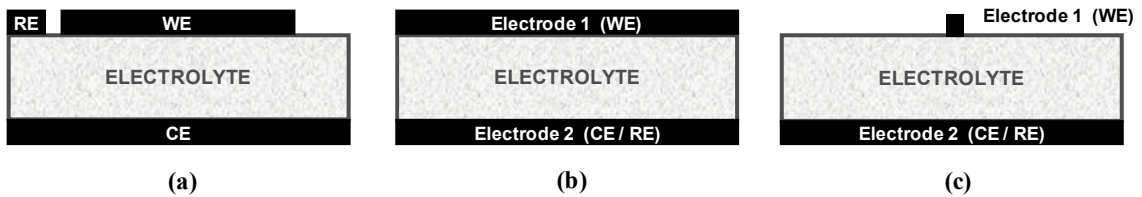


Figure 2.12 Possible electrode geometry configurations for solid state electrochemical measurements: (a) three-electrode configuration, (b) asymmetric activity electrodes, $\tilde{R}_1 \gg \tilde{R}_2$ and (c) asymmetric electrode geometry, $A_2 \gg A_1$. WE = working electrode, CE = counter electrode and RE = reference electrode

In general, either of the geometries shown in Figure 2.12(b–c), or a combination of the two, can be used in symmetric gas conditions to isolate the electrochemical reactions occurring at a single electrode under bias. The reference voltage corresponds to

the electrochemical reaction which occurs in at the reference electrode, for example, $2\text{H}_{2(\text{g})} \rightleftharpoons 4\text{H}^+ + 4\text{e}^-$ if the measurement was performed under uniform $\text{H}_2\text{-H}_2\text{O}$ atmospheres, or $\text{O}_{2(\text{g})} + 4\text{H}^+ + 4\text{e}^- \rightleftharpoons 2\text{H}_2\text{O}_{(\text{g})}$ for uniform $\text{O}_2\text{-H}_2\text{O}$ atmospheres. The choice of geometry for obtaining asymmetry depends on the situation, but as mentioned previously, fabrication of asymmetric electrode geometries is usually a more straightforward route. The main consideration, in this case, is to take into account the behavior of the equipotential lines which vary with the degree of asymmetry (Figure 2.13). For example, for a given electrode asymmetry, a thinner electrolyte membrane results in the utilization of a smaller portion of the counter/reference electrode (Figure 2.13a). While a thicker electrolyte membrane improves utilization of the counter electrode (Figure 2.13b), an increase in the ohmic losses can mask electrode response. A quantitative analysis of the geometric requirements can be found in work by Sasaki et al.³⁶

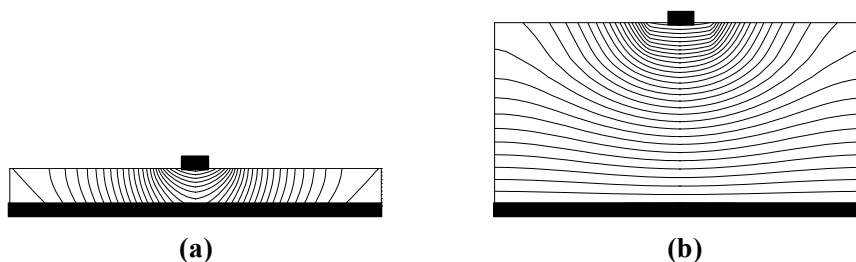


Figure 2.13 Effect of electrolyte membrane thickness on equipotential lines in asymmetric geometry electrode configuration. In (a), a majority of the current is passing through a small region of the counter electrode whereas in (b), the current is more uniformly distributed throughout the entire counter electrode.

2.5.3 *Electrode Microstructure*

In the laboratory, there are several types of electrode structures which can be fabricated for use in fundamental electrochemical studies. The most obvious are composite electrodes which mimic those used in real fuel cells. However, while composite electrodes are application-relevant, they are often extremely complex, with random distributions of two-phase and three-phase boundaries (Figure 2.14a). Such a complicated microstructure prevents the correlation of the measured electrochemical response to the corresponding active sites which often are not known to begin with. Thus, there is an advantage to simplifying the microstructure to one in which the experimentalist has a specified level of control over the electrode microstructure and therefore the active sites. Figure 2.14(b–d) shows several examples of electrodes for which the microstructure can be controlled. Thin film techniques can be used to grow a film with a known microstructure, such as one with a porous columnar morphology (Figure 2.14b) for which the porosity and surface area can be controlled. In another case, photolithographic techniques can be employed to fabricate dense, patterned films^{46–49} with defined edges and interfaces (Figure 2.14c). Given optimization of microfabrication conditions, patterned electrodes are extremely flexible because a wide range triple-phase and two-phase boundary sites can be fabricated. Also commonly employed are dense films for which the film thickness and/or perimeter can be controlled.^{37, 50–55} These are the simplest of geometries and are relatively easy to fabricate in the laboratory.

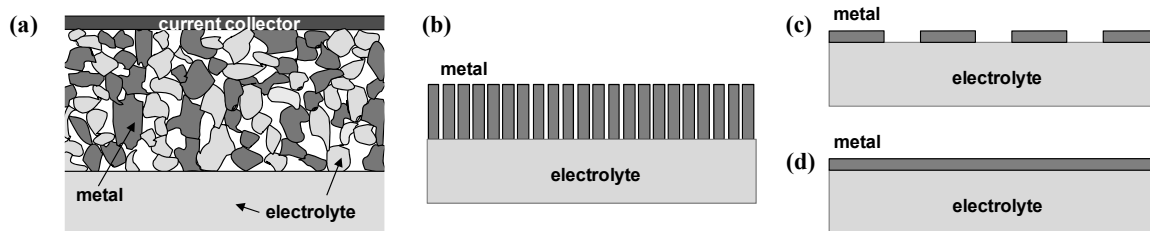


Figure 2.14 Various electrode microstructures in metal/catalyst-electrolyte system for electrochemical studies: (a) application-relevant composites, (b) electrode films with controlled microstructure, e.g., columnar, (c) patterned films and (d) dense films

2.6 Solid Acid Compounds for Electrode Studies: Challenges

2.6.1 Water Solubility

While patterned electrodes are ideal for fundamental electrode studies in the metal | solid acid system, the solubility of solid acid compounds in water precludes the use of photolithography which routinely involves the use acids and/or water-miscible solvents. In order to study electrocatalysis in systems based on water-soluble electrolytes, the most straightforward method is to fabricate thin dense metal films (Figure 2.14d) by shadow-masking. Although using shadow masks, particularly in conjunction with sputtering, results in metal edges which are not as well-defined as those made by photolithography, the technique provides good control of the film thickness and the fabrication procedure is straightforward. Thin film electrodes were fabricated using this technique for hydrogen electro-oxidation studies in Chapter 3.

There has been work to synthesize solid acid electrolytes which are not water-soluble and therefore amenable to further electrode fabrication techniques. For fundamental electrode studies, water-insoluble compounds provide an enormous advantage with respect to processing, for example, compatibility with wet polishing

methods to generate smooth substrate surfaces and with photolithography processes to fabricate well-defined electrode | electrolyte boundaries. Some success was found for $\text{Ba}_{3-x}\text{K}_x\text{H}_x(\text{PO}_4)_2$ which crystallizes, with $x \approx 0.5\text{--}0.9$, in the trigonal phase, similar to known superprotonic compounds such as $\text{Rb}_3\text{H}(\text{SeO}_4)_2$.²⁴ However, its relatively poor proton conductivity, two to three orders lower than that those for typical superprotonic solid acids, may render it unsuitable as a representative electrolyte substrate for probing electrocatalysis in solid acid systems.

2.6.2 *Mechanical Properties*

Although the room temperature phases of solid acid compounds are brittle, superprotonic phases are plastic and susceptible to irreversible deformation under stress.^{17–19, 56} This ductility has consequences in terms of application of pressure to electrochemical cells, sometimes done to make electrical contact to electrodes and avoid solvents in conductive paints (Appendix C.2.4). Over time, the cell may deform slightly, destroying carefully fabricated electrode structures.

2.6.3 *Superprotonic Phase Transition*

The superprotonic phase transition is a solid-to-solid phase transformation between two different crystal structures, and thus, incompatibilities between the two solid phases can cause cracks to form in the material. Cycling of the temperature through the phase transition (Figure 2.15) shows that the open-circuit voltage depends on whether the electrolyte is above or below the phase transition temperature; the open-circuit voltage corresponds closely to the theoretical (Nernst) voltage at superprotonic conditions but drops to voltages below 0.5 V at temperatures below the phase transition temperature.

The lower voltages suggest that fuel and oxidant may be meeting via microcracks formed in the relatively thin CsH_2PO_4 membrane, while high open-circuit voltages at high temperatures indicate that, should such microcracks form, they fortuitously heal under the plastic flow of the electrolyte. (An alternative explanation is that poor electrochemical kinetics below the phase transition temperature precludes accurate voltage measurements, resulting in an artificial drop in the measured voltage.)

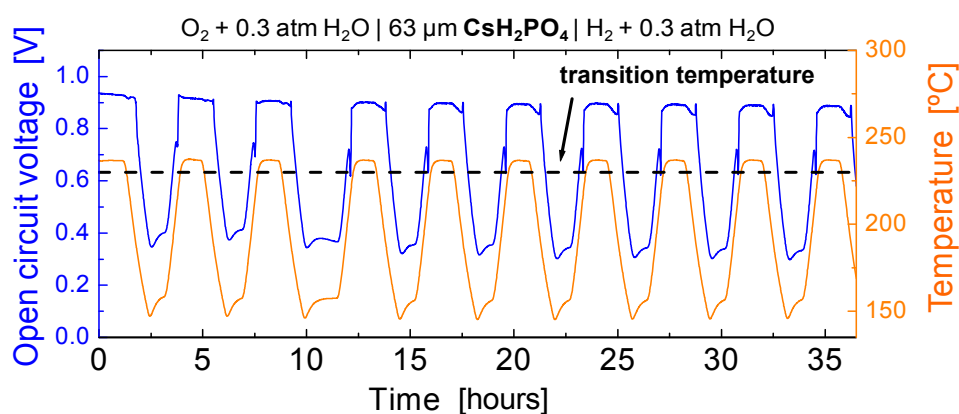


Figure 2.15 Fuel cell open-circuit voltage with temperature cycling.⁵⁷ The voltage drops on cooling across the phase transition and recovers on heating to the superprotonic phase.

Cracking also has implications in fundamental electrochemical studies. Cracks can be propagated to any conformal electrode structure that is fabricated on top of these solid acid electrolytes, lowering the efficacy of carefully-fabricated electrode structures. In Chapter 5, we examine the origin of the incompatibility between phases and explore ways to reduce incompatibility and cracking. The density of cracks varies between solid acid compounds, so it may be possible to use solid acid substrates which have little to no cracks. Solid acids which fall under this categories are CsHSO_4 and $\text{Rb}_3\text{H}(\text{SeO}_4)_2$.¹⁹ $\text{Ba}_{3-x}\text{K}_x\text{H}_x(\text{PO}_4)_2$ compounds are also crack-free substrates because, by design, they do

not undergo a superprotonic phase transition;²⁴ however, as mentioned previously, it is unclear whether the proton conductivity is high enough to be used for electrode studies.

2.6.4 Thermal and Chemical Stability

As the solid acid electrolyte of choice, CsH_2PO_4 is chemically stable in both oxidizing and reducing conditions. However, its tendency to dehydrate increases with temperature.^{10, 15} As discussed in Chapter 1, such behavior is not problematic for fuel cell operation; however, it limits the temperature and water partial pressure range that can be used to probe activation energy and partial pressure dependences when performing fundamental electrode studies. Furthermore, the water partial pressure requirements preclude the use of CsH_2PO_4 in electrochemical AFM studies which cannot accommodate the water partial pressures required to suppress CsH_2PO_4 dehydration.

Several other systems can be used as representative substrates for studying electrocatalysis at electrode | solid acid interfaces, although they do not come without their own limitations. CsHSO_4 is very stable against dehydration and thus can be used in instrumentation that cannot accommodate high water vapor contents (e.g., electrochemical AFM, Chapter 4). However, studies cannot be performed in reducing conditions since sulfates (and selenates) can be reduced by hydrogen.¹² Low-temperature solid acids stable in reducing environments include CsHPO_3H and related compounds,^{11, 22, 23} although, in the case of CsHPO_3H , careful handling would be required because it is deliquescent at ambient conditions. Again, $\text{Ba}_{3-x}\text{K}_x\text{H}_x(\text{PO}_4)_2$ compounds for $x \approx 0.5\text{--}0.9$ has been found to be chemical and thermally stable up to $\sim 300^\circ\text{C}$ and remains an option for future studies, particularly for experiments via electrochemical AFM (as demonstrated in Appendix G).

Chapter 3 Hydrogen Electro-oxidation over Thin Film Pt Electrodes

Louie, M. W.; Haile, S. M. Platinum Thin Film Anodes for Solid Acid Fuel Cells. *submitted 2011*

Abstract

Hydrogen electro-oxidation kinetics at the Pt | CsH₂PO₄ interface have been evaluated. Thin films of nanocrystalline platinum 7.5–375 nm thick and 1–19 mm in diameter were sputtered atop polycrystalline discs of the proton-conducting electrolyte, CsH₂PO₄, by shadow-masking. The resulting Pt | CsH₂PO₄ | Pt symmetric cells were studied under uniform H₂-H₂O-Ar atmospheres at temperatures of 225–250 °C using AC impedance spectroscopy. For thick platinum films (> 50 nm), electro-oxidation of hydrogen was found to be limited by diffusion of hydrogen through the film, whereas for thinner films, diffusion limitations are relaxed and interfacial effects play an increasingly dominant role. Extrapolation to vanishing film thickness implies an ultimate interfacial resistance of 2.2 Ω cm², likely reflecting a process at the Pt | H_{2(g)} interface. Films 7.5 nm in thickness displayed a total electro-oxidation resistance, \tilde{R} , of 3.1 Ω cm², approaching that of Pt-based composite anodes for solid acid fuel cells (1–2 Ω cm²). In contrast, the Pt utilization (\tilde{R}^{-1} /Pt loading), 19 S mg⁻¹, significantly exceeds that of composite electrodes, indicating that the thin film approach is a promising route for achieving high performance in combination with low platinum loadings.

3.1 Introduction

Elucidation of electrochemical reaction pathways is essential for optimizing electrode microstructure as well as catalyst selection. However, as is the case for a majority of fuel cell systems, the mechanism for electrocatalysis in solid acid fuel cells is not known. Composite electrodes used in operating fuel cells are designed to maximize the number of active sites and improve electrode performance but are not suitable for mechanistic studies because the complex microstructure precludes an unambiguous analysis of the resulting electrochemical response. Accordingly, electrochemical cells for which the electrode | electrolyte boundaries are well-defined are ideal for studying fundamental electrochemistry in solid state systems. By varying the geometric parameters of the electrode, one can examine how the rate-limiting process varies with the number density of the active sites, e.g., triple-phase boundary (TPB) and two-phase boundary sites.

The thin film electrode | electrolyte interface has been used as a model system for examining reaction kinetics in solid state electrochemistry.^{37, 38, 46, 47, 50, 53, 55, 58–62} At a minimum, such a configuration consists of a thin dense electrode film deposited on an electrolyte material,^{37, 50, 53, 55, 58–60} either covering the entire surface or confined to a specific area, and provides control over the film thickness and/or area. In systems that require the examination of a larger range of geometric parameters, microfabrication techniques are employed to fabricate electrode films of various patterns,^{38, 46, 47, 61, 62} enabling the manipulation of electrode dimensions such as the film thickness, perimeter (i.e., triple-phase boundary length) and the interfacial electrode | electrolyte area (i.e., two-phase boundary). While both uniform and patterned electrodes allow for precise

control over electrode dimensions, patterned electrodes enable more flexible and independent control over the two-phase and three-phase boundary sites.

Although patterned electrodes are, in general, the preferred choice for kinetic studies, the water solubility and temperature sensitivity of CsH_2PO_4 , that is, its tendency to dehydrate at elevated temperatures and low humidities,¹⁵ precludes the use of most conventional microfabrication techniques for film deposition and pattern creation. In this work, we employed shadow masks, placing them over CsH_2PO_4 substrates to fabricate platinum film electrodes of various thicknesses and areas by sputter deposition. The resulting $\text{Pt}|\text{CsH}_2\text{PO}_4|\text{Pt}$ symmetric cells were characterized by AC impedance spectroscopy and the rate-limiting step for hydrogen electro-oxidation probed as a function of the metal film dimension and environmental parameters, specifically, temperature and hydrogen partial pressure.

3.2 Experimental

3.2.1 Sample Preparation

Dense polycrystalline CsH_2PO_4 discs were fabricated by uni-axial compression of CsH_2PO_4 powders (synthesis detailed elsewhere⁵⁸) at a pressure 138 MPa for 20 min. The discs were mechanically polished with silicon carbide sandpaper (grit sizes 600 followed by 800) and then sonicated in acetone, followed by isopropanol, before drying in air at $\sim 100^\circ\text{C}$. The final discs were 19 mm in diameter and ~ 1 mm thick, with densities $95 \pm 2\%$ of theoretical.

Thin film Pt electrodes were deposited onto CsH_2PO_4 discs by DC magnetron sputtering at room temperature using a AJA International ATC Orion system (3 mTorr Ar, 150 W plasma power) or a Cressington 208HR system (~ 15 mTorr Ar, 80 mA plasma current). The CsH_2PO_4 substrates were shadow-masked to restrict the exposed area to that corresponding to 19, 15, 12.6, 10, 4.7, and 1.3 mm in diameter. The sputtering time was varied to obtain films with thicknesses ranging from 7.5 to 375 nm. The deposition of 10 nm Au films was carried out using the ATC Orion system, with sputtering conditions identical to those for Pt. All cells were fabricated with a symmetric geometry.

3.2.2 Characterization

The general crystallinity of the platinum films, adhered to the substrates, was evaluated using a Phillips X'Pert Pro powder X-ray diffractometer using $\text{Cu K}\alpha$ radiation (45 kV, 40 mA) with a 2θ range of $15\text{--}90^\circ$. Additional analysis was performed using films that were isolated from the substrate. Double-sided tape was applied and the Pt film removed either mechanically or by dissolution of the substrate in water. Diffraction measurements were performed over the 2θ range of $38\text{--}42^\circ$ to access the strongest, (111) peak of Pt, using a step size of 0.008° and various dwell times, depending on the film thickness, to collect sufficient signal intensity for analysis. The full-width half-max of the (111) peak was extracted from a Lorentzian fit and the grain size calculated using the Scherrer equation,⁶³ $t \approx 0.9\lambda/B\cos\theta$, where t is the grain size, $\lambda = 0.1541$ nm, and B is the instrument-corrected full-width half-max at $2\theta \approx 40^\circ$ at which instrument broadening was determined to be $\sim 0.08^\circ$.

The morphology of the metal films both before and after electrochemical characterization was observed by scanning electron microscopy, SEM, (LEO 1550VP, Carl Zeiss SMT) using a 3 kV accelerating voltage. Film thickness was measured by cross-sectional SEM imaging of fractured cells, and the deposition rate of Pt was determined to be 9.8 nm min^{-1} . Image analysis, specifically, evaluation of the number density of cracks in the films that formed due to thermal cycling, was performed using ImageJ software.⁶⁴ The film connectivity was assessed by measuring the sheet resistance of the films, using a hand-held multimeter, both before and after testing.

Impedance spectra were collected, in the majority of cases, using a Solartron Analytical 1260 frequency response analyzer with a 10 mV perturbation voltage about zero bias over frequencies of 10 MHz to 100 mHz configured with a four-probe measurement geometry. For experimental convenience, some spectra were collected using a Solartron 1250 analyzer equipped with a potentiostat (Princeton Applied Research, EG&G 273A). In this case, a three-probe configuration was used, and the high-frequency limit was 60 kHz. For the frequency range of interest, the two instruments yielded excellent agreement in the impedance response. Electrical connection to the cells was made using an in-house constructed sample holder in which the cells were sandwiched between two pieces of Toray carbon fiber paper (280 μm thick) placed between two stainless steel porous discs. Using the sample holder, adequate pressure was applied to the assembly to mechanically contact silver wire leads to the stainless steel discs. The use of carbon fiber paper, with estimated interfiber spacings of $\sim 100 \mu\text{m}$, ensured sufficient current collection for thin 7.5 nm Pt films. For a subset of the thicker films, electrical connection was made by the direct attachment of silver wires using

colloidal silver paint (Ted Pella, #16032); such a method did not yield electrode responses different from that with Toray paper.

Electrochemical impedance measurements were collected under uniform H₂-H₂O-Ar atmospheres at temperatures between 225 and 250 °C. The range of temperatures explored is limited, at one end, by the (reverse) phase transition temperature of ~ 221 °C on cooling⁶⁵ and, at the other end, by the tendency for CsH₂PO₄ to dehydrate at elevated temperatures.^{15, 66} Hydrogen partial pressures between 0.1 and 0.5 atm, for a fixed water partial pressure of 0.5 atm, were achieved by flowing inlet H₂-Ar mixtures through a heated water bubbler. The water partial pressure of the resulting gas stream was measured with a humidity sensor (HygroFlex 2 with IM 1 probe, Rotronic Instrument Corp). The total gas flow rate of ~ 160 mL min⁻¹ was verified to be sufficiently high so as to eliminate possible mass transport effects, and the perturbation voltage of 10 mV was confirmed to yield a linear impedance response. Data presented in this work were acquired once the electrode resistance (arc width) exhibited a degradation rate below 2% h⁻¹.

Acquired impedance spectra were analyzed using the commercial software ZView (Version 2.9b, Scribner Associates, Inc.). In addition to fitting the electrode response, additional circuit elements were placed in series with the electrode circuit to account for contributions from wire resistance, system inductance and bulk transport properties of the CsH₂PO₄ substrate. The latter, based on the appropriate cell dimensions, was confirmed to yield a proton conductivity value of $2.8 \pm 0.7 \times 10^{-2} \text{ S cm}^{-1}$ at 250 °C, consistent with the value of $2.4 \times 10^{-2} \text{ S cm}^{-1}$ reported in literature.¹⁰ For reasons of clarity and for ease of comparison between spectra, the high-frequency, non-electrode contributions are

subtracted from all impedance data presented in this work. A detailed discussion of the high-frequency impedance response is presented in Appendix C.3.

3.3 Results and Discussion

3.3.1 Film Morphology and Structure

A typical X-ray diffraction pattern of Pt deposited on CsH_2PO_4 (Figure 3.1, 75 nm Pt) shows broad Pt peaks⁶⁷ overlaid with monoclinic CsH_2PO_4 peaks.⁶⁸ The presence of Pt diffraction peaks, observed even for films as thin as 7.5 nm (not shown), indicates that the deposited film is crystalline in nature, whereas the peak breadth suggests a small grain size.

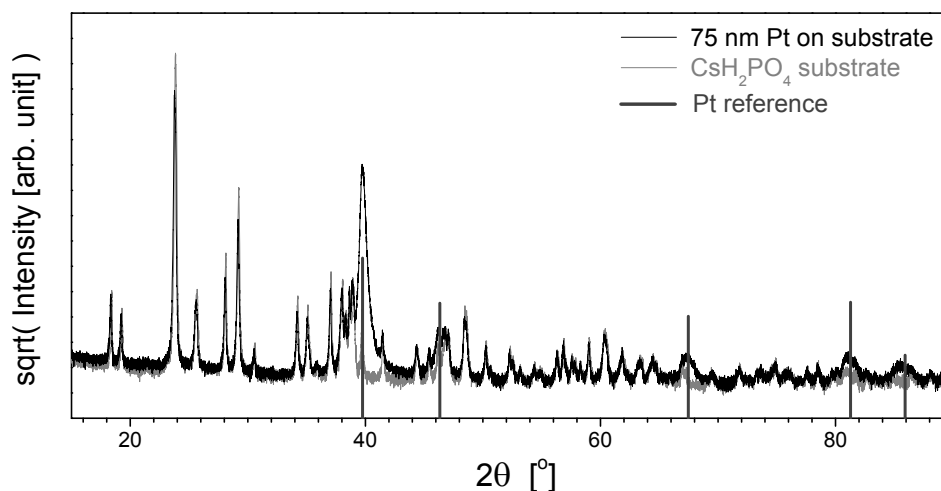


Figure 3.1 A representative X-ray diffraction pattern of as-deposited Pt films on a polycrystalline CsH_2PO_4 substrate. Visible are broad Pt peaks, the most prominent at $2\theta = 39.8^\circ$, overlaid with monoclinic CsH_2PO_4 peaks. Pt film shown: 75 nm thick, 15 mm dia.

Representative scanning electron micrographs of Pt on CsH_2PO_4 are shown in Figure 3.2. The plane-view image of an as-deposited 75 nm film (Figure 3.2a), shows that the Pt conforms to the substrate, revealing the underlying grains of CsH_2PO_4 , 0.4–5 μm

in size, as well as streaks due to polishing. From the cross-sectional image of a 375 nm film (Figure 3.2b), it is apparent that the films are dense and formed of nanometric grains. The film has slightly detached during fracture, giving rise to the small gap at the interface. The conformal and dense nature of the films (away from the edge) is further evident from Figure 3.2c, in which an SEM micrograph of the underside of a 7.5 nm Pt film isolated from its CsH_2PO_4 substrate is shown. As is the case for all films examined, the morphology of the substrate is replicated and the film appears free of pores.

The conformal and dense nature of the as-deposited films is ideal for the intended electrochemical study because the TPB sites are limited to the film perimeter region. The boundaries, however, are defined by sloped rather than sharp edges, Figure 3.2d, suggesting possible increases to the TPB length relative to an ideal boundary. The slope is so gradual, in fact, that the boundary is barely visible in the high magnification image. Furthermore, and perhaps more significantly, changes in film morphology were observed as a consequence of thermal cycling. The superprotonic transition in CsH_2PO_4 involves a large volume change and structural rearrangement, and this transformation was found to generate microcracks in the electrolyte, which then propagate into the Pt film. The SEM image in Figure 3.2e shows a representative image of the boundary region of Pt films on CsH_2PO_4 after thermal cycling. While microcracks were not, in any instance, observed in as-deposited films, cracks of the type evident in the figure were ubiquitous after thermal cycling. It is evident that microcracks extend from the Pt-free region of the substrate into that on which Pt has been deposited, indicating that the electrolyte is indeed the source of the cracks in the film. The density of TPB sites generated by such cracks is $\sim 0.018 \pm 0.004 \mu\text{m}^{-1}$, estimated by measuring the number and lengths of cracks across

ten SEM images. On average, the sheet resistance of the Pt films increased by $\sim 35\%$ after testing, consistent with the formation of microcracks through the film.

Based on observations of the film characteristics, the structure of the gas | Pt | CsH_2PO_4 half-cell differs from that expected for a perfectly dense film. Figure 3.3 shows a schematic of the structure.

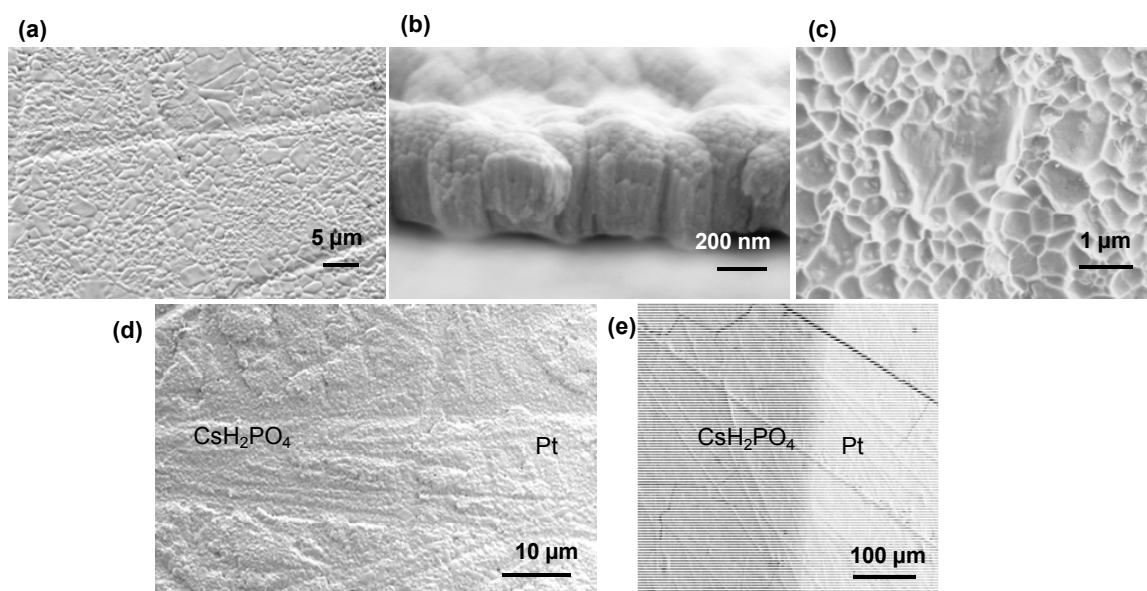


Figure 3.2 SEM micrographs of Pt films: (a) as-deposited 75 nm Pt on CsH_2PO_4 , (b) as-deposited 375 nm thick Pt film in cross-section, (c) underside of as-deposited 7.5 nm film isolated from its substrate, (d) Pt- CsH_2PO_4 boundary for a 375 nm Pt film, and (e) Pt- CsH_2PO_4 boundary for a 375 nm film after electrochemical characterization at 250 °C. Additional images of Pt films are shown in Appendix C.2.



Figure 3.3 A schematic of the Pt | CsH_2PO_4 | Pt cell, with the plane of symmetry denoted by a dashed line. Microcracks, resulting from heating the substrate to above the superprotonic phase transition temperature, are generated in the Pt films.

High resolution SEM images and diffraction data, Figure 3.4 and Figure 3.5, respectively, indicate that the Pt grain size increases with film thickness. While difficult to quantify from the SEM micrographs, the increasing breadth of the (111) diffraction peak with decreasing film thickness is immediately evident in Figure 3.5a, in which the normalized diffraction intensities are compared for a series of films post electrochemical characterization. The particle size implied by the Scherer equation (microstrain effects are considered negligible) is plotted as function of thickness in Figure 3.5b. The grain size depends sharply on film thicknesses for films thinner than ~ 50 nm and then apparently tends towards a finite value with increasing thickness. Selected evaluations of as-deposited films revealed similar grain sizes, indicating that minimal Pt grain growth occurs under the electrochemical characterization conditions (250°C , total time ≈ 4 days), an expected result.

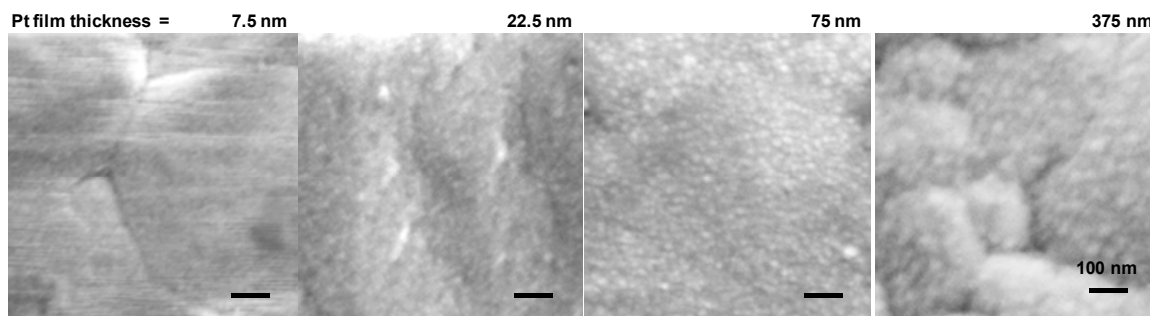


Figure 3.4 High magnification SEM micrographs of Pt of various thicknesses on top of CsH_2PO_4 (imaged after electrochemical characterization), showing the Pt grain structure.

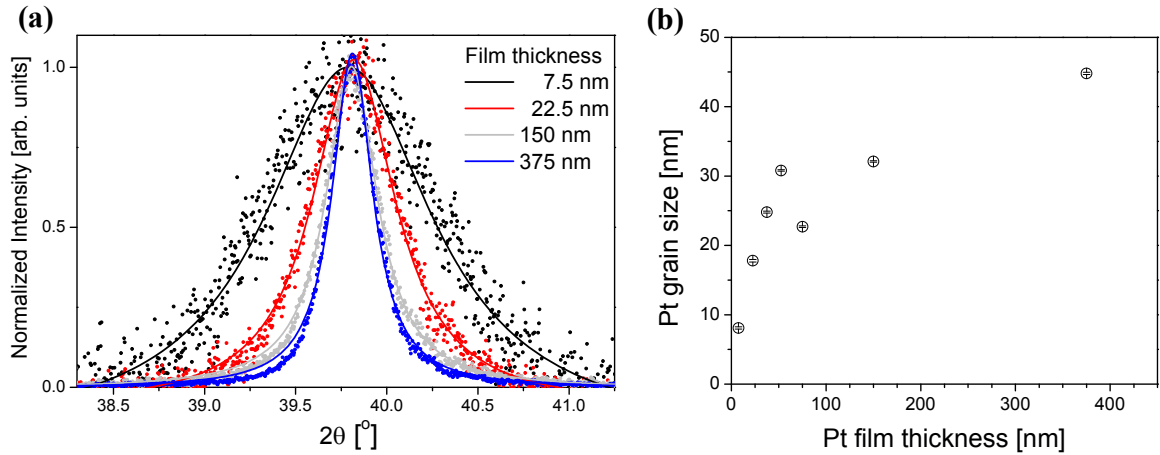


Figure 3.5 Correlation of grain size with Pt film thickness: (a) the broadening of the (111) diffraction peak for Pt at $2\theta = 39.8^\circ$, shown here for select films, and (b) Pt grain size as a function of film thickness determined from (a). Films measured were isolated from CsH_2PO_4 substrate (after electrochemical characterization).

3.3.2 Impedance Response: Effect of Platinum Film Dimension

Representative impedance spectra collected from the symmetric Pt | CsH_2PO_4 | Pt cells are presented in Figure 3.6. For this series of spectra, in which the film diameter is held constant (15 mm) and the film thickness is varied, it is apparent that the nature of the impedance response differs between thick and thin films. Specifically, the thicker films displayed a response in the Nyquist representation (Figure 3.6a) that appeared as an asymmetric arc, with a 45° slope at high frequencies and circular appearance at low frequencies. This half-teardrop shape is functionally described by a “distributed” finite-length Warburg diffusion element, Z_{dFLW} , with impedance

$$Z_{dFLW}(i\omega) = R_0 \frac{\tanh[(i\omega\tau)^n]}{(i\omega\tau)^n} \quad (3.1)$$

where i is $\sqrt{-1}$, ω is angular frequency, τ is the characteristic diffusion time, R_0 corresponds to the real impedance at the low-frequency limit (as indicated in Figure

3.6a), and n is a constant whose deviation from 0.5 reflects the dispersion of the response due to non-uniform diffusion.³⁴ The solid lines in Figure 3.6(a–b) show the high quality of the fit using this expression and thus the suitability of this function for representing the measured response. It is further apparent that for thicker films, R_0 increases with film thickness.

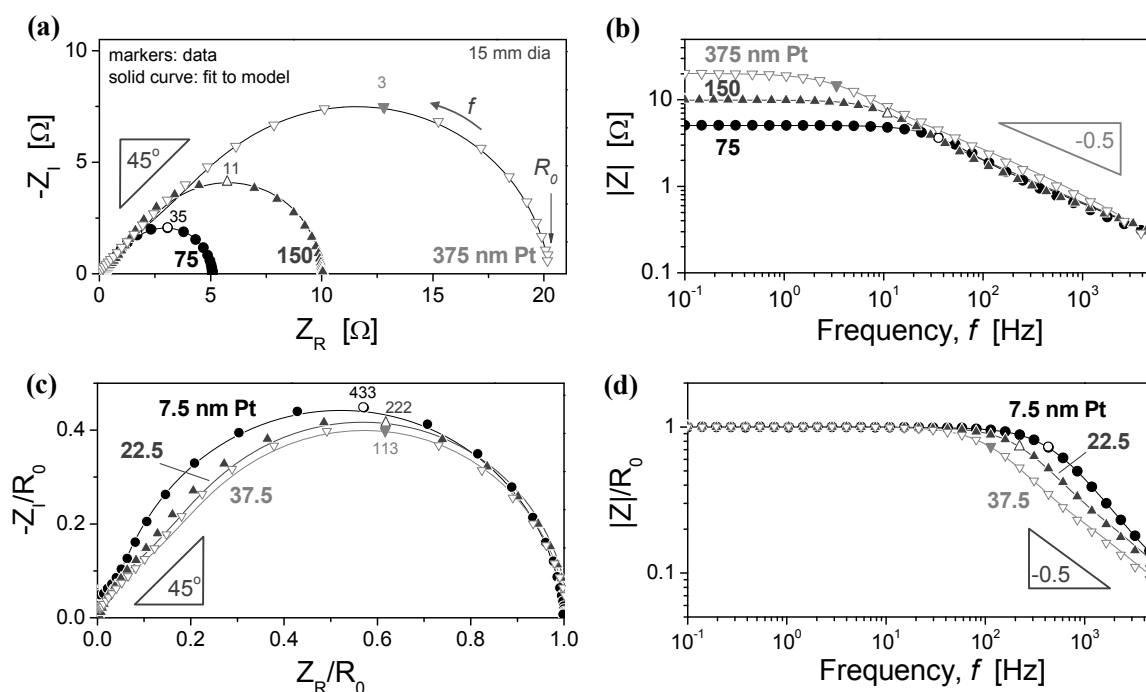


Figure 3.6 Impedance spectra for select Pt film electrodes of different thicknesses (15 mm dia.): (a) Nyquist and (b) Bode magnitude representations for thicker films, and (c) Nyquist and (d) Bode magnitude representations of thinner films. Thick Pt films yield a characteristic half-teardrop shape in the Nyquist plot (a), whereas thin Pt films yield a more symmetric response (c). For the thin films (c–d), the impedance response is normalized by the arc width to show the transition in arc shape from half-teardrop to semi-circle. Lines indicate fits to the distributed finite-length Warburg element, with the exception of the 7.5 nm Pt film which was fitted using two parallel RQ sub-circuits.

In contrast, the thinner films, Figure 3.6(c–d), displayed responses that are not adequately represented by Equation (3.1). With decreasing film thickness, the electrode arc became increasingly symmetric and the 45° slope at the high-frequency limit was

almost absent for the 7.5 nm film. The solid lines in this case are fits using two parallel RQ sub-circuits, where R is a resistor and Q is a constant phase element ($Z_Q = 1/Y(i\omega)^n$, where Y is a constant and $0 \leq n \leq 1$) placed in series with one another. Moreover, although the spectra are presented in normalized form for ease of comparison of the shapes, it was found (as will be shown quantitatively below) that R_0 is almost independent of film thickness for films thinner than ~ 50 nm.

The characteristics represented by the spectra for 15 mm diameter Pt films in Figure 3.6 were observed to be independent of film diameter. That is, irrespective of diameter, all films with thickness ≥ 50 nm displayed the type of response shown in Figure 3.6(a–b), whereas all films thinner than 50 nm showed increasingly symmetric arcs, as shown in Figure 3.6(c–d). For either type of response, it is possible to evaluate the real impedance of the electrode in the DC limit, explicitly noted as R_0 , in Figure 3.6a. The results are summarized in Figure 3.7, in which R_0 is plotted in double-logarithmic form as a function of film thickness (Figure 3.7a) and of film diameter (Figure 3.7b). The trends shown in Figure 3.7a reflect a clear differentiation between regimes. For thicker films (Regime I), which exhibited the half-teardrop response, the double-logarithmic plot displays an average slope of 0.9 ± 0.1 , revealing that R_0 scales linearly with thickness. Thinner films (Regime II), in contrast, tend towards an apparently limiting value of R_0 , with further reductions in film thickness having negligible impact. It is noted that reliable impedance measurements could not be made using films thinner than 7.5 nm because of loss of connectivity in the film (Appendix C.2.2). Turning to the diameter dependence of R_0 (Figure 3.7b), it is evident that for all films, the data fall along a line with an average slope of -2.1 ± 0.1 , indicating that R_0 is inversely proportional to the area of the Pt film.

The behavior of R_0 as a function of temperature and hydrogen partial pressure (Figure 3.8) further suggests a mechanistic distinction between thicker (Regime I) and thinner (Regime II) films. Specifically, the reaction order for $p\text{H}_2$ (i.e., r in $R_0^{-1} \propto p\text{H}_2^r$) is roughly constant at ~ 0.4 for thicker Pt films (Regime I) but increases sharply with decreasing film thickness (Regime II), yielding a value of ~ 0.75 for 7.5 nm films. Likewise, the activation energy for R_0^{-1} is somewhat flat in Regime I, with a value of $\sim 42 \text{ kJ mol}^{-1}$ for film thicknesses $\geq 150 \text{ nm}$ and decreasing with decreasing film thickness to $\sim 27 \text{ kJ mol}^{-1}$ at 7.5 nm.

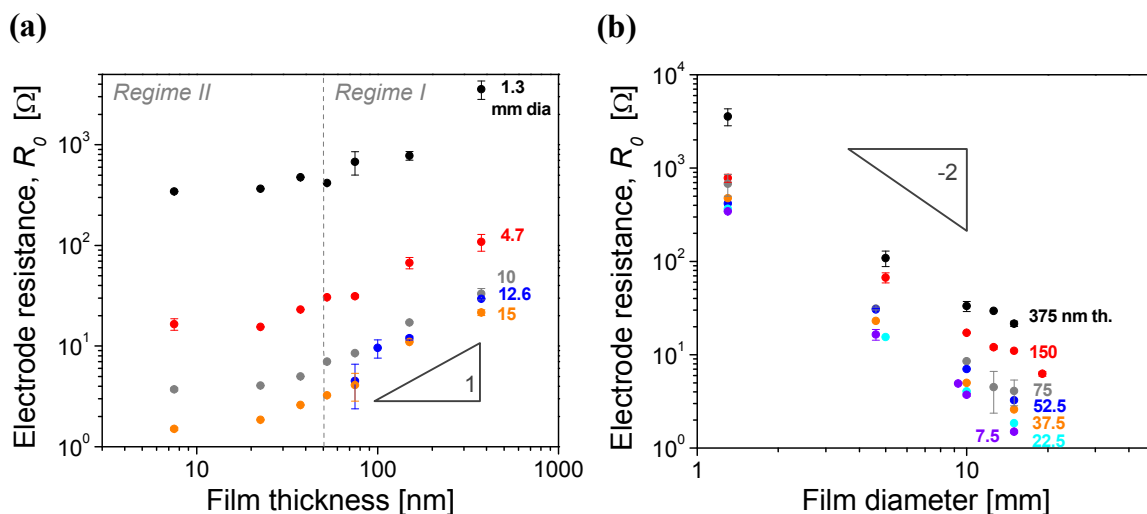


Figure 3.7 Double-logarithmic plots of Pt film electrode resistance, R_0 , as a function of: (a) film thickness for various diameters and (b) film diameter for various thicknesses. The thickness dependence reveals two different regimes: data fall along lines with a slope of 1 for thicker films but show little dependence for films below $\sim 50 \text{ nm}$. For all Pt films, R_0 scales with film area.

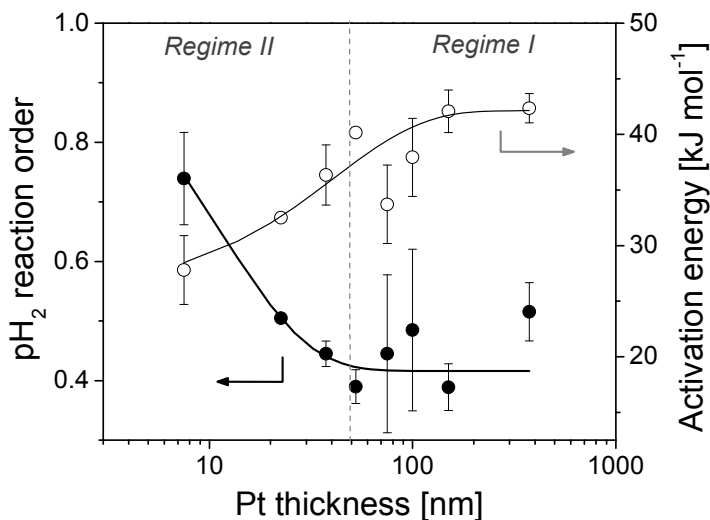


Figure 3.8 Plot of the pH_2 reaction order and the activation energy of the electrode process as a function of film thickness, showing a change in mechanism with film thickness.

The combination of the observed geometric (thickness and area) dependences of both the absolute value of R_0 and the form of the impedance response can be interpreted as follows. In all cases examined, the rate-limiting step occurs at sites that scale in number density with film area. For thicker films, diffusion to access these sites is rate limiting, giving rise to the linear dependence of R_0 on film thickness and the characteristic half-teardrop shape of the impedance response. For thinner films, diffusion no longer plays a role in limiting the rate of the process, however, the pathway continues to involve sites distributed through the film area. For truly dense films, one could readily conclude from these results that, for the range of film geometries examined, TPB sites do not contribute to the measured electrochemical activity. Even the sloped, irregular film boundaries do not create a significant concentration of active sites as this would lead to a diameter rather than area dependence of the overall activity. However, the existence of cracks throughout the films that cause an increase in the TPB site density in a manner that scales with film area precludes a definitive conclusion simply based on geometric

arguments. To address this ambiguity, we turn to the results obtained from cells in which Au was applied atop the Pt films.

3.3.3 Impedance Response: Impact of Gold Overlayers

SEM imaging of Au | Pt films with ~ 10 nm Au deposited on 75 nm Pt (not shown) revealed that the bilayer films attained morphologies essentially identical to those with Pt only (e.g., Figure 3.2). That is, the as-deposited films were crack-free, but after a thermal cycle microcracks were evident throughout the film area. Given that the cracks formed after Au deposition, all TPBs generated as a result of cracking are taken to be free of Au and thus equally active as those formed in the absence of Au. The inferred geometry is presented in Figure 3.9.

A comparison of the impedance responses for samples (75 nm Pt) with and without an Au overlayer (10 nm Au) reveals the dramatic impact of changing the nature of the exposed metal surface on the overall reaction impedance, Figure 3.10. The two spectra overlap almost perfectly at high frequencies ($f > 600$ Hz) at which the spectra are linear with a 45° slope in the Nyquist representation (Figure 3.10a). They deviate substantially at intermediate and especially low frequencies, and the DC electrode resistance is over an order of magnitude higher in the presence of Au (Figure 3.10b). The retention of the linear, 45° phase angle response at high frequencies upon deposition of Au is evidence that the diffusive process is retained. The dramatic increase in the absolute resistance at low frequency, on the other hand, reveals that the overall electrochemical reaction pathway must involve a step at the Pt | Au | H₂ interfaces. That is, the diffusion step must occur in serial with a step at these interfaces, where the interfacial step(s) becomes extremely slow in the presence of Au. These results thus rule

out the possibility that TPBs generated by cracking play any significant role on the electro-oxidation of hydrogen for the film geometries employed here.



Figure 3.9 A schematic of the Au | Pt | CsH₂PO₄ | Pt | Au symmetric cell, with the plane of symmetry denoted by a dashed line. Microcracks, resulting from heating the substrate to above the superprotonic phase transition temperature, are propagated to the Pt | Au film.

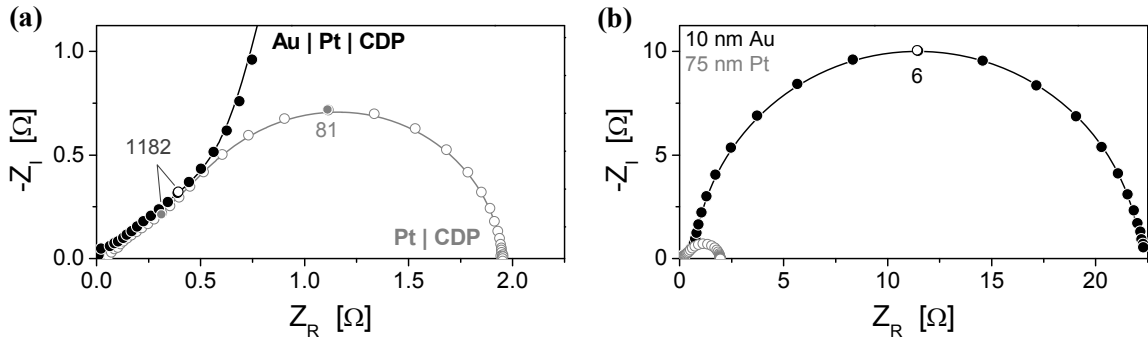


Figure 3.10 Comparison of electrode responses from Au | Pt | CsH₂PO₄ | Pt | Au and Pt | CsH₂PO₄ | Pt symmetric cells (15 mm dia. films, 10 nm Au, 75 nm Pt): (a) At high frequencies, both spectra overlap and exhibit a phase angle of 45°, while (b) at lower frequencies, the behavior the Au | Pt cell deviates significantly from that of the Pt cell.

3.3.4 Diffusion Analysis

With bulk diffusion through Pt having been revealed as the rate-limiting step for thicker films, the impedance data can be used for the determination of diffusion parameters. Specifically, the impedance response for the diffusion of a neutral species through a medium bounded by reversible planes/electrodes³³ has the form given in Equation (3.1), with $n = 0.5$ and $\tau = L_F^2 / \tilde{D}$, where L_F is the film thickness and \tilde{D} is the (ambipolar) diffusion of a neutral species, taken here to be interstitial hydrogen

(irrespective of possible dissociation into protons and electrons or into hydride ions and holes).^{31, 69} When the solution furthermore behaves ideally (dilute solution limit), the resistance in the DC limit is given by

$$R_0 = \frac{k_B T}{e^2 D_H c_H} \frac{L_F}{A_F} \quad (3.2)$$

where k_B , T and e have their usual meanings, c_H is the concentration of hydrogen in the Pt film, and A_F is the film area. An absolute valence of 1 is assigned to the transported species which is ultimately incorporated as protons at the Pt | CsH₂PO₄ interface. (The derivation of Equations (3.1) and (3.2) are shown in Appendix A.2.) Although n in Equation (3.1) is strictly 0.5 for a finite-length Warburg diffusion response, treating it as a fitted parameter, as was done here, provides an indication of microstructural imperfections/variations present in the films. Across 44 samples, n ranged from 0.41 to 0.58, a relatively small deviation from 0.5, with an average value of 0.48 ± 0.03 . Moreover, no correlation between n and any obvious experimental conditions or parameters was observed, suggesting that random sample-to-sample variations in film microstructure are responsible for the slight scatter.

Analysis of the impedance data of 44 symmetric cells in the manner described above yielded hydrogen diffusion coefficients (D_H) and concentrations (c_H) on the order of $10^{-12} \text{ m}^2 \text{ s}^{-1}$ and 10^{-4} H/Pt , respectively, Table 3.1. Over the relatively narrow temperature window explored, c_H was largely unchanged, whereas from the temperature dependence of D_H an activation energy of $47 \pm 6 \text{ kJ mol}^{-1}$ was determined. It is not possible to directly compare these values to those in the literature because all other reported studies address different temperature ranges. Extrapolation of literature

values^{70–73} to the temperatures examined here suggest a hydrogen diffusion coefficient in the range of 10^{-12} to $10^{-9} \text{ m}^2 \text{ s}^{-1}$ and a concentration in the range 10^{-8} – 10^{-4} H/Pt. The present values, though apparently reflecting low diffusivity and high solubility, lie within these ranges and are physically realistic. Reported activation energies for Pt^{70–73} are between 25 to 40 kJ mol^{-1} , the wide scatter likely being a consequence of the low solubility of hydrogen in this metal. While the value measured here, $47 \pm 6 \text{ kJ mol}^{-1}$, is somewhat high relative to this range, given the uncertainty in the literature data and the atypical temperature regime of the present study, it is reasonable to accept that the measurement reflects the same general type of process.

Beyond the expected temperature dependence of D_{H} , an unexpected dependence on film thickness was observed, Figure 3.11. Notably, c_{H} displayed an approximately inverted dependence on film thickness such that the product $D_{\text{H}} \times c_{\text{H}}$ remained approximately constant (not shown). Given the dependence of average Pt grain size on film thickness, Figure 3.4 and Figure 3.5, such behavior immediately suggests that the hydrogen transport mechanism depends on microstructure in a systematic manner. Specifically, the combination of somewhat high activation energy for hydrogen transport, low value of D_{H} , and microstructure dependence all suggest bulk diffusion through the films with grain boundaries as trapping sites. More significant in the present context than the details of hydrogen transport through Pt, is the fact that the absolute values of D_{H} and c_{H} support the surprising conclusion that the hydrogen electro-oxidation pathway involves hydrogen diffusion through the bulk of the films. Thus, for the range of geometries explored, the process is limited by the quantity of two-phase boundary sites (either Pt | gas or Pt | CsH_2PO_4) rather than the quantity of three-phase boundary sites.

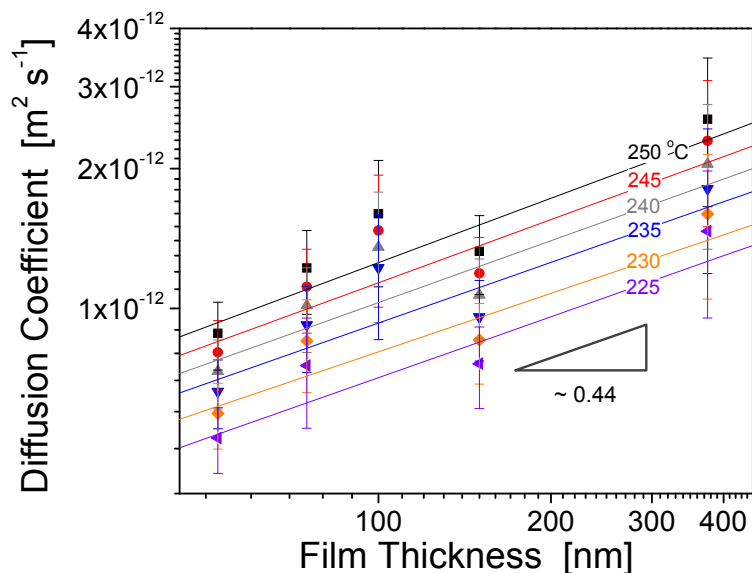


Figure 3.11 A plot of the extracted hydrogen diffusion coefficient as a function of film thickness for several temperatures. Error bars indicate the scatter of the value over several samples. Linear fits to each data set yield slopes with an average value of 0.44.

Table 3.1 Experimentally-determined parameters for hydrogen transport in Pt, shown for two temperatures. Values reported are taken from averaging over films greater than 50 nm in thickness.

T [°C]	D_H [$\times 10^{-12} \text{ m}^2 \text{ s}^{-1}$]	c_H [$\times 10^{-4} \text{ H/Pt}$]
250	1.6 ± 0.7	2.4 ± 0.8
225	0.9 ± 0.5	2.8 ± 0.8

3.3.5 Ultra-thin Platinum Films

For the thinnest films for which reliable data could be obtained (7.5 nm), the change in the features of the impedance response from those of thicker films is most certainly due to a change in the nature of the rate-limiting step. As the transport distance is decreased, diffusion limitations are relaxed, and interfacial effects at either or both the Pt | gas and Pt | CsH₂PO₄ boundaries become rate limiting. In the absence of transport of

a neutral species as the dominant response, the impedance response is expected to adopt a characteristic symmetric shape in the Nyquist representation, and the Z_{dFLW} element becomes inadequate for representing the response. An equivalent circuit with two parallel RQ sub-circuits placed in series with one another was used to analyze the data, as shown in Figure 3.6(c–d). From this analysis, we find the total electrode resistance, across twelve different samples, to have a value of $3.1 \pm 0.5 \Omega \text{ cm}^2$.

For the serial set of steps suggested by this analysis, the total, area-normalized electrode resistance, \tilde{R} , is expected to be the simple sum of the interfacial reaction resistance(s), \tilde{R}_{rxn} , and the thickness-dependent diffusion resistance, $\tilde{R}_D^* L_F$:

$$\tilde{R} = \tilde{R}_{\text{rxn}} + \tilde{R}_D^* L_F \quad (3.3)$$

The area-normalized data from Figure 3.7a indeed collapse into a single curve, Figure 3.12, which, in the double-logarithmic plot, display the expected flat regime at small film thickness and regime of slope 1 at large film thickness. The fit to Equation (3.3), also shown in the figure, implies $\tilde{R}_{\text{rxn}} = 2.2 \Omega \text{ cm}^2$ and $\tilde{R}_D^* = 0.081 \Omega \text{ cm}^2 \text{ nm}^{-1}$. For the thinnest film that could be evaluated (7.5 nm) with a total electrode resistance of $3.1 \pm 0.5 \Omega \text{ cm}^2$, the diffusion contribution is $0.9 \Omega \text{ cm}^2$, or approximately 27% of the total. Thus, both interfacial and bulk effects play a role even in very thin films.

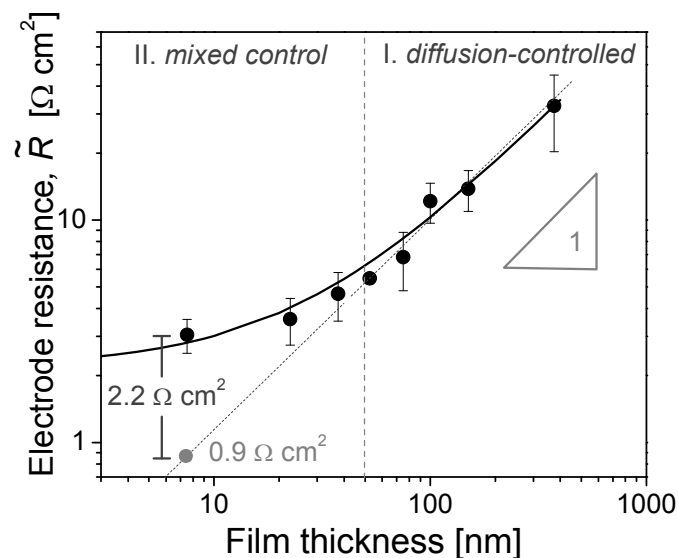


Figure 3.12 Area-normalized electrode resistance plotted against film thickness for all Pt | CsH₂PO₄ | Pt cells tested in this study. The solid curve corresponds to Equation (3.3), and the surface resistance was determined by extrapolation of the resistance due to diffusion to a Pt film thickness of 7.5 nm (dotted line).

3.4 Implications for Electrode Design

Platinum is known to display relatively poor hydrogen permeation characteristics and accordingly was not anticipated to facilitate hydrogen electro-oxidation via a bulk diffusion pathway. The dominance of the two-phase boundary pathway over the triple-phase boundary pathway results, in part, from the thin film geometry employed, which maximizes the Pt | CsH₂PO₄ interfacial area while minimizing the number of triple-phase boundary sites. In principle, the triple-phase boundary activity would be accessed by increasing the thickness platinum until the two-phase boundary pathway, governed by hydrogen diffusion through the film, is effectively blocked. However, because physical shadow masks are limited to relatively large areas (the smallest diameter used here was 1 mm), unrealistically thick films of Pt would be needed. An estimate of the lower bound for the resistance of the triple-phase boundary pathway is instead made using impedance

data acquired from electrode films with configurations similar to that shown in Figure 3.9. Specifically, blocking studies with 50 nm Au films yielded electrode resistances as high as $225 \Omega \text{ cm}^2$, while retaining diffusion characteristics at high frequencies of the type evident in Figure 3.10. The shape of the spectra implies that even with such extreme resistance in the blocking layers, the triple-phase boundary pathway is not favorable and can be used to establish the maximum activity of TPB sites. Based on a TPB density of $\sim 180 \text{ cm}^{-1}$, the lower bound for the triple-phase boundary resistance is estimated at $\sim 41 \text{ k}\Omega \text{ cm}$.

Irrespective of the absolute resistance values, one can expect the triple-phase boundary pathway to overtake the two-phase boundary pathway for Pt dimensions (diameter and thickness) which provide sufficient triple-phase site density relative to the two-phase interfacial area. One can speculate that a continuous Pt film with nanometric pores would lead to maximum overall activity. For a two-phase boundary resistance of $3.1 \Omega \text{ cm}^2$ and a minimum TPB resistance of $41 \text{ k}\Omega \text{ cm}$, an area-to-perimeter ratio of $\sim 7.6 \mu\text{m}$ or less is required to observe comparable total activity between two-phase and three-phase boundary sites in films with thickness 7.5 nm. While eventual fabrication of such structures could likely be achieved, because of the uncertainty with respect to the TPB site activity, there is no guarantee that such electrodes would, in fact, provide higher activity than the dense films examined here. Furthermore, films provide the inherent advantages of high electronic conductivity and good thermal stability.

These factors prompt a direct comparison of the activity of dense Pt thin films to state-of-the-art composite electrodes employed in solid acid fuel cells, Table 3.2. The absolute (area-normalized) resistance of the 7.5 nm film is within a factor of two of that

of composite electrodes formed solely of nanoparticulate Pt and CsH_2PO_4 . Specifically, electrodes fabricated by electrospray deposition²⁷ and by mechanical mixing³⁶ yield comparable resistance values of 1.5 and 1.7 $\Omega \text{ cm}^2$, respectively. Pre-commercial solid acid fuel cells, in which Pt/C is also an electrode component and thus take advantage of carbon to enhance electronic conductivity, have much smaller electrode resistances, just 0.06 $\Omega \text{ cm}^2$.¹⁰ Although the thin film Pt electrode displays the highest resistance, the amount of Pt applied is the lowest (by a factor of 10–500 in mass) such that the Pt utilization or mass-normalized activity ($\tilde{R}^{-1}/\text{Pt loading}$) is the highest, 19 S mg^{-1} . The poor activity in the nanoparticulate cases suggests a large fraction of the Pt is not utilized because of the lack of electronic connectivity. The results further suggest that increasing the overall electrode activity can be increased simply by increasing the projected Pt | CsH_2PO_4 contact area. Promising results taking advantage of precisely such an electrode geometry, albeit targeting the cathode, have been recently reported.^{3,28} In that work, a uniform Pt coating is applied to sub-micron CsH_2PO_4 powders using a metal organic chemical vapor deposition method.²⁸ A decrease in the CsH_2PO_4 particle size led to a monotonic decrease in electrode resistance³ indicating the importance of the total Pt | CsH_2PO_4 surface area. Using such techniques, one can readily envision a substantial increase in specific surface area over that of a flat interface, and from the quantitative studies reported here, the impact on performance metrics can be assessed. For CsH_2PO_4 particle-based electrodes of moderate thickness, we presume the activity will scale linearly with surface area, and thus, a 50-fold increase in the specific surface area, for example, will decrease the electrode resistance to a highly attractive value of $\sim 0.06 \Omega \text{ cm}^2$ for the 7.5 nm thick film. The Pt loading will also increase proportionally,

but would remain at just 0.86 mg cm^{-2} . Thus, thin, continuous film electrodes have the potential to dramatically reduce Pt loadings while also enhancing power output.

Table 3.2 Comparison of platinum-based anodes for solid acid fuel cells at temperatures of 238–250 °C. \tilde{R} = area-normalized electrode resistance

Electrodes	\tilde{R} $\Omega \text{ cm}^2$	Pt loading mg cm^{-2}	$\tilde{R} / \text{Pt loading}$ S mg^{-1}
7.5 nm Pt film – <i>sputtered (this work)</i>	3.1 ± 0.5	0.017	19
Pt:CsH ₂ PO ₄ (1:2) – <i>electrosprayed</i> ²⁷	1.5	0.3	2.2
Pt:CsH ₂ PO ₄ (1:2) – <i>mech. mix.</i> ³⁶	1.7	10	0.059
Pt:Pt/C:CsH ₂ PO ₄ (3:1:3) – <i>mech. mix.</i> ^{10, 25}	0.06	7.7	2.2

3.5 Summary

The rate-limiting step for hydrogen electro-oxidation over Pt thin film electrodes has been identified. Pt films between 7.5 and 375 nm thick were determined to electrocatalytically oxidize hydrogen via the two-phase boundary pathway. Pt films greater than 50 nm in thickness are rate-limited by diffusion of hydrogen through the film, whereas for films thinner than 50 nm, interfacial processes, with a resistance of $2.2 \Omega \text{ cm}^2$, begin to overtake diffusion as the rate-limiting step. That the two-phase boundary pathway is preferred over that three-phase boundary pathway has significant implications for the design of electrodes in solid acid fuel cells. Specifically, electrodes based on 7.5 nm Pt films with electrode resistances of $3.1 \Omega \text{ cm}^2$, have the potential to reach state-of-the-art performances while using one order of magnitude less Pt by mass. This improvement is a consequence of the inherent interconnectivity of the platinum in the thin film configuration and the resulting improvement in catalyst utilization compared to conventional electrodes based on Pt nanoparticles.

Chapter 4 Oxygen Electro-reduction at Nano-Pt | CsHSO₄

Adapted with permission from: Louie, M. W.; Hightower, A.; Haile, S. M. Nanoscale Electrodes by Conducting Atomic Force Microscopy: Oxygen Reduction Kinetics at the Pt | CsHSO₄ Interface. *ACS Nano* **2010**, 4, 2811–2821.

Abstract

We quantitatively characterized oxygen reduction kinetics at the nanoscale Pt | CsHSO₄ interface at ~150 °C in humidified air using conducting atomic force microscopy (AFM) in conjunction with AC impedance spectroscopy and cyclic voltammetry. From the impedance measurements, oxygen reduction at Pt | CsHSO₄ was found to be comprised of two processes, one displaying an exponential dependence on overpotential and the other only weakly dependent on overpotential. Both interfacial processes displayed near-ideal capacitive behavior, indicating a minimal distribution in the associated relaxation time. Such a feature is taken to be characteristic of a nanoscale interface in which spatial averaging effects are absent and, furthermore, allows for the rigorous separation of multiple processes that would otherwise be convoluted in measurements using conventional, macroscale electrode geometries. The complete current-voltage characteristics of the Pt | CsHSO₄ interface were measured at various points across the electrolyte surface and reveal a variation of the oxygen reduction kinetics with position. The overpotential-activated process, which dominates at voltages below –1 V, was interpreted as a charge transfer reaction. Analysis of six different sets of

Pt|CsHSO₄ experiments, within the Butler-Volmer framework, yielded exchange coefficients (α) for charge transfer ranging from 0.1 to 0.6 and exchange currents (i_0) spanning five orders of magnitude. The observed counter-correlation between the exchange current and exchange coefficient indicates that the extent to which the activation barrier decreases under bias (as reflected in the value of α) depends on the initial magnitude of that barrier under open-circuit conditions (as reflected in the value of i_0). The clear correlation across six independent sets of measurements further indicates the suitability of conducting AFM approaches for careful and comprehensive study of electrochemical reactions at electrolyte-metal-gas boundaries.

4.1 Introduction

The power output of high-performance, thin-electrolyte fuel cells is, by definition, limited by the rate of electrochemical reactions at the electrode rather than by ion transport through the electrolyte. Accordingly, substantial effort has been directed towards understanding electrochemical reaction pathways and identifying rate-limiting steps, with the ultimate aim of developing new electrode materials and/or structures with enhanced activity. The vast majority of such electrochemical studies have relied on fuel cell electrodes of macroscopic dimensions, in some cases with geometrically well-defined structures^{36–38, 46, 50, 53, 55, 58–60, 62, 74, 75} and in others with composite electrodes more directly relevant to technological applications.^{39, 40, 76, 77} While such studies have led to important insights and advances, a comprehensive understanding of reaction pathways remains elusive for virtually every fuel cell type. It is to be expected that electrochemical reactions, which occur on surfaces that naturally display nanoscale heterogeneity, themselves occur at rates that are heterogeneous on the nanometer length scale. Thus, the limitations of macroscale measurements, which, by definition, cannot probe such heterogeneity and instead provide ensemble-averaged data with little information even about the distribution range of properties, may inherently complicate elucidation of electrochemical reaction pathways. Despite the recognition that nanoscale heterogeneity may play an important role in fuel cell electrode kinetics, few studies have been directed towards explicitly uncovering variations in electrochemical reaction rates and possibly even mechanisms at the nanometer scale.

In this work, we utilize conducting atomic force microscopy (AFM) for quantitative electrochemical characterization of metal|solid electrolyte interfaces.

Configurationaly, the approach is similar to that employed in recent studies in which conducting AFM has been employed to evaluate nanoscale heterogeneity in the transport properties of ion conducting electrolyte materials.^{78–83} The electrolyte material is contacted over its entire area to an electrochemically active counter electrode, Figure 4.1, and the conducting AFM probe contacted to the opposite surface. Because the electrolyte is electronically blocking, net current flow through the system requires electrocatalysis to occur at sufficient rates at both the counter and working (AFM tip) electrode. For the study of the distribution of ion conducting and insulating regions, as has been done for polymers^{78–82, 84, 85} and more recently for ceramics,⁸³ it is sufficient to scan the electrolyte surface and differentiate between regions of high and low current flow. From such measurements, it is also possible to characterize the nature of contact between the probe and electrolyte.^{24–25} Here, we evaluate the complete current-voltage characteristics at each point of interest on the electrolyte surface to study directly the kinetics of the electrochemical reaction and its nanoscale heterogeneity.

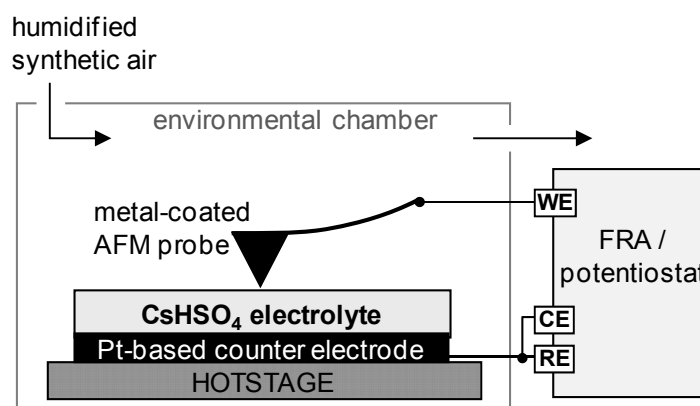
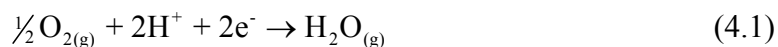


Figure 4.1 Schematic of nanoelectrode setup comprised of an atomic force microscope coupled with an external potentiostat and a frequency response analyzer capable of measuring fA current range. The hotstage can heat samples to temperatures as high as 240 °C. The environmental chamber encloses the probe-sample assembly and is equipped with several inlet/outlet ports, enabling controlled atmospheres.

The electrolyte material selected for study in this work is CsHSO₄, a so-called superprotonic solid acid, which exhibits a proton conductivity of $\sim 6 \times 10^{-3} \text{ S cm}^{-1}$ at a moderate temperature of 150 °C.^{6, 86} We consider it a representative material for superprotonic solid acids in general,¹² and specifically for those such as CsH₂PO₄ which have been demonstrated in fuel cells but require somewhat higher temperatures to attain comparably high proton conductivities.^{1, 10} The electrochemical reaction of interest (examined at 150 °C for all experiments in this study) is that of oxygen electro-reduction. The relevant global reaction for a proton-conducting electrolyte is given as



An attractive feature of the conducting AFM geometry is the extreme asymmetry in the electrode areas. As discussed in detail elsewhere,³⁶ such asymmetry ensures that the overpotential (excess voltage drop relative to equilibrium) at the large counter electrode is negligible relative to that at the working (AFM tip) electrode. That is, because the current through each component of the cell is the same, the current density is orders of magnitude greater at the working electrode than it is at the counter electrode, and accordingly, the contribution of the counter electrode | electrolyte interface to the voltage drop measured across the system is negligible. Indeed, in the conducting AFM configuration, even the voltage drop across the electrolyte is negligible relative to that due to the finite kinetics at the working electrode. Thus, employing a nanoelectrode enables electrochemical studies of a single metal | electrolyte interface without the need for an external reference electrode, the placement of which has been shown to be problematic in solid electrolyte systems.^{44, 45} Such a measurement directly yields the

potential at the working electrode, referenced to the counter electrode, which, in turn, for the measurement temperature of $\sim 150\text{ }^{\circ}\text{C}$ is at -1.13 V relative to $2\text{H}^{+} + 2\text{e}^{-} \rightleftharpoons \text{H}_2$.

With this understanding, both cyclic voltammetry and AC impedance spectroscopy were used for quantitative electrochemical characterization. The former has the benefits of providing complete DC current-voltage characteristics at short timescales, before instrument drift becomes problematic, but cannot deconvolute resistance contributions resulting from multiple reaction steps. Impedance spectroscopy provides the benefits of deconvolution and, when carried out as a function of bias, can also provide complete current-voltage characteristics. The timescale of such measurements, however, is not sufficient to eliminate the possibility of a drifting probe | sample contact over the course of the experiment. The complementary information provided by these two techniques has proven to be indispensable in the present work.

4.2 Experimental

4.2.1 Half-cell Fabrication

CsHSO_4 powder was synthesized by rapid precipitation of a mixture of aqueous Cs_2SO_4 (99.99%, Alfa Aesar) and aqueous H_2SO_4 (95 wt% in water, EMD Chemicals) by acetone, followed by filtration and drying at $\sim 100\text{ }^{\circ}\text{C}$. Electrocatalyst mixtures were made from a toluene slurry comprised of Pt black ($> 99.9\%$, fuel cell grade, Sigma Aldrich), Pt/C (40% on carbon black, Alfa Aesar), and CsHSO_4 in a Pt:Pt/C: CsHSO_4 weight ratio of 3:1:3; the slurry was sonicated and dried at $\sim 100\text{ }^{\circ}\text{C}$. Half-membrane electrode assemblies were fabricated by uniaxially pressing CsHSO_4 powder onto a

Pt:Pt/C:CsHSO₄ composite electrode supported on Toray paper (TGP-H-120) for 20 min at 490 MPa. The CsHSO₄ surface of the resulting half-cell was then polished with a $\sim 2\ \mu\text{m}$ grit silicon carbide cloth and blown with a dry air jet. Fabricated assemblies were 9.3 mm in diameter and 0.5–1 mm thick.

4.2.2 *Experimental Conditions*

Fabricated half-cells were mounted onto the hotstage of a PicoSPM atomic force microscope (Series 4500, Agilent Technologies) equipped with an environmental chamber and a scanner head with x - y and z ranges of ~ 30 and $\sim 6\ \mu\text{m}$, respectively. The temperature of the hotstage was set to $\sim 170\ ^\circ\text{C}$ to attain a CsHSO₄ surface temperature of $\sim 150\ ^\circ\text{C}$. (The temperature gradient across the cell generated an open-circuit voltage of less than 1 mV.) Humidified synthetic air, generated by bubbling $\sim 15\ \text{mL min}^{-1}$ of air through water at room temperature (~ 0.02 – $0.03\ \text{atm H}_2\text{O}$), was continuously fed through the environmental chamber. Electrochemical characterization was carried out using an externally connected potentiostat equipped with a femtoammeter and a frequency response analyzer (ModuLab, Solartron Analytical) which were calibrated using high impedance circuits comprising of 0.01–100 G Ω resistors and 1–10 pF capacitors. Electrochemical characterization was carried out in potentiostatic mode; voltages are applied across the entire cell (probe | CsHSO₄ | composite electrode), with the probe as the working electrode and the large composite electrode serving as the counter and reference electrode. All voltages reported in this work are, therefore, with respect to the large composite counter electrode, that is, an air electrode reference which is $-1.13\ \text{V}$ relative to $2\text{H}^+ + 2\text{e}^- \rightleftharpoons \text{H}_2$ at $\sim 150\ ^\circ\text{C}$. To reduce contributions of external noise, the microscope was placed in a copper mesh Faraday cage which, like the

shielding for the electrical leads, was grounded through the potentiostat ground. The microscope body, which was separately grounded, was electrically isolated from the cage. Stray capacitance and other spurious contributions were found to depend on the current range of the potentiostat, and therefore, open-circuit corrections were obtained by withdrawing the probe from the sample and taking impedance measurements at each current range. Point-wise open-circuit corrections were applied to all impedance spectra presented (Appendix F.2.1). Short-circuit measurements, obtained by contacting the conductive probe to a piece of gold foil, displayed the behavior of a pure resistor with a resistance on the order of 5 k Ω , negligible relative the high impedances of the nanoprobe setup employed in this work.

4.2.3 *Measurement Conditions*

Cyclic voltammograms were collected by sweeping between -1.1 and 0.5 V with scan rates, ν , of 5 – 400 mV s $^{-1}$. Impedance measurements were carried out with a 100 mV perturbation about voltages ranging from -0.6 to -1.2 V with frequencies of 10^6 – 10^{-1} Hz. The acquisition time for each spectrum was ~ 2.5 min, and three spectra for each voltage were acquired. The working electrodes were metal-coated Si-based AFM probes (MikroMasch) with specifications shown in Table 4.1. A majority of the platinum data presented in this work are from Probes 1 and 3. Forces applied with the Pt probes were between 0.2 and 0.5 μ N during electrochemical measurements and ~ 0.1 μ N when rastering the surface for imaging. Stationary cyclic voltammograms collected as a function of position were comprised of three cycles at 100 mV s $^{-1}$ (to attain stable voltammograms) followed by two cycles at 25 mV s $^{-1}$ (used for quantitative analysis) for Probes 1–4, and five cycles at 100 mV s $^{-1}$ for Probes 5–6. Impedance spectra at -1.0 and

−0.9 V were measured at select spatial positions to verify that the primary features of the spectra had not changed. The thermal drift of $\sim 0.1 \text{ nm s}^{-1}$, estimated by the imaging and tracking of surface features, impacts bias-dependent impedance measurements which required $\sim 50 \text{ min}$ acquisition time. On the other hand, cyclic voltammetry measurements required only several minutes of acquisition time (depending on the scan rate employed), and, moreover, the voltage range used for analysis only required $\sim 30 \text{ s}$ (corresponding to a drift of no more than 3 nm) to acquire.

Table 4.1 Conducting AFM probes employed in this study.

	Adhesion Layer	Spring Constant $k \text{ [N m}^{-1}\text{]}^*$	Total Tip Radius $r_{tip} \text{ [nm]}^*$
Probe 1	10 nm Pt on 20 nm Ti	5	40
Probe 2	10 nm Pt on 20 nm Ti	5	40
Probe 3	10 nm Pt on 20 nm Ti	5	40
Probe 4	10 nm Pt on 20 nm Ti	1.8	40
Probe 5	25 nm Pt on 5 nm PtSi	3.5	40
Probe 6	25 nm Pt on 5 nm PtSi	5	40
Probe 7	20 nm Au on 20 nm Cr	40	50

*nominal values

4.2.4 Data Analysis

Fitting of impedance spectra was carried out using the commercial package Zview (Version 2.9b, Scribner Associates, Inc.). Spectra were fitted using two parallel RQ sub-circuits in series. The value of n for the high-frequency arc, when treated as a free parameter during fitting, exceeded unity (by no more than 10%) and was therefore held fixed at 1. Such a fitting procedure yielded n values of 0.91–0.98 for the low-frequency process. Stray capacitance contributions, which are not negligible in such low current systems were accounted for by a point-wise open correction procedure, as shown in

Appendix F.2.1. Short-circuit measurements, obtained by contacting the conductive probe to a piece of gold foil, displayed the behavior of a pure resistor with a resistance on the order of 5 k Ω , negligible relative the high impedances of the nanoprobe setup employed in this work. The stability of the impedance measurements was verified by collecting the spectra by sweeping the frequency in both directions (Appendix F.2.2).

All cyclic voltammetry data were corrected for a non-zero offset current present in the system. Analysis of spatial variation of electrochemistry was done so using a voltammograms with a scan rate 25 mV s⁻¹ which was determined to be sufficiently slow for measuring oxygen reduction kinetics but fast enough to minimize effects of thermal drift. (Appendix F.2.3). The magnitude of force applied between the probe and sample in the measurements was determined to have negligible impact on electrochemical results (Appendix F.2.4). To collect spatial variation data, the probe was lifted from the sample surface temporarily; we determined that this had no impact on the electrochemical measurements. (Appendix F.2.4)

4.3 Results and Discussion

4.3.1 Cyclic Voltammetry

An initial comparison between the behavior of Au and Pt was performed to verify that contact could be made between the electrolyte surface and the AFM probe. Cyclic voltammograms for Au | CsHSO₄ and Pt | CsHSO₄ are presented in Figure 4.2. The observation of low currents, ~ pA, is consistent with the small size of the AFM probe (tip radius \approx 40 nm). Noise appearing in the voltammograms, resulting from a combination of

the relatively low spring constant of the probe cantilever and elevated operating temperatures, is minimal and does not mask any of the salient characteristics. The voltammogram for Au | CsHSO₄ is featureless and displays less than 0.1 pA current across all voltages. In contrast, the voltammogram for Pt | CsHSO₄ exhibits a peak at -0.34 V (onset ≈ -0.1 V) overlaid with an overpotential-activated rise in current at negative biases. At -1.1 V, the measured current for Pt is ~ 15 pA, over two orders of magnitude higher than that for Au. These observations are consistent with the relative activities of bulk gold and platinum and confirm contact by the probe tip.

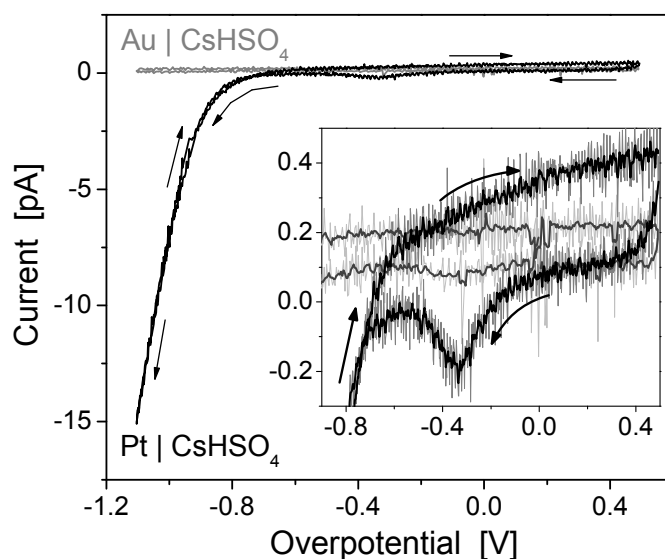


Figure 4.2 Comparison of typical cyclic voltammograms for Au | CsHSO₄ and Pt | CsHSO₄ collected at ~ 150 °C in air (~ 0.03 atm H₂O) with a scan rate of 100 mV s^{-1} ; the voltammograms shown are those obtained after cycling to ensure stability. Inset is an enlargement of the Pt oxide reduction peak at -0.34 V and displays both raw data (gray) and smoothed data (black). The applied force was ~ 2 and ~ 0.5 μN for Au and Pt, respectively. The Pt probe utilized is identified as Probe 3 in Table 4.1.

The peak evident in the Pt voltammogram is readily attributed to the reduction of platinum oxide. Based on calculations from thermodynamic data⁸⁷ for $T = 150\text{ }^{\circ}\text{C}$ and $p\text{O}_2 = 0.21\text{ atm}$, reduction of PtO , PtO_2 , and $\text{Pt}(\text{OH})_2$ is expected to occur at -0.16 , -0.14 , and -0.06 V , respectively, whereas measured platinum oxide reduction potentials, for both smooth Pt surfaces in aqueous acidic electrolytes^{88–90} and for Pt-carbon | Nafion systems,^{84, 91, 92} range from -0.03 to -0.3 V , depending on temperature and experimental conditions. The total charge, $\sim 0.5\text{ pC}$, implied by the integrated area under the reduction peak and the scan rate, assuming the formation of any of the possible oxides, corresponds to the reduction of a plausible fraction of the Pt coating available on the AFM tip. The absence of a corresponding Pt oxidation peak on the reverse sweep indicates that chemical oxidation of Pt, which by definition, cannot generate a peak in the voltammogram, dominates the process of oxide formation over electrochemical oxidation.

While the Pt oxide reduction behavior on CsHSO_4 bears some similarities to that at the interface with aqueous and polymeric electrolytes, the Pt | CsHSO_4 system differs sharply from those in terms of interaction with hydrogen. In aqueous, acidic electrolytes or with polymer membrane electrolytes, hydrogen adsorption or desorption peaks are typically observed in the region between -0.8 and -1.2 V at temperatures between 25 and $150\text{ }^{\circ}\text{C}$.^{41, 84, 92–96} The absence of such peaks here suggests that hydrogen sorption onto the surface of Pt is negligible in the Pt | CsHSO_4 system. An unfortunate consequence of this behavior is that, in contrast to aqueous and polymer systems, hydrogen adsorption peaks cannot be used to estimate the surface area of Pt available for electrocatalysis in solid acid fuel cell electrodes. Similarly, without further information on the characteristics of

Pt oxide reduction, the corresponding peak in the voltammogram cannot be employed for determining the Pt | CsHSO₄ contact area.

4.3.2 *Impedance Spectroscopy*

Selected impedance spectra representative of oxygen reduction at the Pt | CsHSO₄ interface are presented as Nyquist plots in Figure 4.3 and Figure 4.4. While the bulk of the experimental details regarding acquisition of such spectra are provided in the Experimental section and in Appendix F.2, some aspects are highlighted here because the high impedance of the Pt | CsHSO₄ system in the nanoprobe geometry requires special consideration with respect to effects from external noise. All spectra collected were corrected with an open-circuit measurement which accounted for stray capacitance and other spurious contributions, and furthermore, the impedance analyzer was calibrated with precision circuits comprised of high resistance (0.01–100 GΩ) and low capacitance (1–10 pF) elements comparable in value to those measured in the present nanoprobe system. We also verified that the impedance response is stable, i.e., the spectra features are not transient artifacts, by examining the agreement between two spectra collected consecutively at –1.0 V, with one measured by sweeping the frequency in the opposite direction of the other (see Appendix F.2.2). With these precautions taken, the general features of the experimental data were found to be satisfactorily reproducible.

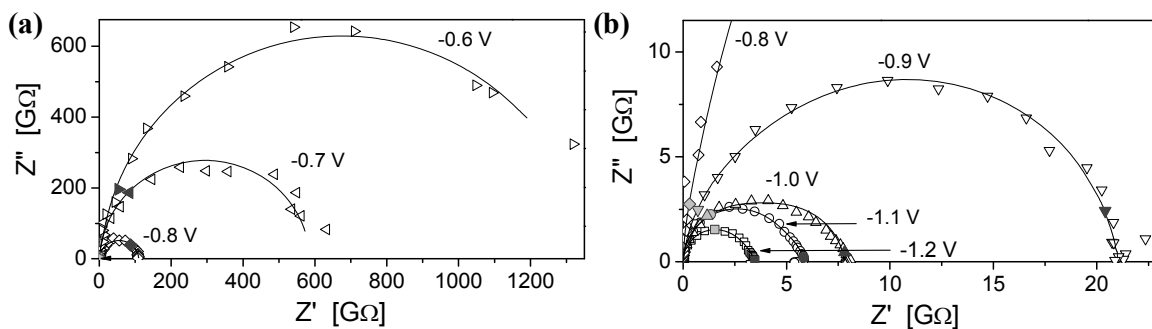


Figure 4.3 AC impedance spectra for Pt | CsHSO₄ as a function of overpotential, collected at ~ 150 °C in humidified air (~ 0.03 atm H₂O), for overpotentials between (a) -0.6 and -0.8 V, and (b) -0.8 and -1.2 V. The filled data points correspond to frequencies of 200 and 2 Hz, and solid curves indicate equivalent circuit fits to two parallel RQ sub-circuits in series. The Pt probe utilized is identified as Probe 3 in Table 4.1.

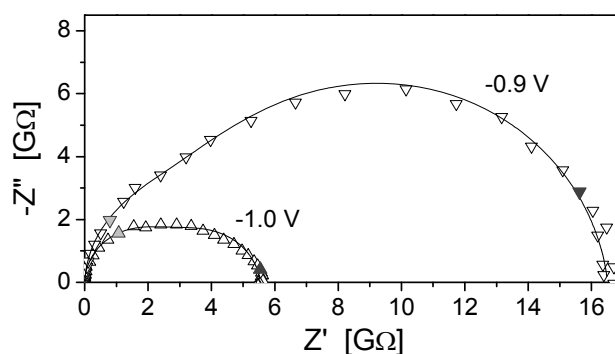


Figure 4.4 Typical impedance spectra for Pt | CsHSO₄ at overpotentials of -1.0 and -0.9 V, collected at ~ 150 °C in humidified air (~ 0.03 atm H₂O), showing the presence of two processes. The filled data points correspond to frequencies of 200 and 2 Hz, and solid curves indicate equivalent circuit fits to two parallel RQ sub-circuits in series. The Pt probe utilized is identified as Probe 2 in the Table 4.1.

The Nyquist plots presented in Figure 4.3 and Figure 4.4 reflect data collected from two different Pt probes, where the response for each was examined as a function of the applied voltage. In both cases, the total polarization resistance is a strong function of bias, spanning almost three orders of magnitude in Figure 4.3, from ~ 3 G Ω at -1.2 V to ~ 1 T Ω at -0.6 V. Proton conduction through bulk CsHSO₄, typically manifested in bulk

conductivity measurements as an ohmic offset at high frequencies,¹⁰ is not visible in Figure 4.3 and Figure 4.4, since its contribution is negligible compared to the electrode processes.

In the absence of a physical model, impedance spectra are commonly analyzed by employing equivalent circuits, for which the simplest building block is a resistor (R) in parallel with a constant phase element (Q). The latter generally represents capacitive effects and has impedance

$$Z_Q = \frac{1}{Y(i\omega)^n} \quad (4.2)$$

where Y is a constant, ω is the angular frequency, and n ranges from 0 to 1. When $n = 1$, the constant phase element becomes a perfect capacitor with capacitance Y , and the parallel RQ sub-circuit is represented in the Nyquist plot as a semi-circle with its center lying on the real axes. Deviations of n from 1 are typically interpreted in terms of a distribution of relaxation times within a globally measured response.^{32, 34}

The impedance spectra shown in Figure 4.3 are comprised of two arcs; the frequency overlap of the two processes varied with experiment and spatial position, with some measurements more clearly depicting the presence of two electrode processes (Figure 4.4). The impedance spectra were fitted to an empirical equivalent circuit model comprised of two parallel RQ circuits in series. Fitting results yielded $n > 0.9$ for both processes, indicating ideal capacitive behavior with a low dispersion in the characteristic frequency of each process. These n values are considerably higher than those observed for macroscale interfacial processes for which depression of the electrode arc in the Nyquist plot reflects n values in the range 0.6–0.8.^{36–40} Low n values for interfacial

processes are commonly attributed to spatial heterogeneities at the electrode | electrolyte interface.^{32, 34} The observation of a low dispersion of relaxation times in the present measurement suggests that, at the nanoscale, averaging effects are eliminated. In turn, because of the low dispersion, it is possible from these measurements to clearly observe two processes, despite the similarity of their relaxation times. In a macroscopic measurement with low n , deconvolution of interfacial processes that are close in characteristic frequencies would likely not be possible.

The bias dependence of the resistances associated with the two processes (Figure 4.5) reveals that the resistance of the low-frequency process, R_{LF} , is strongly dependent on voltage, decreasing from 1 T Ω at -0.6 V to less than 1 G Ω at -1.2 V. In the semi-log plot, an apparent exponential dependence is evident. In contrast, the resistance of the high-frequency process, R_{HF} , is largely independent of bias, displaying an erratic voltage dependence between 1 and 10 G Ω that is almost within the noise of the measurement. The total electrochemical resistance, R_{TOT} , which is simply the sum of R_{LF} and R_{HF} , is accordingly dominated by R_{LF} at low bias and by the fixed value of R_{HF} at high bias. While the data here are presented for one representative set of impedance spectra, such behavior was observed in multiple measurements. An analysis of the capacitances associated with the two processes and their bias dependence is not presented here due to their relatively high fitting errors.

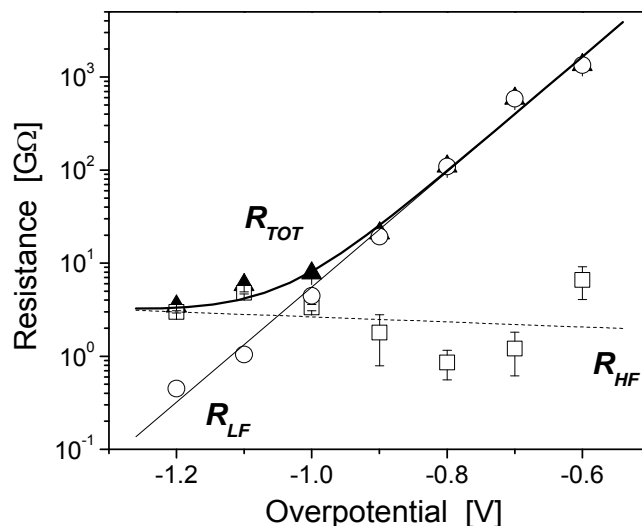


Figure 4.5 Total polarization resistance (R_{TOT}) and electrode resistances (R_{LF} , R_{HF}) determined by fitting AC impedance spectra (shown in Figure 3) to two parallel RQ circuits in series. Lines indicate the general trends of each parameter and were obtained by linear fits of R_{HF} and R_{LF} and their sum, R_{TOT} . Resistance is plotted on a logarithmic scale.

The electrochemical reaction of interest, Equation (4.1), is represented by the cathodic branch of the cyclic voltammogram. Cyclic voltammograms obtained at slow scan rates (such that capacitive and other transient effects are reduced) can be employed for quantitative analysis of oxygen reduction kinetics. For such an analysis, it is essential to recognize that the oxygen reduction reaction occurs on Pt metal only at voltages negative of that for the Pt-PtO_x couple; at all other voltages, $O_2 + 4H^+ + 4e^- \rightleftharpoons 2H_2O$ occurs on platinum *oxide*. An implication of Pt oxide formation is that, for a fuel cell under open-circuit conditions, platinum catalyst at the cathode is oxidized, and the initial current drawn contains a contribution from Pt oxide reduction.

4.3.3 Analysis of Oxygen Electro-reduction Kinetics

The behavior revealed in Figure 4.5 suggests that the DC current across the Pt | CsHSO₄ interface should, like the AC resistance, display an exponential dependence

on bias within an appropriate range of voltages. In Figure 4.6, we plot, on a semi-log scale, data obtained from the return sweep (implying the oxide has already been reduced to the metal) of the cathodic branch of a cyclic voltammogram collected at a 5 mV s^{-1} scan rate, and, indeed, linearity is observed between -1 and -0.6 V . At higher biases (beyond -1 V), the deviation from linearity in the semi-log plot is readily attributed to the increasing importance of the bias-independent resistance term (Figure 4.5). At smaller biases (less than -0.6 V), the scatter is a result of the overall low current and a non-zero offset current (correction procedures for which are described in the Appendix F.2.3). In principle, the results of Figure 4.5 and Figure 4.6 can be numerically converted from one form to the other, however, the thermal drift in the system (estimated to be $\sim 0.1 \text{ nm s}^{-1}$ at 150°C) precludes quantitative comparisons. Nevertheless, the overall agreement between the AC and DC measurements, in terms of the functional form of the data, demonstrates the robustness of the experimental approach pursued here for examining electrode kinetics. Both measurements methods are utilized, as AC impedance spectroscopy provides invaluable mechanistic information, i.e., the elucidation of multiple processes and their relative timescales, whereas cyclic voltammetry enables quantification of selected kinetic parameters.

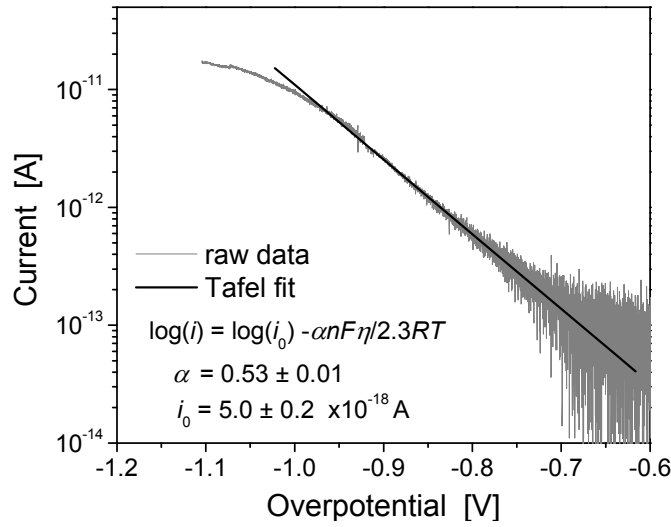
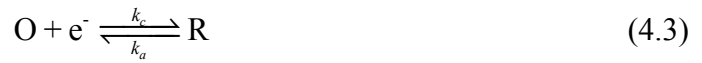


Figure 4.6 Semi-log plot of the cathodic branch of the cyclic voltammogram for Pt | CsHSO₄. The voltammogram was collected with a 5 mV s⁻¹ scan rate at ~ 150 °C in humidified air (~ 0.03 atm H₂O). The exchange coefficient and exchange current can be extracted from the slope and intercept, respectively, by fitting the linear regime to the Tafel equation, Equation (4.6). The Pt probe utilized is identified as Probe 3 in Table 4.1.

A voltage-dependent resistance is a typical feature of charge transfer electrochemical reactions, and the exponential dependence of R_{LF} on bias suggests analysis in terms of conventional Butler-Volmer reaction kinetics. In a generic sense, the charge transfer reaction associated with oxygen electro-reduction at the Pt | CsHSO₄ interface can be described as⁴¹



where k_c and k_a are the rate constants for the cathodic and anodic directions, respectively, and a single-electron process has been assumed. The kinetics associated with this reaction can be expressed in terms of the Butler-Volmer equation (derived in Appendix A.1),

$$\frac{i}{i_0} = \exp\left[-\frac{\alpha F}{RT}\eta\right] - \exp\left[\frac{(1-\alpha)F}{RT}\eta\right] \quad (4.4)$$

where i_0 is the exchange current, $\eta = E - E_{eq}$ is the overpotential, α is the exchange coefficient which ranges from 0 to 1, and F , R and T have their usual meanings. At the large negative overpotentials selected for the analysis performed here (due to both Pt oxidation and significant offset current at small overpotentials), only the cathodic branch of the Butler-Volmer equation need be considered. For $\eta \ll 0$, Equation (4.4) reduces to

$$i = i_0 \exp\left(-\frac{\alpha F}{RT}\eta\right) \quad (4.5)$$

or, in Tafel form,

$$\log(i) = \log(i_0) - \frac{\alpha F}{2.3RT}\eta \quad (4.6)$$

Thus, from a linear fit to the semi-log data, one obtains the exchange current density (from the extrapolated intercept at zero bias or overpotential) and the exchange coefficient (from the slope). As an alternative to Equation (4.6), one can consider introduction of a term that accounts for the observation of an additional, bias-independent process (effectively accounting for R_{HF}). Attempts to fit an appropriately modified expression, however, were largely unsuccessful because of the insensitivity of the fit parameters, and hence the determination of properties associated with the high-frequency process from the voltammograms was not pursued.

For the specific data set presented in Figure 4.6 and a fit over the potential range from -0.65 to -1.0 V, we obtain $\alpha = 0.53 \pm 0.01$ and $i_0 = 5.0 \pm 0.2 \times 10^{-18}$ A. Because the area of electrochemical activity at the probe tip is unknown, the value determined for the exchange current cannot be readily interpreted quantitatively or compared to literature measurements. The exchange coefficient, in contrast, is independent of these uncertainties and its absolute value has significance. This parameter provides a measure

of the asymmetry of the activation barrier for the charge transfer. For a single-electron process, α should lie between 0 and 1, with $\alpha = 0.5$ corresponding to perfect symmetry of the anodic and cathodic directions of the charge transfer step. A value of 0.53 as obtained here falls within the range typically observed in aqueous electrolyte systems ($\alpha = 0.3\text{--}0.7$).⁴¹

4.3.4 *Heterogeneity of Electrochemical Kinetics*

As already noted, conducting atomic force microscopy enables an exploration of the spatial variation of electrode kinetics at Pt | CsHSO₄ with relative ease. A scanning electron micrograph (Figure 4.7a) shows typical surface features of polycrystalline CsHSO₄ after testing. Alongside it is an AFM topography scan of a $5 \times 5 \mu\text{m}^2$ region, collected under operating conditions, that includes (nominal) spatial positions at which electrochemical measurements were acquired (Figure 4.7b). The electron micrograph shows large crystalline grains, 5–10 μm in size, whereas the topography scan, collected at higher resolution, reveals finer features ($< 1 \mu\text{m}$) and a RMS roughness of $\sim 30 \text{ nm}$. Cyclic voltammograms measured at each position were stable upon cycling and, within a moderate range (Appendix F.2), insensitive to the value of the applied force, and therefore the data are considered reliable for evaluating the electrochemical response at each position. However, the extent of thermal drift after measuring several positions precludes a precise correlation of electrochemical reaction rates with surface features.

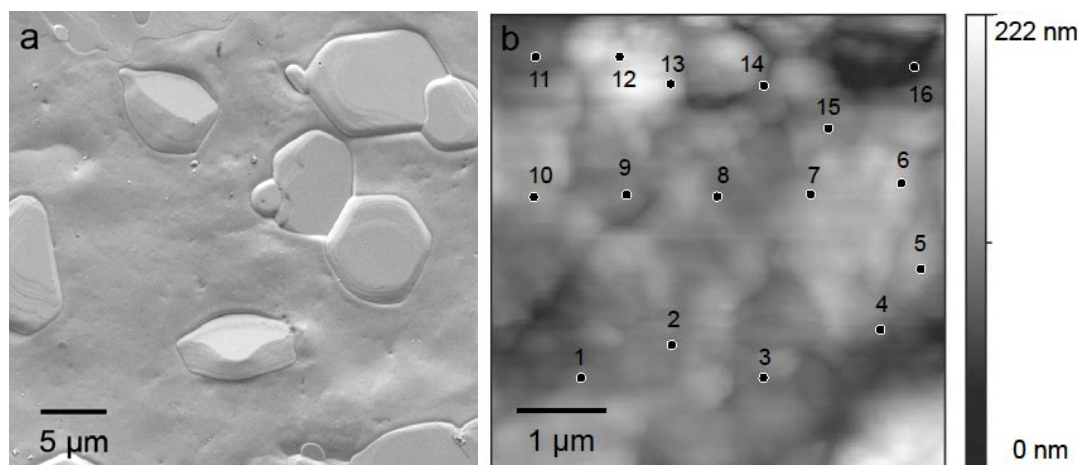


Figure 4.7 (a) Scanning electron micrograph of a typical CsHSO_4 surface acquired after electrochemical testing. (b) Topography scan of the polycrystalline CsHSO_4 surface collected at $\sim 150^\circ\text{C}$ in humidified air (~ 0.03 atm H_2O). Labels denote nominal positions at which electrochemical measurements were acquired (Figure 4.8).

The voltammograms obtained at 16 different points across the electrolyte surface (Figure 4.8a) exhibited features similar to that in Figure 4.6. Specifically, for each voltammogram, a plot of $\log(i)$ as function of bias revealed a linear regime at low bias followed by a decrease in the slope at high bias. Furthermore, impedance spectra collected at -1.0 and -0.9 V for select positions (not shown) were qualitatively similar to one another and to the results in Figure 4.4, indicating, in all cases, a high-frequency process with a (largely) bias-independent resistance and a low-frequency process with a resistance that decreased sharply with bias. Thus, one can conclude that the mechanistic steps involved in oxygen electro-reduction at the $\text{Pt}|\text{CsHSO}_4$ interface are maintained across the electrolyte surface.

While the general shape of the voltammograms and impedance spectra were reproduced at different locations, the specific values differed substantially. For example,

in the voltammetry experiments, at -0.95 V, the measured current ranged between -1.5 and -4.5 pA, a three-fold variation. This variation is, in turn, manifested as notable variations of the exchange coefficient and exchange current across the electrolyte surface, as extracted from a Tafel analysis of the linear regime of each voltammogram, typically occurring at overpotentials between -1.0 and -0.6 V. For the specific surface shown in Figure 4.7b, α ranges from 0.22 to 0.39 and i_0 from 0.2 to 6 fA (Figure 4.8b), with the two parameters apparently counter-correlated (i.e., i_0 decreases as α increases). Rather remarkably, a summary of the data for measurements of six different Pt | CsHSO₄ interfaces (Figure 4.9) reveals a counter-correlation between α and i_0 that extends over several orders of magnitude in i_0 and a factor of six in α . Specifically, across the six experiments, α spans from 0.1 to 0.6, with an average value of 0.3 ± 0.1 , and i_0 correspondingly spans from 5×10^{-14} to 5×10^{-19} A. The spatially-averaged exchange coefficient of 0.3 falls in the range, 0.35 ± 0.05 , measured for the Pt-wire | CsH₂PO₄ system at ~ 240 °C in humidified O₂ with ~ 0.35 atm H₂O (unpublished data). For Pt-wire | CsH₂PO₄, the working electrode was a 250 μ m diameter Pt wire embedded in CsH₂PO₄, and thus, the exchange coefficient from such a geometry can be treated as representative of an area-averaged electrochemical response.

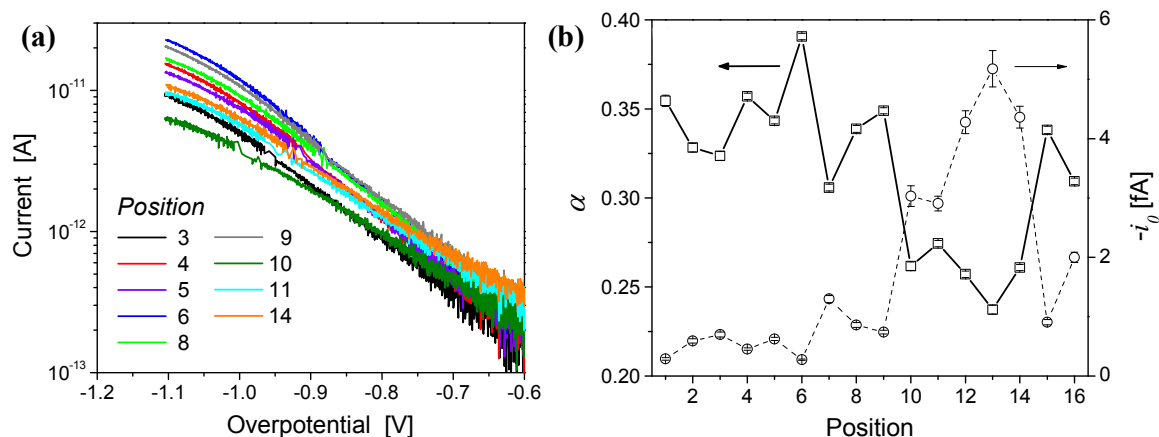


Figure 4.8 (a) Semi-log plot of cyclic voltammograms (cathodic branch) for Pt | CsHSO₄ at select points across the surface shown in Figure 4.7b. Data were acquired with a 25 mV s⁻¹ scan rate at ~150 °C in humidified air with ~0.03 atm H₂O (using Probe 1, Table 4.1). (b) Exchange coefficient, α , and exchange current, i_0 , plotted as functions of position. Parameters were extracted from fitting the linear regime of each curve in (a) to the Tafel equation (Equation (4.6)). In some instances, the error bars for α are smaller than the data markers.

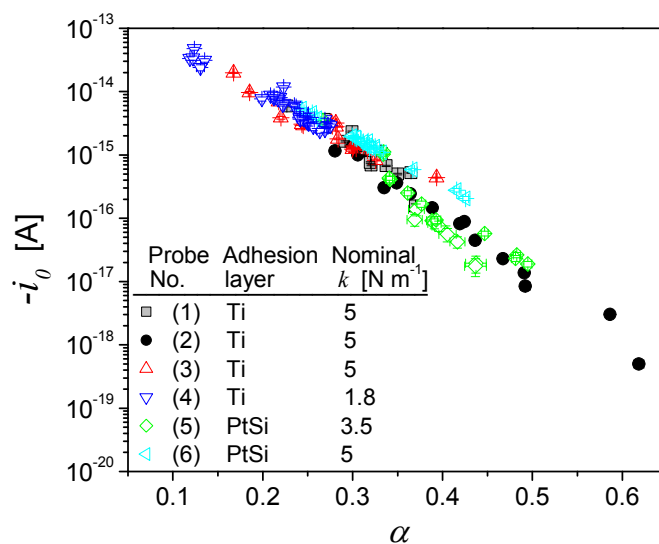


Figure 4.9 Semi-log plot of i_0 as a function of α , showing a linear relationship across six different data sets, with the probe type indicated in the legend. Data were collected at ~150 °C in humidified air (0.01–0.03 atm H₂O). In some instances, the error bars for i_0 and α are smaller than the data markers.

Ignoring for the moment the counter-correlation between α and i_0 , the simple observation that these parameters vary so substantially with position demonstrates that electrochemical reaction rates at Pt | CsHSO₄ are indeed highly influenced by nanoscale surface features of the polycrystalline electrolyte. Because variations in applied force produced no detectable change in the features of the voltammograms (see Appendix Figure F.11a), changes in the extent of electrochemical reaction area are unlikely to be responsible for the large variations in i_0 or α . The relevant surface features may include the crystallographic orientation of the surface termination and the occurrence of grain or domain boundaries, or even dislocations with surface termination. Any of these features may influence the residual surface charge and be a means of influencing electrochemical reaction rates. As stated at the outset, because the electrochemical reactions in solid electrolyte fuel cells involve surface reaction steps, nanoscale heterogeneity is to be expected. The clear counter-correlation between α and i_0 , however, is unexpected. The observation of a common correlation between α and i_0 for six different Pt | CsHSO₄ interfaces, furthermore, leaves little doubt that the phenomenon is real and suggests a common mechanism for these different interfaces. Within the Butler-Volmer framework, a large value of i_0 corresponds to a small reaction barrier between oxidized and reduced states, Equation (4.3), under equilibrium conditions. A small value of α , which occurs for those reactions sites with large i_0 , corresponds to a minimal decrease in the activation barrier under bias. The counter-correlation thus reflects a physical situation in which reaction pathways with small barriers under equilibrium conditions are relatively unaffected by the applied bias, whereas those with high barriers under equilibrium conditions are strongly decreased under bias. While there is no fundamental basis for

expecting such a result, *a priori*, the counter-correlation creates a situation in which, under a given bias, all reaction sites attain a comparable level of electrochemical activity, as reflected in the value of the current (under bias) rather than the exchange current (under zero bias). A direct correlation between α and i_0 , in contrast, would imply that sites with low barriers under open-circuit conditions become even more active relative to other sites, under bias, and hence an immediate divergence in activity. An extensive search of the relevant literature did not uncover any studies showing such a wide-ranging, systematic and correlated variation of α and i_0 within a given electrochemical system, although, in some instances, variations as a function of a third parameter (e.g., temperature, electrode/electrolyte composition, or electrode particle size)^{97–104} have been explored. Further study to explicitly identify the surface features that influence electrochemical reaction kinetics at the Pt | CsHSO₄ interface and electrolyte-metal-gas boundaries in general is under way.

4.4 Summary

We demonstrate the use of conducting atomic force microscopy as a tool to quantitatively probe oxygen reduction kinetics in controlled environments and at elevated temperatures. We employ AC impedance spectroscopy to gain insight into the mechanism of electrocatalysis and cyclic voltammograms for quantitative analysis of oxygen reduction kinetics in the Pt | CsHSO₄ system. The oxygen reduction reaction is limited primarily by an overpotential-activated process that exists at low frequencies, with an additional impedance contribution, at high overpotentials, from a process that is weakly overpotential-dependent. Our ability to deconvolute these two processes derives,

we believe, from the nanoscale measurements. At this scale, the measurements are free of averaging effects, leading to near-ideal capacitive behavior and minimal dispersion in the frequency response. The overpotential-activated step was interpreted as charge transfer and evaluated using the Butler-Volmer equation. Within the Butler-Volmer framework, a spatial variation in kinetics, represented by the exchange coefficient and exchange current, was observed across six independent measurements. That the correlation between $\log(i_0)$ and α for all six experiments collapses into a single line demonstrates the robustness of our experimental approach.

Chapter 5 Phase Transformation Hysteresis in Solid Acid Compounds

Adapted with permission from: Louie, M. W.; Kislitsyn, M.; Bhattacharya, K.; Haile, S. M. Phase Transformation and Hysteresis Behavior in $\text{Cs}_{1-x}\text{Rb}_x\text{H}_2\text{PO}_4$. *Solid State Ionics* **2010**, *181*, 173–179.

Abstract

A new theory on the origin of hysteresis in first order phase transformations was evaluated for its applicability to the phase transformation behavior in the $\text{Cs}_{1-x}\text{Rb}_x\text{H}_2\text{PO}_4$ solid solution system. Specifically, the correlation between λ_2 , the middle eigenvalue of the transformation matrix describing the cubic-to-monoclinic superprotonic transition, and the transformation hysteresis was examined. The value of λ_2 was estimated from a combination of variable temperature diffraction data and thermal expansion measurements obtained for select compositions in the solid solution system. The transformation hysteresis was determined for $\text{Cs}_{1-x}\text{Rb}_x\text{H}_2\text{PO}_4$ compositions ($x = 0, 0.25, 0.50$, and 0.75) by single-frequency impedance measurements. It was found that the transition temperature increases monotonically with increasing Rb content, from 227.6 ± 0.4 °C for the end-member CsH_2PO_4 to 256.1 ± 0.3 °C for $\text{Cs}_{0.25}\text{Rb}_{0.75}\text{H}_2\text{PO}_4$, as does the hysteresis in the phase transition, from 13.4 °C to 17.4 °C. The computed values of λ_2 were far from 1, ranging from 0.932 (for $x = 0$) to 0.919 (for $x = 0.5$). The observation of λ_2 decreasing with Rb content is consistent with the theoretical expectations.

We furthermore examined the phase transformation characteristics of CsH_2PO_4 and CsHSO_4 , and assessed the correlation between microstructure and the phase transformation hysteresis. CsHSO_4 was found to undergo phase transformation with significantly fewer cracks compared to CsH_2PO_4 , consistent with its lower transformation hysteresis of $\sim 5^\circ\text{C}$. Domain patterns were observed on the surface of CsHSO_4 single crystals after thermal cycling through the phase transition. However, domain patterns were not readily visible in single crystals of CsH_2PO_4 .

5.1 Introduction

Many solid acid compounds undergo a solid-to-solid phase transition, typically from a monoclinic phase to a cubic, tetragonal, or trigonal phase on heating. Discontinuous changes in the lattice parameters (or volume) and enthalpy, etc. across the transition have been observed for many solid acid compounds,^{9, 11, 22, 105–108} and, moreover, solid acid compounds, particularly $\text{Rb}_3\text{H}(\text{SeO}_4)_2$, have been observed to form domain patterns upon heating from the room temperature phase.¹⁰⁹ In this chapter, we evaluate the applicability and utility of a newly introduced theory of martensitic phase transformations^{110, 111} to solid acid compounds. This theory predicts hysteresis behavior (and microstructure) solely from arguments of crystal symmetry and geometric compatibility between the high- and low-temperature phases. Specifically, the criterion for zero hysteresis is the direct compatibility between the two phases, mathematically described by the condition, $\lambda_2 = 1$, where λ_2 is the middle eigenvalue of a transformation matrix that maps the transformation of the high-temperature, high-symmetry phase to the low-temperature, low-symmetry phase. A clear relationship between the measured hysteresis and the middle eigenvalue has been demonstrated for the shape-memory alloy system, Ni-Ti-Cu,¹¹⁰ enabling the identification of a low-hysteresis alloy with unprecedented durability in thermal cycling.¹¹²

Solid acid compounds are ideal for evaluating the broader applicability of the theory of martensitic transformations. Many solid acid compounds can be chemically modified as a way to tune the lattice parameters for compatibility. For example, the compounds $\text{Rb}_2(\text{HSO}_4)(\text{H}_2\text{PO}_4)$, $(\text{NH}_4)_2(\text{HSO}_4)(\text{H}_2\text{PO}_4)$, $\text{K}_2(\text{HSO}_4)(\text{H}_2\text{PO}_4)$ are all isostructural with $\text{Cs}_2(\text{HSO}_4)(\text{H}_2\text{PO}_4)$ which has been shown to undergo a monoclinic-to-

cubic transition at $\sim 91\text{ }^{\circ}\text{C}$ and a reverse transition on cooling at temperatures as low as $\sim 30\text{ }^{\circ}\text{C}$.⁹ The possibility of forming solid solutions renders solid acids a useful class of materials with which to further explore the principles of crystallographic compatibility.

In turn, the investigation of the phase transformation behavior of solid acid compounds can shed light on the effect of hysteresis on the robustness of solid acid compounds as electrolytes in electrochemical devices. A consequence of crystallographic incompatibility between the high- and low-temperature phases is the formation of strain energy during phase transformation, released in the form of cracks. As evident in Chapter 3, the formation of microcracks in CsH_2PO_4 prevents the fabrication of well-defined and well-controlled electrode | electrolyte interfaces and active sites. Not only this, the existence of cracks in the electrolyte membrane may have implications for fuel cell operation, as shown in Figure 2.15. Although cracks which form on heating through the transition heal under fuel cell operating conditions, it is unclear how robust such a system is for long-term operation and repeated on-off (temperature) cycling.

In this chapter, we gain an understanding of reversibility of the superprotonic phase transition in solid acid compounds and its implications for using solid acids as electrolytes for electrochemical applications. As CsH_2PO_4 is presently the electrolyte of choice for solid acid fuel cells, we have chosen to investigate the phase transformation behavior of $\text{Cs}_{1-x}\text{Rb}_x\text{H}_2\text{PO}_4$ and its correlation to the compatibility condition, $\lambda_2 = 1$. $\text{Cs}_{1-x}\text{Rb}_x\text{H}_2\text{PO}_4$ has been shown to crystallize into the $P2_1/m$ structure of the end-member CsH_2PO_4 for x up to ~ 0.8 .^{113, 114} All of the crystal chemical parameters (cell volume, lattice parameters, hydrogen bond length, etc.) vary gradually and monotonically with an increase in Rb content. Furthermore, a superprotonic phase transition has been shown to

occur for these compounds at temperatures between ~ 220 °C and ~ 250 °C. Combined, the high solubility of Rb into CsH_2PO_4 and the ease with which transition behavior can be evaluated via proton conductivity measurement renders $\text{Cs}_{1-x}\text{Rb}_x\text{H}_2\text{PO}_4$ an attractive system for exploration. Because incorporation of Rb into CsH_2PO_4 does not detrimentally lower the proton conductivity,¹¹³ $\text{Cs}_{1-x}\text{Rb}_x\text{H}_2\text{PO}_4$ compounds may also prove to be useful as electrolytes, particularly if such materials exhibit greater phase transition reversibility.

We furthermore explore the widespread applicability of the compatibility condition by comparing the phase transformation characteristics of CsHSO_4 and CsH_2PO_4 . We examine the physical characteristics of these two solid acid compounds, specifically the effect of the superprotonic phase transition on crack density and microstructure. With hysteresis and microstructure studies, combined, we evaluate the applicability of the theory of crystallographic compatibility to the superprotonic phase transition and discuss the implications of these studies on the rational design of solid acid electrolytes with minimal hysteresis and strain energy during transformation.

5.2 Theory of Crystallographic Compatibility

Martensitic transformations are diffusionless, solid-to-solid transitions between phases of different crystalline structures. It has recently been proposed and demonstrated that the structural relationship between the two phases establishes not only the microstructural patterns that emerge upon cooling from the high-temperature austenite phase to the low-temperature martensite phase¹¹⁵ but also the degree of hysteresis associated with the transition.^{110, 111} Here, we present the mathematical framework for the

theory of crystallographic compatibility, specifically for the $\text{Cs}_{1-x}\text{Rb}_x\text{H}_2\text{PO}_4$ system which undergoes a monoclinic-to-cubic transformation.

To evaluate the geometric compatibility of the two crystalline phases, we examine the crystallographic relationship between the high-temperature superprotonic and low-temperature paraelectric phases of CsH_2PO_4 (Figure 5.1). The superprotonic (austenite) phase adopts the CsCl structure type, with Cs atoms arranged at the corners of a simple cubic unit cell and an orientationally disordered polyanion group located at the cell center, whereas the paraelectric (martensite) phase is monoclinic and the $(\text{H}_2\text{PO}_4)^-$ groups reside in fixed orientations. Shown in Figure 5.1 is just one way in which the paraelectric phase can emerge from the superprotonic phase upon cooling through the transition. Due to the relative symmetries of the two phases, there are exactly twelve ways in which the cubic phase can be transformed to the monoclinic phase. In general, the number of ways the transformation can occur, that is, the number variants (N) is

$$N = \frac{\# \text{rotations in } P_a}{\# \text{rotations in } P_m} \quad (5.1)$$

where P_a and P_m are the point groups of the austenite and martensite phases, respectively.

In the case of CsH_2PO_4 , $N = 24/2 = 12$.

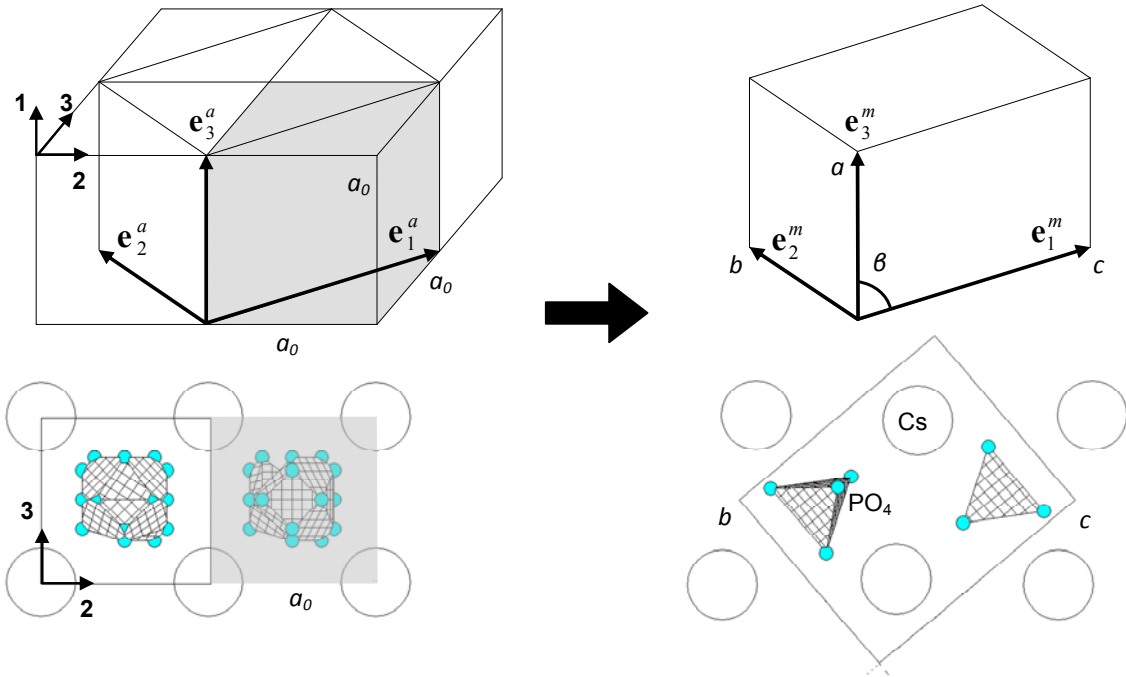


Figure 5.1 Schematic of one of twelve ways the high-temperature cubic phase can transform to the low-temperature monoclinic phase: the relationship between the lattices (top) and with atomic sites for CsH_2PO_4 (bottom). In the high-temperature phase (left), the PO_4 groups are orientationally disordered, taking on one of six possible orientations, whereas in the low-temperature phase (right), the PO_4 groups reside in fixed orientations. (Hydrogen atoms are not shown.)

The mapping of the lattice of the austenite to that of the martensite can be described by the homogeneous deformation matrix, \mathbf{U}_j , defined by

$$\mathbf{e}_i^m = \mathbf{U}_j \mathbf{e}_i^a \quad (5.2)$$

where the subscript j refers to the twelve possible martensite variants. (By convention, \mathbf{U}_j is chosen to be symmetric. The procedure for satisfying this criterion is detailed in Appendix I.) For CsH_2PO_4 , the lattice vectors of the austenite, \mathbf{e}_i^a , are chosen to be the edges of a tetragonal unit cell constructed from the contents of two cubic unit cells. Those of the martensite, \mathbf{e}_i^m , are taken to correspond directly to the monoclinic unit cell. Using an orthonormal basis parallel to the cubic unit cell, we obtain for the specific variant indicated by Figure 5.1,

$$\mathbf{e}_1^a = a_0 \begin{pmatrix} 0 \\ 1 \\ 1 \end{pmatrix} \quad \mathbf{e}_2^a = a_0 \begin{pmatrix} 0 \\ -1 \\ 1 \end{pmatrix} \quad \mathbf{e}_3^a = a_0 \begin{pmatrix} 1 \\ 0 \\ 0 \end{pmatrix} \quad (5.3)$$

$$\mathbf{e}_1^m = \frac{c}{\sqrt{2}} \begin{pmatrix} \sqrt{2} \cos \beta \\ \sin \beta \\ \sin \beta \end{pmatrix} \quad \mathbf{e}_2^m = \frac{b}{\sqrt{2}} \begin{pmatrix} 0 \\ -1 \\ 1 \end{pmatrix} \quad \mathbf{e}_3^m = a \begin{pmatrix} 1 \\ 0 \\ 0 \end{pmatrix} \quad (5.4)$$

The deformation matrix, \mathbf{U}_1 , then becomes

$$\mathbf{U}_1 = \begin{pmatrix} \gamma & \varepsilon & \varepsilon \\ \varepsilon & \alpha & \delta \\ \varepsilon & \delta & \alpha \end{pmatrix} \quad (5.5)$$

where

$$\gamma = \frac{a(\sqrt{2}a + c \sin \beta)}{a_0 \sqrt{2a^2 + c^2 + 2\sqrt{2}ac \sin \beta}} \quad (5.6)$$

$$\varepsilon = \frac{1}{\sqrt{2}a_0} \left(\frac{ac \cos \beta}{\sqrt{2a^2 + c^2 + 2\sqrt{2}ac \sin \beta}} \right) \quad (5.7)$$

$$\alpha = \frac{1}{2\sqrt{2}a_0} \left(\frac{c(c + \sqrt{2}a \sin \beta)}{\sqrt{2a^2 + c^2 + 2\sqrt{2}ac \sin \beta}} + b \right) \quad (5.8)$$

$$\delta = \frac{1}{2\sqrt{2}a_0} \left(\frac{c(c + \sqrt{2}a \sin \beta)}{\sqrt{2a^2 + c^2 + 2\sqrt{2}ac \sin \beta}} - b \right) \quad (5.9)$$

Once \mathbf{U}_1 is known, the other variants can be obtained by applying the rotations of the cubic austenite lattice to this matrix. Variants, $\mathbf{U}_1, \mathbf{U}_2, \dots, \mathbf{U}_N$ have the form

$$\mathbf{U}_j = \mathbf{R}^T \mathbf{U}_1 \mathbf{R} \quad (5.10)$$

where \mathbf{R} is a rotation in the point group of the austenite. All twelve variants are shown in Table I.3. Because these twelve variants are related by symmetry, they are energetically equivalent, with equal likelihood of forming on cooling from the austenite phase. Furthermore, they all share the same eigenvalues, $\lambda_1, \lambda_2, \lambda_3$, where $\lambda_1 < \lambda_2 < \lambda_3$ are the ordered eigenvalues of \mathbf{U}_j . The condition for the middle eigenvalue, $\lambda_2 = 1$, implies compatibility between a single variant of martensite and the austenite. In this case, the two phases coexist during transformation by the formation of a perfect, strain-free interface, and the transformation is expected to be reversible. However, the more frequently observed scenario is one in which $\lambda_2 \neq 1$. In this case, the low-temperature phase is not compatible with the high-temperature phase, and the material transforms on cooling by adopting multiple variants of the low-temperature phase (i.e., twinning) in an attempt to minimize strain at the interface. The observed transformation hysteresis is attributed to additional driving force required on cooling in order for the material to transform by way of this incompatible interface. Additionally, by similar compatibility arguments, the microstructure of the martensite, namely geometrically compatible variant pairs can be identified, and their orientations with respect to one another and with the austenite phase can be predicted. The procedure for determining the possible variant pairs and austenite-martensite interfaces is presented in Appendix I.

5.3 Experimental

5.3.1 *Synthesis and Fabrication*

The end-member compounds CsH_2PO_4 and RbH_2PO_4 were individually prepared from aqueous solutions of Cs_2CO_3 (99.9%, Alfa Aesar, 12887) and Rb_2CO_3 (99.9%, Alfa Aesar, 12893), respectively, and H_3PO_4 (85%, Mallinckrodt, 2796). These aqueous solutions were introduced into methanol to induce rapid precipitation, and the resulting precipitates dried at $\sim 100^\circ\text{C}$. Materials in the solid solution series, $\text{Cs}_{1-x}\text{Rb}_x\text{H}_2\text{PO}_4$, were synthesized by dissolving CsH_2PO_4 and RbH_2PO_4 powders in water in the desired molar ratios corresponding to $x = 0.25, 0.50, 0.75$ and then injecting the mixed aqueous solution into a sonicated methanol bath. The resulting precipitates were dried at $\sim 100^\circ\text{C}$ to remove surface water and methanol. Polycrystalline discs ~ 9.3 mm diameter, ~ 0.7 mm thick and $> 93\%$ of theoretical density, were prepared for conductivity measurements by uni-axially pressing at ~ 491 MPa for 20 min. Colloidal silver paint (Ted Pella, 16032) was applied to both sides of the dense compacts for electrical contact.

Single crystals of CsH_2PO_4 and CsHSO_4 were grown from their respective aqueous solutions. (The synthesis of CsH_2PO_4 and CsHSO_4 powders is detailed in Chapters 3 and 4, respectively.) Solutions were filtered through a $0.2\ \mu\text{m}$ syringe filter to remove dust particles and then placed at ambient conditions, partially covered, to allow for water evaporation and crystal growth. As-grown crystals were pulled directly out of solution and rinsed quickly with water; for imaging studies presented in this chapter, these crystals were denoted “as-grown”. In some cases, crystals were polished with fine $2\ \mu\text{m}$ grit size sandpaper before use, while others were fractured using a sharp razor

blade. Polished crystals were sanded uni-directionally so that the resulting streaks could be easily distinguished from any microstructural changes that appeared due to heating.

5.3.2 Characterization

Synthesized $\text{Cs}_{1-x}\text{Rb}_x\text{H}_2\text{PO}_4$ powders were characterized with a Phillips X'Pert Pro powder X-ray diffractometer (XRD) using $\text{Cu K}\alpha$ radiation (45 kV, 40mA) with a 2θ range of $5\text{--}70^\circ$ and a step size and dwell time of 0.017° and 50 s, respectively. Variable temperature diffraction data were collected for CsH_2PO_4 using an Anton Parr HTK1200 furnace at temperatures up to $\sim 256^\circ\text{C}$, well above the superprotonic phase transition temperature. Lattice parameters were obtained by Rietveld refinement (Phillips X'Pert Plus software) with initial reference structures for the monoclinic¹¹⁶ and cubic¹¹⁷ phases respectively. Chemical compositions were verified by an Oxford INCA 300 X-ray energy dispersive spectrometer (EDS) utilized in conjunction with a scanning electron microscope (LEO 1550 VP) at an accelerating voltage of 10 kV.

Phase transformation behavior was studied by single frequency AC impedance measurements at 10 kHz and with a perturbation of 50 mV (HP 4284 precision LCR meter). While a full range of frequencies is desirable for determining sample conductivity via equivalent circuit fitting, transformation behavior is more appropriately captured by rapid, single-frequency measurements. The frequency of 10 kHz was selected on the basis of preliminary measurements of complete impedance spectra which demonstrated this value to accurately reflect bulk transition characteristics. The samples were placed in a tube furnace and sandwiched between two sheets of Toray carbon paper which, in turn, was mechanically contacted to silver mesh connected to silver wires. In order to mitigate potential dehydration effects¹⁵, measurements were made under high water partial

pressure (≥ 0.5 atm), achieved by bubbling inlet N_2 ($\sim 2.5 \text{ mL min}^{-1}$) through a water bath held at temperatures of 82–95 °C. The temperature was measured with a thermocouple located ~ 3 mm from the sample. The majority of the measurements were carried out at a heating rate of $1 \text{ }^\circ\text{C min}^{-1}$, with data recorded at 5 s intervals. The reproducibility of the transition behavior was established by collecting data upon repeated temperature cycling. From the impedance data, the transition temperatures were defined as the onset of a change in conductance, determined from the intersection of lines fitted to the linear regions of the conductivity curves.

To evaluate the influence of the phase transition on the microstructure of solid acid compounds, single crystals of CsH_2PO_4 and CsHSO_4 were heated to temperatures above the superprotonic phase transition temperature, specifically to 235 °C under flowing synthetic air with ~ 0.35 atm H_2O for CsH_2PO_4 and to 155 °C in ambient air for CsHSO_4 . Macroscale images of entire single crystals were taken using a digital camera in conjunction with a Nikon optical microscope. Additional examination of the microstructure before and after heat treatment were carried out using scanning electron microscopy (LEO 1550VP, Carl Zeiss SMT) with a 3 kV accelerating voltage. For CsHSO_4 , topographical imaging, in situ at superprotonic conditions, was carried out using a PicoSPM atomic force microscope (Series 4500, Agilent Technologies) operated in contact mode. The microscope was equipped with a hotstage heated to temperatures between room temperature and 160 °C. A thermocouple was attached to the top surface of the crystal by Kapton tape to monitor the temperature of the crystal surface.

5.3.3 Determination of Eigenvalues

Using the expressions developed in Section 5.2, the eigenvalues for the transformation matrix were computed using the software Mathematica (Wolfram Research). Essential to such a computation is knowledge of the lattice parameters just above and below the transformation. Variable temperature diffraction data for CsH_2PO_4 to temperatures as high as 256 °C was obtained (see Section 5.4.1). Dehydration effects in the Rb-containing samples (in the dry atmosphere of the XRD hot stage) made direct measurements of the high-temperature cell constants for these compositions challenging, particularly for compounds with high Rb content. Lattice parameters for $\text{Cs}_{1-x}\text{Rb}_x\text{H}_2\text{PO}_4$ for $x = 0.25$ and 0.50 were taken from the work of Kislitsyn.¹⁹ In this referenced work, the lattice parameters for $\text{Cs}_{0.75}\text{Rb}_{0.25}\text{H}_2\text{PO}_4$ across the phase transition were determined by high-temperature diffraction. However, the dehydration of compounds with higher Rb content was too severe for diffraction measurements of the high-temperature cubic phase. In the case of $\text{Cs}_{0.5}\text{Rb}_{0.5}\text{H}_2\text{PO}_4$, it was possible to collect diffraction data at temperatures up to the phase transition before dehydration took over; by estimating the phase transition volume change via dilatometry, the lattice parameters of the cubic phase could be estimated.

5.4 Results and Discussion: $\text{Cs}_{1-x}\text{Rb}_x\text{H}_2\text{PO}_4$

5.4.1 Phase and Chemical Characterization

The X-ray diffraction patterns for compounds synthesized with nominal Rb compositions of $x = 0, 0.25, 0.50$, and 0.75 (Figure 5.2) indicate the formation of single

phase monoclinic structures with clear shifts in peak positions with increasing Rb content, consistent with the formation of a solid solution. Room temperature lattice parameters, Table 5.1, are comparable to previously reported values in this system, and the measured Rb contents, also reported in Table 5.1, confirm, within error, that the desired stoichiometry has been obtained.

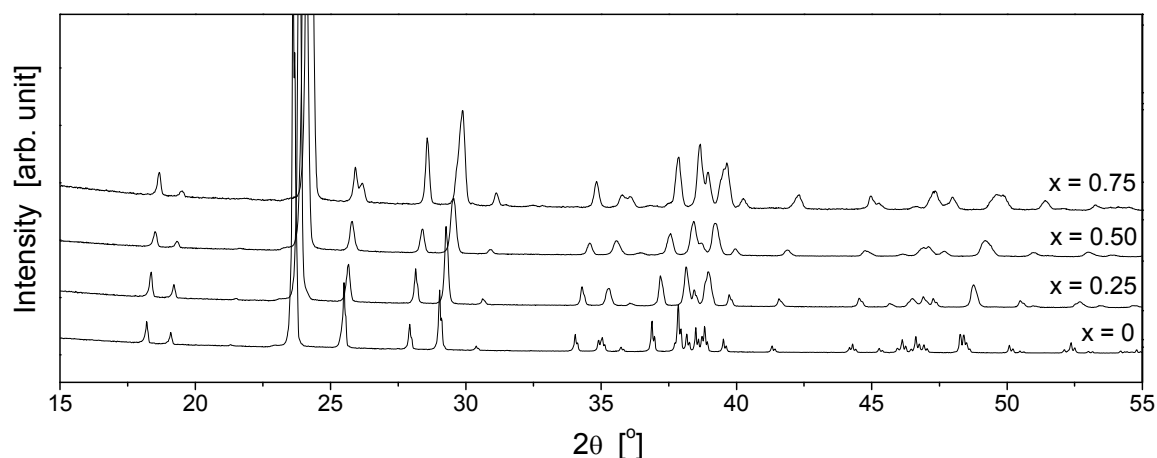


Figure 5.2 Powder X-ray diffraction patterns of $\text{Cs}_{1-x}\text{Rb}_x\text{H}_2\text{PO}_4$ at room temperature for nominal compositions $x = 0, 0.25, 0.50$, and 0.75 . Patterns indicate the formation of single phase monoclinic structures with shifts in peak positions upon Rb incorporation.

Table 5.1 Lattice parameters and chemical compositions for the $\text{Cs}_{1-x}\text{Rb}_x\text{H}_2\text{PO}_4$ solid solution series. Compositions determined by EDS are averages of at least ten measurements on powder samples.

mol % Rb nominal	mol % Rb (EDS)	a [Å]	b [Å]	c [Å]	β [°]
0	Not detected	4.8768(2)	6.3867(3)	7.9057(3)	107.705(2)
25	23 ± 2	4.8538(3)	6.3363(3)	7.8416(4)	107.865(3)
50	48 ± 5	4.8414(3)	6.3002(3)	7.7940(7)	108.126(6)
75	74 ± 5	4.8035(6)	6.2561(7)	7.736(1)	108.527(5)

High-temperature diffraction data and thermal expansion behavior of CsH_2PO_4 are shown in Figure 5.3 and Figure 5.4, respectively. The lattice expansion on heating is clearly evident from the shift in the diffraction peaks, as is the transition to a cubic phase by a temperature of 231.5 °C. Rietveld analysis indicates a high-temperature cubic structure with $a_0 = 4.9653(1)$ Å at 243.5 °C (where the number in parentheses indicates the uncertainty in the final digit), similar to previously reported values of the cell constant ranging from 4.9549(4) to 4.961(3) Å at temperatures between 237 and 242 °C.^{117–119} The volume change at the transition is found here to be 1.7%, which is measurably larger than that in CsHSO_4 , 0.54%.⁵⁶ In contrast, the volumetric thermal expansion coefficient of the paraelectric phase of CsH_2PO_4 , $1.12(3) \times 10^{-4} \text{ K}^{-1}$, is comparable to the values of $1.62(3)$ and $1.76(2) \times 10^{-4} \text{ K}^{-1}$ for phase III and II, respectively, of CsHSO_4 .⁵⁶ The expansion coefficient of the superprotonic phase of CsH_2PO_4 , estimated from just three data points, is $1.98(2) \times 10^{-4} \text{ K}^{-1}$, again similar to that reported for superprotonic CsHSO_4 , $2.66(6) \times 10^{-4} \text{ K}^{-1}$. The complete thermal expansion behavior of CsH_2PO_4 is summarized in Table 5.2. It is apparent (Figure 5.4 and Table 5.2) that the effect of temperature on the a and c parameters of the monoclinic phase is small compared to that on b .

While the structures of the superprotonic phases of $\text{Cs}_{1-x}\text{Rb}_x\text{H}_2\text{PO}_4$ for $x = 0.50$ and 0.75 have not been explicitly determined, based on the similarity to CsH_2PO_4 and $\text{Cs}_{0.75}\text{Rb}_{0.25}\text{H}_2\text{PO}_4$, and based on the widespread occurrence of the cubic CsCl structure type in superprotonic phases with a cation:polyanion ratio of 1:1,^{2, 5, 22} we assume for this study that all Rb-substituted superprotonic phases are isostructural to that of superprotonic CsH_2PO_4 .

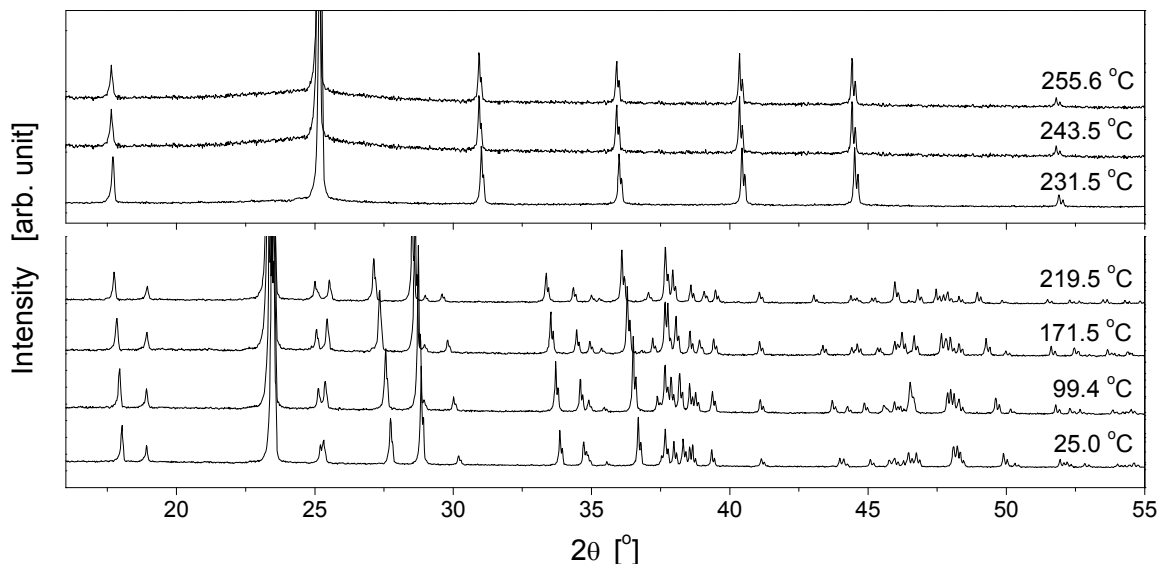


Figure 5.3 Powder XRD patterns for CsH_2PO_4 as a function of temperature for the low-temperature monoclinic phase (bottom) and the high-temperature cubic phase (top).

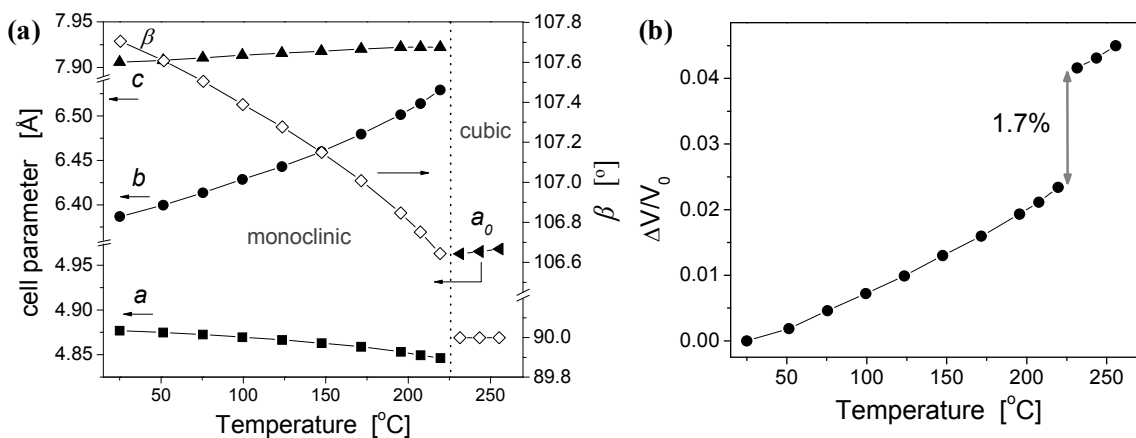


Figure 5.4 Thermal expansion of CsH_2PO_4 (25–256 °C) determined by powder XRD: (a) Anisotropic thermal expansion in the monoclinic phase and isotropic thermal expansion in the cubic phase. Error bars are within the size of data markers. (b) Relative thermal expansion $\Delta V/V_0$ (V_0 taken at 25.0 °C). The volume change during transformation is 1.7%.

Table 5.2 Thermal expansion parameters for CsH_2PO_4 corresponding to: $\Delta a/a_0 = A(T-T_0) + B(T-T_0)^2$, where $T_0 = 25.0^\circ\text{C}$

Relative thermal expansion	$A \times 10^{-4} \text{ [K}^{-1}\text{]}$	$B \times 10^{-7} \text{ [K}^{-1}\text{]}$	$T_{\text{meas}} \text{ [}^\circ\text{C]}$
$\Delta a/a_0$	-0.102(13)	-1.10(8)	25–220
$\Delta b/b_0$	0.662(30)	2.38(18)	25–220
$\Delta c/c_0$	0.145(8)	-0.167(50)	25–220
$\Delta \beta/\beta_0$	-0.303(11)	-1.00(7)	25–220
$\Delta V/V_0$ (monoclinic)	0.804(23)	1.99(14)	25–220
$\Delta V/V_0$ (cubic)	1.98(2)	0*	232–256

* For the cubic phase, relative volumetric thermal expansion is taken to be linear with temperature.

5.4.2 Conductivity and Phase Transformation Hysteresis

The hysteresis behavior of CsH_2PO_4 at a temperature ramp rate of 1°C min^{-1} is shown in Figure 5.5, in which the inverse of the real component of the impedance (effectively the conductance because the imaginary component of the impedance is small at this frequency) is presented as a function of temperature in Arrhenius form. The sharp transition behavior is immediately evident, with the superprotonic phase displaying a conductance that is three orders of magnitude higher than the paraelectric phase. As demonstrated in the figure, extrapolations from linear portions of the data were utilized to define the transition temperature, and, overall, the transition behavior was slightly more gradual on heating than on cooling, an effect observed for all compositions examined. For the measurement of CsH_2PO_4 shown in Figure 5.5, the superprotonic transition occurs at 227.9°C upon heating, whereas the reverse transformation occurs at 214.0°C . Repeated cycling (at 1°C min^{-1}) demonstrated highly reproducible behavior, both in terms of the magnitude of the conductance and the temperature of the transition (Figure 5.6). From an average over almost 20 cycles, the superprotonic transition of CsH_2PO_4 is found to be $227.6 \pm 0.4^\circ\text{C}$ on heating, consistent with previous studies^{119–122} and $214.2 \pm 0.8^\circ\text{C}$ on cooling. For all compositions a slightly higher variability in the

transition temperature was observed on cooling (± 0.4 – 0.8 °C) than on heating (± 0.2 – 0.4 °C).

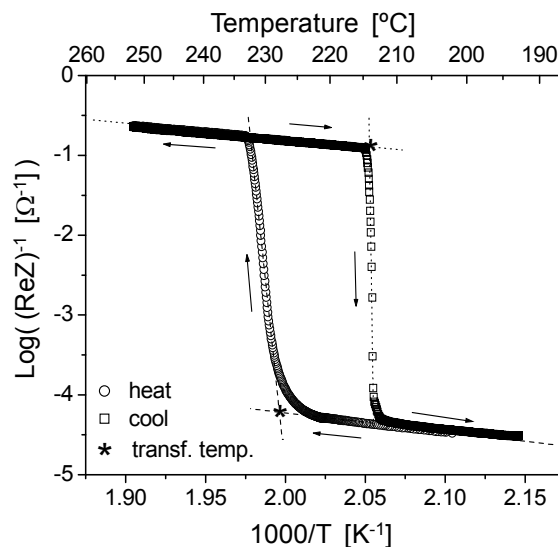


Figure 5.5 Arrhenius behavior of the proton conductivity of CsH_2PO_4 measured at a heating rate of 1 °C min^{-1} under flowing $\text{N}_2\text{-H}_2\text{O}$ gas (~ 0.5 atm H_2O). Arrows indicate heating and cooling cycles. The phase transition temperatures, denoted by *, are determined by the intersection of fitted lines to be 227.9 °C on heating and 214.0 °C on cooling.

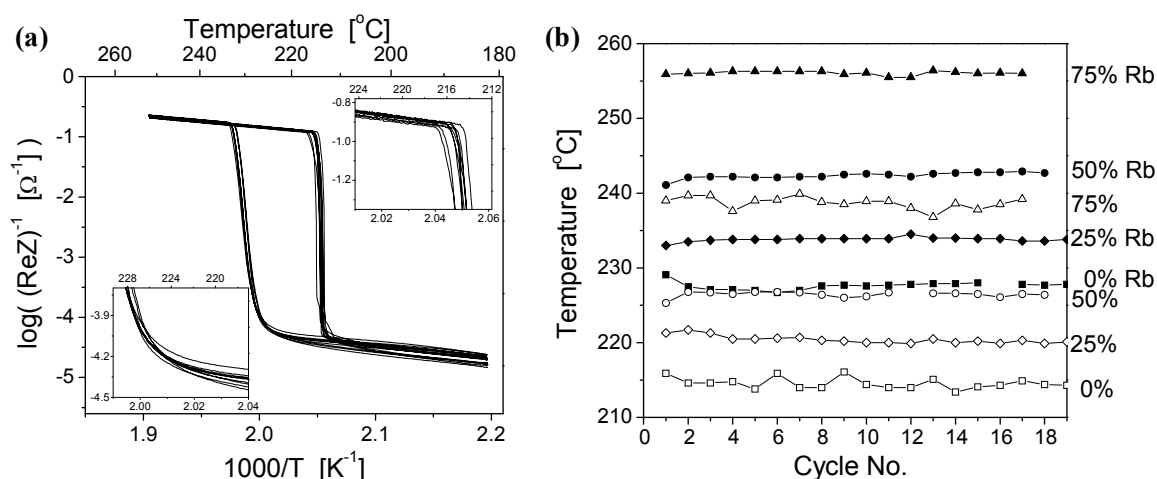


Figure 5.6 Reproducibility and stability of the $\text{Cs}_{1-x}\text{Rb}_x\text{H}_2\text{PO}_4$ system upon repeated temperature cycling at 1 °C min^{-1} under flowing $\text{N}_2\text{-H}_2\text{O}$ gas (~ 0.5 atm H_2O): (a) Conductivity behavior of CsH_2PO_4 and (b) transformation temperatures on heating (filled markers) and on cooling (open markers) demonstrate stability.

It is widely appreciated that finite heating rates can impact transformation temperatures, and ideally one extrapolates to a zero heating (or cooling) rate on the basis of measurements carried out at several different rates. Here, the transformation temperature on heating was found to be largely independent of heating rate for measurements at 0.1, 0.2, 0.5, and 1.0 °C min⁻¹ rates. In contrast, the transition on cooling displayed a somewhat erratic dependence on cooling rate. It is possible this behavior, along with the overall greater variability of the occurrence of the reverse transition even under a given cooling rate (Figure 5.6b), reflects a fundamental characteristic of the material behavior. Specifically, transformations on cooling between equilibrium phases are exothermic and local heat release may influence, for the Cs_{1-x}Rb_xH₂PO₄ system, the kinetics of transformation in an unpredictable manner. Given the difficulty in obtaining hysteresis values under zero heating rate conditions from an extrapolation procedure and the acceptable reproducibility of the results at a rate of 1 °C min⁻¹, the data collected under this rate were used for additional analysis.

As summarized in the phase diagram presented in Figure 5.7a, the superprotonic transition temperature (onset on heating) increases with Rb content, from 227.6 ± 0.4 °C for CsH₂PO₄ to 256.1 ± 0.3 °C for Cs_{0.25}Rb_{0.75}H₂PO₄. Similarly, the hysteresis (the difference between the onset of the transition on heating and on cooling) also increases with Rb content (Figure 5.7b). However, the impact here is slight, with the hysteresis increasing from 13.4 ± 0.8 °C for CsH₂PO₄ to only 17.4 ± 0.8 °C for Cs_{0.25}Rb_{0.75}H₂PO₄.

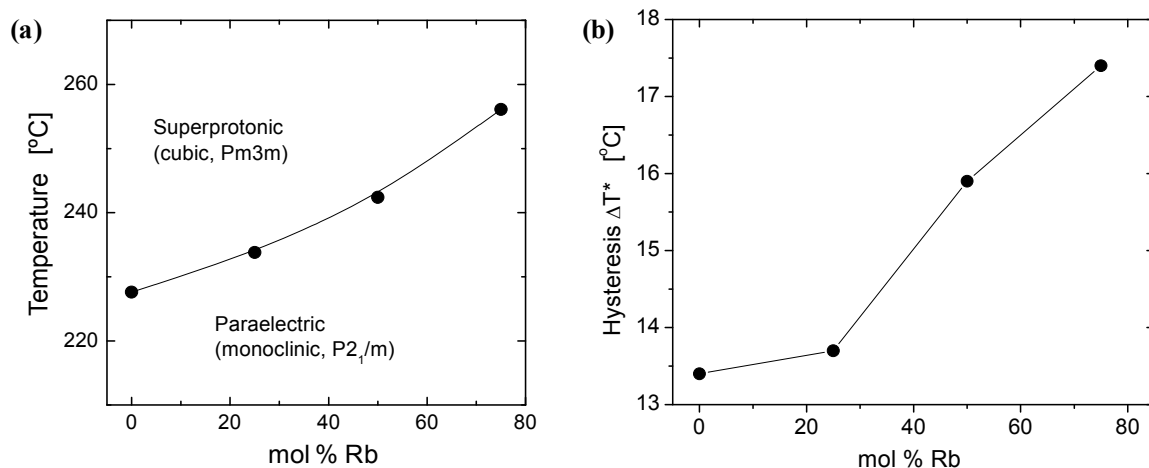


Figure 5.7 (a) Temperature-composition diagram for the $\text{Cs}_{1-x}\text{Rb}_x\text{H}_2\text{PO}_4$ system and (b) hysteresis width as a function of composition, as determined by impedance measurements at a heating rate of $1.0\text{ }^\circ\text{C min}^{-1}$ under flow $\text{N}_2\text{-H}_2\text{O}$ mixtures ($\sim 0.5\text{--}0.85\text{ atm H}_2\text{O}$).

5.4.3 Eigenvalues and Correlation to Hysteresis

From the expression of \mathbf{U}_1 given in Equations (5.5)–(5.9), it is possible to obtain analytical expressions for the eigenvalues. Given the particular lattice parameters of the $\text{Cs}_{1-x}\text{Rb}_x\text{H}_2\text{PO}_4$ system, the ordered eigenvalues of the cubic-to-monoclinic transformation matrix yield a middle eigenvalue that depends only on two crystallographic parameters, b (low-temperature phase) and a_0 (high-temperature phase).

$$\lambda_2 = \frac{b}{a_0\sqrt{2}} \quad (5.11)$$

The computed dependence of λ_2 on Rb content,¹⁹ is shown in Figure 5.8a. The data indicate that λ_2 decreases with Rb content from 0.932 for CsH_2PO_4 to 0.919 for $\text{Cs}_{0.5}\text{Rb}_{0.5}\text{H}_2\text{PO}_4$. Thus, while there is some sensitivity to composition, the range of λ_2 values encountered here ($\Delta\lambda_2 < 0.015$) is smaller than the previously studied ternary shape-memory alloy systems in which the eigenvalues could be readily manipulated from ~ 0.95 to 1.02 .¹¹⁰ The theory of martensite predicts that transformation hysteresis

decreases as λ_2 approaches 1, implying in this case that the hysteresis should increase with Rb content. This is precisely what is observed (Figure 5.7b). The correlation between the hysteresis and the middle eigenvalue is more clearly depicted in Figure 5.8b. As the middle eigenvalue increases toward 1, indicating the superprotonic cubic phase becomes more compatible with the monoclinic phase, the hysteresis width decreases.

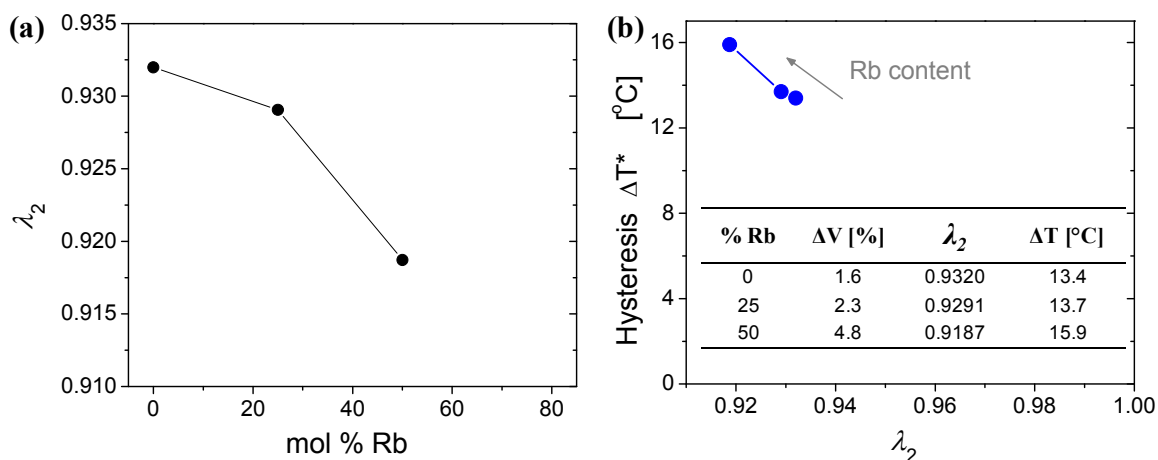


Figure 5.8 (a) Middle eigenvalue, λ_2 , as a function of composition showing a decrease in λ_2 with Rb content and (b) hysteresis with as a function of the middle eigenvalue, λ_2 , showing a decrease in hysteresis as λ_2 increases towards 1. Inset table shows values for the middle eigenvalue, phase transformation volume change (on heating) and hysteresis width.

The observed hysteresis widths for $\text{Cs}_{1-x}\text{Rb}_x\text{H}_2\text{PO}_4$ system are rather narrow (Figure 5.8b) given the fact that the middle eigenvalues are considerably far from 1. For example, previous studies of ternary shape-memory alloys revealed hysteresis widths as large as 63 °C for a middle eigenvalue of ~ 0.96 .¹¹⁰ Such an observation may indicate that elastic compliance can allow otherwise incompatible phases to coexist and thus undercooling need not proceed to such great extents to induce the martensite transformation. (It is interesting to note that physical observations of the $\text{Cs}_{1-x}\text{Rb}_x\text{H}_2\text{PO}_4$

discs before and after testing indicate the plasticity of the high-temperature phase increase with Rb content.)

That the behavior of hysteresis with the middle eigenvalue is consistent with the theory of crystallographic compatibility indicates the theory is applicable to materials beyond shape-memory alloys and furthermore is a promising tool for studying additional solid acid compounds. It is important to note, however, that the observation of increasing hysteresis (and incompatibility between phases) with Rb incorporation implies that, Rb-containing compounds are not likely to replace CsH_2PO_4 as crack-free electrolytes for use in fuel cells.

5.5 Results and Discussion: Microstructure of CsH_2PO_4 and CsHSO_4

5.5.1 Microcrack Formation

SEM micrographs of single-crystal surfaces of CsH_2PO_4 and CsHSO_4 after heating to the high-temperature phase are shown in Figure 5.9. In CsH_2PO_4 , cracks are clearly visible, varying in width and length and occurring with relatively high density, consistent with observations made for polycrystalline CsH_2PO_4 (Figure 3.2). Cracks in CsHSO_4 are narrow and barely visible.

Optical images of single crystals before and after heat treatment reveal the influence of cracking on the clarity of CsH_2PO_4 and CsHSO_4 crystals (Figure 5.10). The as-grown CsH_2PO_4 crystal was transparent, with some visible defects due to inclusions of solution, but was almost completely opaque after heat treatment and was comprised of many facets (Figure 5.10a). The CsHSO_4 single crystal was also transparent initially,

although the clarity of the crystal was not as well-captured as that for CsH_2PO_4 because of the presence of fine crystallites/precipitates on the surface. Even so, the CsHSO_4 crystal exhibited a less dramatic change in its clarity, appearing hazy but retaining some transparency after heat treatment (Figure 5.10b). The observation of higher clarity in CsHSO_4 is consistent with lower crack densities and the smaller phase transformation hysteresis width of $5.2\text{ }^\circ\text{C}^{19}$ compared to $13.4\text{ }^\circ\text{C}$ for CsH_2PO_4 .

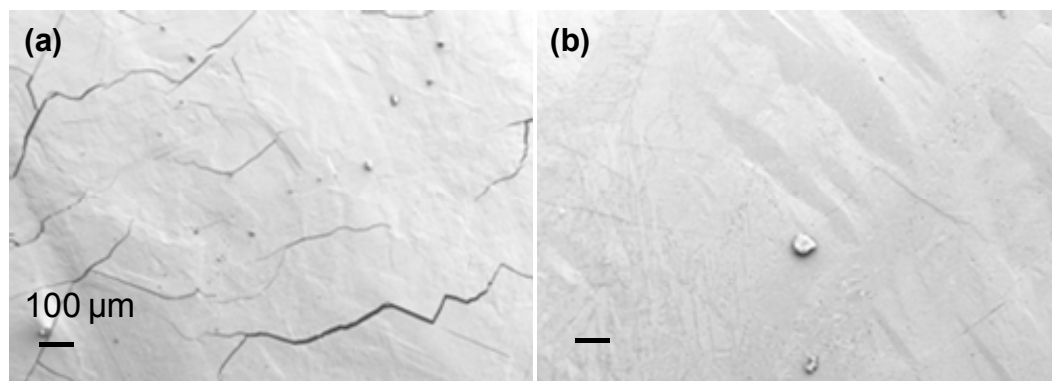


Figure 5.9 SEM micrographs of polished surfaces of (a) CsH_2PO_4 and (b) CsHSO_4 single crystals, taken after heat treatment at temperatures above the phase transition temperature ($235\text{ }^\circ\text{C}$ and $155\text{ }^\circ\text{C}$, respectively).

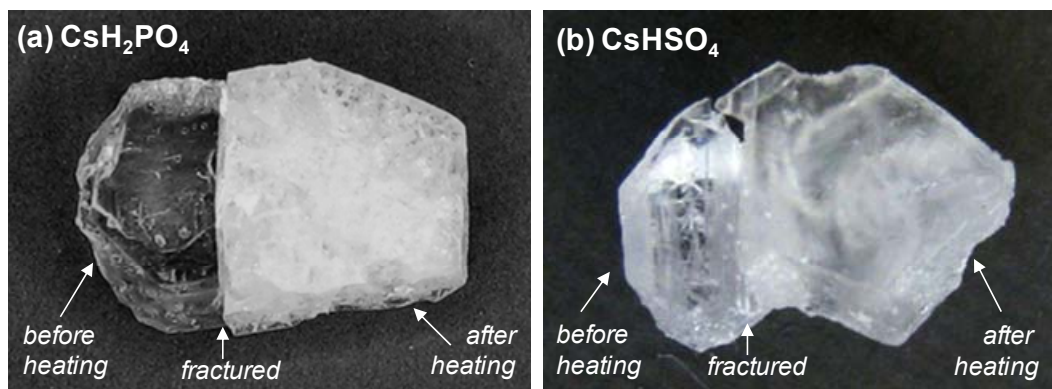


Figure 5.10 Optical images of two halves of a fractured single crystal of (a) CsH_2PO_4 and (b) CsHSO_4 . The right half for each crystal was heat-treated at above its phase transition temperature.

5.5.2 *Microstructure of Single-crystal Surfaces*

Micrographs of single-crystal CsH_2PO_4 surfaces, both polished (Figure 5.11a) and fractured (Figure 5.12a), show that surfaces were smooth before heat treatment. In the case of polished crystals (Figure 5.11a), streaks running diagonally in the image are visible to the uni-directional polishing of the crystals. As-fractured crystal surfaces contained crystal steps in the plane of the image but were smooth otherwise (Figure 5.12a). For samples prepared by both methods, changes in the CsH_2PO_4 surface after heating were clearly visible. Figure 5.11(b–c) and Figure 5.12(b–c) are SEM images of polished and fractured surfaces, respectively, showing that the surfaces appeared faceted after heat treatment. Polishing streaks visible in Figure 5.11 are relatively easy to distinguish from features that appeared due to heat treatment. However, without any noticeable patterning or symmetry, it is unclear if these features correspond to twins of monoclinic phase. Higher magnification images generally revealed little additional information, with the exception of Figure 5.13 collected for a fractured crystal. In this image, patterning at the micron-scale is visible, and an angle of $\sim 45^\circ$ can be extracted for the two sets of patterns. It is interesting to note that the surface of the crystal appeared roughened with uniformly distributed sub-micron particulates. The formation of CsH_2PO_4 particles on the surface of the fractured crystal likely occurred at superprotonic temperatures at which CsH_2PO_4 is relatively mobile.

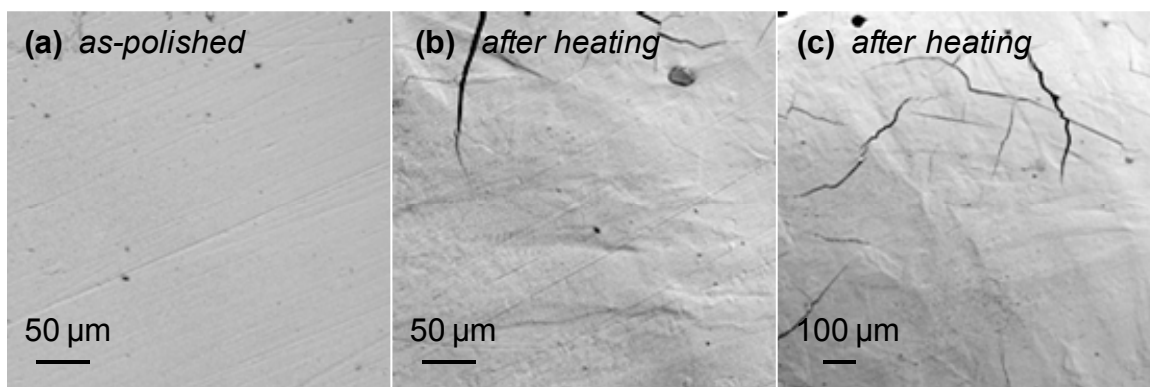


Figure 5.11 SEM micrographs of a polished surface of a CsH_2PO_4 single crystal (a) before and (c) after heating to 235 °C in synthetic air with ~ 0.35 atm H_2O .

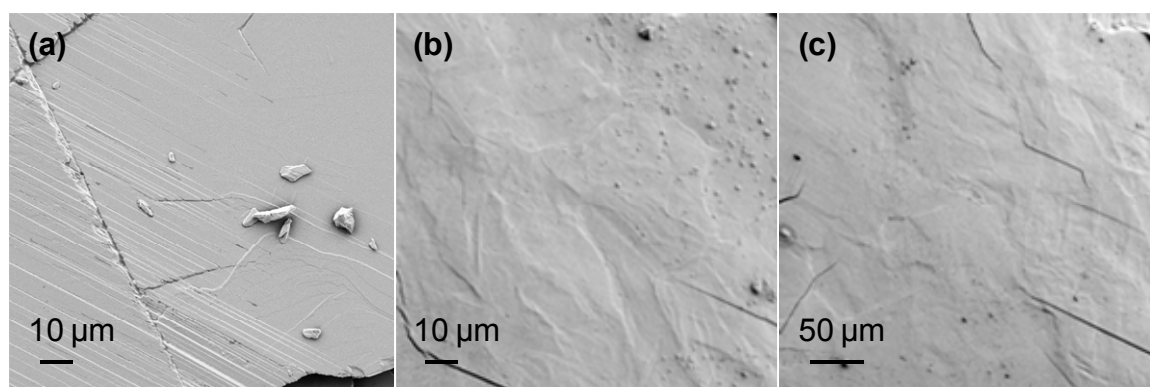


Figure 5.12 SEM micrographs of a fractured surface of a CsH_2PO_4 single crystal (a) before and (c) after heating to 235 °C in synthetic air with ~ 0.35 atm H_2O .

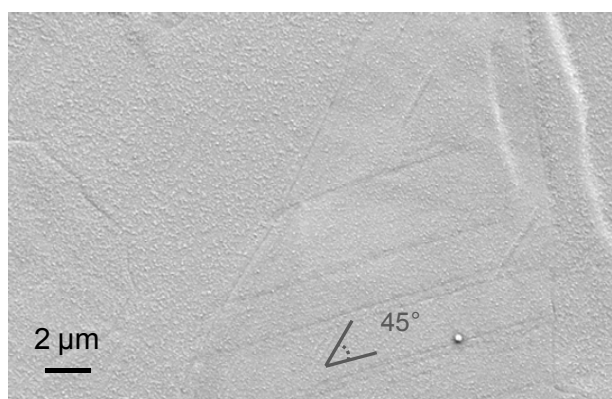


Figure 5.13 SEM micrograph of a fractured CsH_2PO_4 single crystal after heat treatment at 235 °C under flowing synthetic air with ~ 0.35 atm H_2O . Features appear to be twins, with internal twins at an angle of 45° to larger twins.

CsHSO_4 , on the other hand, formed twinned regions that were easily visible regardless of the method used to prepare the single-crystal surface. Untreated, as-grown CsHSO_4 single-crystal surfaces before and after heat treatment at superprotonic conditions are shown in Figure 5.14a and Figure 5.14(b–c), respectively. The surface of the as-grown crystal was smooth in most regions. Some contoured crystal steps are evident in Figure 5.14a; elsewhere, small crystallites had grown from the surface, characteristic of the surfaces of solid acid crystals taken directly out of solution. Overall, the crystal was considered sufficiently smooth for use in microstructures studies. After heat treatment, patterning of the surface was clearly visible; triangular-shaped features, with widths of 10–50 μm , emerged from the surface (Figure 5.14c). The edges of these features ran in the same direction, diagonally through the image. The surface also appeared to be roughened at a smaller length scale (Figure 5.14b); ignoring these imperfections, some internal twinning on the order of $\sim 1 \mu\text{m}$ is visible within the larger $\sim 10 \mu\text{m}$ twins.

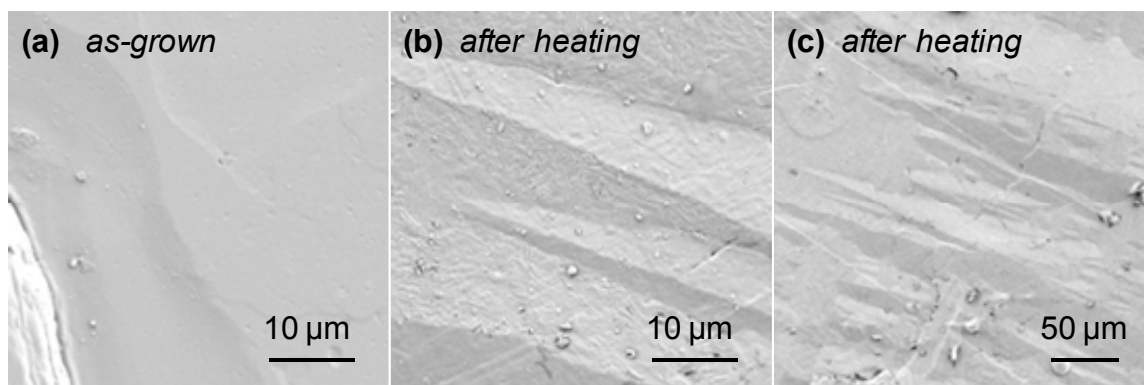


Figure 5.14 SEM micrographs of the surface of an as-grown CsHSO_4 single crystal (a) before and (b,c) after heating to 155 $^{\circ}\text{C}$ in ambient air.

The complexity of the microstructure is more clearly shown for polished crystals (Figure 5.15). Crystal surfaces before testing, Figure 5.15(a–c), revealed polishing streaks but were otherwise relatively featureless. The microstructure of crystal after heat treatment, Figure 5.15(d–f), can be assessed easily due to the high contrast in the image, the origin of which remains unknown. Visible in these three images are features of several scales, from hundreds of microns down to under ten microns in size, the latter appearing to be internal twins within the former (Figure 5.15f). Closer examination revealed that the large twins intersect at angles of 95 (or 85°), as noted in the Figure 5.15e.

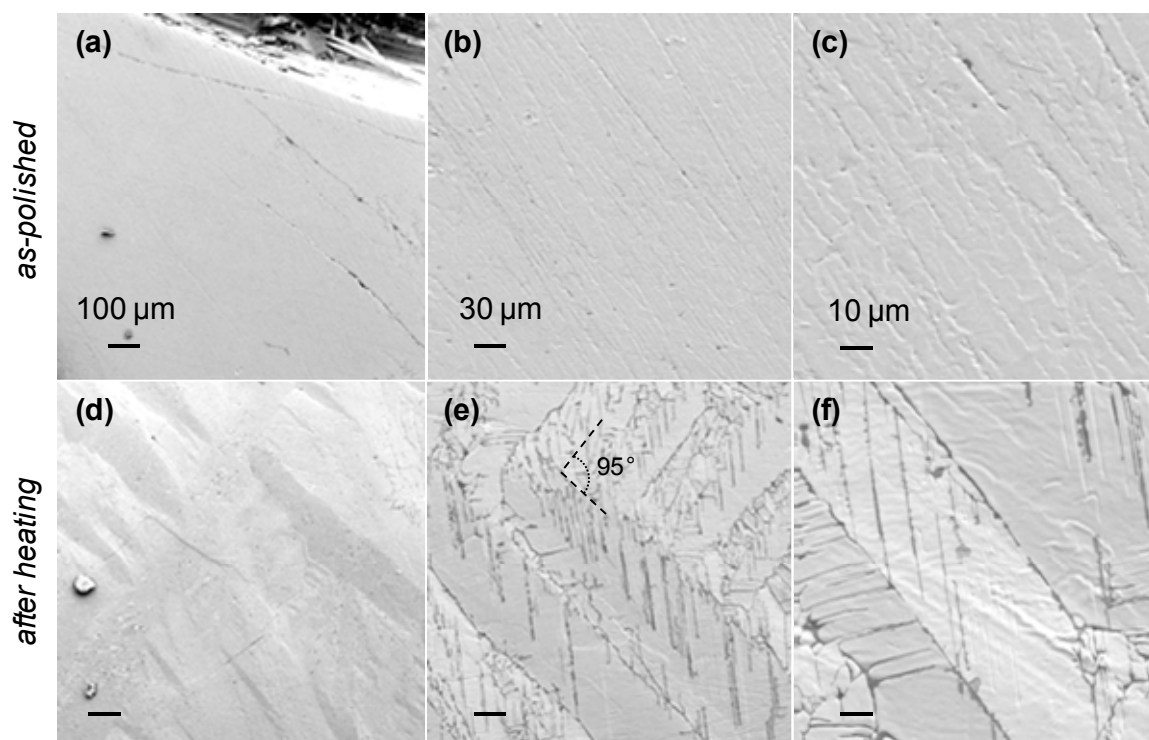


Figure 5.15 SEM micrographs of a polished surface of a CsHSO_4 single crystal (a–c) before and (d–f) after heating to 155 °C in ambient air.

5.5.3 *In situ Imaging of CsHSO₄*

A more reliable assessment of the microstructure can be obtained by topography images measured by AFM. Although the maximum x - y range of $\sim 35\ \mu\text{m}$ for AFM prevented the mapping of the larger features which could be observed by SEM, AFM enabled the capture of finer features. Shown in Figure 5.16 are planar and three-dimensional representations of the surfaces of two different single crystals obtained by fracturing. The features presented in these images are considered representative of those found using AFM in general. The features in all three images were qualitatively similar and revealed twinning with well-defined patterns. The larger feature sizes on the order of $10\ \mu\text{m}$ are consistent with those in Figure 5.14 and Figure 5.15. Finer features which appeared as steps $\sim 1\ \mu\text{m}$ in size were also visible in all three images in Figure 5.16.

From Figure 5.16(b–c), for which the intersections of twins are visible, an angle of $\sim 95^\circ$ (or 85°) was extracted; this angle is consistent with observations made by SEM (Figure 5.15e). Topographical profile analysis of the twins (not shown) provided the angles at which the two variants met, out of the x - y plane, to form an apex (right column of Figure 5.16). From profile analysis of the images in Figure 5.16, we determined this angle to be 170° . This value is twice that for the in-plane angles of $\sim 85^\circ$ (or, $\sim 95^\circ$). The measured angles of select features are marked in the figure.

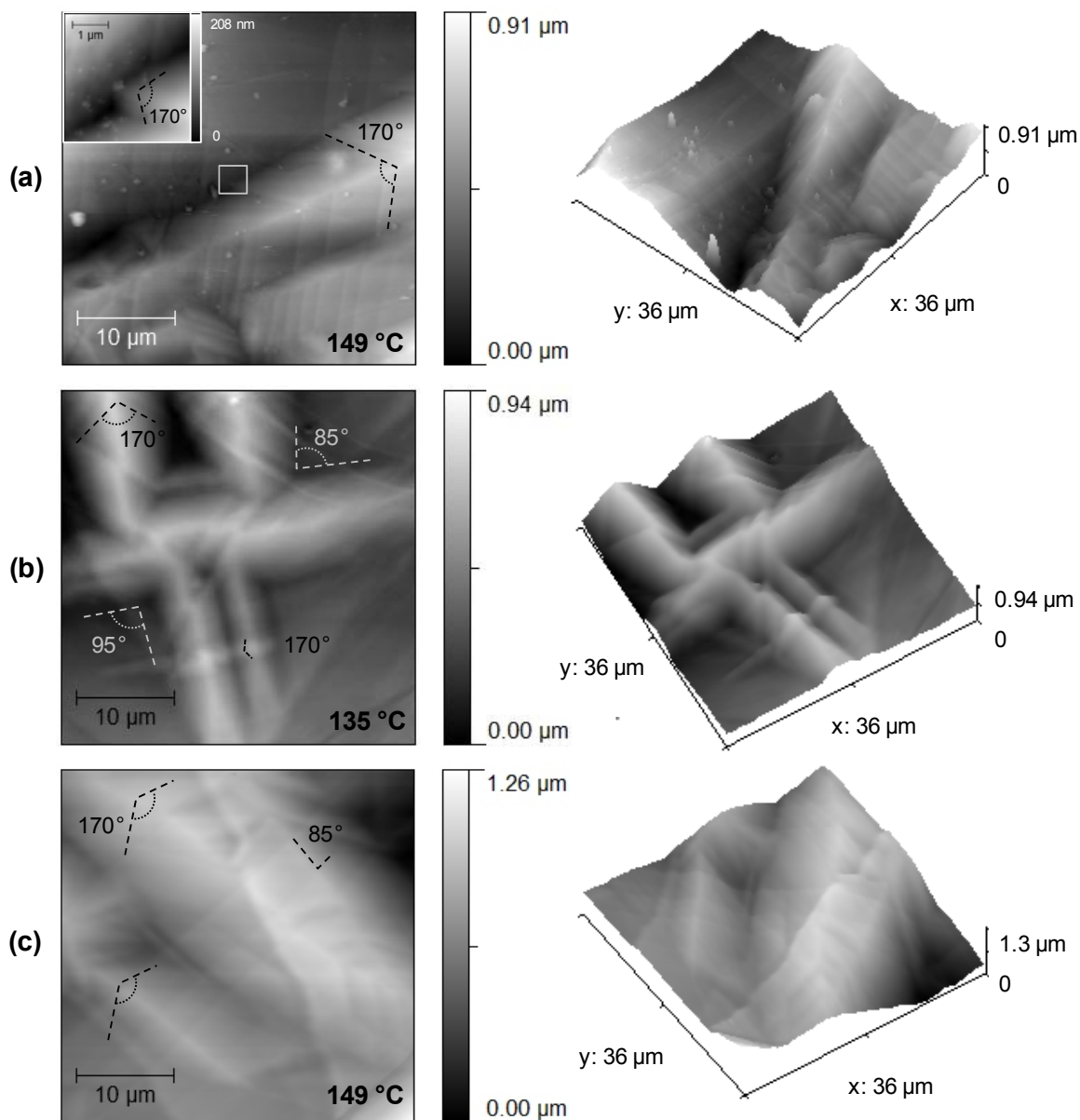


Figure 5.16 Topography of a CsHSO_4 single-crystal surface obtained by fracturing. Images were acquired in synthetic air with 0.03 atm H_2O at superprotonic temperatures of (a) 149 °C for one crystal and (b) 135 °C and (c) 149 °C for a second crystal. Horizontal features in the 2D representations are scan lines and not topographical features. In the 3D representations, z is not to scale with x/y .

The observation of twins at high temperature at which the high-symmetry tetragonal phase of CsHSO_4 is expected to exist is somewhat surprising. The image in Figure 5.16(a), which clearly revealed twinning, was taken after five hours at

temperatures between 145 and 149 °C, above the superprotonic transition temperature of ~ 141 °C. For the single crystal in Figure 5.16(b–c), twins were visible both before and after transition, with the different features being imaged being due to thermal expansion and sample movement as the temperature was heated from 135 to 149 °C.

We further explored this phenomenon by mapping the topography of a fractured CsHSO_4 crystal as it was heated and cooled through the phase transition (Figure 5.17). For this particular crystal, the as-fractured surface revealed contoured steps running through what appeared to be grain boundaries. As the temperature approached the phase transition temperature of ~ 141 °C, a “crease” appeared at the left-hand side of the image (Figure 5.17b) and remained visible, albeit less defined, even at 145 °C (Figure 5.17d). The apparent “smoothing” of this feature at higher temperatures could be indicative of the transformation of CsHSO_4 to the high-temperature tetragonal phase, or alternatively, an artifact of poor image quality due to the plasticity of the superprotonic phase and/or contamination of the AFM probe. From topographical profile analysis, the crease has a slight rise from the x-y plane, with an apex angle of 177° , slightly larger than the value of 170° determined above. This deviation is likely a consequence of the noise in the images, making accurate determination of the angle difficult.

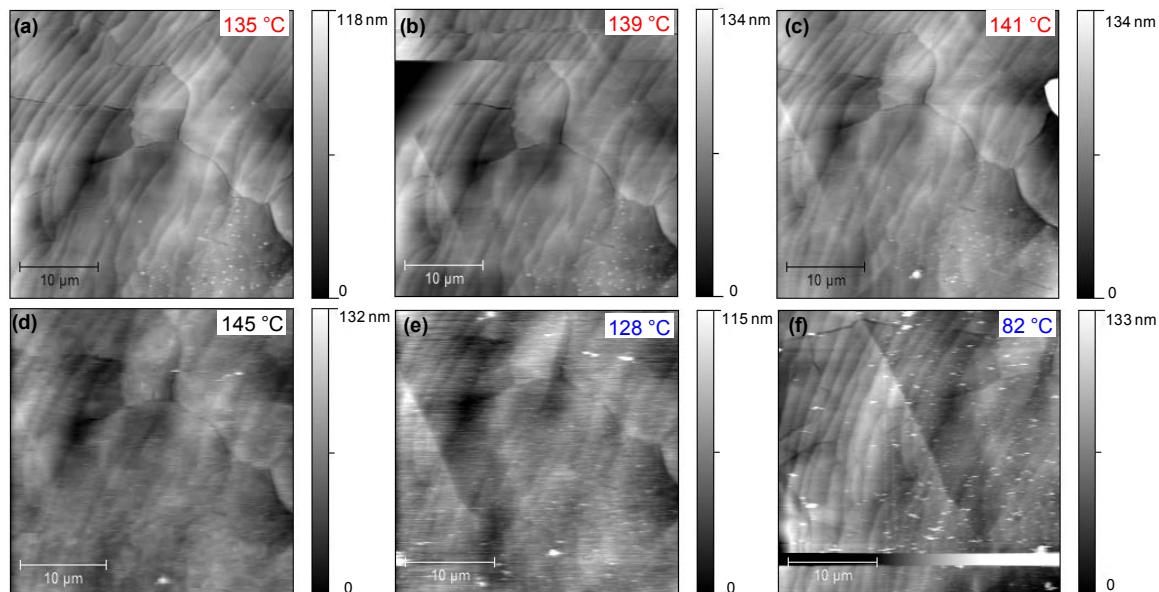


Figure 5.17 Topography of a CsHSO₄ single-crystal surface obtained by fracturing, examined as a function of temperature. On heating (a–c), a feature appeared on the left-hand side of the image. The feature was less prominent at the maximum temperature (d), but then reappeared on cooling (e–f). Small white spots in (e) and (f) are due to either a damaged sample or a contaminated AFM probe.

Twinning is expected to occur on heating and cooling through the phase transition, that is, at any condition in which both the low-temperature (monoclinic) and high-temperature (tetragonal) phases co-exist. The observation of twinning in the superprotonic (austenite) phase may be a consequence of a temperature gradient which exists across the single crystal such that the surface temperature of the crystal is lower than that at the AFM hotplate. Thus, despite high setpoint temperatures, 10–20 °C in excess of the phase transition temperature of 141 °C, the crystal surface may not have been completely transformed. Another possible explanation for the existence of twins at high temperatures can be explained by arguments of crystallographic compatibility, that is, the strain existing between the monoclinic and cubic phases during transformation prevents the martensite phase from transforming. In the case of CsHSO₄, it is unclear

whether such a phenomenon can exist. Because of the plasticity of the superprotonic, tetragonal phase of CsHSO_4 ,^{17, 19, 56} the austenite phase may be able to accommodate strain present in the system. To address these issues, additional in situ studies of twinning are required. Capturing twinning as a function of temperature is non-trivial due to the limited scan range in AFM. As shown in previous SEM micrographs (Figure 5.14 and Figure 5.15), twinned regions can be dispersed, and thus, finding a region of a single crystal that will twin on heating is not guaranteed.

5.6 Summary and Outlook

The phase transformation behavior of the solid acid solution series, $\text{Cs}_{1-x}\text{Rb}_x\text{H}_2\text{PO}_4$, as determined by AC impedance measurements, was explored with respect to the principles of crystallographic compatibility between phases. The hysteresis of $\text{Cs}_{1-x}\text{Rb}_x\text{H}_2\text{PO}_4$ was found to increase with Rb content, from $\sim 13.4^\circ\text{C}$ for the end-member CsH_2PO_4 to $\sim 17.4^\circ\text{C}$ for $x = 0.75$. The middle eigenvalues varied from 0.932 to 0.919 for $x = 0$ to 0.50. The increase in the hysteresis width and the corresponding decrease in λ_2 (away from unity) are consistent with the theory of crystallographic compatibility. However, the broadening of the hysteresis with Rb incorporation implies that we cannot minimize cracking of the electrolyte by Rb substitution, and the end-member, CsH_2PO_4 , still remains the electrolyte of choice for solid acid fuel cells (and electrochemical studies).

The physical properties of CsH_2PO_4 and CsHSO_4 single crystals correlated well with their measured hysteresis widths. CsHSO_4 ($\sim 5.2^\circ\text{C}$ hysteresis, $\lambda_2 = 1.010^{19}$) displayed a far lower crack density than CsH_2PO_4 ($\sim 13.4^\circ\text{C}$ hysteresis, $\lambda_2 = 0.932$) when

taken through the phase transition. Although CsHSO_4 is not a practical fuel cell electrolyte due to instability under reducing conditions,⁵⁶ CsHSO_4 may prove valuable as a substrate for fundamental cathode studies due to its low crack density and its relative stability with respect to dehydration. Microstructure changes due to the superprotonic phase transition were observed for both crystals, but twinned regions were not easily observable in CsH_2PO_4 . Further exploration of the orientation of twinned domains in CsHSO_4 is required, specifically, the existence of frequently occurring angles of 170° and 85° and, more curiously, the persistence of martensite twins at temperatures above the phase transition temperature.

Although we have demonstrated that the hysteresis behavior of $\text{Cs}_{1-x}\text{Rb}_x\text{H}_2\text{PO}_4$ and CsHSO_4 can be explained by the theory of crystallographic compatibility, we have not ruled out effects of strain due to differences in the volume of the two phases. In the case of the $\text{Cs}_{1-x}\text{Rb}_x\text{H}_2\text{PO}_4$ solid solution series, as more Rb was incorporated, the volume change at transition also increased from 1.7% to 4.8% on heating.¹⁹ Similarly, the lower hysteresis width of CsHSO_4 relative to $\text{Cs}_{1-x}\text{Rb}_x\text{H}_2\text{PO}_4$ can be explained by the lower volume change of CsHSO_4 across the phase transition ($\sim 0.5\%$) compared to that for the $\text{Cs}_{1-x}\text{Rb}_x\text{H}_2\text{PO}_4$ series. $\text{Rb}_3\text{H}(\text{SeO}_4)_2$ is presently the only solid acid compound we have examined in the context of crystallographic compatibility that, when compared to CsH_2PO_4 and CsHSO_4 , displays lower phase transformation hysteresis, a computed λ_2 value closer to unity, and a *larger* volume change across the phase transition. The hysteresis width and its correlation with λ_2 and volume change are summarized in Figure 5.18. The middle eigenvalues for CsH_2PO_4 , CsHSO_4 , and $\text{Rb}_3\text{H}(\text{SeO}_4)_2$ were found to be 0.932, 1.010, and 1.007 corresponding to hysteresis widths of 13.4, 5.2,¹⁹ and 2°C ,¹⁰⁸

respectively. A plot of hysteresis against λ_2 (Figure 5.18a) shows a lowering of the hysteresis as the eigenvalue approaches unity from both sides, consistent with theory. However, while CsH_2PO_4 and CsHSO_4 exhibited volume changes of 1.7 and 0.5%, respectively, on heating, $\text{Rb}_3\text{H}(\text{SeO}_4)_2$ exhibits a large negative volume change of -2.7% . Consequently, a plot of hysteresis against the phase transformation volume change (Figure 5.18b) shows $\text{Rb}_3\text{H}(\text{SeO}_4)_2$ falling off the trend, implying that strain existing between the austenite and martensite phases during transformation does not originate from a volume difference between the two. The correlation of the hysteresis with the middle eigenvalue, despite the differing crystal transformations (i.e., monoclinic-to-cubic, monoclinic-to-tetragonal, and monoclinic-to-trigonal for CsH_2PO_4 , CsHSO_4 and $\text{Rb}_3\text{H}(\text{SeO}_4)_2$, respectively), is an indication of the widespread applicability of the theory to solid acid systems.

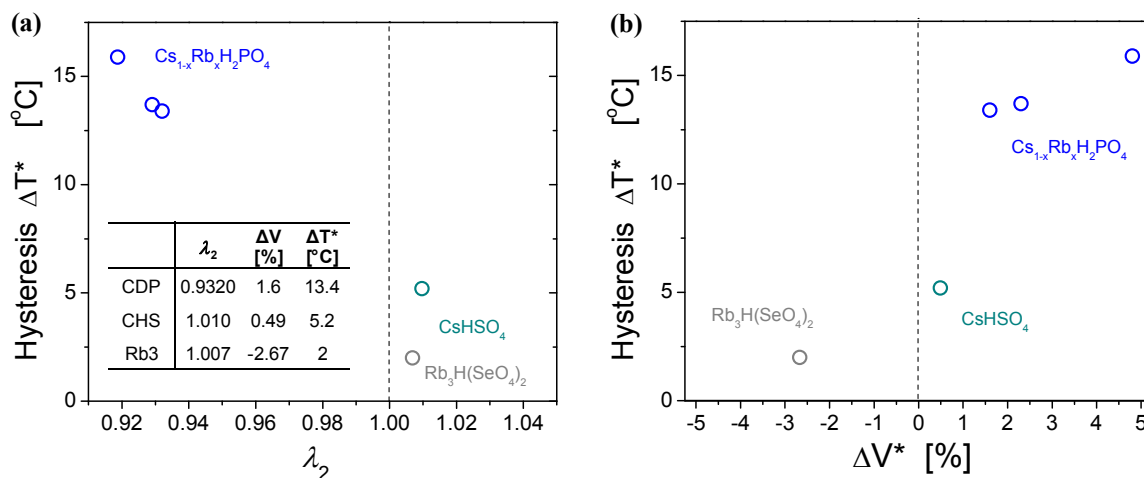


Figure 5.18 Plot of superprotonic phase transition hysteresis as a function of (a) the middle eigenvalue, λ_2 and (b) the phase transformation volume change (on heating) for three classes of solid acid compounds.

Appendix A Derivations

A.1 Kinetics of Electrode Reactions: Butler-Volmer Equation

In this section, a relationship between the potential of the electrode and resulting current is derived for a simple one-electron process. This derivation will serve as a basis for further understanding of observed kinetics in fuel cell electrodes.⁴¹

A simple one-electron transfer process occurring on the surface of an electrode can be represented as



where O represents the oxidized species, R is the reduced species, and k_{red} and k_{ox} are the reduction and oxidation rate constants, respectively. At the equilibrium or standard potential of the redox couple, denoted by E^0 , the standard free energy profiles of the reactants and products are as shown in Figure A.1, where ΔG_{0c}^\ddagger and ΔG_{0a}^\ddagger represent the cathodic and anodic standard energies of activation, respectively. Changes in electrode potential are reflected by shifts in the free energy profile for $\text{O} + \text{e}^-$, and the intersection of the two profiles represents the transition state of the reaction. When the potential of the electrode is changed to E , the free energy of the electron on the electrode changes by $-F\Delta E$, where $\Delta E = E - E^0$. This change is depicted as a shift in the energy profile for $\text{O} + \text{e}^-$, downward in this case. At this new state, the barriers for reduction and oxidation are denoted by ΔG_c^\ddagger and ΔG_a^\ddagger , respectively. Notice that $\Delta G_c^\ddagger > \Delta G_{0c}^\ddagger$ and $\Delta G_a^\ddagger > \Delta G_{0a}^\ddagger$. It can be seen that the barrier for reduction increases by an amount that is a fraction α of

the total energy change, while the barrier for oxidation decreases. The new activation barriers are given by

$$\Delta G_c^\ddagger = \Delta G_{0c}^\ddagger + \alpha F(E - E^0) \quad (\text{A.2})$$

$$\Delta G_a^\ddagger = \Delta G_{0a}^\ddagger - (1 - \alpha) F(E - E^0) \quad (\text{A.3})$$

where α , the transfer coefficient, gives an indication of the fraction of the potential that assists the reaction. In most cases, α lies between 0.3 and 0.7 but is often approximated as 0.5 in the absence of measurements.⁴¹ Equations (A.2) and (A.3) can be related to rate constants k_{red} and k_{ox} by assuming the rate constants have Arrhenius form,

$$k_{red} = A_{red} \exp\left(-\frac{\Delta G_c^\ddagger}{RT}\right) \quad (\text{A.4})$$

$$k_{ox} = A_{ox} \exp\left(-\frac{\Delta G_a^\ddagger}{RT}\right) \quad (\text{A.5})$$

where A_{red} and A_{ox} are pre-exponential factors. Equations (A.2) and (A.3) are inserted into equations (A.4) and (A.5), respectively, to obtain

$$k_{red} = A_{red} \exp\left(-\frac{\Delta G_{0c}^\ddagger}{RT}\right) \exp\left[-\frac{\alpha F(E - E^0)}{RT}\right] = k^0 \exp\left[-\frac{\alpha F(E - E^0)}{RT}\right] \quad (\text{A.6})$$

$$k_{ox} = A_{ox} \exp\left(-\frac{\Delta G_{0a}^\ddagger}{RT}\right) \exp\left[\frac{(1 - \alpha) F(E - E^0)}{RT}\right] = k^0 \exp\left[\frac{(1 - \alpha) F(E - E^0)}{RT}\right] \quad (\text{A.7})$$

where k^0 is the standard rate constant, defined for the case when the interface is equilibrated, $E = E^0$, with an environment in which $C_O^* = C_R^*$. k^0 is a measure of the how facile the reaction kinetics are, i.e., how fast this couple will achieve equilibrium. The net current density ($j = i/A$) for the process is

$$j = j_c - j_a = Fk_{red}C_O(0,t) - Fk_{ox}C_R(0,t) \quad (A.8)$$

$$j = Fk^0 \left[C_O(0,t) \exp^{-\alpha F(E-E^0)/RT} - C_R(0,t) e^{(1-\alpha)F(E-E^0)/RT} \right] \quad (A.9)$$

where A is the electrode area, and $C_O(0,t)$ and $C_R(0,t)$ refer to concentrations at the electrode surface.

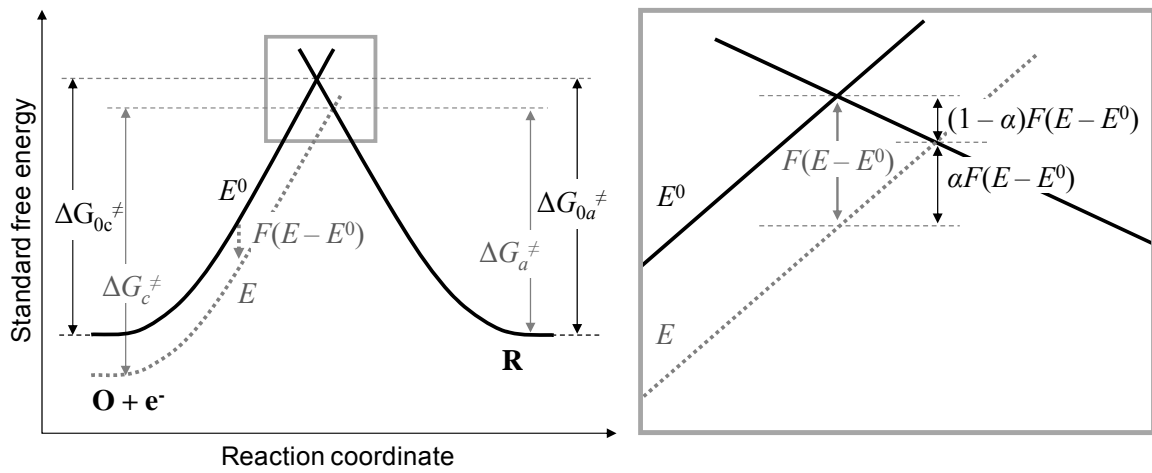


Figure A.1 The effect of potential change on the standard free energy profiles for the reaction, $O + e^- \rightleftharpoons R$.

At equilibrium ($E = E_{eq}$), the net current is zero, and the surface concentrations are the same as the bulk concentrations, C_O^* and C_R^* . Equation (A.9) simplifies to the Nernst equation, and the equilibrium potential is related to the standard potential by the concentrations of the species involved.

$$E_{eq} = E^0 + \frac{RT}{F} \ln \frac{C_O^*}{C_R^*} \quad (A.10)$$

The exchange current density, defined as the forward and reverse current densities ($j_0 = j_a = j_c$) at equilibrium, can be expressed in terms of the standard rate constant and the bulk concentrations.

$$j_0 = Fk^0 C_O^{*(1-\alpha)} C_R^{*\alpha} \quad (\text{A.11})$$

The exchange current density, similar to k^0 , indicates how likely it is for the reaction to occur in either direction. To obtain a more useful current-overpotential relationship, Equation (A.11) can be used to express Equation (A.9) in terms of the equilibrium potential rather than the standard potential.

$$j = j_0 \left[\frac{C_O(0,t)}{C_O^*} e^{-\alpha\eta F/RT} - \frac{C_R(0,t)}{C_R^*} e^{(1-\alpha)\eta F/RT} \right] \quad (\text{A.12})$$

If mass transfer is not rate limiting, e.g., when convection is high, the surface and bulk concentrations are the same and

$$j = j_0 \left[e^{-\alpha\eta F/RT} - e^{(1-\alpha)\eta F/RT} \right] \quad (\text{A.13})$$

Equation (A.13), historically known as the Butler-Volmer equation, describes the relationship between the overpotential, $\eta = E - E_{eq}$, needed to drive the reaction and the resulting current.

The importance of j_0 can be seen when the Butler-Volmer equation is plotted for various values of j_0 . (Figure A.2) For a small j_0 , significant current will not flow unless a large overpotential is applied. This can be understood intuitively as well; the exchange current indicates how likely it is for the reaction to occur in either direction. The most effective way to improve the activation overpotential is to increase j_0 . This is accomplished by choosing an active catalyst, followed by increasing the electrode roughness or surface area. Improving catalyst site occupancy by increasing reactant

concentration or pressure is also possible. For a system that obeys Butler-Volmer kinetics, the slope near the origin provides information about the exchange current and therefore the relative activities of different electrode materials.

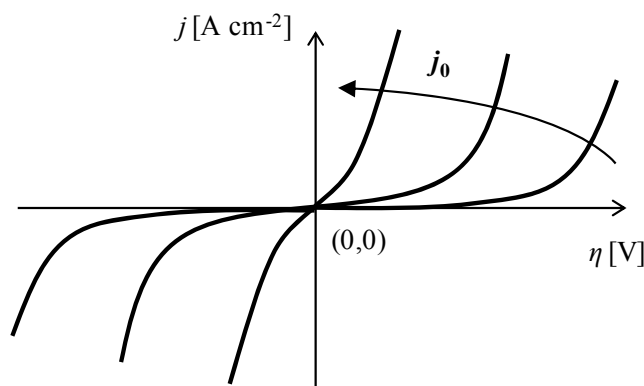


Figure A.2 Effect of exchange current on the current-overpotential behavior.

In low-temperature fuel cells, reaction kinetics are slow and large activation overpotentials are needed at both electrodes. In such systems, the Tafel equation is more useful. The Tafel equation, first introduced empirically, can be obtained from the Butler-Volmer equation. At high positive or negative η , either j_a or j_c can be neglected. For example, at large negative overpotentials,

$$j = j_0 e^{-\alpha n F \eta / RT} \quad (\text{A.14})$$

or

$$\eta_{act} = \frac{RT}{\alpha F} \ln \left(\frac{j_0}{j} \right) \quad (\text{A.15})$$

It is common to modify the Tafel equation for a system in which more than one electron is transferred, i.e., $n > 1$ where n denotes the number of electrons transferred in the redox reaction.

$$\eta_{act} = \frac{RT}{n\alpha F} \ln(j_0) - \frac{RT}{n\alpha F} \ln(j) \quad (\text{A.16})$$

Experimental data obtained at high overpotentials plotted in the form of $\ln(j)$ as a function of η yields a line from which n or α (slope) and j_0 (intercept) can be calculated.

A.2 Finite-Length Warburg with Reversible Bounds

In this section, we will derive the impedance expression for the finite-length Warburg element (Equation 3.1) used to analyze the impedance response of the Pt thin film electrode system. This section is based on derivations in the references, Orazem & Tribollet³³ and Franceschetti & MacDonald.¹²³ The Pt thin film system can be generalized as shown in Figure A.3 for a electrolyte | metal | gas system, in which a neutral species, A, enters the metal at the metal | gas interface ($x = L$) and diffuses a distance L to the metal | electrolyte interface ($x = 0$) where it is electrochemically oxidized,



In the charge transfer reaction, (A.17), n denotes the number of electrons transferred and, therefore, also the charge of the ionic species, A^{n+} , formed in the electrolyte. “*met*” and “*lyte*” denote that metal and electrolyte phases, respectively. We assume in this system, that supply of A at the metal | gas interface and charge transfer kinetics at the electrolyte | metal interface are fast relative to diffusion.

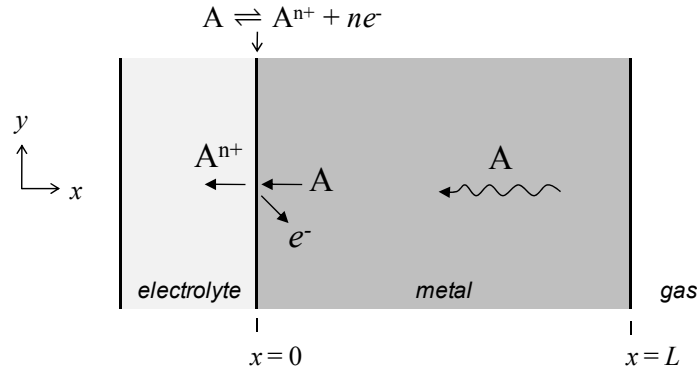


Figure A.3 Diffusion of a neutral species, A, through a metal film of finite thickness, L , to be oxidized at $x = 0$ via the charge transfer reaction $A \rightleftharpoons A^{n+} + ne^-$.

The movement of chemical species under an electrochemical potential gradient is described by the Nernst-Planck equation, which, in general is given by

$$J_k = -D_k \nabla c_k + \frac{\sigma_k}{z_k F} \nabla \phi \quad (\text{A.18})$$

where J_k denotes the flux of species k under both a concentration gradient, ∇c_k , and an electric potential gradient, $\nabla \phi$. D_k is the diffusivity, σ_k is the conductivity and z_k is the charge of the species k . F , R , and T have their usual meanings. In general, for the transport of a chemical species in any medium, the second (migration) term in Equation (A.18) can be neglected if the species is uncharged, i.e., $\sigma_k = 0$, or if the movement of the (charged) species is balanced by fast-moving ions in the diffusing medium, i.e., $\partial \phi / \partial x = 0$. For the problem we are interested in, that is, the diffusion of A in a metal (Figure A.3), we set $\sigma_A = 0$. We also assume that the film extends infinitely in the y - and z -directions, that is, the film is thin by comparison to its lateral dimensions. The resulting equation is simply Fick's first law of diffusion in one dimension, which, written for the transport of species A, is

$$J_A = -D_A \frac{\partial c_A}{\partial x} \quad (\text{A.19})$$

Application of mass conservation yields Fick's second law

$$\frac{dc_A}{dt} = D_A \frac{\partial^2 c_A}{\partial x^2} \quad (\text{A.20})$$

Under a small signal perturbation of a voltage (or current) to the system, a perturbation in the concentration of species A in the film about its steady-state value occurs; the concentration can be separated into its steady-state and time-dependent components

$$c_A = \bar{c}_A + \Delta c_A e^{j\omega t} \quad (\text{A.21})$$

where j is the imaginary number, $\sqrt{-1}$, \bar{c}_A is the steady-state concentration and Δc_A is a function of the angular frequency, ω , and corresponds to the perturbation amplitude of c_A resulting from the applied perturbation in the electric field. That is, although A is uncharged, its movement is driven by the electrochemical reaction at $x = 0$. Inserting Equation (A.21) into (A.20) and canceling steady-state terms results in Fick's second law expressed in terms of the perturbation amplitude,

$$j\omega\Delta c_A = D_A \frac{\partial^2 \Delta c_A}{\partial x^2} \quad (\text{A.22})$$

The reversible boundary conditions for (A.22) are given by

$$\Delta c_A = 0 \text{ @ } x = L \text{ and } \Delta c_A = \Delta c_{A0} \text{ @ } x = 0 \quad (\text{A.23})$$

where Δc_A at $x = L$ is selected to be fixed at zero, while a finite value of Δc_{A0} is specified at the electrode ($x = 0$). For convenience, we can define dimensionless concentration and length as

$$\theta_A = \frac{\Delta c_A}{\Delta c_{A0}} \text{ and } \delta = \frac{x}{L} \quad (\text{A.24})$$

respectively. Inserting these dimensionless variables into Equation (A.22) and defining the dimensionless frequency,

$$K_A = \frac{\omega L^2}{D_A} \quad (\text{A.25})$$

we obtain

$$\frac{\partial^2 \theta_A}{\partial \delta^2} - jK \theta_A = 0 \quad (\text{A.26})$$

The general solution to Equation (A.26) is well-known and has the form,

$$\theta_A = B e^{\delta \sqrt{jK_A}} - C e^{-\delta \sqrt{jK_A}} \quad (\text{A.27})$$

where the constants B and C can be determined by the boundary conditions of Equation (A.23) in dimensionless form,

$$\theta_A = 0 \quad @ \quad \delta = 1 \quad \text{and} \quad \theta_A = 1 \quad @ \quad \delta = 0 \quad (\text{A.28})$$

Applying these boundary conditions to Equation (A.27), we find that

$$B = \frac{e^{-\sqrt{jK_A}}}{e^{-\sqrt{jK_A}} - e^{\sqrt{jK_A}}} \quad \text{and} \quad C = \frac{e^{\sqrt{jK_A}}}{e^{-\sqrt{jK_A}} - e^{\sqrt{jK_A}}} \quad (\text{A.29})$$

Inserting Equations (A.29) in to (A.27) and employing the relation, $2\sinh(z) \equiv e^z - e^{-z}$, Equation (A.27) becomes

$$\theta_A = \frac{\sinh\left[(\delta - 1)\sqrt{jK_A}\right]}{\sinh\left(-\sqrt{jK_A}\right)} \quad (\text{A.30})$$

which describes the concentration perturbation profile of A in the film. The dimensionless frequency K_A , Equation (A.25), gives the characteristic parameters of the system. Specifically, Equation (A.25) can be written as

$$K_A = \frac{\omega}{\omega_A^*} = \omega \tau_A^* \quad \text{where } \tau_A^* = \frac{L^2}{D_A} \quad (\text{A.31})$$

where ω_A^* and τ_A^* are the characteristic frequency and time, respectively, of the diffusion of A through the film.

The diffusion impedance can be obtained from the ratio of the applied perturbation voltage and the resulting current that flows at $x = 0$ (or $\delta = 0$). The current flowing at the electrode is related to the flux of the diffusing species, that is, $\Delta i_A|_{\delta=0} = nFA \Delta J_A|_{\delta=0}$, where n is the number of electrons transferred (as shown in Figure A.3), A is the interfacial area at the electrolyte | metal interface (or the cross-sectional area for diffusion). Thus, the perturbation current at $\delta = 0$ is

$$\Delta i_A|_{\delta=0} = nFA \Delta J_A|_{\delta=0} = -\frac{nFAD_A \Delta c_{A0}}{L} \frac{\partial \theta_A}{\partial \delta} \Big|_{\delta=0} \quad (\text{A.32})$$

for which the relationship between ΔJ_A and the gradient of θ_A is obtained from Fick's first law, (A.19), under perturbation. The dimensionless concentration gradient at $\delta = 0$ is

$$\frac{d\theta_A}{d\delta} \Big|_{\delta=0} = \frac{\sqrt{jK_A} \cosh[(\delta-1)\sqrt{jK_A}]}{-\sinh(\sqrt{jK_A})} \Big|_{\delta=0} = \frac{-\sqrt{jK_A}}{\tanh(\sqrt{jK_A})} \quad (\text{A.33})$$

The expression of the applied voltage perturbation can be determined from recognizing that, under the assumption of rapid charge transfer kinetics, i.e., a reversible boundary condition at $x = 0$, electrochemical equilibrium is reached at the electrode.

$$\tilde{\mu}_{A^{n+}}^{(lyte)} \Big|_{x=0} + n\tilde{\mu}_{e^-}^{(met)} \Big|_{x=0} = \mu_A^{(met)} \Big|_{x=0} \quad (\text{A.34})$$

where $\tilde{\mu}$ denotes the electrochemical potential, μ is the chemical potential, the subscript denotes the species and the superscript indicates the phase/medium in which the species resides. We assume that Equation (A.34) holds locally upon perturbation

$$\Delta\tilde{\mu}_{A^{n+}}^{(lyte)}\Big|_{x=0} + n\Delta\tilde{\mu}_{e^{-}}^{(met)}\Big|_{x=0} = \Delta\mu_A^{(met)}\Big|_{x=0} \quad (\text{A.35})$$

We also assume that the transport of A^{n+} in the electrolyte is fast, which combined with fast charge transfer kinetics at $x=0$, implies that $\Delta\tilde{\mu}_{A^{n+}}^{(lyte)} = 0$. Recognizing that the voltage perturbation, ΔV , is

$$\Delta V = \frac{1}{F} \Delta\tilde{\mu}_{e^{-}}^{(met)} \quad (\text{A.36})$$

we can obtain from Equations (A.35) and (A.36) that ΔV at $x=0$ is directly proportional to $\Delta\mu_R^{(met)}\Big|_{x=0}$, that is,

$$\Delta V\Big|_{x=0} = \frac{1}{nF} \Delta\mu_A^{(met)}\Big|_{x=0} \quad (\text{A.37})$$

The perturbation of the chemical potential, $\Delta\mu_A$, can be determined by carrying out a Taylor expansion of μ_A about of the steady-state value of \bar{c}_A by the quantity Δc_A . This yields

$$\Delta\mu_A = RT \left(\frac{\Delta c_A}{\bar{c}_A} \right) \quad (\text{A.38})$$

Inserting Equation (A.38) into (A.37), the voltage amplitude at $\delta=0$ can be expressed as

$$\Delta V\Big|_{\delta=0} = \frac{RT}{nF} \left(\frac{\Delta c_{A0}}{\bar{c}_A} \right) \quad (\text{A.39})$$

Therefore, the impedance response of the system shown in Figure A.3 is

$$Z(\omega) \equiv \frac{\Delta V|_{\delta=0} e^{j\omega t}}{\tilde{i}_A|_{\delta=0} e^{j\omega t}} = \frac{RT}{(nF)^2 D_A \bar{c}_A} \frac{L}{A} \frac{\tanh(\sqrt{jK_A})}{\sqrt{jK_A}} \quad (\text{A.40})$$

or, collecting the constants in the beginning of the expression,

$$Z(\omega) = R_{A0} \frac{\tanh(\sqrt{jK_A})}{\sqrt{jK_A}} \quad (\text{A.41})$$

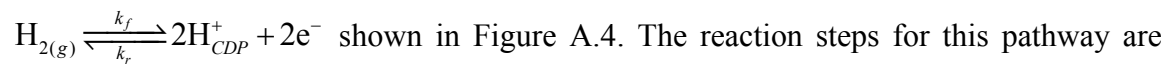
where

$$R_{A0} = \frac{RT}{(nF)^2 D_A \bar{c}_A} \frac{L}{A} \quad (\text{A.42})$$

In the limit of zero frequency, i.e., $K_A = 0$, the impedance, Z approaches the value R_{A0} , shown in Equation (A.42). Equation (A.42) is similar to the Nernst-Einstein equation for the transport of a charged species but is derived for the diffusion of a neutral species; n can be thought of as the “effective” charge of the neutral species A, that is, it is the charge of A once it is incorporated into the electrolyte as A^{n+} .

A.3 Reaction Mechanism

In this section, we obtain the pH_2 and pH_2O dependences of the hydrogen electro-oxidation for several possible rate-limiting steps. For the Pt thin film presented in Chapter 3, we propose the two-phase reaction pathway for the half-cell reaction,



shown in Equations (A.43)–(A.46).

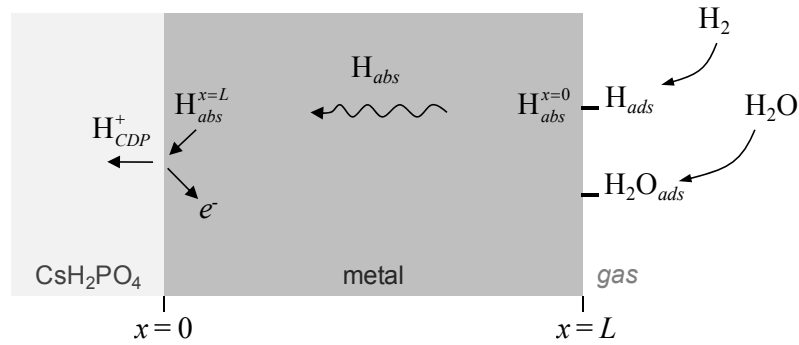
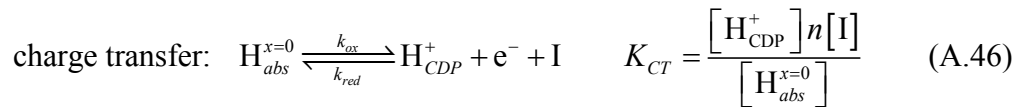
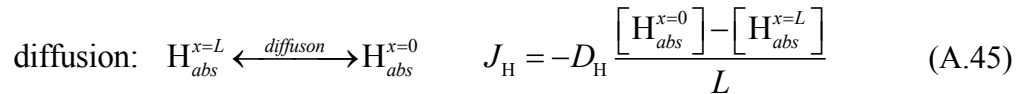
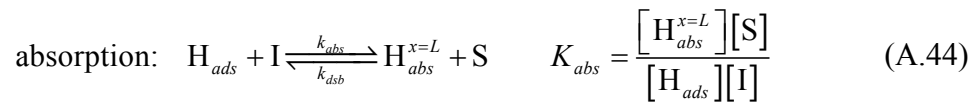
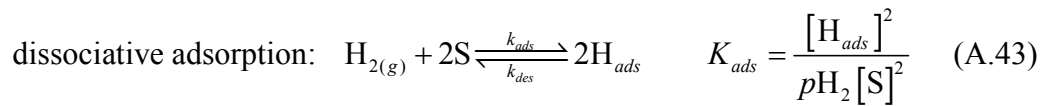
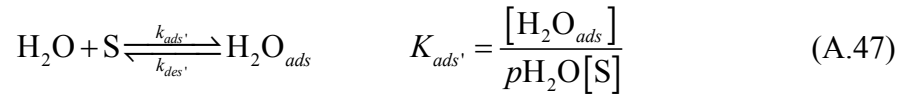


Figure A.4 Two-phase boundary pathway for hydrogen electro-oxidation.



S denotes a surface site on the metal available for adsorption, I denotes an interstitial site in the metal, the subscripts *ads* and *abs* adsorbed and absorbed species. Forward and reverse reaction rate constants, k_i , and equilibrium constants, K_i , are denoted by appropriate subscripts, as indicated in (A.43), (A.44), and (A.46). The flux of hydrogen through the film is denoted as J_{H} and the diffusion coefficient is D_{H} . The positions $x = 0$ and $x = L$ are shown in Figure A.4.

Although water is not expected to play a direct role in the reaction, we suspect that water may adsorb reversibly onto surface sites of the metal. We assume that water occupies only one metal surface site,



Consequently, the site balance for the metal surface is:

$$S_T = [\text{S}] + [\text{H}_{ads}] + [\text{H}_2\text{O}_{ads}] \quad (\text{A.48})$$

where S_T denotes the total number a surface sites available on the metal. The number of absorption sites in the metal must also be considered, but in the case of platinum (and even palladium) the fraction of the interstitial sites occupied by hydrogen is small,

$$I_T = [\text{I}] + [\text{H}_{abs}] \approx [\text{I}] \quad (\text{A.49})$$

where I_T is the total number of interstitial sites.

We employ the above expressions to determine the $p\text{H}_2$ and $p\text{H}_2\text{O}$ reaction orders for hydrogen electro-oxidation for four possible scenarios, each with a different rate-limiting step. Because we measure the impedance response at equilibrium, both the forward and reverse directions of the rate-limiting steps are probed, that is,

$$r_{RLS} = r_{RLS-f} = r_{RLS-r} \quad (\text{A.50})$$

where r_i denotes the rate step i , RLS denotes rate-limiting step, and f and r denote forward and reverse, respectively.

A.3.1 Hydrogen Adsorption as a Rate-Limiting Step

Following Equation (A.50), the rate of the slowest step, hydrogen adsorption, can be expressed as:

$$r_{ads} = k_{ads} pH_2 [S]^2 = k_{des} [H_{ads}]^2 \quad (A.51)$$

Because absorption, diffusion and charge transfer steps are fast relative to adsorption, they reach equilibrium and the concentrations the involved species are expressed by the equilibrium constants in (A.44) and (A.46). In the case of fast hydrogen diffusion, the concentration gradient of absorbed hydrogen in the metal film is negligible, that is,

$$[H_{abs}^{x=0}] = [H_{abs}^{x=L}] \quad (A.52)$$

Further employing the site balance shown in Equation (A.48) and the equilibrium relation for water adsorption in Equation (A.47), we find that

$$[S] = \frac{S_T}{\left(1 + \frac{[H_{CDP}^+]}{K_{CT} K_{abs}} n + K_{ads} pH_2 O \right)} \quad (A.53)$$

and, therefore, from the first equality in Equation (A.51), the rate of adsorption is

$$r_{ads} = \frac{S_T^2 k_{ads} pH_2}{\left(1 + \frac{[H_{CDP}^+]}{K_{CT} K_{abs}} n + K_{ads} pH_2 O \right)^2} \quad (A.54)$$

Because the concentrations of protons in the CsH_2PO_4 , $[H_{CDP}^+]$, and electrons in a metal, n , are constant, Equation (A.54) implies that the total reaction rate scales with pH_2 with a reaction order of 1 when pH_2O is held constant.

A.3.2 Hydrogen Absorption as a Rate-Limiting Step

For process limited by the absorption/desorption of hydrogen in the metal film,

$$r_{abs} = k_{abs} [H_{ads}] [I] = k_{dsb} [H_{abs}^{x=L}] [S] \quad (A.55)$$

Employing a similar procedure as in the previous section, that is, assuming all other steps reach equilibrium and using the site balances in (A.48) and (A.49), we obtain

$$[H_{ads}] = \frac{K_{ads}^{1/2} pH_2^{1/2} S_T}{1 + K_{ads}' pH_2O + K_{ads}^{1/2} pH_2^{1/2}} \quad (A.56)$$

and from the first equality in (A.55),

$$r_{abs} = k_{abs} \frac{S_T I_T}{1 + \left(\frac{1 + K_{ads}' pH_2O}{K_{ads}^{1/2} pH_2^{1/2}} \right)} \quad (A.57)$$

Unlike the case of adsorption as a rate-limiting step, both the pH_2 and pH_2O reaction orders cannot be explicitly extracted from a log-log plot of the rate as a function of partial pressure.

It should be noted that if water occupies none or a small fraction of the metal surface sites such that $S_T = [S] + [H_{ads}]$, one can obtain a much simpler expression for the rate of the reaction,

$$r_{abs} = S_T I_T k_{abs} K_{ads}^{1/2} pH_2^{1/2} \quad (A.58)$$

A.3.3 Hydrogen Diffusion as a Rate-Limiting Step

For the diffusion of hydrogen as the slowest step, we obtained

$$J = -D_H \frac{[H_{abs}^{x=0}] - [H_{abs}^{x=L}]}{L} = -\frac{D_H I_T}{L} \left(\frac{[H_{CDP}^+]}{K_{CT}} n - K_{abs} K_{ads}^{1/2} pH_2^{1/2} \right) \quad (A.59)$$

Therefore, the reaction rate when limited by diffusion is not directly proportional to $pH_2^{1/2}$. This is a consequence of the concentration of absorbed hydrogen in the metal at the metal | CsH_2PO_4 interface being fixed by the proton concentration of CsH_2PO_4 . (This

is in contrast to the rate of hydrogen diffusion in permeation membranes which exhibits a direct proportionality to $pH_2^{1/2}$ due to both sides of the metal being exposed to hydrogen gas.)

A.3.4 Charge Transfer as a Rate-Limiting Step

Following Equation (A.50), the rate of charge transfer near equilibrium is

$$r_{CT} = k_{ox} [H_{abs}^{x=0}] = k_{red} [H_{CDP}^+] n [I] \quad (A.60)$$

Using the appropriate equilibrium relations and site balances, we obtain the concentration of hydrogen in the metal at the metal | CsH_2PO_4 interface to be

$$[H_{abs}^{x=0}] = K_{abs} K_{ads}^{1/2} I_T pH_2^{1/2} \quad (A.61)$$

The rate of a process limited by charge transfer is then proportional to $pH_2^{1/2}$,

$$r_{CT} = k_{ox} K_{abs} K_{ads}^{1/2} I_T pH_2^{1/2} \quad (A.62)$$

Appendix B Reactivity of Candidate Electrocatalysts with CsH_2PO_4

B.1 Motivation

For low-temperature fuel cells, many metals exist as their oxides at open-circuit conditions and/or under operating voltages. Figure B.1 shows a list of metal oxides and the Gibbs free energy for their formation from their metals in air at 240 °C.⁸⁷ The corresponding equilibrium potentials, with respect to an air reference, are also shown. (To determine the corresponding potential for the cathode of a fuel cell, add the open-circuit voltage of ~ 1.1 V to the y-axis.) All metals above the zero line will be stable in air at open-circuit conditions of a fuel cell, whereas all metals below the zero line will be oxidized at open-circuit conditions. However, an applied voltage can change the state of the material (as demonstrated by the electrochemical reduction of Pt oxide in Chapter 3) and keep the metal as the thermodynamically preferred phase. For example, during fuel cell operation, typically at a cell voltage of ~ 0.7 V (or ~ -0.4 V in Figure B.1), metals that will be stable as oxides are all those residing above the -0.4 V line. Thus, thermodynamics predicts that PtO_2 , PtO , PdO , IrO_2 and Ir_2O_3 (Figure B.1 inset), while stable in a fuel cell at the open-circuit voltage, will be reduced when current is drawn and the cell operated at 0.7 V.

The state of the electrocatalyst under fuel cell operating potentials is important because it dictates how to construct experiments to screen for or study catalysts. For

example, in order to conduct fundamental studies of oxygen electro-reduction over Pt metal, a bias must be applied to the cell, and thus symmetric cell studies are not possible.

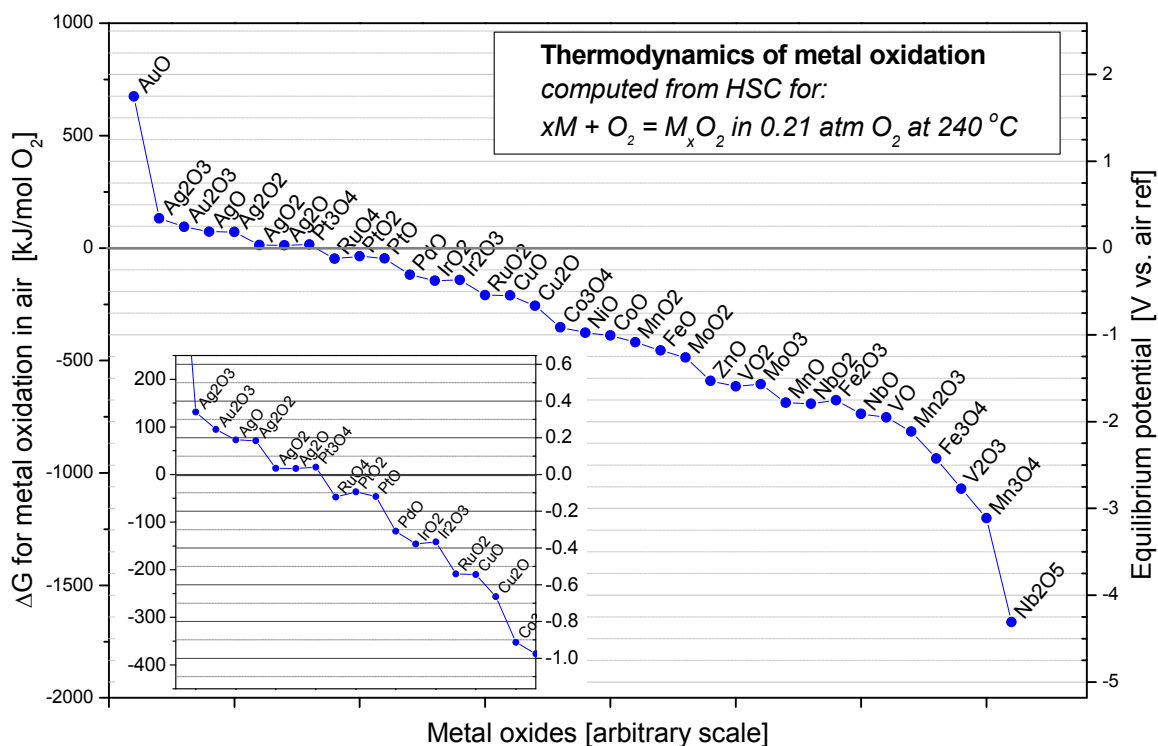


Figure B.1 Plot of Gibbs free energy for metal oxide formation at 240 °C in 0.21 atm O_2 for various metal oxides.

Both metals and metal oxides can be active electrocatalysts for reducing oxygen. However, some oxides have been observed in the laboratory to react with CsH_2PO_4 and thus would not be viable as electrocatalysts in SAFC electrodes. In this section, we summarize results of a study that evaluates the reactivity between potential electrocatalysts and CsH_2PO_4 . We also extend the investigation to metal carbides and nitrides.

B.2 Experimental

B.2.1 Sample Preparation and Heat Treatment

Course CsH_2PO_4 powders were mixed with metal or metal oxide powders (various sources and particle sizes) and a mortar and pestle, placed in a quartz (or Pyrex) cup and heated to various temperatures under humidified air flow (~ 0.4 atm H_2O). In some cases, the mixtures were characterized after heat treatment at 150°C for 48 h before heat treatment at 240°C to evaluate the effect of the superprotonic transition and kinetics on the reactivity of CsH_2PO_4 with the metal/oxide powders. Samples that did not exhibit reaction at 150°C were further heated at 240°C for times ranging between 5 and 41 h.

Metal nitrides and carbides were first tested for their resistance to oxidation by heating the powders in quartz (or Pyrex) cups at 240°C for 24–82 h under flowing air with ~ 0.4 atm H_2O . Those that did not exhibit signs of oxidation were mixed with CsH_2PO_4 and heated at similar conditions for 24 h.

B.2.2 Characterization

All powders and their mixtures, before and after heat treatment, were characterized by X-ray diffraction using a Phillips X'Pert Pro powder diffractometer with $\text{Cu K}\alpha$ radiation (45 kV, 40 mA) with a 2θ range of 5° to 90° .

B.3 Results and Discussion

Table B.1 tabulates all the oxide materials (with the exception of a tungstic acid which is not an oxide) tested under various conditions, as specified. In the case of the oxides, most products generated from the reaction were unidentified. Reaction products

which were identified are noted in the table. Bolded starting material names indicate compounds that did not appear to react with CsH_2PO_4 . Note that for Fe_3O_4 , all the CsH_2PO_4 peaks disappeared but there were no product peaks.

Table B.2 tabulates the oxidation stability of some nitrides and carbides and their reactivity with CsH_2PO_4 . Several of the carbides are readily oxidized in air, whereas almost all the nitrides tested were stable in air. Of the carbides, only TaC and ZrC appeared to be stable with CsH_2PO_4 . Of the nitrides, all exhibited no reaction with CsH_2PO_4 , with the exception of iron nitride.

It is important to note that the computed thermodynamic driving force for metal carbide oxidation, specifically for NbC, TaC and ZrC (no thermodynamic data was available for B_4C), indicates that these carbides are not stable in air (Figure B.2a). Their apparent resistance to oxidation is likely a consequence of a blocking oxide layer that kinetically limits further oxidation. This also would imply that it is this oxide surface that is relevant for electrocatalysis (and reactivity). However, the observed reactivity of NbC, which is expected to have a layer of oxide on top, after 24 h is surprising since no reaction of Nb_2O_5 with CsH_2PO_4 was observed after 36 h. The oxides of Ta and Zr were not available for testing, so it is unclear what the stability of TaC and ZrC with CsH_2PO_4 implies.

Metal nitrides are generally more stable in air than metal carbides, primarily because of the high partial pressures of nitrogen in air (0.27 atm N_2 compared to < 0.0005 atm). Thermodynamics predicts Fe_2N and Fe_4N are stable in air and, thus, it is unclear why oxidation of Fe_xN was observed.

Table B.1 Reactivity of CsH_2PO_4 (CDP) with metal oxides at various temperatures for as-specified times under flowing air with ~ 0.4 atm H_2O . Bolded means no reaction with CDP.

Starting material		150 °C, 48 h	240 °C, + 5 h		240 °C, + 36 h (unless otherwise noted)	
		<i>Rxn?</i>	<i>Rxn?</i>	<i>Product(s)</i>	<i>Rxn?</i>	<i>Product(s)</i>
aluminum oxide	Al_2O_3	N	N		Y	
silver(I) oxide	Ag_2O	Y	Y	AgPO_3	—	
copper(II) oxide	CuO	N	Y	unidentified	—	
zinc oxide	ZnO	Y	Y	CsZnPO_4 + unidentified	—	
nickel(II) oxide	NiO	N	N		N	
palladium	Pd	N	Y	unidentified	—	
ruthenium(IV) oxide	RuO_2	N	N		N	
cobalt(II,III) oxide	Co_3O_4	N	N		Y	unidentified
cobalt (II) oxide	CoO	N	Y	unidentified	—	
iron (III) oxide	Fe_2O_3	N	N		N	
iron(II,III) oxide	Fe_3O_4	N	N?	CDP peaks missing	N?	CDP peaks missing
molybdenum(VI) oxide	MoO_3	N	Y	unidentified	—	
molybdenum(IV) oxide	MoO_2	N	Y	one new peak unidentified	Y	unidentified
niobium(V) oxide	Nb_2O_5	N	N		N	
manganese(III) oxide	Mn_2O_3	N	Y	unidentified	—	
manganese(II) oxide	MnO	N	N		N (41 h)	
chromium(III) oxide	Cr_2O_3	N	—		—	
vanadium(V) oxide	V_2O_5	Y.	Y	CsHVPO_6 + unidentified	—	
titanium(IV) oxide	TiO_2	—	—		N (41 h)	
tin(IV) oxide	SnO_2	—	—		N (41 h)	
tungsten oxide	$\text{WO}_{2.9}$	—	—		Y (41 h)	
tungstic acid	H_2WO_4	—	—		Y (41 h)	
barium zirconate	BaZrO_3	N	Y	one new peak unidentified	—	

Table B.2 Reactivity of CsH_2PO_4 (CDP) with metal nitrides and carbides at 240 °C for as-specified times under flowing air with ~ 0.4 atm H_2O . Bolded means no reaction with CDP.

Starting material		240 °C, 24 h (unless otherwise noted)		240 °C, 24 h
		Oxidized?	Product(s)	Rxn w/ CDP?
boron carbide	B_4C	N		Y
tungsten carbide	WC	Y (34 h)	WO_3	—
tungsten carbide	W_2C	Y (34 h)	WO_3	—
molybdenum carbide	Mo_2C	Y	MoO_3	—
niobium carbide	NbC	N		Y
tantalum carbide	TaC	N		N
vanadium carbide	VC	Y (82 h)	V_2O_5	—
titanium carbide	TiC	Y	TiO_2 anatase	—
zirconium carbide	ZrC	N		N
iron nitride	Fe_xN	N		Y
niobium nitride	NbN	N		N
tantalum nitride	TaN	N		N
titanium nitride	TiN	N		N
zirconium nitride	ZrN	N		N

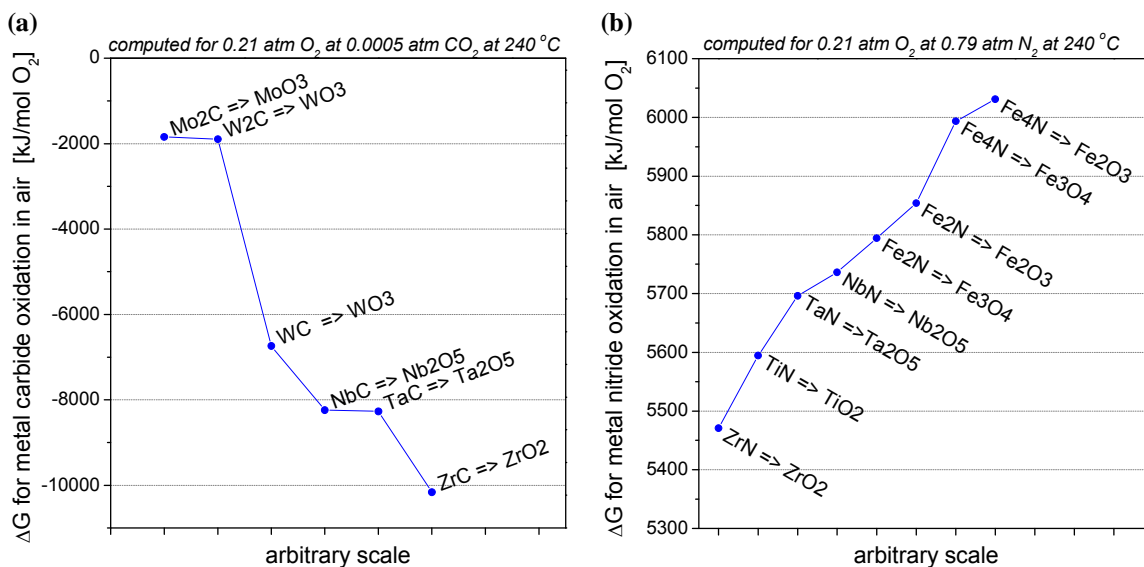


Figure B.2 Stability of select metal carbides and nitrides in air at 240 °C. The Gibbs free energy of oxidation of metal (a) carbides and (b) nitrides. Metal carbides are thermodynamically unstable while metal nitrides are stable.

Appendix C Platinum Thin Film Anodes

C.1 Experimental Setup

Figure C.1 is a schematic of the experimental setup used for symmetric cell studies. The flow rates of gases (H_2 and Ar, in this case) are controlled by digital mass flow controllers (Advanced Energy, 7800 series). Inlet gases were fed into a water bubbler, heated by a gravity convection oven. The resulting humidified flow is delivered to the reactor chamber via stainless steel pipes heated by rope heaters to prevent condensation. At the outlet, water vapor is condensed in a trap (not shown) before the gas stream is vented. The water partial pressure of the gas stream is recorded at the inlet of the reactor. The flow rates of the gases were calibrated using a bubble flow meter.

Three symmetric cell holders are available for multiplexed measurements. A schematic of the holder is shown in the inset of Figure C.1. Cells are placed between two silver ring contacts which in turn are connected to electrical leads (two on each ring for four-probe configuration). A thermocouple is located ~ 3 mm from the cell to monitor the temperature.

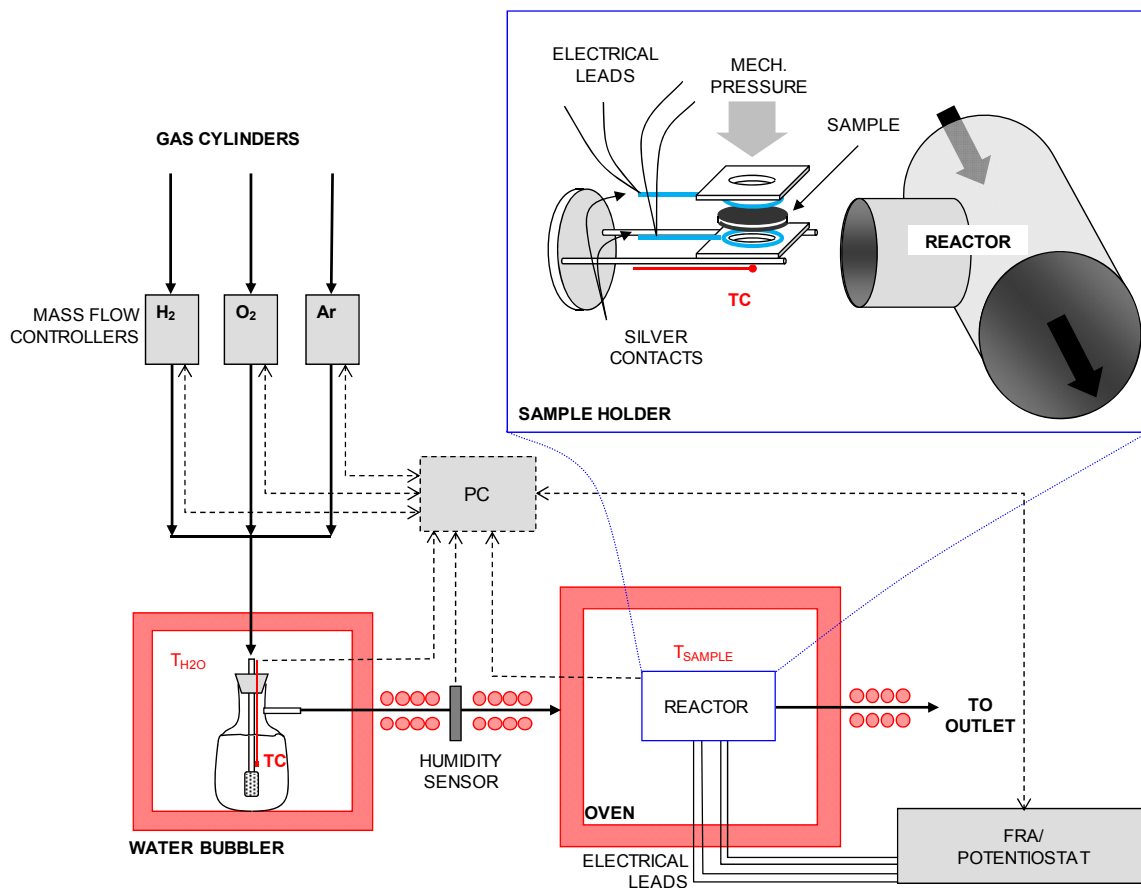


Figure C.1 Drawing of test station for symmetric cell measurements.

C.2 Platinum Film Quality

C.2.1 Before and After Electrochemical Characterization

After electrochemical testing at 250 °C in H₂-H₂O-Ar environments, Pt films with thicknesses ≥ 7.5 nm remain intact for the most part, as shown in before-after images of 375, 75, and 7.5 nm thick films (Figure C.2, Figure C.3, Figure C.4, respectively). Also shown are images of 7.5, 22.5, 37.5, and 52.5 nm thick films after testing (Figure C.5). Of these four films, 7.5 and 22.5 nm thick films exhibit wave-like features, Figure

C.4(c–d) and Figure C.5(a–b), possibly because the films accommodate microstructural changes in CsH_2PO_4 substrate without breaking.

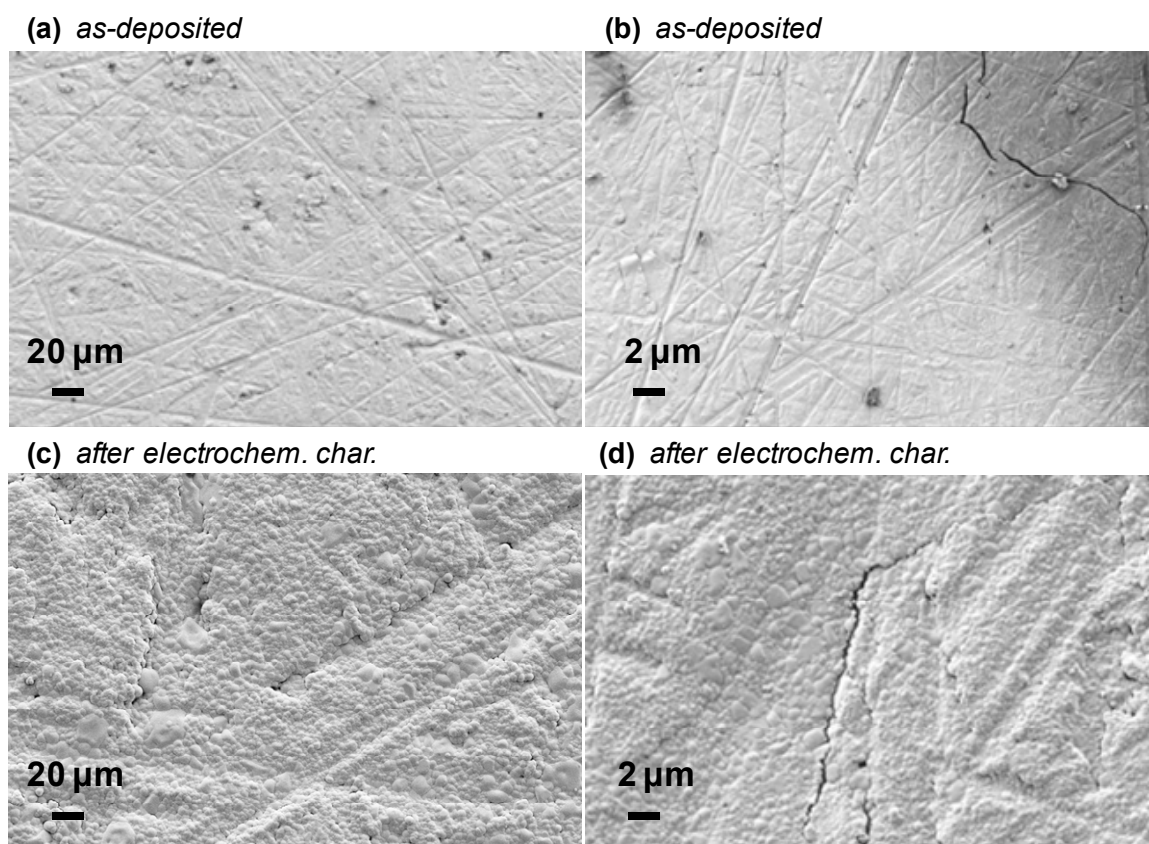


Figure C.2 Representative SEM micrographs of 375 nm Pt films on top of CsH_2PO_4 before (a–b) and after (c–d) electrochemical characterization at 250 °C in H_2 - H_2O -Ar atmospheres. The Pt- CsH_2PO_4 boundary is visible in (b) in which the darker region is the exposed CsH_2PO_4 .

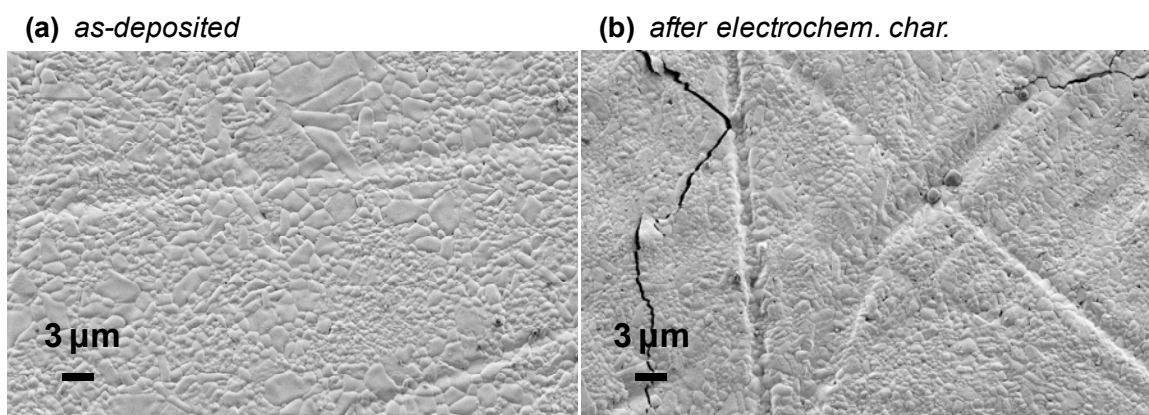


Figure C.3 Representative SEM micrographs of 75 nm Pt films on top of CsH_2PO_4 , before (a) and after (b) electrochemical characterization at 250 °C in H_2 - H_2O -Ar atmospheres. Films with either 10 nm Au on top of or below the Pt film display similar film characteristics.

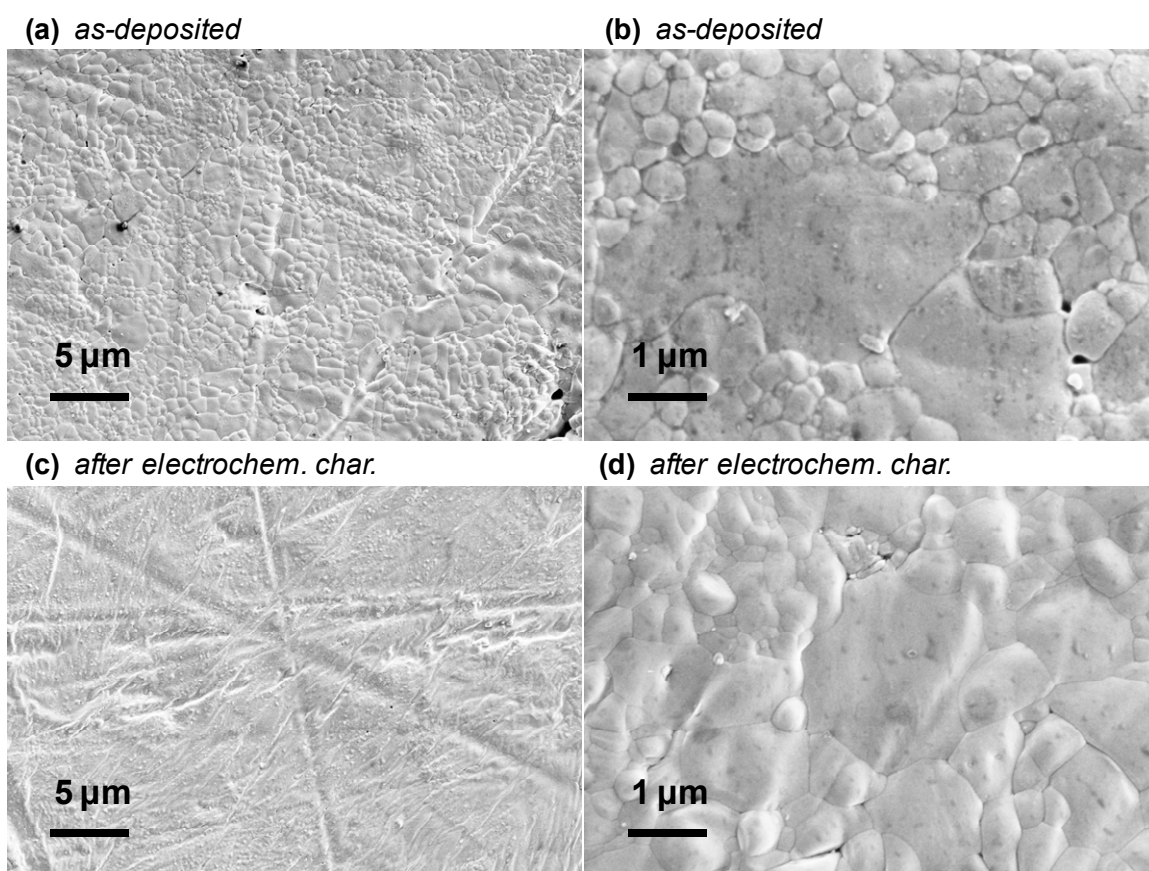


Figure C.4 Representative SEM micrographs of 7.5 nm Pt films on top of CsH_2PO_4 , before (a–b) and after (c–d) electrochemical characterization at 250 °C in H_2 - H_2O -Ar atmospheres.

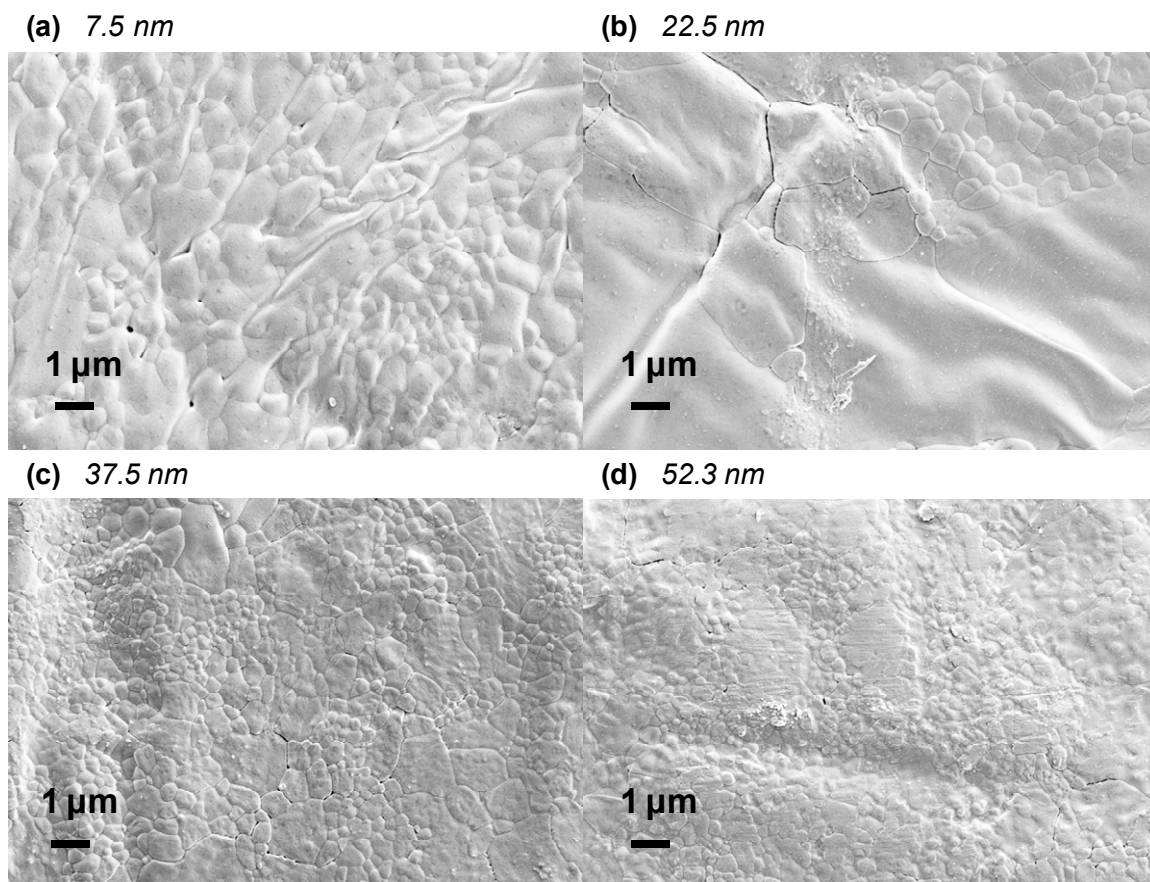


Figure C.5 Representative SEM micrographs of (a) 7.5 nm, (b) 22.5 nm, (c) 37.5 nm and (d) 52.5 nm Pt films on top of CsH_2PO_4 after electrochemical characterization at 250 °C in H_2 - H_2O -Ar atmospheres.

C.2.2 Film Structure and Impedance Response of Sub-5 nm Films

The observation of the electrode response for 7.5 nm films being co-limited by multiple processes, that is, diffusion of hydrogen and one (or more) interfacial processes suggests that further reducing the film thickness should give additional reduction in the electrode resistance. Unfortunately, Pt films before and after testing clearly revealed that intact, conformal, as-deposited Pt films degrade after electrochemical testing at superprotonic conditions. SEM micrographs for as-deposited 1.5, 3, and 4.5 nm films appear to be fully intact as indicated by the undersides of the films, Figure C.6(a–c). In

these images, cracks in the film are due to the fragility of the films when removing them from their substrates, and white spherical particles, particularly visible in Figure C.6(a,c) are precipitated CsH_2PO_4 particles formed as a result of substrate dissolution processes. The films examined after electrochemical characterization, Figure C.6(d–f), show different characteristics depending on the film thickness. 4.5 nm films (Figure C.6d) appeared relatively intact after electrochemical characterization, with a few microcracks occurring near the grain boundaries of CsH_2PO_4 (inset) and features that appear to be folds and creases in the film, whereas 1.5 nm films (Figure C.6f) aggregated into small islands of different sizes, from 500 nm to below 50 nm (inset). Although temperatures around 250 °C are not high enough to induce the sintering of Pt metal, the mobile and ductile solid acid substrate,^{17, 19, 28} combined with the extremely thin Pt layers deposited, may enable the migration of Pt species on the substrate surface. The film characteristics of the sub-5 nm films are in agreement with the sheet resistance of the films before and after electrochemical characterization, that is, the sheet resistance of the 1.5 and 3 nm films increase by almost three-fold after testing. As expected, based on Figure C.6d, the sheet resistance of the 4.5 nm films after testing increased only slightly, comparable to that observed for 7.5 nm films.

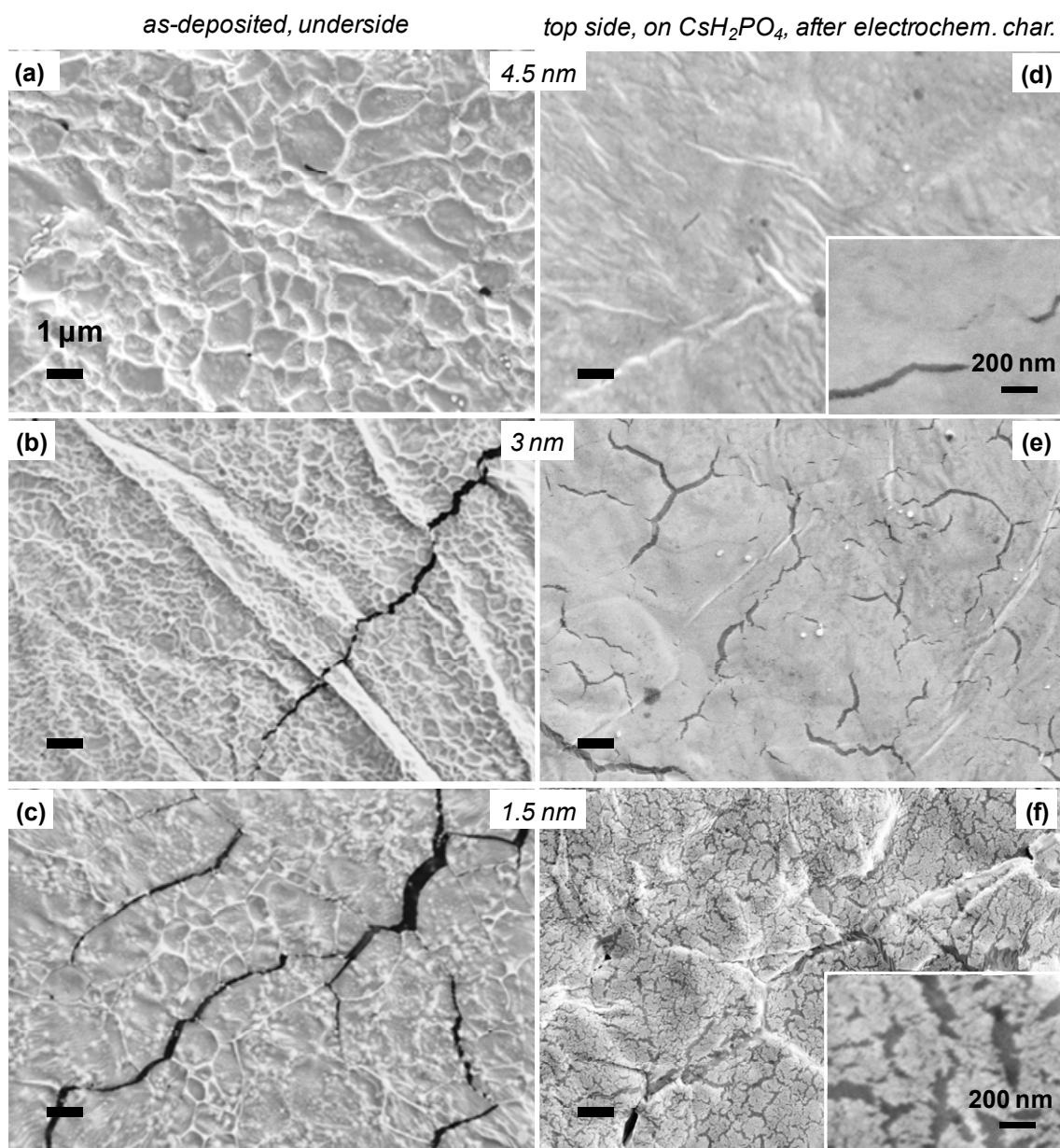


Figure C.6 SEM micrographs of sub-5 nm thin Pt films: (a–c) Undersides of Pt films, isolated from their CsH_2PO_4 substrates, before electrochemical characterization, showing that the films conformed to the features of the CsH_2PO_4 substrate. Large cracks in the films are a consequence of the removal process. (d–f) Pt on CsH_2PO_4 , after testing. Light gray = Pt, dark gray = exposed CsH_2PO_4 substrate

Pt films below 5 nm in thickness yield impedance spectra similar in shape to that for 7.5 nm films, that is, an arc is that more symmetric (Figure C.7a). However, the electrode resistance increases with decreasing film thickness, from $\sim 4 \Omega \text{ cm}^2$ for a Pt

film thickness of 4.5 nm to almost $10 \Omega \text{ cm}^2$ for a thickness of 1.5 nm. This is counter to the expectation that as the Pt film thickness is decreased, the diffusion step becomes negligible compared to interfacial processes, and the total electrode resistance should approach an interfacial resistance value of $2.2 \Omega \text{ cm}^2$ (Figure 3.12). As shown in Figure C.7b, the resistances of 1.5, 3, and 4.5 nm Pt films are larger than predicted (solid curve). For 1.5 and 3 nm thick films, this observation is consistent with SEM observations of the degrading film quality (Figure C.6) and suggests that degradation of the film into small islands reduces the utilization of Pt. The degradation in activity for the 4.5 nm film electrode was surprising given its apparent structural stability (Figure C.6d).

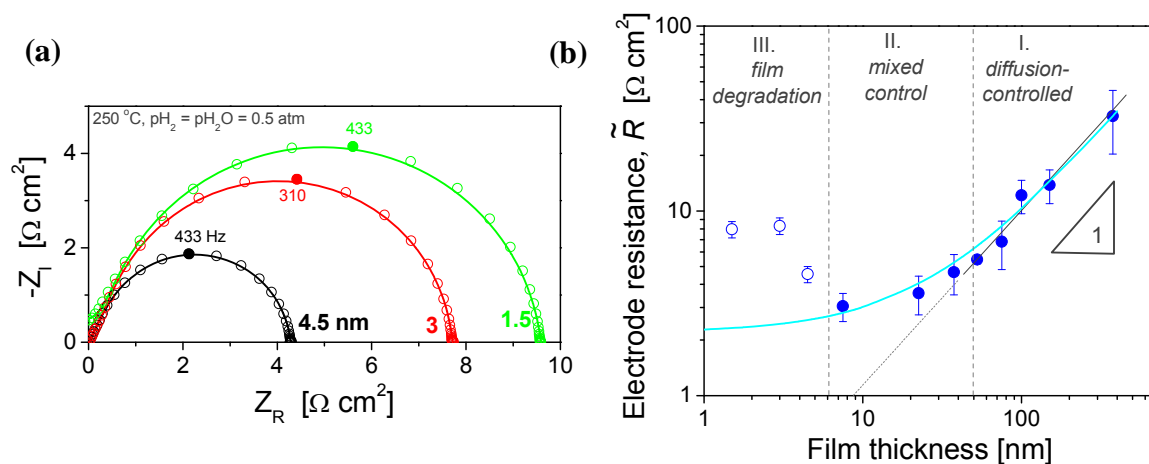


Figure C.7 (a) Nyquist spectra for 1.5, 3, and 4.5 nm thick Pt film electrodes in Pt | CsH_2PO_4 | Pt symmetric cells, showing semi-circular arcs which increased in width with decreasing film thickness. Lines show fits parallel RQ sub-circuits. Non-electrode responses have been subtracted. (b) Double-logarithmic plot of area-normalized electrode resistance as a function of Pt film thickness. Filled data markers are for films which remained intact during electrochemical testing. Open data markers are for 1.5, 3, and 4.5 nm Pt films.

Despite the differences in the resistance values for 1.5–4.5 nm films, the characteristic frequencies displayed no observable trend with thickness and, across six

samples (two for each thickness), the average characteristic frequency was found to be $\omega_0 = 2.6 \pm 0.7$ kHz. The temperature and $p\text{H}_2$ dependences also displayed no trend with thickness; the $p\text{H}_2$ reaction order ranged between 0.68 and 0.79 and activation energies were ~ 33 kJ mol⁻¹, values which are comparable to those observed for 7.5 nm films (~ 0.75 and 28 kJ mol⁻¹ from Figure 3.8). That the characteristic frequency, $p\text{H}_2$ reaction order and activation energy are virtually unchanged between films with thicknesses of 1.5–7.5 nm suggests that, despite larger electrode resistances and notably different microstructures for sub-5 nm films, the rate-limiting step is the same as that for the 7.5 nm film. In other words, the larger electrode resistance is purely a consequence of the decrease in interfacial Pt | CsH₂PO₄ area due to film degradation; the small islands (under 500 nm in size) are too small to be accessible by the 100- μm scale features of carbon current collector, resulting in poor utilization of the deposited Pt.

It is interesting to note that the stabilization time for 1.5–4 nm thick Pt films at superprotonic conditions were notably longer than that for thicker films, taking over two days instead of approximately one day to reach a steady-state conditions satisfying the criterion of $\leq 2\%$ h⁻¹ change in the electrode resistance. The longer stabilization times indicate that Pt in the thinnest films was able to migrate freely whereas thick films appeared not to be affected by the substrate and were significantly more stable.

C.2.3 Mechanical Integrity: 375 nm vs. Sub-8 nm Films

Additional images of the undersides of 4.5 and 7.5 nm films (Figure C.8) appear to confirm the accommodating nature of the Pt; thin Pt films conformed to the underlying carbon tape substrate which was attached to the top side of the film before dissolution of CsH₂PO₄. The underlying features of the carbon tape are visible as mounds (10–50 μm)

in the image, and furthermore, the film exhibited wrinkles as it conformed the features of the carbon tape. Films that were very thin, such as those 1.5 and 3 nm thick (Figure C.9), were more fragile and display many more tears from handling, when compared to 4.5 and 7.5 nm films. This fragility may be correlated with their tendency to aggregate into islands after testing (Figure C.6), that is, the poor interconnectivity of the Pt grains and minimal pinning of grains to neighbors allow its free migration over the CsH_2PO_4 surface at superprotonic conditions.

On the other hand, thicker films tended to be stronger, as indicated by Figure C.10, but sometimes buckled when the underlying CsH_2PO_4 moved. Buckling was observed for 375 nm films (Figure C.11), and the spatial distribution of buckling is consistent with cracking of the CsH_2PO_4 substrate, that is, when there is a crack in CsH_2PO_4 , the two sides of CsH_2PO_4 can move in such a way as to cause the films to delaminate and compress. The film typically broke at weaker points of the film, primarily along polishing lines. Because buckling occurred on the 100- μm scale and with relative low density, they did not affect the shape of the impedance arc, i.e., the half-teardrop shape characteristic of diffusion (Figure 3.6a). That the Warburg behavior remained suggests that the rate-limiting step was still hydrogen diffusion through the Pt film, although the total resistance of the process likely increased a small amount due to the lower Pt | CsH_2PO_4 interfacial area. Furthermore, buckling effects may also explain the frequency dispersion observed in the Warburg impedance response, that is, a deviation of n from 0.5 in the distributed finite-length Warburg expression (Equation 3.1).

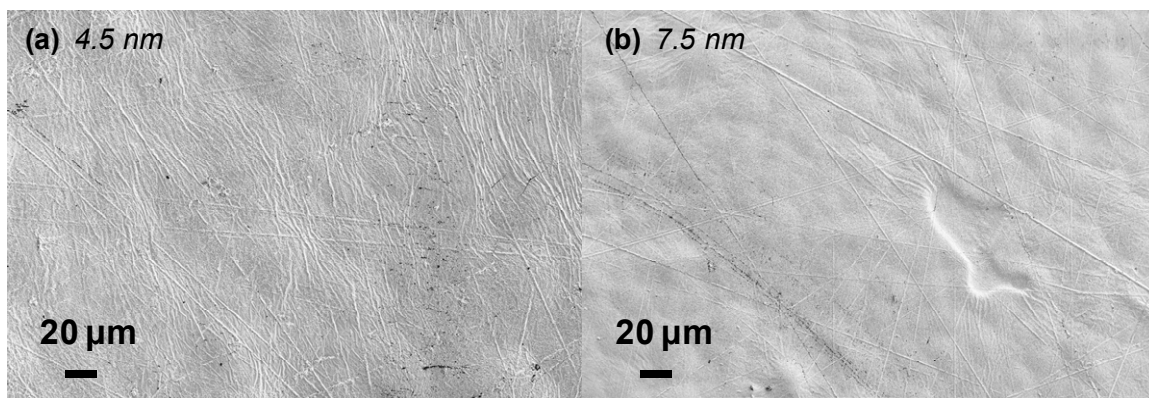


Figure C.8 SEM micrographs of the undersides of (a) 4.5 and (b) 7.5 nm films, as deposited, isolated from the CsH_2PO_4 substrate. Films conformed to the underlying carbon tape.

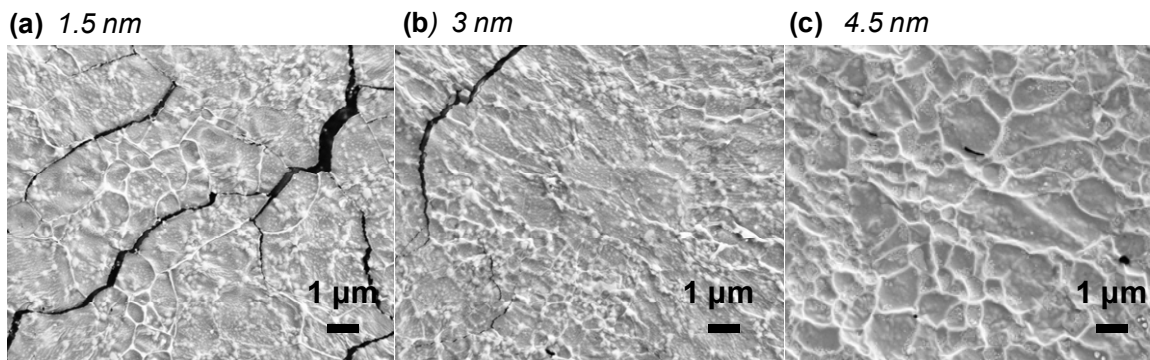


Figure C.9 Representative SEM micrographs of the undersides of 1.5, 3, and 4.5 nm films, as-deposited and isolated from their CsH_2PO_4 substrates. Cracks in the films resulted from handling. Small sub-micron light-gray features are imprints from the underlying carbon tape substrate, visible through the very thin films. For the 4.5 nm film (c), sub-100 nm precipitates of CsH_2PO_4 were also visible.

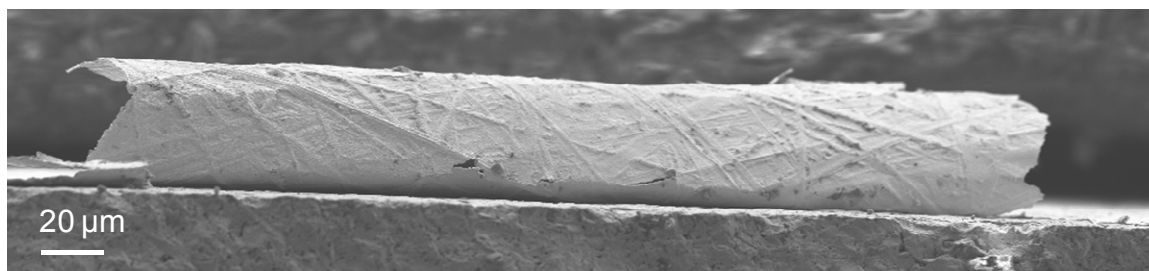


Figure C.10 A cross-section image of the Pt | CsH_2PO_4 interface where a portion of a 375 nm Pt film had delaminated.

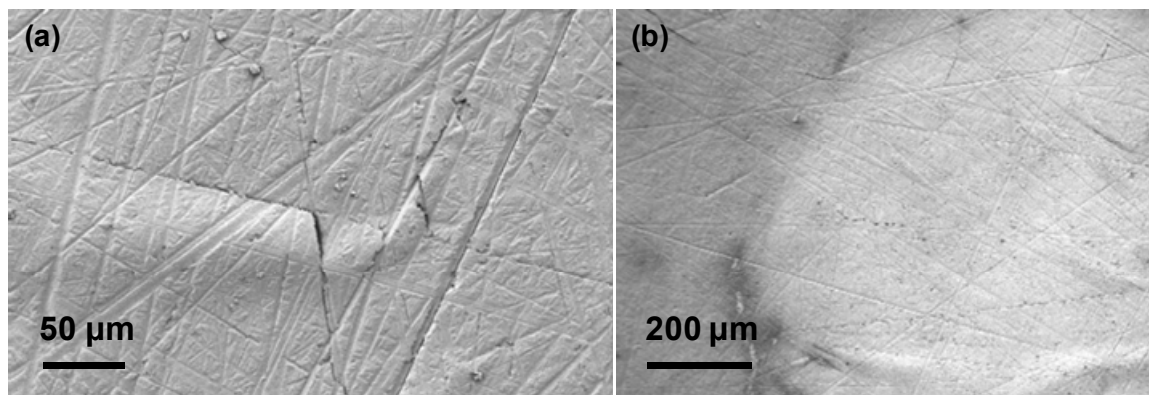


Figure C.11 SEM micrographs of a 375 nm Pt film deposited onto CsH_2PO_4 , after electrochemical testing. Buckling occurred on the 100- μm scale, ending at polishing lines (left). The distribution of features suggests they are correlated to cracks in the CsH_2PO_4 substrate (right).

C.2.4 Effect of Mechanical Pressure from Current Collector

It should be noted that the quality of the films, on the micron-scale, depended on the mechanical pressure applied to the symmetric cells using the sample holder shown in Figure C.1. A pressure that is too low caused a metal-metal contact that fluctuated with external vibrations (e.g., that form the mechanical convection oven used to heat the reactor). For films which had sufficient sheet conductivity (i.e., films 7.5 nm and thicker), this only caused the ohmic offset in the impedance spectra to jump intermittently and did not affect the electrode response. However, applying too much pressure caused damage to the cell since superprotonic CsH_2PO_4 deforms under pressure. From Figure C.12, comparing (a) and (c) for 7.5 nm films, it is apparent that the effect of applied mechanical pressure is significant. The carbon fiber paper current collector left a significant number of fiber imprints in the cell (a), but when the pressure was reduced, the film was much less damaged (b). The extent of damage depended not only on the pressure applied but also on the Pt film thickness. Comparison of (a) and (b) for 7.5 nm films to (c) and (d) for

75 and 150 nm films, respectively, in Figure C.12 reveals that a greater amount of damage was incurred for thinner films than thicker films. There was not a significant impact of the applied pressure on the electrode response of the cell, but the damage, in any case, should be kept to a minimum. (A systematic way to do this is to measure the resistance across the electrical leads when the cell is loaded and apply the minimum amount of pressure needed to register a finite resistance value the cell. This method works for diameters 10 mm and greater, otherwise the resistance is too high to be measured by a hand-held multimeter, regardless of the pressure.)

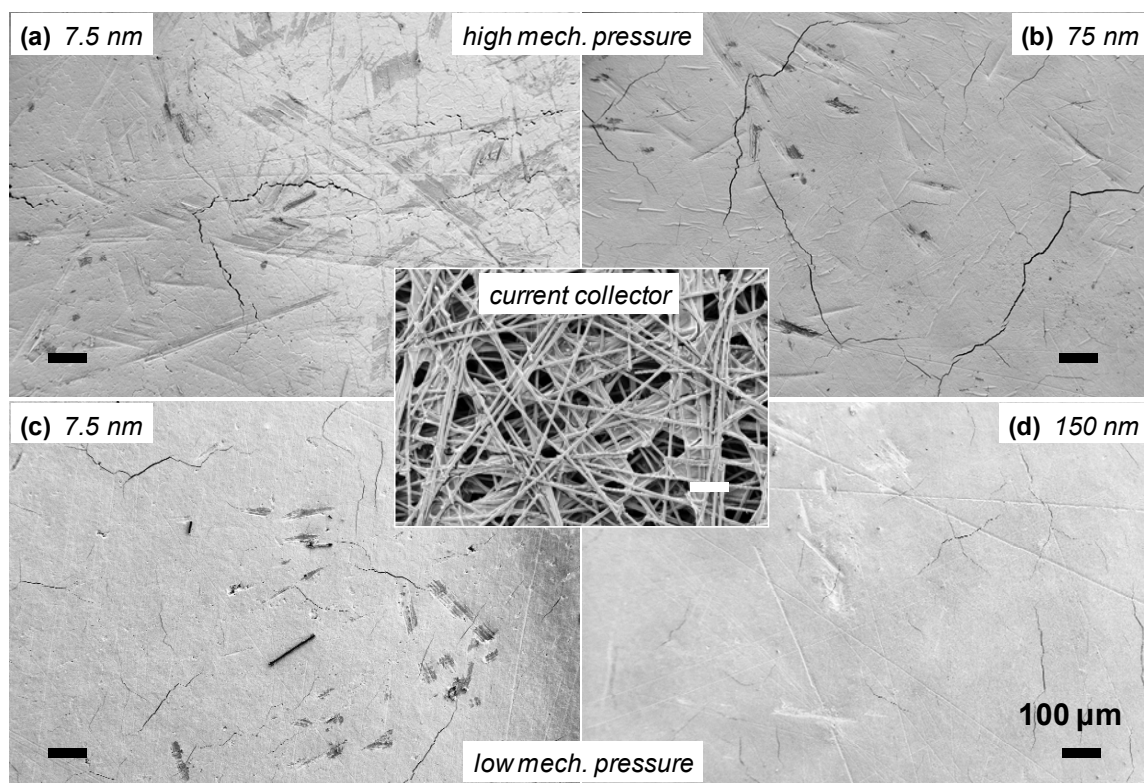


Figure C.12 Pt film quality, after electrochemical characterization, as a function of film thickness and mechanical pressure applied to the cell. (a) and (b) show 7.5 and 75 nm films, respectively, with a relatively high pressure applied. (c) and (d) show 7.5 and 150 nm films, respectively, with a relatively low pressure applied. The center image, shown for the same magnification as (a–d), displays the structure of the carbon fiber paper that was in contact with the cell as a current collector during electrochemical characterization.

C.3 Non-electrode Impedance Responses

C.3.1 *Origin of Spurious Electrical Effects*

When studying electrode reactions in electrochemical cells, it is necessary to consider spurious contributions to the electrical response. For Pt | CsH₂PO₄ | Pt symmetric cell measurements, inductance contributions from electrical lead wires as well as from instrumentation (e.g., FRA, multiplexer, etc.) are present. The presence of inductance effects can be confirmed by first running a short correction (i.e., with no sample and the electrical leads shorted together). Correction of the raw data can be carried out in one of two ways. If the short correction is adequately represented by the inductor element, then raw experimental data can be corrected by subtract the term $Z_L = i\omega L$ (where L is the inductance value obtained by fitting the short correction data) from the imaginary portion of the data. This was the procedure employed, in this case. If the short correction has other unknown contributions, a point-wise correction would be preferred.

While the contribution of inductance is rather common in electrical measurements, the presence of constriction effects is less frequently addressed. Figure C.13 shows a schematic of the Pt | CsH₂PO₄ | Pt cell and the source of constriction. At extremely high frequencies of voltage perturbation, protons migrate through CsH₂PO₄ with a cross-sectional area that corresponds to the diameter of the CsH₂PO₄ disc. As the frequency is decreased, protons begin to interact with the Pt | CsH₂PO₄ and C | CsH₂PO₄ interfaces, where C denotes the carbon current collector. Because the electrochemical activity of Pt is higher than that of carbon, protons will preferential pass through the Pt | CsH₂PO₄ interface. The resistance associated with the high-frequency constriction arc

is attributed to the additional distance that protons must travel to reach the Pt film edge, while the capacitance is due to that at $C | CsH_2PO_4$. Symmetric cell measurements of $C | CsH_2PO_4 | C$ gives an interfacial capacitance for the $C | CsH_2PO_4$ interface of $\sim 3 \mu F cm^{-2}$ compared to $1.1 \pm 1.9 \mu F cm^{-2}$ for the constriction arcs observed in the impedance spectra for $Pt | CsH_2PO_4 | Pt$ cells with 5–13 mm dia. Pt films.

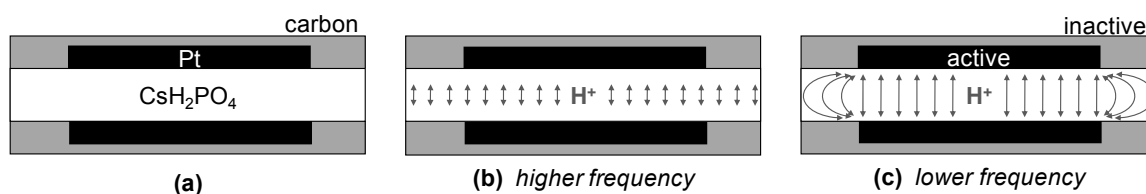


Figure C.13 The constriction effect: (a) no voltage perturbation, (b) high perturbation frequencies at which proton conduction occurs throughout the entire cross-section of CsH_2PO_4 , and (c) intermediate frequencies at which protons must pass through a cross-sectional area corresponding to the Pt film area.

C.3.2 Appearance of Constriction Effect

Whether or not the high-frequency constriction arc is visible during an impedance measurement appears to be a function of several parameters. Figure C.14 shows a 19 mm diameter cell with a 10 mm diameter Pt film (75 nm thick) measured using two different frequency response analyzer units, a Solartron Analytical 1250 frequency response analyzer (FRA) coupled to a Princeton Applied Research 273A potentiostat and a Solartron Analytical 1260 FRA. Because the electrical leads in the experimental setup run through a multiplexing unit, the Solartron 1250 (which has a three-probe configuration) gave higher ohmic offsets and higher inductance. The Solartron 1260 has a four-probe configuration and thus minimizes wire inductance and resistance contributions.

The size of the high-frequency arc increased with decreasing film diameters, as shown in the second column of Figure C.17. The resistance of the high-frequency arc (extracted from raw, un-normalized data) was 1.5, 2.6, and 14 Ω for film diameters of 12.6, 10, and 5 mm, respectively. This observation is consistent with constriction; as the film diameter is decreased, the constriction arc increases as the protons in CsH_2PO_4 must travel a greater distance to reach the edge of the Pt film.

When sufficient mechanical pressure was applied such that intimate contact was made between the carbon paper and the CsH_2PO_4 disc, a semi-circular arc appeared at high frequencies. It was observed that when a lower pressure was applied to the cell, the arc decreased in size or disappeared altogether. One explanation for this is that the nature of the $\text{C} | \text{CsH}_2\text{PO}_4$ interface was changed, that is, the capacitance of this interface contained additional contributions from the gas environment due to the increased spacing between the carbon paper and CsH_2PO_4 . In any case, the combined effect of mechanical pressure, film diameter and choice of instrumentation can make the appearance of the constriction arc seem rather sporadic and irreproducible, and thus some care must be taken when trying to determine whether a constriction effect exists.

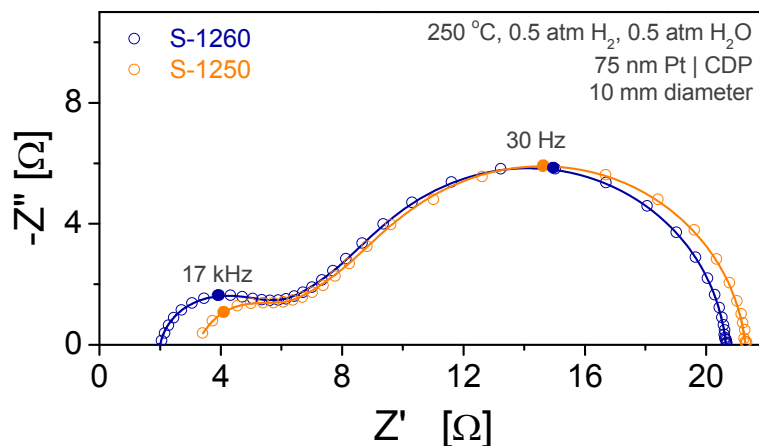


Figure C.14 Impedance response of a Pt | CsH₂PO₄ | Pt symmetric cell measured using two different frequency response analyzers (FRAs). Measurement with the Solartron 1250 FRA (coupled to a potentiostat) results in a higher inductance effect than that with the Solartron 1260 FRA.

C.3.3 Evidence of Constriction Effect

Several observations support the identification of the high-frequency arc in Figure C.14 as that resulting from the constriction phenomenon. As shown in the second column of Figure C.17(b–d) for the Au-Pt layered electrode system, the addition of Au in any configuration did not impact the high-frequency arc, as indicated by the almost perfect overlap of the spectra at high frequencies. This is to be expected, since the configuration of the electrode should not influence constriction.

Since the origin of the constriction arc is due to confinement of proton transport to the Pt | CsH₂PO₄ interface, it is to be expected that the conductivity of CsH₂PO₄ can be extracted using the appropriate impedance characteristics and cell geometry. That is, from Figure C.13b, the ohmic offset at high frequencies corresponds to proton conduction through the entire area of the CsH₂PO₄ disc, whereas the total resistance (offset resistance together with the resistance of the high-frequency arc) corresponds to proton transport

through a reduced cross-sectional area, roughly approximated by the Pt film area (Figure C.13c), that is,

$$\sigma_{offset} = \frac{L_{CDP}}{R_{offset} A_{CDP}} \quad (C.1)$$

$$\sigma_{constrict} = \frac{L_{CDP}}{(R_{offset} + R_{HF}) A_{Pt}} \quad (C.2)$$

Where σ_{offset} is the conductivity calculated (in the cases where a high-frequency arc surfaces) from the ohmic offset of the impedance, R_{offset} , and the area of the 19 mm CsH_2PO_4 disc, while $\sigma_{constrict}$ is the conductivity calculated from the ohmic offset and the resistance of the high-frequency arc, R_{HF} . From averaging over all the cells that displayed a reliable constriction arc (specifically, those with of 5–12.6 mm diameter Pt films and measured using the Solartron 1260 FRA with sufficiently high mechanical pressure applied to the cells), 15 cells in total, the value calculated for σ_{offset} was $1.8 \pm 0.6 \times 10^{-2} \text{ S cm}^{-1}$ at 250 °C. From all cells in which sufficient pressure was applied (such that there was no erratic jumps in the ohmic offset, as discussed in C.2.4), $\sigma_{constrict}$ was found to be $2.3 \pm 0.7 \times 10^{-2} \text{ S cm}^{-1}$ at 250 °C. These values are consistent with that reported for proton transport in CsH_2PO_4 , $2.2 \times 10^{-2} \text{ S cm}^{-1}$ at 240 °C.¹⁰

The dependence of the high-frequency arc on environmental parameters, such as gas partial pressure and temperature, provides additional support of the constriction phenomenon. As the hydrogen partial pressure is decreased, the low-frequency electrode arc (half-teardrop shape) increases in resistance, as expected (Figure C.15). In contrast, the high-frequency arc and the ohmic offset are unchanged, with the arcs perfectly overlapping with one another as the gas environment is varied. Similar observations are

made for when the water partial pressure was varied (not shown). The observation of the p_{H_2} and p_{H_2O} reaction orders of zero for R_{HF} and R_{offset} is consistent with the behavior of CsH_2PO_4 , that is, the migration of protons in CsH_2PO_4 does not depend on the gas composition. Furthermore, the temperature dependence of the high-frequency arc is, to within error, the same as that for the ohmic offset (Figure C.16). Activation energies of 41 and 38 kJ mol^{-1} for R_{HF} and R_{offset} , respectively, agree with values for proton migration in superprotonic CsH_2PO_4 , 40 kJ mol^{-1} (0.42 eV).¹⁰

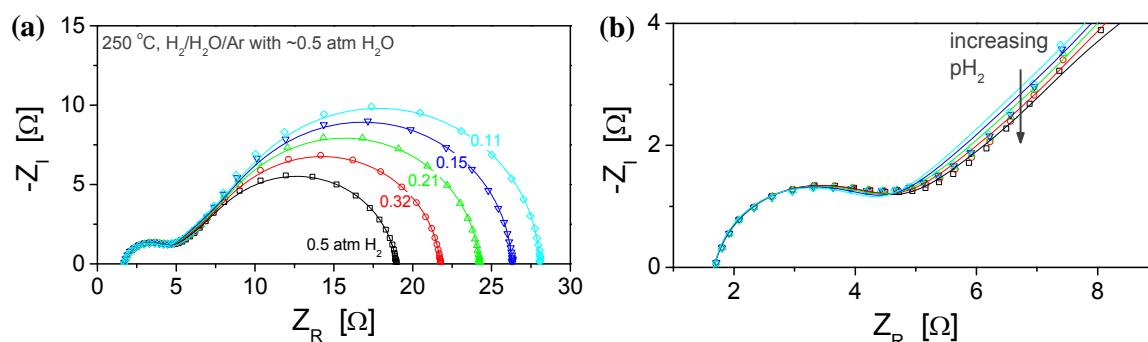


Figure C.15 Representative impedance spectra for a Pt | CsH₂PO₄ | Pt cell that (a) displays both an electrode response (a half-teardrop for a 75 nm thick and 10 mm diameter Pt film) and a high-frequency arc. (b) The hydrogen partial pressure has no effect on the ohmic offset and the high-frequency arc.

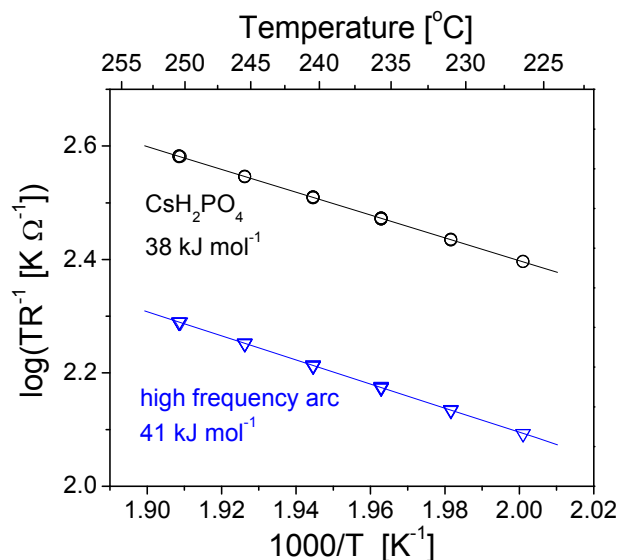


Figure C.16 Temperature dependence of the ohmic offset (CsH₂PO₄) and the width of the high-frequency arc. $p_{\text{H}_2} \approx p_{\text{H}_2\text{O}} \approx 0.5$ atm

C.4 Layered Pt-Au Film Electrodes

As discussed in Chapter 3, employing films of a catalytically inactive materials such as gold can be used to further probe the hydrogen electro-oxidation mechanism in the metal | CsH₂PO₄ system. In this section, we report additional geometries of Pt-Au films examined under uniform H₂-H₂O environments.

Figure C.17 and Table C.1 summarizes the results of the various Pt-Au geometries examined. Ignoring the high-frequency constriction arc visible in Figure C.17(b–c), it is immediately clear that the electrode configurations shown in Figure C.17(a–c) retained the 45° regime attributed to diffusion, indicating that diffusion through the Pt film is still the preferred pathway for hydrogen oxidation. However, the presence of the large blocking arc at intermediate-to-low frequencies indicates that Au has a significant impact on the total electrode resistance. Configurations (a) and (b) in Figure C.17 and Table C.1 show the effect of the Au film thickness at the metal | gas interface.

When the Au film thickness was increased from (nominally) 10 nm to 50 nm, the blocking arc increased approximately four-fold in width. The characteristic frequency dropped, but the capacitances of the two arcs were comparable, indicating that the change in the characteristic frequency of the process is a consequence of the change in the resistance rather than the capacitance of the process. All other parameters, including gas partial pressure dependences and activation energies were comparable. Although the increase in the resistance of the blocking arc with film thickness indicates diffusion through Au as the corresponding process, it is important to keep in mind that the coverage of the Pt surface using 10 nm Au may be poor and, therefore, the smaller resistance associated with the 10 nm blocking films may be due to partially exposed Pt.

To probe the surface activity of the metal|gas interface, we compared configurations (b) and (c) in Figure C.17 and Table C.1. Adding a 7.5 nm Pt layer on top of a Au | Pt | CsH₂PO₄ cell resulted in a decrease in the resistance, almost by a factor of two. The capacitance increased while the characteristic frequencies were virtually unchanged. The partial pressure dependences and the activation energies were comparable between the two configurations. The observation that the resistance of the process improved only by a factor of two indicates that the Au | gas interface was likely not the rate-limiting step in (b) since we expect the surface activity at Pt | gas to be significantly greater than that at Au | gas. Furthermore, the comparable characteristic frequencies between (b) and (c) also suggest that the rate-limiting step has not changed.

Unlike configurations (a–c), configuration (d), i.e., Pt | Au | CsH₂PO₄, did not display the 45° regime (characteristic of diffusion) at high frequencies. This implies that the arc generated as a result adding Au can be attributed to a process occurring at either

the Au | CsH₂PO₄ or Au | Pt interface. Compared to configuration (a) in which 10 nm Au was placed at the metal | gas interface, Au at the metal | CsH₂PO₄ interface, configuration (d), displayed a characteristic frequency that was over one order of magnitude larger. The resistances of their blocking arcs were comparable, indicating that the characteristic frequency difference results from capacitive differences.

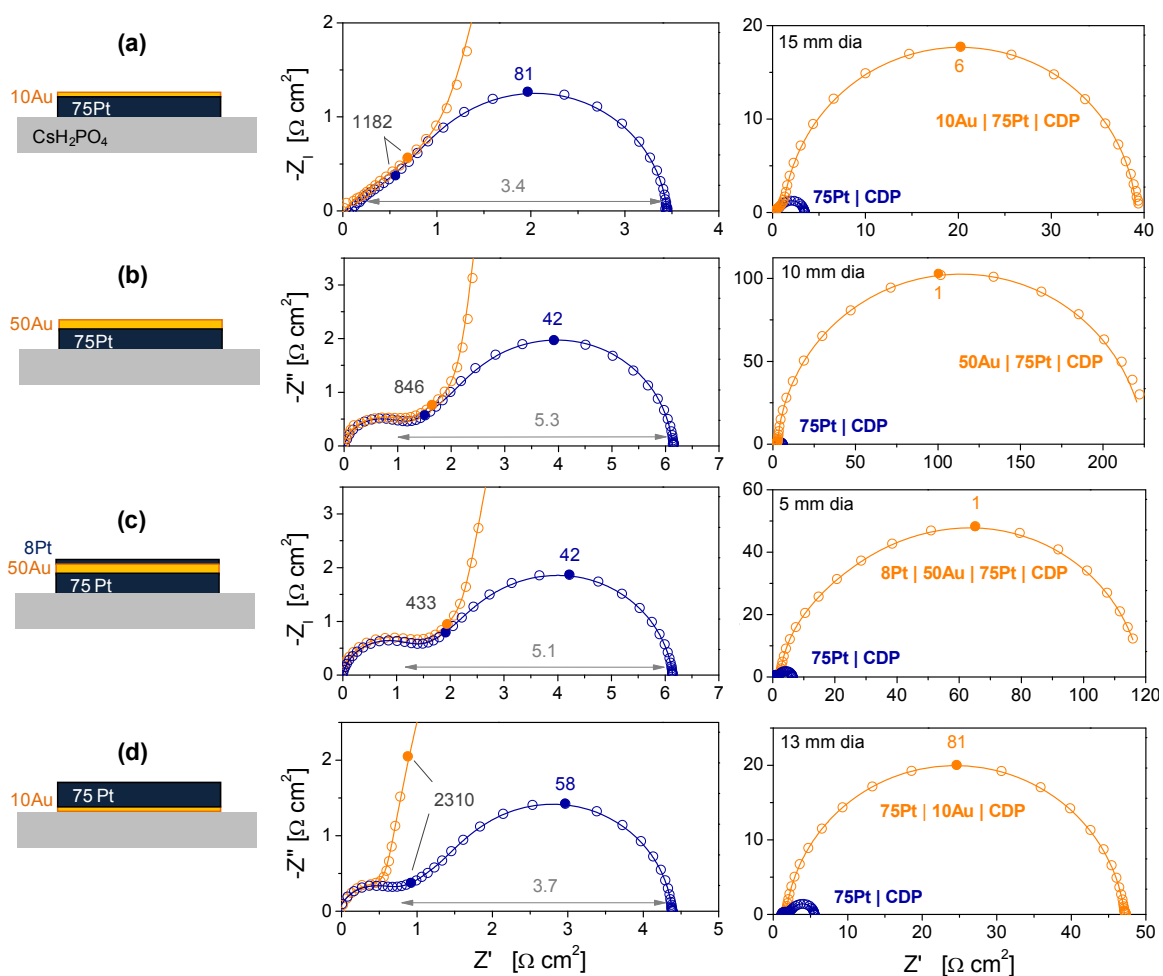


Figure C.17 The Pt-Au layered thin film electrode system at 250 °C with $p_{H_2} \approx p_{H_2O} \approx 0.5$ atm: (a) 10Au | 75Pt | CDP, (b) 50Au | 75Pt | CDP, (c) 8Pt | 50Au | 75Pt | CDP, and (d) 75Pt | 10Au | CDP. CDP denotes CsH₂PO₄, and the number preceding the metal denotes the film thickness in nm. The half-cell configuration is shown in the left column. The second and third columns show the corresponding high and low-frequency behavior, respectively. The Warburg resistance, R_0 , is indicated by the arc width, and select frequencies f are labeled.

Table C.1 Summary of extracted fit parameters for the low-frequency arc generated by the addition of Au to the Pt | CsH₂PO₄ cell. Values in bold correspond to the spectra plotted in Figure C.17. For comparison, values for the 7.5 nm Pt film electrode are also shown. CDP = CsH₂PO₄, HF = high frequency, \tilde{R} = area-normalized resistance, C_{equiv} = equivalent capacitance, ω_0 = characteristic frequency, E_A = activation energy.

	Cell Geometry	\tilde{R} [Ω cm ²]	C_{equiv} [μ F cm ⁻²]	ω_0 [Hz]	45° @ HF?	pH ₂	pH ₂ O	E_A [kJ mol ⁻¹]
	7.5Pt CDP	3	132	2740	Y	0.74	0.30	31
(a)	10Au 75Pt CDP	38–70	749–832	17–35	Y	.51–.71	–0.03	48
(b)	50Au 75Pt CDP	193–227	763–783	5.6–6.8	Y	.61–.78	–0.01	48
(c)	7.5Pt 50Au 75Pt CDP	115–119	1135–1155	7.3–7.6	Y	.77–.80	0.02	50
(d)	75Pt 10Au CDP	46–53	43–46	413–515	N	.55–.64	0.06	54
(e)	(HF arc) 50Au CDP	476–833	41–47	73–36	—	—	—	—
(f)	(LF arc) 50Au CDP	82–170	37100– 39200	0.46–0.21	—	—	—	—

We also electrochemically characterized 10 and 50 nm Au films deposited directly onto CsH₂PO₄ in order to understand hydrogen electro-oxidation at Au | CsH₂PO₄ and further clarify the processes occurring in the Pt-Au bilayer systems. In the case of 10 nm Au films, the electronic connectivity of the films degraded after electrochemical testing. The sheet resistances measured for the Au films were reasonable initially, comparable to values for as-deposited 7.5 nm Pt films, but after electrochemical testing, the sheet resistances were too high to be measured using a hand-held multimeter. The impedance response was consistent with this behavior; the currents were too small to be measured using a Solartron 1260 unit, implying an electrode resistance of at least several M Ω . On the other hand, 50 nm films remained intact and retained its sheet connectivity and low sheet resistance after electrochemical characterization. The total electrode resistances for 50 nm Au films were 390–710 Ω cm². The impedance response

was comprised primarily of two arcs (Figure C.18a), a large arc at high frequencies with a resistance of 476–833 $\Omega \text{ cm}^2$ and a smaller arc at low frequencies with a resistance of 82–170 $\Omega \text{ cm}^2$. These resistance values are listed in Table C.1 for comparison to the Pt-Au layered electrode systems. At very high frequencies, an additional process is visible (Figure C.18b); at present, it is unclear whether this arc is due to diffusion (suggested by the shape) or constriction (as indicated by the high characteristic frequency).

The observation of such a large resistance, relative to the values of the blocking arcs exhibited by the Pt-Au systems, is somewhat surprising and suggests that the Pt-Au systems are more active. Since 50 nm Au in configuration (b), Au | Pt | CsH₂PO₄, displayed lower electrode resistance than 50 nm Au in Au | CsH₂PO₄, the source of the high resistance in the Au | CsH₂PO₄ cell is likely a process that is not located at the Au | gas interface. To confirm if the source of the high resistance is, indeed, a process at the Au | CsH₂PO₄ interface, it would be necessary construct a similar to configuration (d), i.e., Pt | Au | CsH₂PO₄ | Au | Pt cell, but with a 50 nm layer of Au rather than a thin 10 nm layer. The observation that 10 nm Au alone degrades significantly may mean that 10 nm Au films may not remain interconnected when deposited under (or on top of) Pt. Thus, the observation of a lower resistance in configuration (d) compared to that for 50 nm Au alone presently does not provide enough information for drawing any meaningful conclusions. Note that although interdiffusion of bulk metals at temperatures near 250 °C is expected to be negligible, it cannot be ruled out in nanograined thin film systems. Thus, it remains a possibility that increased activity of Pt-Au bilayer electrodes compared to Au alone is due to alloy formation.

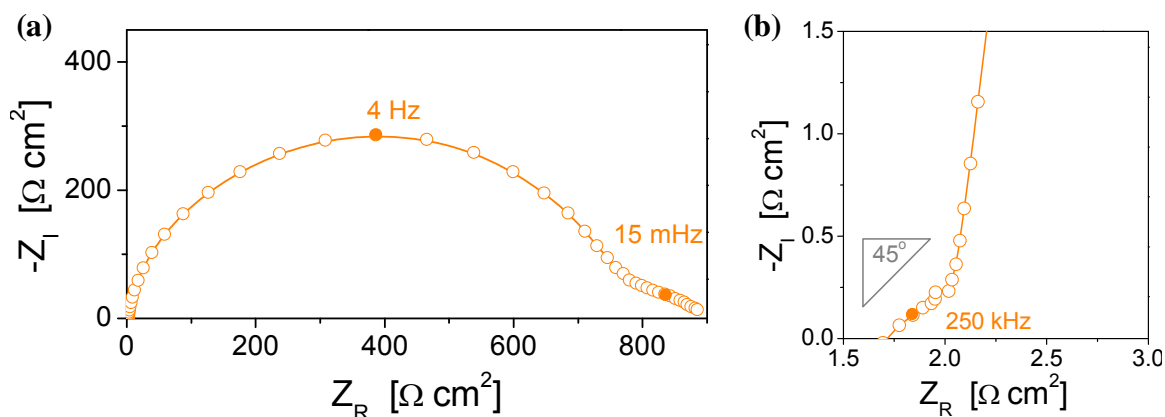


Figure C.18 Impedance spectra of a Au | CsH₂PO₄ | Au symmetric cell, collected at 250 °C with $p\text{H}_2 \approx p\text{H}_2\text{O} \approx 0.5 \text{ atm}$, (a) comprised primarily of two arcs, with (b) an additional low-resistance process visible high frequencies.

C.5 Electrolyte Effects: Cs_{0.25}Rb_{0.75}H₂PO₄ vs. CsH₂PO₄

To clarify the role of charge transfer at the Pt | solid acid electrolyte interface in the reaction mechanism, we perform impedance studies of the Pt | Cs_{0.25}Rb_{0.75}H₂PO₄ | Pt system. The CsH₂PO₄-RbH₂PO₄ system has been shown to form solid solutions up to a Rb content of $x \approx 0.8$.¹¹³ The proton conductivity of Cs_{1-x}Rb_xH₂PO₄ ($x < 0.8$) is approximately 2–3 times lower than that of the end-member, CsH₂PO₄, and the lattice parameters and hydrogen bond lengths vary monotonically with Rb content.^{113, 124} We suspect that the change in the properties of Cs_{1-x}Rb_xH₂PO₄ with Rb content makes this solid solution system valuable for exploring the effect of the Pt | electrolyte interface on the rate-limiting step of hydrogen electro-oxidation. In this section, we compare the impedance response of Pt | Cs_{0.25}Rb_{0.75}H₂PO₄ to Pt | CsH₂PO₄.

C.5.1 150 nm Platinum Films

The Nyquist spectra for 150 nm Pt film electrodes (Figure C.19) deposited on CsH_2PO_4 and $\text{Cs}_{0.25}\text{Rb}_{0.75}\text{H}_2\text{PO}_4$, show notable differences in arc shape and width. At high frequencies, the spectra behavior similarly, displaying a slope of 45° . However, at intermediate frequencies, the spectrum for $\text{Pt} | \text{Cs}_{0.25}\text{Rb}_{0.75}\text{H}_2\text{PO}_4 | \text{Pt}$ deviates from that for $\text{Pt} | \text{Cs}_{0.25}\text{Rb}_{0.75}\text{H}_2\text{PO}_4 | \text{Pt}$, extending to an additional arc at low frequencies. The impedance spectrum for $\text{Pt} | \text{CsH}_2\text{PO}_4$, as shown in Chapter 3, can be fitted to the distributed finite-length Warburg (dFLW) model. For the impedance response of $\text{Pt} | \text{Cs}_{0.25}\text{Rb}_{0.75}\text{H}_2\text{PO}_4 | \text{Pt}$, an additional (empirical) RQ element was added in series to the dFLW element to account for the low-frequency arc. Extracted values are shown in Table C.2. The extracted fit parameters for $\text{Pt} | \text{CsH}_2\text{PO}_4 | \text{Pt}$ and the dFLW portion of $\text{Pt} | \text{Cs}_{0.25}\text{Rb}_{0.75}\text{H}_2\text{PO}_4 | \text{Pt}$ spectra are comparable, with Warburg resistances of 17 and $14 \Omega \text{ cm}^2$, respectively. The characteristic frequencies (26–36 Hz) and $p\text{H}_2$ reaction orders (0.32–0.34) are also comparable, with differences in the characteristic frequencies being attributed to errors from the fitting of convoluted processes in the $\text{Pt} | \text{Cs}_{1-x}\text{Rb}_x\text{H}_2\text{PO}_4 | \text{Pt}$ system. The additional low-frequency arc present in the $\text{Pt} | \text{Cs}_{0.25}\text{Rb}_{0.75}\text{H}_2\text{PO}_4 | \text{Pt}$ spectrum had a resistance of $13 \Omega \text{ cm}^2$, with a notably different $p\text{H}_2$ dependence of 0.65. The ohmic offset (not shown) yielded a proton conductivity of $8 \times 10^{-3} \text{ S cm}^{-1}$ for $\text{Cs}_{0.25}\text{Rb}_{0.75}\text{H}_2\text{PO}_4$ at 255°C , almost one-third of that for CsH_2PO_4 at the same temperature, $2.5 \times 10^{-2} \text{ S cm}^{-1}$.

The presence of an additional feature at low frequencies suggests that the use of $\text{Cs}_{0.25}\text{Rb}_{0.75}\text{H}_2\text{PO}_4$ as the electrolyte influences the rate-limiting step(s) for hydrogen electro-oxidation. Based on $\text{Pt} | \text{CsH}_2\text{PO}_4 | \text{Pt}$ data for thick Pt films for which diffusion

of hydrogen was found to be the rate-limiting step, small perturbations at the Pt | electrolyte interface, is not expected to influence the rate-limiting step of hydrogen diffusion through the Pt film. Our observation here implies that a step occurring at or affected by the Pt | $\text{Cs}_{0.25}\text{Rb}_{0.75}\text{H}_2\text{PO}_4$ interface is significantly slower than in the Pt | CsH_2PO_4 system. That is, the additional low-frequency arc in Pt | $\text{Cs}_{0.25}\text{Rb}_{0.75}\text{H}_2\text{PO}_4$ spectrum, with a resistance of $13\ \Omega\ \text{cm}^2$, corresponds to a process that occurs at or near the Pt | $\text{Cs}_{0.25}\text{Rb}_{0.75}\text{H}_2\text{PO}_4$ interface. This interfacial resistance value is approximately six times greater than the resistance, $2.2\ \Omega\ \text{cm}^2$, of the interfacial steps occurring in Pt | CsH_2PO_4 | Pt (Figure 3.12). Although the $p\text{H}_2$ reaction order of 0.65 for the Pt | $\text{Cs}_{0.25}\text{Rb}_{0.75}\text{H}_2\text{PO}_4$ interfacial step is comparable to that observed for 7.5 nm Pt films on CsH_2PO_4 , it is not yet clear whether these two interfacial processes, with resistances of 13 and $2.2\ \Omega\ \text{cm}^2$, are the same. In the next section, experiments with 7.5 nm films are examined, in an attempt to further clarify this observed phenomenon.

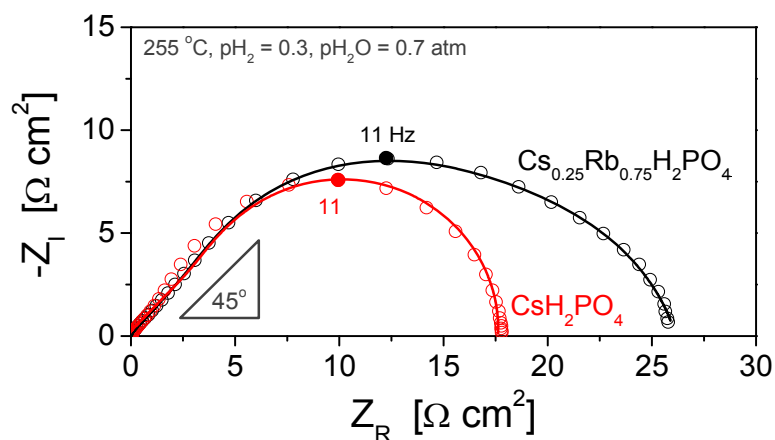


Figure C.19 Nyquist plot for 150 nm Pt film electrode on CsH_2PO_4 and on $\text{Cs}_{0.25}\text{Rb}_{0.75}\text{H}_2\text{PO}_4$ polycrystalline electrolytes. Arc shape and widths were reproducible across three different samples for each substrate. Lines are fits to dLFW (for CsH_2PO_4) and to dFLW in series with RQ (for $\text{Cs}_{0.25}\text{Rb}_{0.75}\text{H}_2\text{PO}_4$).

Table C.2 Comparison of fitted parameters for 150 nm Pt film electrodes on CsH_2PO_4 (CDP) and $\text{Cs}_{0.25}\text{Rb}_{0.75}\text{H}_2\text{PO}_4$ (CRDP75) at 255 °C in 0.3 atm H_2 , 0.7 atm H_2O . \tilde{R} = area-normalized resistance, ω_0 = characteristic frequency

	<i>Warburg diffusion (dFLW)</i>			<i>Low-frequency process</i>		
Cell	\tilde{R} [$\Omega \text{ cm}^2$]	ω_0 [Hz]	$p\text{H}_2$ rxn order	\tilde{R} [$\Omega \text{ cm}^2$]	ω_0 [Hz]	$p\text{H}_2$ rxn order
Pt CDP	17	26	0.34	N/A	N/A	N/A
Pt CRDP75	14	36	0.32	13	20	0.65

C.5.2 7.5 nm Platinum Films

Pt | $\text{Cs}_{0.25}\text{Rb}_{0.75}\text{H}_2\text{PO}_4$ | Pt cells with 7.5 nm Pt films yielded impedance spectra that were symmetric in shape, as shown for both 19 and 9.3 nm Pt films in Figure C.20a and Figure C.20b, respectively. The symmetric nature of the arcs is consistent with an electrode reaction mechanism dominated by an interfacial processes (as demonstrated for 7.5 nm films on CsH_2PO_4 in Chapter 3). Unlike 150 nm Pt film electrodes which displayed reproducible behavior, 7.5 nm electrodes were inconsistent in their electrode arc widths. The electrode resistance for Pt | CsH_2PO_4 (Table C.3) varied from 3.4 to 7.7 $\Omega \text{ cm}^2$, while that for Pt | $\text{Cs}_{0.25}\text{Rb}_{0.75}\text{H}_2\text{PO}_4$ varied from 0.7 to 20 $\Omega \text{ cm}^2$ for 9.3 and 19 nm films, respectively. From a comparison of these values, it is clear that the effect of changing the electrolyte substrate, although irreproducible, is non-negligible. The characteristic frequencies vary notably between arcs, however, the capacitances of the processes for all cells tested are similar, implying that the observed change in the characteristic frequency of the rate-limiting step is a consequence of a change in the resistance rather than the capacitance of the process.

While the scatter in the electrode resistance values for Pt | CsH_2PO_4 may be acceptable (a factor of ~ 2), that for Pt | $\text{Cs}_{0.25}\text{Rb}_{0.75}\text{H}_2\text{PO}_4$ is quite significant (a factor of

~30). This is not surprising since Rb incorporation leads to an increasingly plastic superprotonic phase. In the laboratory, application of mechanical pressure to make electrical connection for conductivity measurements led us to observe that under comparable pressures, a greater extent of deformation (i.e., flattening) of dense $\text{Cs}_{1-x}\text{Rb}_x\text{H}_2\text{PO}_4$ discs occurs for compounds with larger x . Thus, for a given mechanical pressure applied to the symmetric cells (for current collection), those based on $\text{Cs}_{0.25}\text{Rb}_{0.75}\text{H}_2\text{PO}_4$ substrates deformed more than those based on CsH_2PO_4 substrates. Physical observations of the symmetric cells before and after testing suggest that the carbon paper current collector damaged $\text{Cs}_{0.25}\text{Rb}_{0.75}\text{H}_2\text{PO}_4$ cells to a greater extent. Furthermore, based on SEM image analysis of films on CsH_2PO_4 (Figure C.12), we can conclude that thicker films generally remained more intact under mechanical pressure, consistent with the reproducibility of the data for 150 nm films. On the other hand, 7.5 nm films on $\text{Cs}_{0.25}\text{Rb}_{0.75}\text{H}_2\text{PO}_4$ are more easily damaged by the pressure of the carbon paper (Figure C.12) given the lack of stability for 1.5–4.5 nm films (Figure C.6) and the expectation that higher plasticity (of $\text{Cs}_{0.25}\text{Rb}_{0.75}\text{H}_2\text{PO}_4$) implies a more mobile/ductile substrate. Thus, in order to accurately determine the effect of $\text{Cs}_{0.25}\text{Rb}_{0.75}\text{H}_2\text{PO}_4$ on the rate-limiting step, determination of an optimal mechanical pressure for current collection is required.

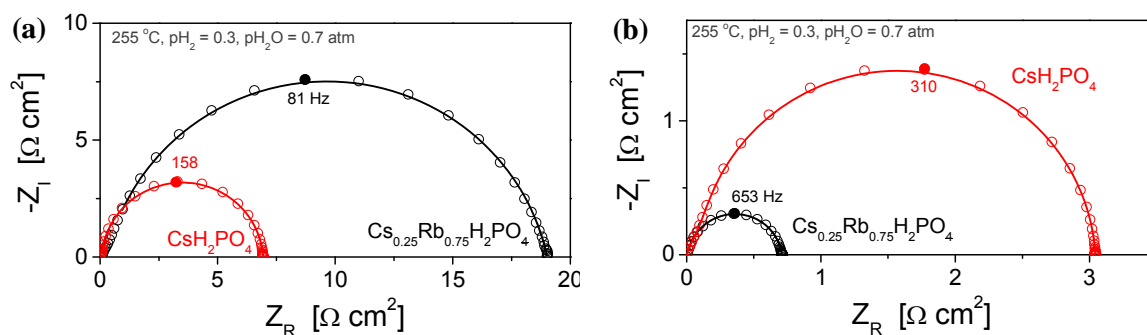


Figure C.20 Nyquist plots for 7.5 nm Pt films deposited on CsH_2PO_4 and on $\text{Cs}_{0.25}\text{Rb}_{0.75}\text{H}_2\text{PO}_4$ polycrystalline electrolytes. Both the cell and Pt film diameters are (a) 19 mm and (b) 9.3 mm. The arc shapes are similar, but the widths of the arcs vary significantly

Table C.3 Comparison of extracted fit parameters for 7.5 nm Pt film electrodes on CsH_2PO_4 (CDP) and $\text{Cs}_{0.25}\text{Rb}_{0.75}\text{H}_2\text{PO}_4$ (CRDP75) at 255 °C in 0.3 atm H_2 and 0.7 atm H_2O . \tilde{R} = area-normalized resistance, C_{equiv} = equivalent capacitance, ω_0 = characteristic frequency

Cell	Dia. [mm]	\tilde{R} [$\Omega \text{ cm}^2$]	C_{equiv} [$\mu\text{F cm}^{-2}$]	ω_0 [Hz]	$p\text{H}_2$ rxn order
Pt CDP	19.1	7.7	157	880	0.86
Pt CDP	9.3	3.4	144	2325	--
Pt CRDP75	19.1	20	121	411	0.89
Pt CRDP75	9.3	0.7	135	10415	--

C.6 Effect of Environmental Parameters

In this section, we show several representative plots to illustrate how activation energy and the $p\text{H}_2$ reaction order values, reported in Chapter 3, are extracted. The reaction order for $p\text{H}_2\text{O}$ is also reported. As is the case for chemical reactions, the reaction rate of electrochemical reactions depends on the amount of reactant/product available (Appendix A.3). In the case of hydrogen electro-oxidation, hydrogen partial pressure, $p\text{H}_2$, is expected to affect the reaction rate, and, furthermore, because of the

high water partial pressure of the gas environment, we also consider the effect of water partial pressure, $p\text{H}_2\text{O}$. Thus, the reaction rate can be expressed as:

$$\text{reaction rate} \propto R_E^{-1} \propto p\text{H}_2^n p\text{H}_2\text{O}^m \quad (\text{C.3})$$

where R_E is the resistance of an electrode process, and n and m are the reaction orders of $p\text{H}_2$ and $p\text{H}_2\text{O}$, respectively. The reaction orders, n and m , are determined independently, specifically, by holding $p\text{H}_2\text{O}$ constant while varying $p\text{H}_2$ (to extract n) and holding $p\text{H}_2$ constant while varying $p\text{H}_2\text{O}$ (to extract m). Figure C.21 and Figure C.22 are plots showing the effect of $p\text{H}_2$ and $p\text{H}_2\text{O}$ on the (inverse) resistances of the electrode, CsH_2PO_4 and constriction processes in $\text{Pt} | \text{CsH}_2\text{PO}_4 | \text{Pt}$, for 7.5 and 75 nm films, respectively. (Processes associated with the bulk of the electrolyte are not expected to depend on gas partial pressure but are plotted here for reference.) For both cells, processes related to proton conduction in CsH_2PO_4 , i.e., the ohmic offset and the high-frequency constriction arc, vary negligibly with gas partial pressure. These results were observed for virtually all the cells tested. The average values, extracted from plots for 20–30 samples are shown in Table C.4. In some cases (Figure C.21a being an example), the dependence of the constriction arc is larger than expected, particularly when the constriction effect is small, because of a larger fitting error of the constriction arc as the low-frequency electrode arc increases in size. This is consistent with the partial pressure dependence for the two processes being equal be opposite in sign.

Table C.4 Hydrogen and water partial pressure dependences of electrolyte-related processes.

	ohmic offset	high-frequency constriction
$p\text{H}_2$	-0.02 ± 0.05	-0.12 ± 0.09
$p\text{H}_2\text{O}$	0.0 ± 0.1	0.02 ± 0.08

In the case of 75 nm Pt (Figure C.21), the electrode process exhibited a dependence on $p\text{H}_2$, with a slope of ~ 0.54 (average ≈ 0.45 for 75 nm films, Figure 3.8) while the $p\text{H}_2\text{O}$ reaction order was much lower, 0.16 (average = 0.30 ± 0.09). In the case of 7.5 nm Pt (Figure C.22), the electrode exhibited a $p\text{H}_2$ reaction order that is notably higher, 0.80, (average ≈ 0.75 , Figure 3.8) than that for thicker films and the $p\text{H}_2\text{O}$ dependence is 0.22 (with an average value of 0.30 ± 0.06) comparable to that for 75 nm Pt.

Given a known rate-limiting step of hydrogen diffusion (in the case of 75 nm Pt films), a $p\text{H}_2$ reaction close to 0.5 is expected (Appendix A.3). That the $p\text{H}_2$ reaction order is significantly larger for 7.5 nm films is consistent with the observed change in the rate-limiting step (Figure 3.8). Presently, identification of this rate-limiting process is not possible, although it is noteworthy that dissociative adsorption of hydrogen can, to first order approximation, yield a slope close to unity. (Appendix A.3)

The observation of a $p\text{H}_2\text{O}$ dependence is somewhat surprising because it is not immediate clear the role of water in the reaction mechanism, particularly in the hydrogen diffusion pathway. The observed $p\text{H}_2\text{O}$ dependence was confirmed to be a small positive value consistently observed across ~ 30 samples, with an average reaction order of ~ 0.30 across all film thicknesses. Without the capability to explore a wider $p\text{H}_2\text{O}$ range, it is not possible to confirm the role of water in the reaction mechanism. In Appendix A.3, we assume that water influences the reaction rate by occupying surface sites on the metal; however, this results in a negative reaction order for $p\text{H}_2\text{O}$, opposite of experimental observations.

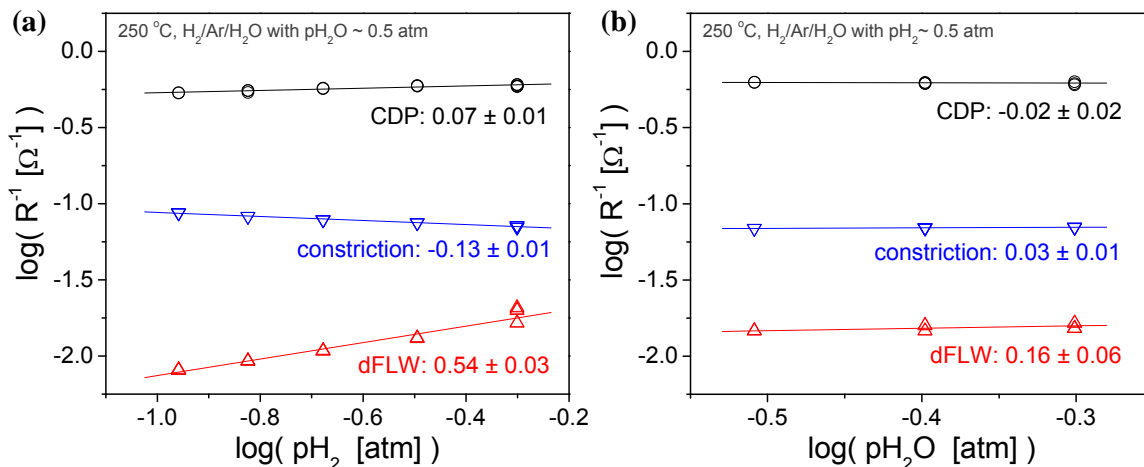


Figure C.21 Partial pressure dependence for Pt | CsH₂PO₄ | Pt (75 nm, 5 mm Pt film) at 250 °C. Plots of inverse resistance as a function of (a) pH_2 at constant pH_2O and (b) pH_2O at constant pH_2 .

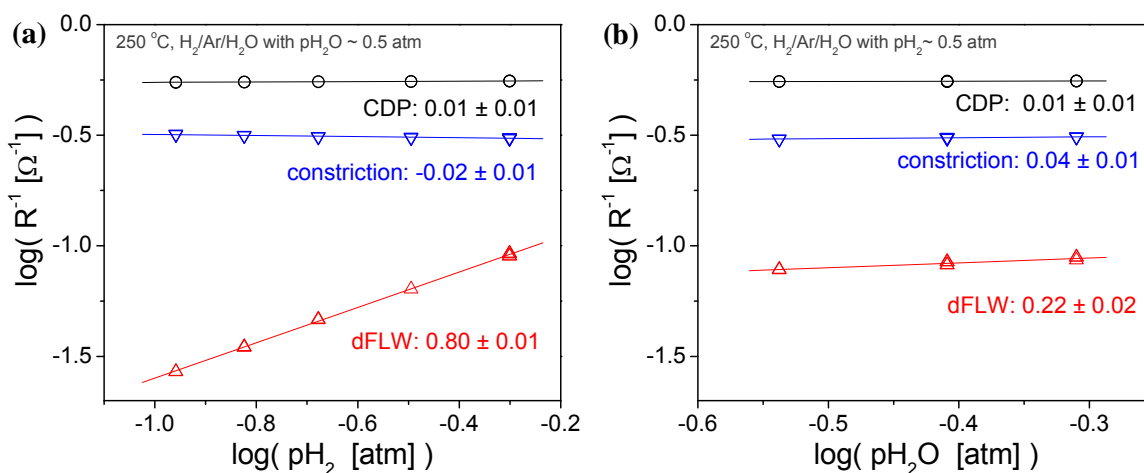


Figure C.22 Partial pressure dependence for Pt | CsH₂PO₄ | Pt (7.5 nm, 10 mm Pt film) at 250 °C. Plots of inverse resistance as a function of (a) pH_2 at constant pH_2O and (b) pH_2O at constant pH_2 .

Figure C.23 and Figure C.24 show the Arrhenius plots for 75 and 7.5 nm Pt films, respectively, in the Pt | CsH₂PO₄ | Pt system. In the case of the 75 nm films (Figure C.23a), we plot $R_E^{-1} \times T$ rather than R_E^{-1} because both proton conduction through CsH₂PO₄ and hydrogen diffusion through Pt depend on temperature,

$$\frac{1}{R_E} \propto \frac{1}{T} \exp\left(\frac{-E_A}{RT}\right) \quad (\text{C.4})$$

where R_E is the resistance of the electrode process, E_A is the activation energy and R and T have their usual meanings. In this case, only from a plot of $R_E^{-1} \times T$ can you extract the correct value of the activation energy. The activation energies for proton conduction through CsH_2PO_4 , extracted from the ohmic offset and the high-frequency constriction arc, are 40 and 42 kJ mol^{-1} , respectively, both in good agreement with that reported in literature, 0.42 eV or 41 kJ mol^{-1} .¹⁰ To extract the activation energy for hydrogen diffusivity, the inverse of the characteristic timescale, τ , (or characteristic frequency) is plotted because

$$D_H = \frac{L_F^2}{\tau} = D_H^0 \exp\left(\frac{-Q}{RT}\right) \quad (\text{C.5})$$

where D_H is the diffusion coefficient for hydrogen in Pt, L_F is the thickness of the Pt film, D_H^0 is the pre-exponential constant, and Q is the activation energy. From Figure C.23b, the activation energy for diffusion was found to be $\sim 48 \text{ kJ mol}^{-1}$.

In the case of cells with 7.5 nm films, the rate-limiting step hydrogen electro-oxidation has not been identified, and thus, the more general approach of plotting R_E^{-1} rather than $R_E^{-1} \times T$ was used. (Figure C.24) The temperature dependence for the CsH_2PO_4 -related processes are also plotted this way to enable comparison to the electrode process. However, the true activation energies are extracted by plotting $R_E^{-1} \times T$; these values are indicated in parentheses in the figure.

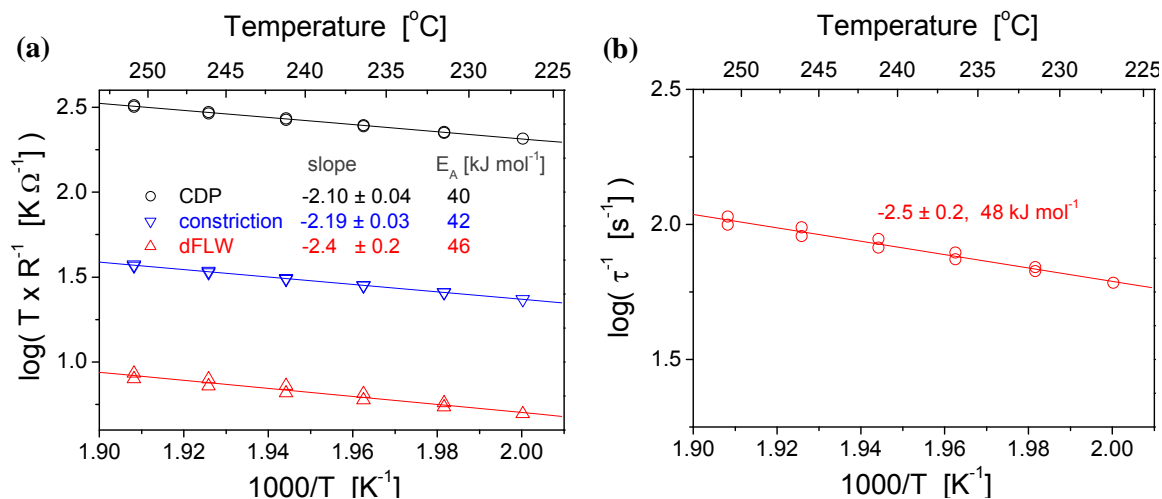


Figure C.23 Arrhenius behavior of Pt | CsH₂PO₄ | Pt (75 nm, 5 mm Pt film) for $p_{\text{H}_2} \approx p_{\text{H}_2\text{O}} \approx 0.5$ atm: (a) $R_E^{-1} \times T$ as a function of inverse temperature for proton conduction in CsH₂PO₄ and H diffusion in Pt, and (b) inverse characteristic timescale for hydrogen diffusion, for extraction of the activation energy for hydrogen diffusivity, $D_{\text{H}} \propto \tau^{-1}$.

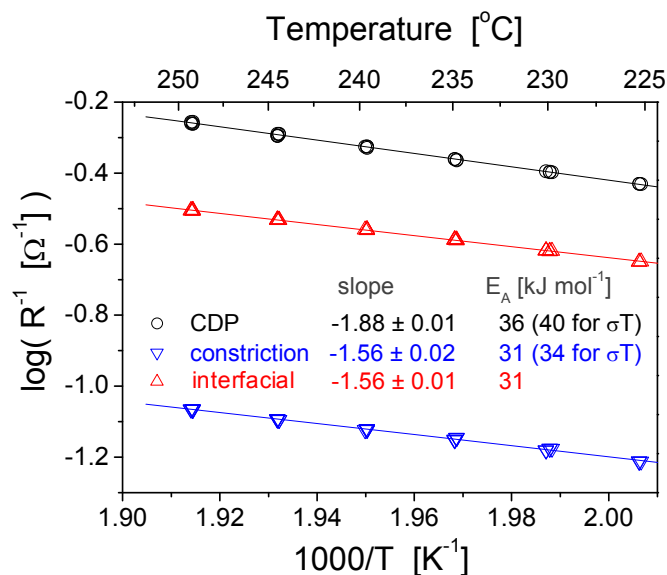


Figure C.24 Arrhenius behavior of Pt | CsH₂PO₄ | Pt (7.5 nm, 10 mm Pt film) for $p_{\text{H}_2} \approx p_{\text{H}_2\text{O}} \approx 0.5$ atm. Because the electrode rate-limiting step has not been identified, R_E^{-1} is plotted as a function of inverse temperature. The activation energies correspond to $R_E^{-1} \times T$ for the CsH₂PO₄ and constriction processes are indicated in parentheses.

C.7 Role of the Superprotonic Phase Transition in Electrode Kinetics

We can utilize phase transformation characteristics of CsH_2PO_4 to provide additional insight into electrochemical reactions. Specifically, because the proton conductivity (or conduction mechanism) changes drastically across the phase transition, such a change is expected to have a significant impact on the electrochemistry that occurs at the metal | CsH_2PO_4 interface.

C.7.1 Temperature Dependence

Figure C.25 shows the Pt | CsH_2PO_4 | Pt cell response for the temperature profile shown. At temperatures above and below the phase transition temperature, the temperature was increased at 5 °C intervals, and the resistances of the CsH_2PO_4 and the electrodes change with temperature in a step-wise fashion. At the phase transition temperature, estimated to be ~ 221 °C on cooling, the equilibration of the electrode and electrolyte resistances take significantly longer times. With the temperature held at 221 °C, between hour 8 and hour 22 (Figure C.25a), CsH_2PO_4 transforms slowly, with a majority transformed by hour 12. The electrode resistance tracks that for CsH_2PO_4 , particularly noticeable at hour 8 at which both the CsH_2PO_4 and the electrode resistances exhibit jumps in their values due to a slight decrease in temperature from 222 to 221 °C. The steady-state values for resistance are used to generate an Arrhenius plot of inverse resistance (Figure C.25b). In qualitative agreement with Figure C.25a, the Arrhenius plot shows a sudden jump in all steady-state resistance values across the phase transition. At superprotonic temperatures, the activation energies were ~ 40 and ~ 38 kJ mol^{-1} for the ohmic offset and high-frequency constriction processes, respectively, (i.e., CsH_2PO_4) and ~ 30 kJ mol^{-1} for the electrode process. At temperatures below the phase transition

temperature, two arcs appeared in the impedance response (not shown), corresponding to the electrolyte and electrode processes. (At temperatures below the phase transition, proton conduction through CsH_2PO_4 is slow and appears as an arc in the Nyquist spectrum.¹⁰⁾ The electrolyte and the electrode processes exhibit comparably high activation energies of 90 and 105 kJ mol^{-1} .

The two plots in Figure C.25, from two different cells, are representative of the temperature behavior of all Pt cells characterized in this study. The change in the rate-limiting step across the phase transition and apparent correlation between the electrode and electrolyte behavior below the phase transition suggest that the rate-limiting step for H_2 oxidation over Pt is related to proton transport. This hypothesis is not unreasonable; as proton conduction in CsH_2PO_4 becomes slower, the rate-limiting process at high temperatures (i.e., hydrogen diffusion through Pt) is overtaken by slow charge transfer at $\text{Pt} \mid \text{CsH}_2\text{PO}_4$.

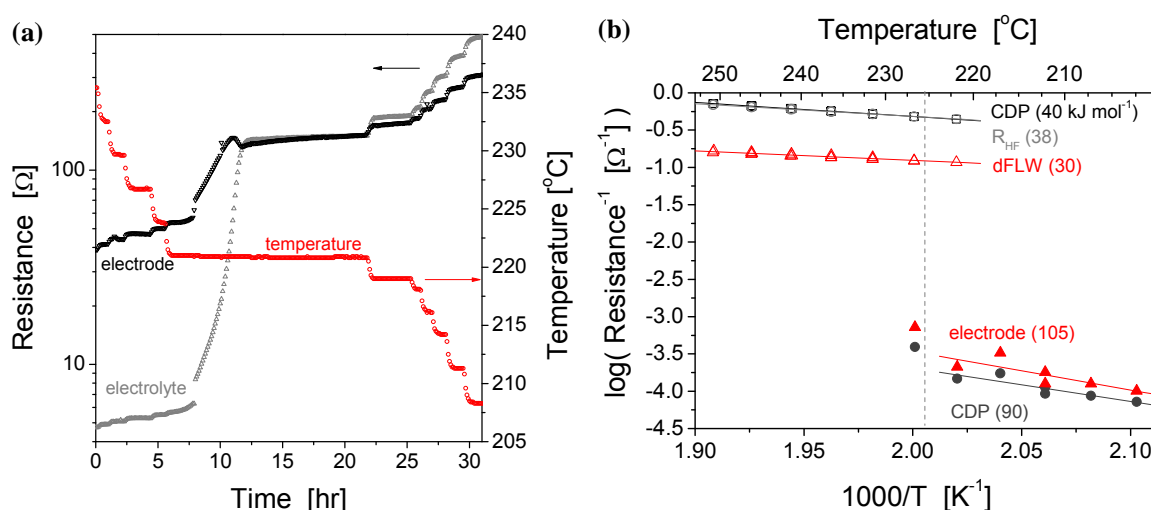


Figure C.25 Plots showing the typical behavior of $\text{Pt} \mid \text{CsH}_2\text{PO}_4 \mid \text{Pt}$ across the phase transition: (a) the cell temperature and the resistances of the electrolyte and electrodes (100 nm thick, 12.6 mm dia. Pt), plotted as a function of time and (b) an Arrhenius plot of the steady-state values (75 nm thick, 12.6 mm dia. Pt). Inverse resistance, R_E^{-1} , is plotted here, but activation energies shown are computed from a plotting $R_E^{-1} \times T$.

C.7.2 Platinum Film Geometry Dependence

Figure C.26 shows how the electrolyte and electrode resistances vary with Pt film geometry at temperatures below the phase transition temperature. As expected, proton conduction through CsH_2PO_4 exhibits no dependence on the Pt film diameter (Figure C.26a). On the other hand, the electrode process varies notably with film diameter, displaying a slope close to -3 on the double-logarithmic plot. Note that the data for all cells, with Pt film thicknesses of 7.5–375 nm, collapse into one line, indicating that the electrode process exhibits no thickness dependence. This is more explicitly shown in Figure C.26b; in this plot, the electrode resistance is area-normalized for clarity of presentation. The film geometry dependence of the electrode resistance at temperatures below the phase transition temperature of CsH_2PO_4 is consistent with an interfacial rate-limiting step, proposed to occur at $\text{Pt} | \text{CsH}_2\text{PO}_4$. Based on the extrapolation of the hydrogen diffusion resistance from superprotonic temperatures to a temperature of 200 °C (Figure C.25b), we expect hydrogen diffusion to be fast, enabling access to the two-phase interface. It is interesting to note that, at $T < T_{SPT}$, Au-Pt electrodes (shown in Figure C.17) also fall within the range resistance values shown in Figure C.26, suggesting that the presence of Au (in any given configuration) no longer influences the kinetics.

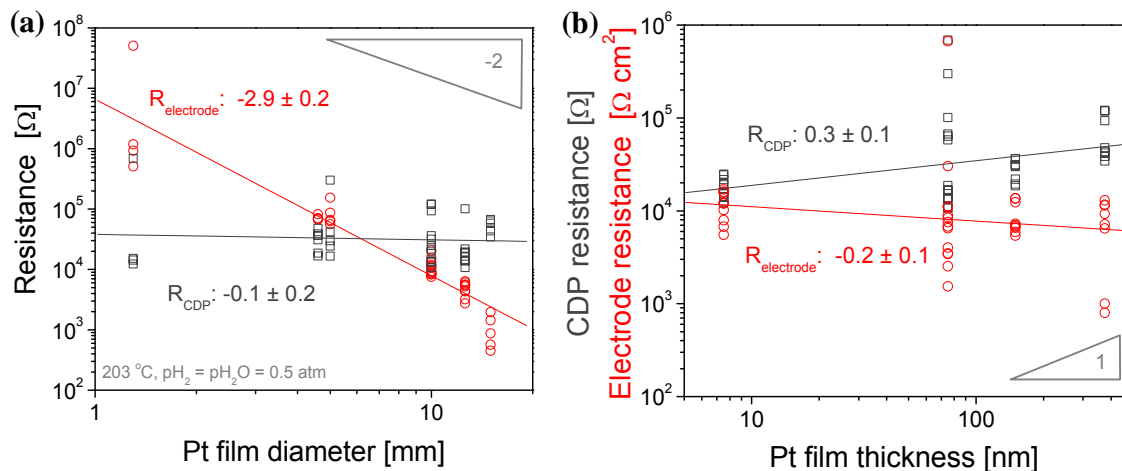


Figure C.26 Geometry dependence of electrode and electrolyte resistances below the phase transition temperature, on a double-logarithmic plot. $T \approx 200^\circ\text{C}$, $p_{\text{H}_2} \approx p_{\text{H}_2\text{O}} \approx 0.5\text{ atm}$. The resistance of CsH_2PO_4 is not dimension-normalized because its dimensions do not vary significantly across samples. The geometry dependence reveals that the electrode resistance decreases with area (a) but is not thickness-dependent (b).

C.7.3 Temperature Cycling and Crack Formation

As reported in Chapter 5, the incompatibility of the monoclinic and cubic phases of CsH_2PO_4 results in the formation of microcracks during phase transformation. In this section, we examine the effect of repeated cycling on the formation and distribution of microcracks in polycrystalline CsH_2PO_4 . Figure C.27 shows a series of images of a polycrystalline CsH_2PO_4 surface taken after each of three heat-cool cycles during which mechanical pressure was applied to the cell (in a similar manner as with the $\text{Pt} | \text{CsH}_2\text{PO}_4 | \text{Pt}$ cells), while Figure C.28 shows images after each of two heat-cool cycles for a sample to which no external pressure was applied. The CsH_2PO_4 surfaces were scratched so that images could be taken at a fixed location after each thermal cycle. In both cases, the distribution of cracks appeared to change with each cycle; new microcracks formed in the substrate while a few existing cracks healed slightly, with the generation of cracks outnumbering the disappearance. From these images, it appears that

cracking healing (as highlighted in the images) occurred more readily when pressure was applied to the sample. In addition, when no pressure is applied to the cell (Figure C.28), the greater number of fine cracks is visible, possibly because of the lack of external force that can aid in healing the cracks. To confirm these speculations, a statistical analysis would be required.

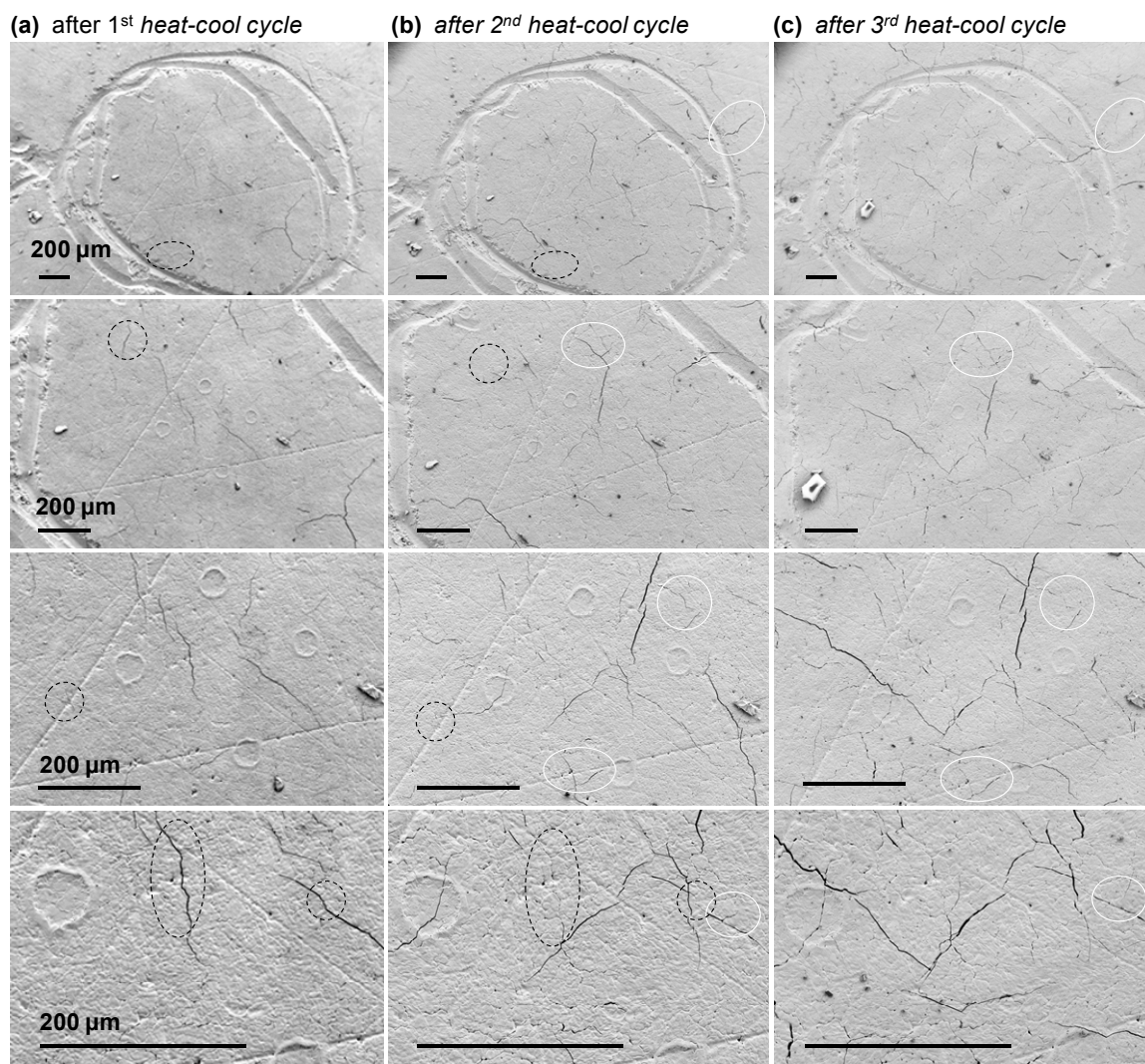


Figure C.27 The effect of the superprotonic phase transition on cracking in densified polycrystalline CsH_2PO_4 disc, with mechanical pressure applied to the disc. SEM micrographs of a CsH_2PO_4 surface, taken at the same location on the surface, after (a) one, (b) two and (c) three heat-cool cycles. Dotted black lines indicate several locations at which cracks had healed between (a) and (b), while solid white lines indicate the healing of cracks between (b) and (c).

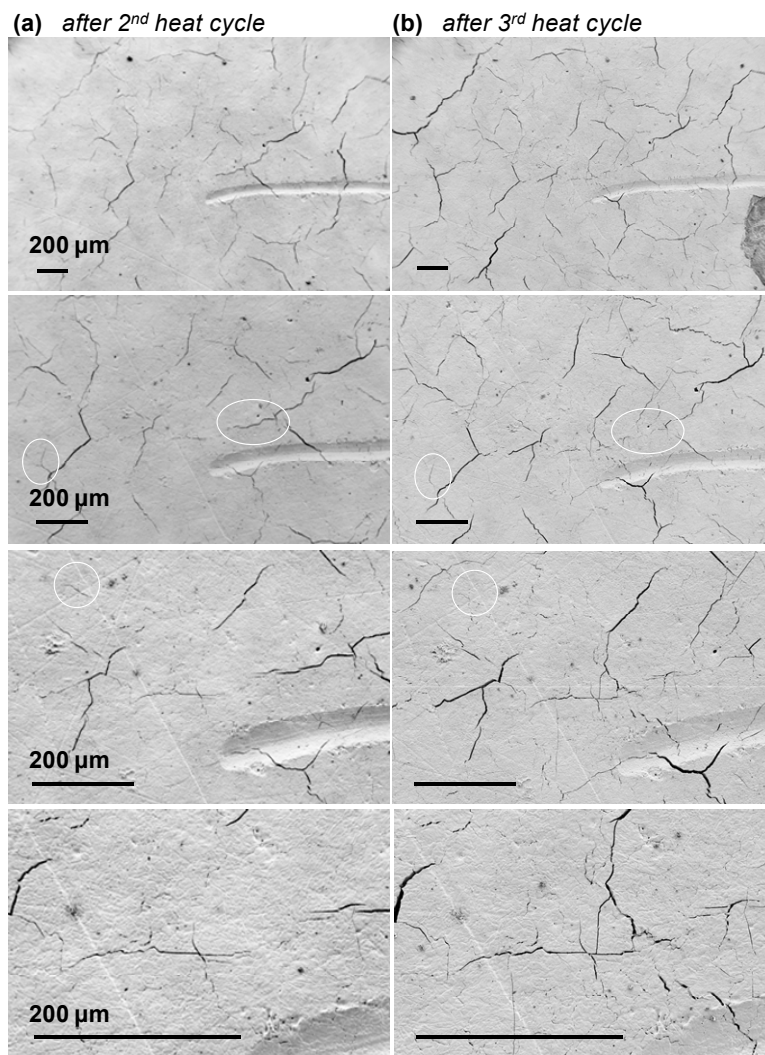


Figure C.28 The effect of the superprotonic phase transition on cracking in polycrystalline CsH_2PO_4 *without* mechanical pressure applied to the substrate. SEM micrographs of a CsH_2PO_4 surface after (a) two heat-cool cycles and (b) three heat-cool cycles taken at the same location on the surface. Solid white lines highlight locations where cracks had healed.

That the density of microcracks increases when CsH_2PO_4 is taken through the transition may have implications for electrode studies. In the case of metal films, new cracks generated after each cycle are propagated to the films while healed cracks do not

affect the film structure (since Pt itself cannot heal). Therefore, if the rate-limiting step occurred at triple-phase boundary sites (e.g., at these cracks, Figures 3.3 and 3.9), then cycling would cause a drop in the measured electrode resistance. On the other hand, for an electrode process rate-limited by a two-phase process, the addition of triple-phase sites would have no impact on the shape or size of the impedance arc (provided that the increase in the number of triple-phase sites is not large enough to overtake the two-phase pathway). Based on these expectations, it is not surprising that in the case of the Pt | CsH₂PO₄ | Pt system, the impedance response varies little with cycling through the phase transition (Figure C.29). The impedance spectra collected before and after temperature cycling, shown here for cells with 7.5 and 150 nm thick Pt films, overlap almost perfectly, indicating that neither the interfacial nor diffusion step (which dominate 7.5 and 150 nm films, respectively) is affected when additional cracks in the Pt film are generated. In some cases, there appeared to be a small decrease in the total combined width of the spectra with cycling, as shown in the case of 52.5 nm Pt films (Figure C.30a). Extracted fit values for the resistances for the ohmic, high-frequency and electrode (dFLW) processes reveal that most of this change comes from processes associated with the electrolyte (ohmic + constriction) rather than the electrode (Figure C.30b). That the constriction arc itself seems to be shrinking suggests that the change in the spectra is related to the contact of the carbon paper to the cell; this is not unreasonable because the volume difference between the two phases of CsH₂PO₄ is ~ 2%.

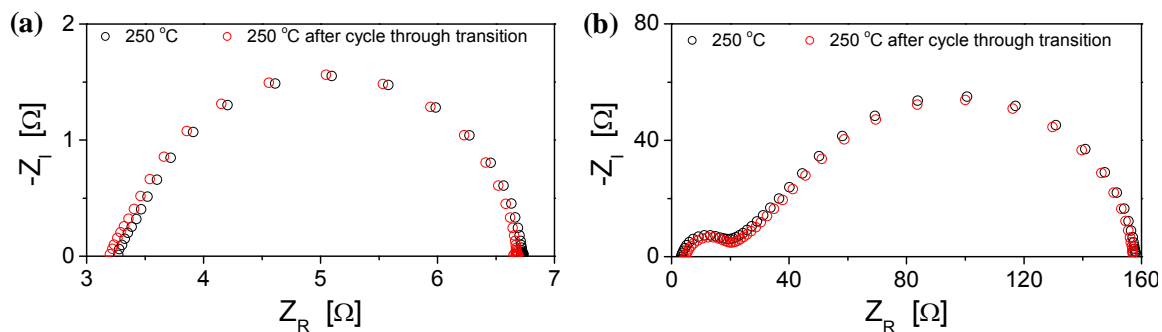


Figure C.29 Impedance spectra for Pt | CsH₂PO₄ | Pt symmetric cells before and after a cool-heat cycle through the phase transition. The two spectra overlap almost perfectly for both (a) 7.5 nm thick, 15 mm dia. and (b) 150 nm thick, 5 mm dia. Pt films.

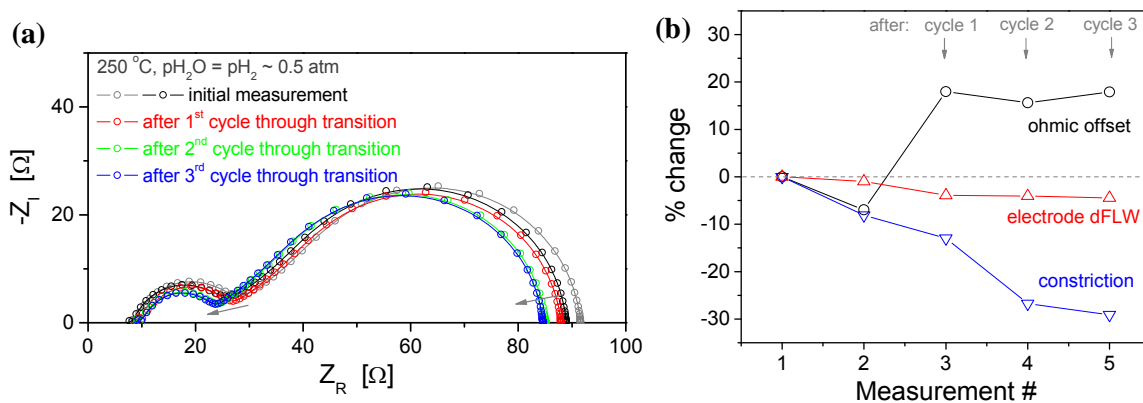


Figure C.30 Effect of thermal cycling on the impedance response of Pt | CsH₂PO₄ | Pt symmetric cells (52.5 nm thick, 5 mm diameter): (a) raw impedance spectra showing how the impedance response behaves after a few cool-heat cycles through the phase transition, (b) a plot of the % change from measurement 1. (Measurement #1 and #2 were both taken before temperature cycling, specifically before and after collecting Arrhenius data at superprotonic temperatures.)

Appendix D Hydrogen Electro-oxidation over Palladium Thin Films

Palladium is known to have high hydrogen solubility and is therefore widely studied as a hydrogen permeation membrane.³¹ Thus, Pd is expected to facilitate hydrogen oxidation (and oxygen reduction) via the two-phase boundary pathway. Not only this, Pd belongs to the same group as Pt on the periodic table and therefore has great potential as a high-activity fuel cell electrocatalyst with lower cost.¹²⁵ In this section, we present our investigation of hydrogen oxidation over Pd thin films deposited atop CsH_2PO_4 . Using thin film techniques, we can make a more meaningful comparison between the Pd and Pt as hydrogen oxidation electrocatalysts for solid acid fuel cells.

D.1 Experimental

The preparation of Pd | CsH_2PO_4 | Pd symmetric cells was identical to that for Pt based cells presented in Chapter 3. Pd films 10–300 nm in thickness were fabricated.

The general crystallinity of the Pd films, adhered to the substrates, was evaluated using a Phillips X'Pert Pro powder X-ray diffractometer using Cu K α radiation (45 kV, 40 mA) with a 2θ range of 15–90°. The morphology of the metal films both before and after electrochemical characterization was examined by scanning electron microscopy, SEM, (LEO 1550VP, Carl Zeiss SMT) using a 3 kV accelerating voltage. Chemical analysis for a subset of the films was carried out using an Oxford INCA 300 X-ray energy dispersive spectrometer (EDS) (in conjunction with the above SEM) at an accelerating voltage of 10 kV. The film thickness was measured by cross-sectional SEM

imaging of fractured cells, and the deposition rate of Pt was determined to be 15 nm min^{-1} . The film connectivity was assessed by measuring the sheet resistance of the films, using a hand-held multimeter, both before and after electrochemical characterization.

Impedance spectra were collected, in the majority of cases, using a Solartron Analytical 1260 frequency response analyzer with a 10 mV perturbation voltage about zero bias over frequencies of 10 or 1 MHz to 100 mHz configured with a four-probe measurement geometry. For experimental convenience, some spectra were collected using a Solartron 1250 analyzer equipped with a potentiostat (Princeton Applied Research, EG&G 273A). Electrical connection to the cells was made using an in-house constructed sample holder in which the cells were sandwiched between two pieces of Toray carbon fiber paper (280 μm thick) placed between two stainless steel porous discs. Using the sample holder, adequate pressure was applied to the assembly to mechanically contact silver wire leads to the stainless steel discs. For a subset of the thicker films, electrical connection was made by the direct attachment of silver wires using colloidal silver paint (Ted Pella, #16032); such a method did not yield electrode responses different from that with Toray paper.

Impedance measurements were collected under the same environmental conditions as was used in the case of Pt-based cells. Because PdO has been observed to react with CsH_2PO_4 in oxidizing conditions at $\sim 240^\circ\text{C}$ (Appendix B), we verified that the formation of PdO, $\text{Pd}(\text{OH})_2$ and $\text{Pd}(\text{OH})_4$ (for which thermodynamic data was available) is unfavorable for all H_2 - H_2O atmospheres and temperatures examined in this

study. Based on these calculations, we expect Pd films to be stable throughout the symmetric cell experiments.

Cells were typically heated to $\sim 50\text{--}100\text{ }^{\circ}\text{C}$ in ambient air before flowing Ar with $\sim 0.03\text{ atm H}_2\text{O}$. After this, the temperature was raised to $150\text{ }^{\circ}\text{C}$ at $\sim 3\text{ }^{\circ}\text{C min}^{-1}$ and held at this temperature for 0.5–1 h until the water bubbler could be heated to supply adequate water partial pressures in the inlet Ar stream. Once an adequate $p\text{H}_2\text{O}$ level is attained, the cells were heated to $250\text{ }^{\circ}\text{C}$ at $2.5\text{ }^{\circ}\text{C min}^{-1}$ under H_2 flow.

D.2 Results and Discussion

D.2.1 Palladium Film Characteristics

Figure D.1 shows X-ray diffraction patterns of as-deposited 100 nm Pd films before and after electrochemical characterization; these patterns were considered representative of Pd films 100–300 nm thick. The breadth of the Pd peak at $2\theta \approx 40^{\circ}$ indicated that the deposited Pd was crystalline with small grains (was was the case for Pt films). In these particularly patterns, the main peak sharpened after electrochemical characterization (though not observed consistently between samples) and a small peak at $2\theta \approx 17.5^{\circ}$ appeared after electrochemical characterization. The peak at $2\theta \approx 17.5^{\circ}$ was not observed in other samples and does not match any peaks for Toray paper (used as a current collector) or for reaction product formed between PdO and CsH_2PO_4 at $240\text{ }^{\circ}\text{C}$ in air (via reactivity tests described in Appendix B). Aside from this peak, all other films 100–300 nm thick behaved similarly. As-deposited 10 nm Pd films generate peaks too

broad and low in intensity to be useful for comparing the film crystallinity before and after electrochemical characterization.

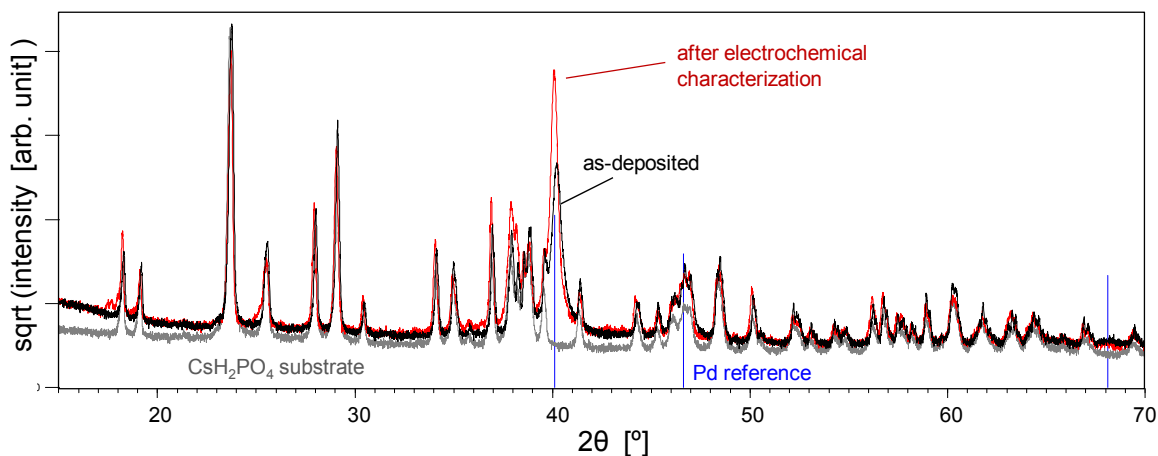


Figure D.1 X-ray diffraction pattern of 100 nm Pd films on top of CsH₂PO₄ before and after electrochemical characterization, shown alongside a CsH₂PO₄ pattern and Pd reference peaks.

Films 100, 200, and 300 nm thick (Figure D.2) appear to be intact and laterally connected. The cross-sections of the film, particularly in Figure D.2c, show film structures similar to those for Pt (Chapter 3). 10 nm Pd films were too thin to be visualized by SEM, so the thickness of 10 nm is estimated from the deposition time.

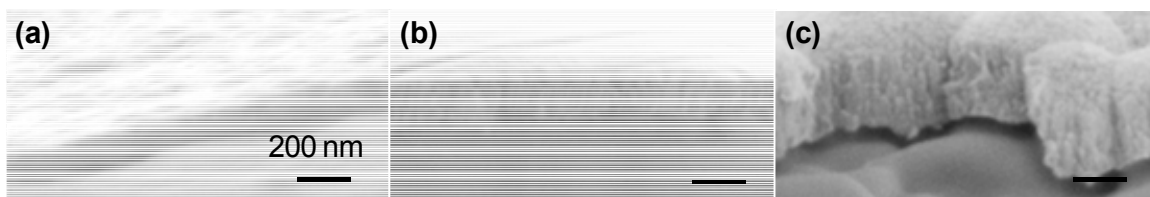


Figure D.2 SEM images of the cross-sections of Pd | CsH₂PO₄ | Pd cells showing as-deposited films Pd films (a) 100 nm, (b) 200 nm, and (c) 300 nm thick.

The characteristics of 10 nm Pd films were different from those of thin Pt films (e.g., 7.5 nm). As-deposited Pd films showed finite values of sheet resistance, comparable to those measured for 7.5 nm Pt films. However, after electrochemical characterization, the sheet resistance was not measurable by a hand-held voltmeter, indicating a virtually non-existent electronic connectivity of the Pd films. This is consistent with SEM observations of the 10 nm Pd films before and after electrochemical characterization (Figure D.3). As-deposited films appeared conformal on the CsH_2PO_4 surface, revealing underlying grains ~ 300 nm to ~ 1 μm in size. After electrochemical tests at superprotonic conditions, however, the films aggregated into small Pd islands 100–200 nm in size.

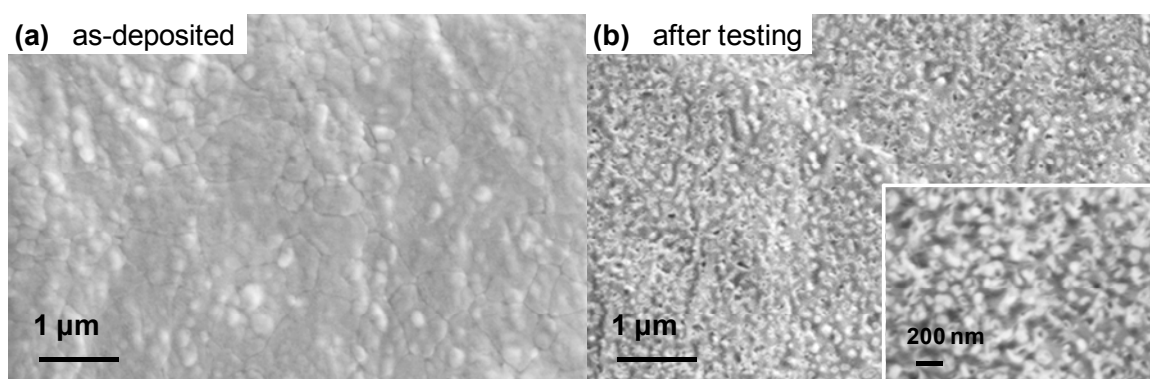


Figure D.3 In-plane SEM micrographs of 10 nm Pd films deposited on top of CsH_2PO_4 , comparing films (a) before and (b) after electrochemical characterization at ~ 250 $^{\circ}\text{C}$ in humidified H_2 -Ar atmospheres.

In-plane images of the films (Figure D.4 and Figure D.5, 100 nm films) show somewhat irreproducible results in terms of film stability. For most of the thicker films examined, the films remained intact after electrochemical characterization (Figure D.4). Some buckling of the films after testing was observed; this is in contrast to Pt films, for which only thick 375 nm films showed any noticeable buckling. For a subset of the films, the film quality degraded after electrochemical characterization (Figure D.5). The films

were penetrated by what appears to be the underlying CsH_2PO_4 . At two different locations across the boundary of the Pd film, Figure D.5b and Figure D.5c, respectively, the films segregated into small islands, with notably different microstructures across the boundary. (A fully masked region of the substrate onto which no Pd was deposited is shown in Figure D.5d for reference). By energy dispersive spectroscopy analysis of regions 1 and 2 (as marked in Figure D.5a), it was determined that region 1 has a lower Pd:Cs atomic ratio but a higher O:Cs ratio; the P:Cs ratios were comparable. That is, region 1 is comprised of a greater amount of oxygen but less of Pd. The P:Cs ratio for both regions were between 1.5 and 2, rather than the expected value of 1 for CsH_2PO_4 . Based on the sampling volume of EDS and the XRD results for CsH_2PO_4 (Figure D.1), this observation implies a P-rich region near the surface of the CsH_2PO_4 disc.

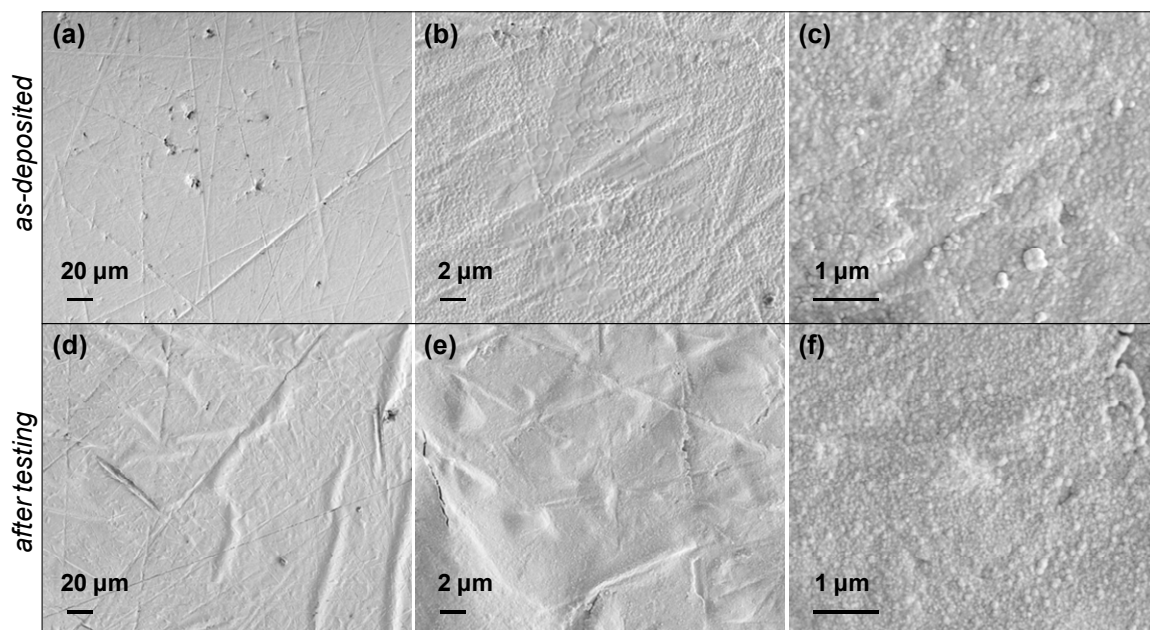


Figure D.4 In-plane SEM micrographs of 100 nm Pd films deposited on top of CsH_2PO_4 , comparing the films (a–c) before and (d–f) after electrochemical characterization at $\sim 250^\circ\text{C}$ in humidified H_2 -Ar atmospheres.

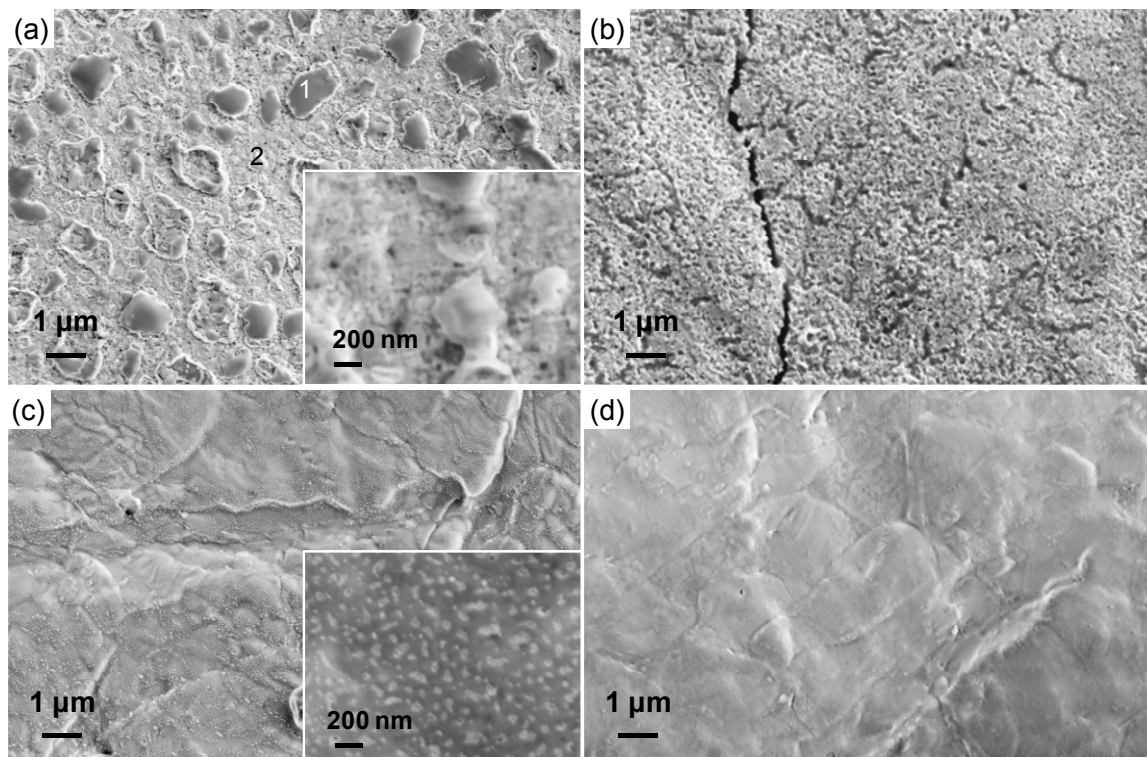


Figure D.5 In-plane SEM micrographs of 100 nm Pd films deposited on top of CsH_2PO_4 (a) near center of film/disc, (b) Pd-rich region and (c) CsH_2PO_4 -rich region at the Pd- CsH_2PO_4 boundary, and (d) masked CsH_2PO_4 surface with no Pd present, for reference. Images were taken after electrochemical characterization at $\sim 250^\circ\text{C}$ in humidified H_2 -Ar atmospheres.

The source of the differences between the two sets of films shown in Figure D.4 and Figure D.5 requires further exploration. One possible explanation is that variations in the length of time as-fabricated symmetric cells reside at ambient conditions before characterization or in the procedure for ramping the cell temperature to superprotonic conditions can lead to the (temporary) formation of Pd oxide. Such variations in the temperature and gas environment history may affect reproducibility in the Pd | CsH_2PO_4 | Pd system.

D.2.2 Characteristics of Impedance Spectra

Figure D.6 shows an impedance spectrum for a Pd | CsH₂PO₄ | Pd symmetric cell with 100 nm Pd, 10 mm in diameter. The spectrum was shifted by its ohmic offset for ease of analysis and corrected for inductance effects. Four features are visible in the spectrum. An arc at frequencies above 133 kHz (originally masked by system inductance, as indicated in the figure) is attributed to constriction (Appendix C.3). As the frequency is decreased, three additional arcs follow, denoted as “HF”, “MF”, and “LF”, with the intermediate MF arc at ~ 620 Hz being convoluted with the HF and LF arcs. The raw data (including ohmic offset) were fitted to an empirical equivalent circuit (Figure D.7) and used to extract the resistance (width) of each arc. Each parallel RQ sub-circuit corresponds to each of the four arcs; an inductor was included to account for system inductance and a resistor for proton transport through CsH₂PO₄. (In Figure D.6, the extracted values for the ohmic offset and inductance were used in order to perform the offset and inductance corrections.)

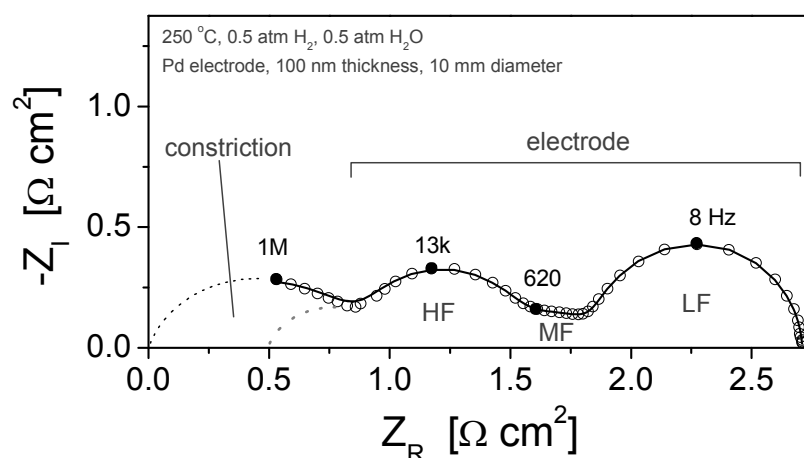


Figure D.6 Impedance spectrum for a Pd | CsH₂PO₄ | Pd symmetric cell with 100 nm Pd films 10 mm in diameter, collected at ~ 250 °C in H₂-H₂O with ~ 0.5 atm H₂O. The solid line is a fit to the equivalent circuit shown in Figure D.7. The thick dotted line at high frequency denotes raw data (before inductance correction) and thin dotted line serves as a guide to the eyes.

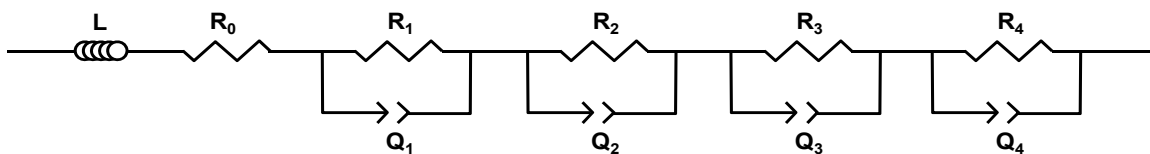


Figure D.7 Equivalent circuit model for the Pd | CsH₂PO₄ | Pd symmetric cell. L = inductance, R_0 = electrolyte resistance, R_i = resistance of process i , and C_i = capacitance of process i .

Although the impedance spectrum in Figure D.6 shows three electrode arcs, data acquired from over 30 cells with film thicknesses of 100–300 nm and diameters of 1–15 mm revealed variations in the shape of the spectra. The appearance of the MF arc was irreproducible, neither dependent on film thickness nor diameter. Figure D.8 shows three impedance spectra for Pd films of three different thicknesses. Based on their characteristic frequencies, it is evident that the HF and LF arcs are present, but the MF arc is masked, surfacing as a small separation between the HF and LF arcs (Figure D.8b). This separation is most noticeable for the 100 nm film and occurred to varying degrees depending on the sample. Although the shape of the spectra varies across samples, the total electrode resistance is fairly reproducible and exhibits no dependence on film thickness (Figure D.6 and Figure D.8a).

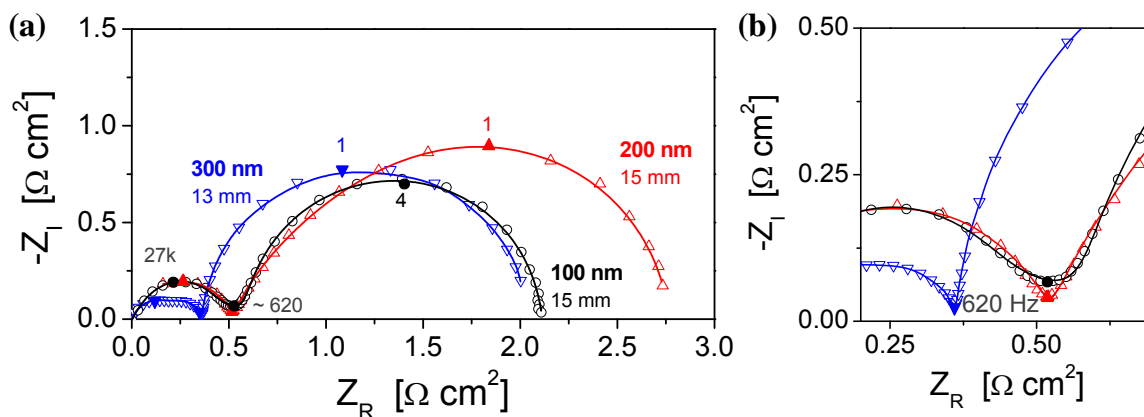


Figure D.8 Select impedance spectra collected at $\sim 250^\circ\text{C}$ in H_2 - H_2O with ~ 0.5 atm H_2O for 100, 200, and 300 nm thick Pd films showing (a) the HF and LF arcs and (b) a partially hidden MF arc.

D.2.3 Effect of Palladium Film Geometry

Despite the apparent variability of the impedance response, we fit the spectra to an equivalent circuit similar to that shown Figure D.7 but with one less parallel RQ sub-circuit depending on whether or not the MF arc is visible. Based on the fit results, we assigned the constriction, HF, MF and LF arcs based on their characteristic frequencies and plotted their corresponding resistances as functions of film diameter (Figure D.9) and thickness (Figure D.10). From Figure D.9, it is immediately clear that the resistance of each electrode process scales with the film area. Based on this result, we plot the area-normalized resistance as a function of thickness (Figure D.10) and show that the electrode processes do not depend on thickness, consistent with the impedance spectra shown in Figure D.8a.

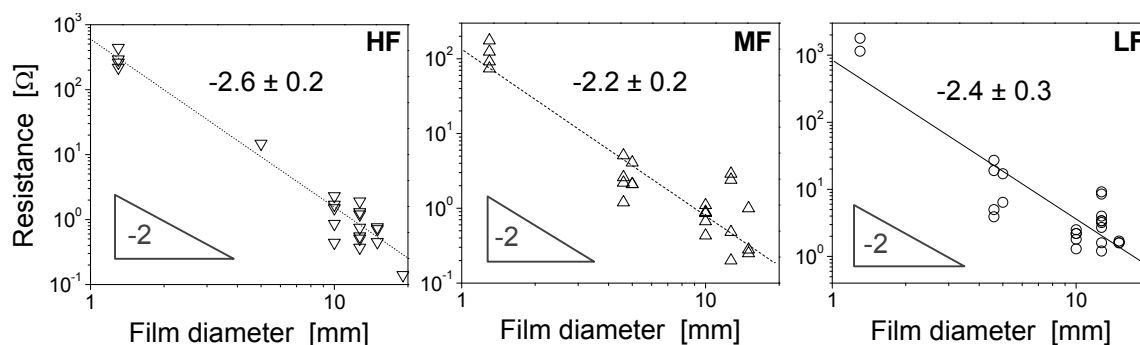


Figure D.9 Plots of electrode resistance ($\sim 250^\circ\text{C}$ in $\text{H}_2\text{-H}_2\text{O}$ with ~ 0.5 atm H_2O) as a function of film diameter. HF, MF and LF denote high-, mid-, and low-frequency arcs, respectively.

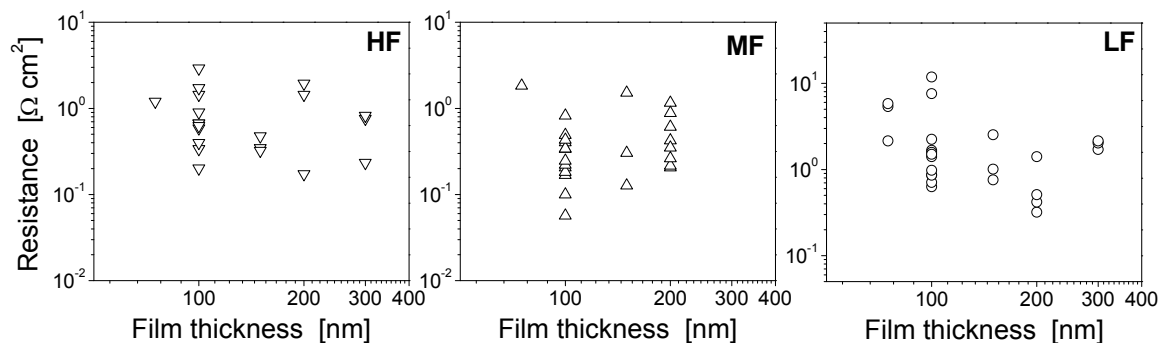


Figure D.10 Plots of area-normalized electrode resistance ($\sim 250^\circ\text{C}$ in $\text{H}_2\text{-H}_2\text{O}$ with ~ 0.5 atm H_2O) as a function of film thickness. HF, MF and LF denote high-, mid-, and low-frequency arcs, respectively. Slopes range between -0.6 to 0.3 with large errors.

D.2.4 Effect of Environmental Parameters

The effect of temperature, hydrogen partial pressure ($p\text{H}_2$) and water partial pressure ($p\text{H}_2\text{O}$) on the electrode processes were examined. Plots of the electrode resistance as a function of $p\text{H}_2$ and temperature for the cell presented in Figure D.6 are presented in Figure D.11a and Figure D.11b, respectively. The $p\text{H}_2$ reaction order and activation energy for each process is noted in the plot. Using similar plots for over 30 symmetric cells, the average reaction orders for $p\text{H}_2$ and $p\text{H}_2\text{O}$ (plot not shown) and the

activation energies were extracted and are tabulated in Table D.1, along with the corresponding values of the area-normalized electrode resistance (in units of $\Omega \text{ cm}^2$).

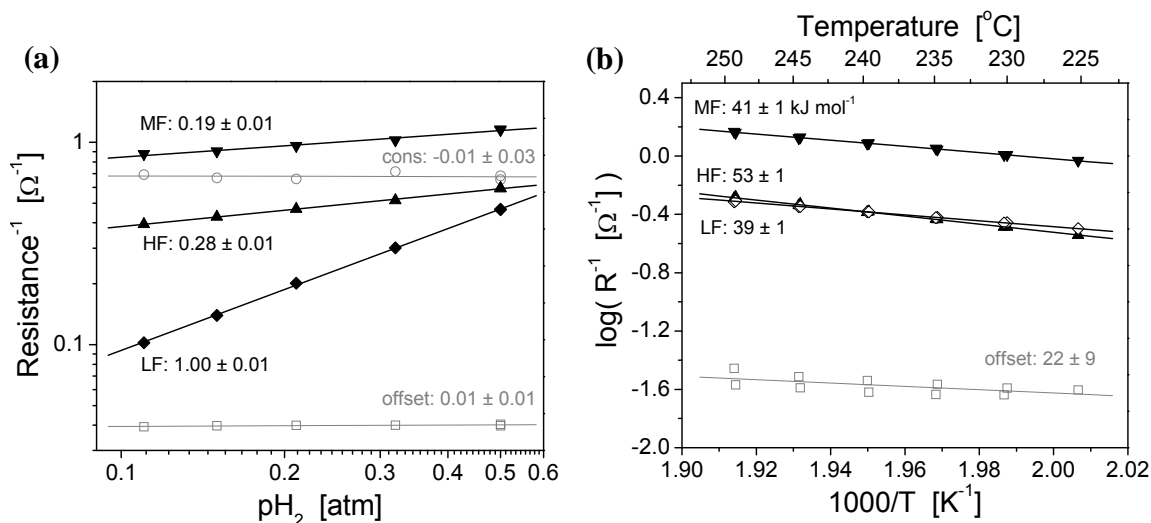


Figure D.11 Representative plots used for extracting (a) $p\text{H}_2$ reaction order and (b) activation energy. Shown are data for a $\text{Pd} | \text{CsH}_2\text{PO}_4 | \text{Pd}$ cell with 100 nm Pd, 10 mm dia.

Table D.1 $\text{Pd} | \text{CsH}_2\text{PO}_4 | \text{Pd}$ symmetric cell: average values of the area-normalized resistance, $p\text{H}_2$ and $p\text{H}_2\text{O}$ reaction orders and the temperature dependence (of $R_E^{-1} \times T$ for the offset and constriction arcs and R^{-1} for HF, MF and LF arcs). \tilde{R} = area-normalized resistance

arc	\tilde{R} [$\Omega \text{ cm}^2$]	$p\text{H}_2$ rxn order (250 °C)	$p\text{H}_2\text{O}$ rxn order (250 °C)	T [kJ mol^{-1}] ($p\text{H}_2 \approx p\text{H}_2\text{O} \approx 0.5 \text{ atm}$)
offset	—	0.02 ± 0.04	-0.02 ± 0.02	37 ± 9
constriction	—	0.01 ± 0.07	0.01 ± 0.05	38 ± 3
HF	0.6 ± 0.3	0.2 ± 0.2	0.05 ± 0.05	38 ± 21
MF	0.4 ± 0.3	0.4 ± 0.2	-0.03 ± 0.05	36 ± 9
LF	1.4 ± 0.6	1.0 ± 0.2	-0.12 ± 0.07	31 ± 6

The electrode resistances of all three processes displayed negligible dependence on $p\text{H}_2\text{O}$. This is in contrast to the Pt thin film electrode response which exhibited a reaction order of ~ 0.3 for all film thicknesses. The $p\text{H}_2$ dependence varies significantly between the arcs, with the HF arc displaying almost zero dependence while the MF and

LF arcs have stronger dependences of 0.4 ± 0.2 and 1.0 ± 0.2 , respectively. The high errors associated with the HF and MF arcs are a consequence of their smaller resistances such that convolution with one another and with the constriction arc induced larger errors during equivalent circuit fitting. The LF arc is notably more resistive than the remaining arcs and, thus, fitting errors associated with this process were smaller. The reaction order of 1 for the low-frequency arc is highly suggestive of a surface exchange step at the Pd | H₂ interface, similar to that observed for the 7.5 nm Pt film electrode. (The $p\text{H}_2$ reaction order for the 7.5 nm Pt film was found to be 0.74 ± 0.08 and includes residual contribution from hydrogen diffusion.) The activation energy of the LF process, $31 \pm 6 \text{ kJ mol}^{-1}$ process is also comparable to that for the 7.5 nm Pt film, $28 \pm 3 \text{ kJ mol}^{-1}$.

Based on the $p\text{H}_2$ reaction order of 0.4 (close to $\frac{1}{2}$) and the activation energy of $36 \pm 9 \text{ kJ mol}^{-1}$, it would be reasonable to hypothesize that the MF arc corresponds to hydrogen diffusion through Pd, with the lower activation energy relative to that for diffusion in Pt being attributed to a smaller influence from hydrogen trapping. However, a quick calculation of the expected resistance, based on known values of hydrogen diffusivity and solubility in Pd, yields a value that is three orders of magnitude smaller than the values obtained here. Specifically, for a temperature of 250 °C and hydrogen partial pressure of 0.5 atm, the solubility of hydrogen in Pd is $\sim 0.01 \text{ H/Pd}^{31}$ and the hydrogen diffusivity is $\sim 3 \times 10^{-9} \text{ m}^2 \text{ s}^{-1}$.¹²⁶ Using Equation (A.42), the area-normalized resistance is computed to be $4 \times 10^{-4} \Omega \text{ cm}^2$ for 300 nm Pd film (thickest film used in this study). The average experimentally determined value for the MF arc, $0.4 \Omega \text{ cm}^2$, is significantly larger than the computed value; any deviations in the computed value due to trapping effects would be unlikely to account for this difference.

D.2.5 Impedance Response of Layered Pt-Au Film Electrodes

Preliminary measurements of Pd-Au bilayers deposited on top of CsH_2PO_4 are presented in Figure D.12. (Note that the films in this figure are 5 mm in diameter, so the HF arc is convoluted with the constriction arc.) Surprisingly, the effect having Au either on top of Pd ($\text{Au} | \text{Pd} | \text{CsH}_2\text{PO}_4$) or between Pd and CsH_2PO_4 ($\text{Pd} | \text{Au} | \text{CsH}_2\text{PO}_4$) is minimal. In the case of $\text{Pd} | \text{Au} | \text{CsH}_2\text{PO}_4$, the high-frequency process appears to be less convoluted with the constriction arc, indicating that the HF arc corresponds to a process the metal $| \text{CsH}_2\text{PO}_4$ interface. However, the LF arc increases relative to the control ($\text{Pd} | \text{CsH}_2\text{PO}_4$), an unexpected result. In the case of $\text{Au} | \text{Pd} | \text{CsH}_2\text{PO}_4$, the impedance response displays no significant changes from the control. Overall, based on Figure D.12, we can conclude that the effect of Au on the impedance response of the Pd system is within the margin of scatter.

It should be noted that the $\text{Pd} | \text{CsH}_2\text{PO}_4$ spectrum plotted in Figure D.12 is consistent in shape and total width to those shown in Figure D.6 and Figure D.8. However, the film quality for these cells after electrochemical characterization (Figure D.5), is significantly degraded in comparison. That the impedance spectra are not dramatically different despite their varied film characteristics (Figure D.4 vs. Figure D.5) implies that the electrode response is not especially sensitive to film morphology.

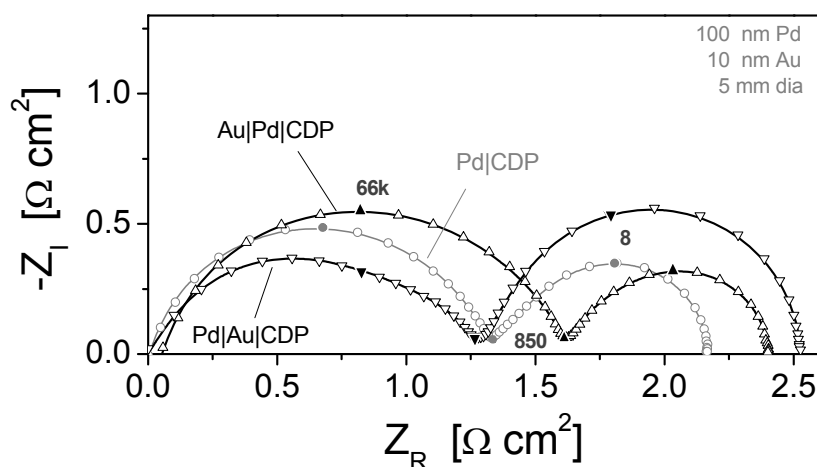


Figure D.12 Impedance spectra, collected at 250 °C in $\text{H}_2\text{-H}_2\text{O}$ with ~ 0.5 atm H_2O , for Pd | CsH_2PO_4 , Au | Pd | CsH_2PO_4 and Pd | Au | CsH_2PO_4 for which Pd and Au films were 100 nm and 10 nm, respectively.

D.2.6 10 nm Palladium Films

As shown in Figure D.3, 10 nm Pd films degraded significantly after testing. This is consistent with their impedance spectra (Figure D.13). The large values for the area-normalized resistance, $> 15 \text{ k}\Omega \text{ cm}^2$, reflect the lack of electronic connectivity in the films. Two arcs are visible, although the total resistance is dominated by the low-frequency arc. The observation that the two arcs are dramatically different in size, compared to the arcs in the impedance spectra of thicker intact films, is interesting since a lack of connectivity if the Pd film should result in the two arcs increasing by the same factor. This implies a difference in the reaction mechanism between thick, intact films and thin degraded films.

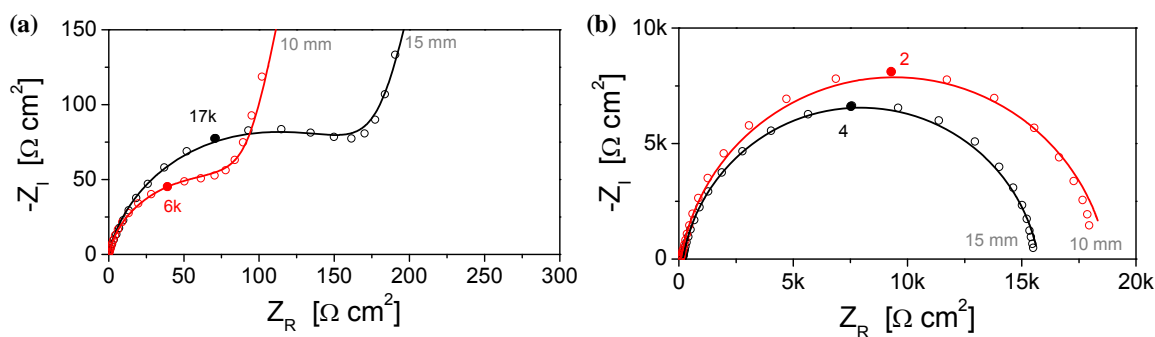


Figure D.13 Impedance spectra for Pd | CsH₂PO₄ | Pd cell (10 nm Pd films) collected at 250 °C in H₂-H₂O with ~ 0.5 atm H₂O: (a) high-frequency arc and (b) low-frequency arc.

D.2.7 Comparison to Platinum

The total Pd electrode resistance, averaged across ~ 30 symmetric cells, was found to be $2.2 \pm 0.8 \Omega \text{ cm}^2$. Because the rate-limiting steps for hydrogen electro-oxidation over Pd do not depend on thickness and therefore are dominated by interfacial processes, it is expected that a direct comparison of the Pd film results to those for ultra-thin Pt films (for which interfacial effects dominate) would provide an adequate comparison of their relative interfacial activities. From Chapter 3, we found that for a 7.5 nm Pt film, the resistance was $\sim 3.1 \pm 0.5 \Omega \text{ cm}^2$, whereas the estimated interfacial resistance was (coincidentally) $2.2 \Omega \text{ cm}^2$, both of which are, to within experimental scatter, comparable to the Pd electrode resistance. This implies that the *interfacial* activity of Pd is comparable to, if not better than, that for Pt.

Although the activity of the Pd film electrode indicates that Pd may surpass Pt in the anode of solid acid fuel cells, the degradation of thin Pd films precludes fabrication of comparably thin films for application purposes. One solution to this problem is to fabricate layered Pt-Pd electrodes. The electrode resistance of each of the three Pd arcs

(Table D.1) has, on average, a value that is smaller than the total electrode resistance of 7.5 nm Pt. Therefore, determining the identity of these rate-limiting processes (and that for thin Pt films) can be extremely valuable for designing an optimal Pd-Pt bilayer catalyst. For example, *if* the interfacial process in Pt and the LF arc in Pd both correspond to surface exchange at the metal | gas interface, and the HF arc in Pd corresponds to charge transfer, then the Pd | Pt | CsH₂PO₄ configuration may minimize the total electrode resistance. This is because Pt | CsH₂PO₄ exhibits no charge transfer resistance in its impedance response and gas | Pd | CsH₂PO₄ exhibits a lower surface exchange resistance than gas | Pt | CsH₂PO₄. One can entertain additional film configurations, depending on the identity of the Pd arcs.

D.3 Summary

- 1) Pd films 100–300 nm thick were found to have a total electrode resistance of $2.2 \pm 0.8 \, \Omega \, \text{cm}^2$. Three electrode processes were observed, all of which scaled with film area but not film thickness.
- 2) 10 nm Pd films degraded significantly after electrochemical testing.
- 3) Preliminary measurements of Pt-Au bilayer films revealed a negligible effect of Au on the rate-limiting steps.
- 4) Reproducibility appeared to be problematic for Pd films (compared to Pt films). It is possible that as-deposited films have a surface oxide, or a surface oxide may form during initial heating of the sample. Reaction between the resulting Pd oxide layer and CsH₂PO₄ may be the source of variability in the impedance response.

- 5) Despite possible oxide formation, the electrode activity of Pd is still comparable to that for Pt. Therefore, Pd remains a promising anode for solid acid fuel cells.

D.4 Recommendations for Future Studies

- 1) It is likely that more reproducible results could be attained by proper handling of the films. After loading the symmetric cell, the reactor should be flushed with Ar at room temperature before heating up the sample in H₂. It is possible that as-deposited Pd is already partially oxidized, but based on the fact that no reaction was observed between nanoparticle Pd and CsH₂PO₄ at 150 °C in air after 48 h, it should be possible to attain stable films for characterization despite some exposure to air. Thus, oxidation of Pd (if any) is more likely due to the temperatures and gas environments experienced by the samples during ramp-up.
- 2) The electrochemical response of the Pd-Au bilayer systems was surprising and should be reproduced. The results would be useful for identifying the rate-limiting steps associated with the Pd electrode arcs.
- 3) Pt-Pd bilayer films would be valuable for investigating not only the rate-limiting steps for the Pd film electrode but also for designing a high-activity electrode.

Appendix E Nickel Thin Films

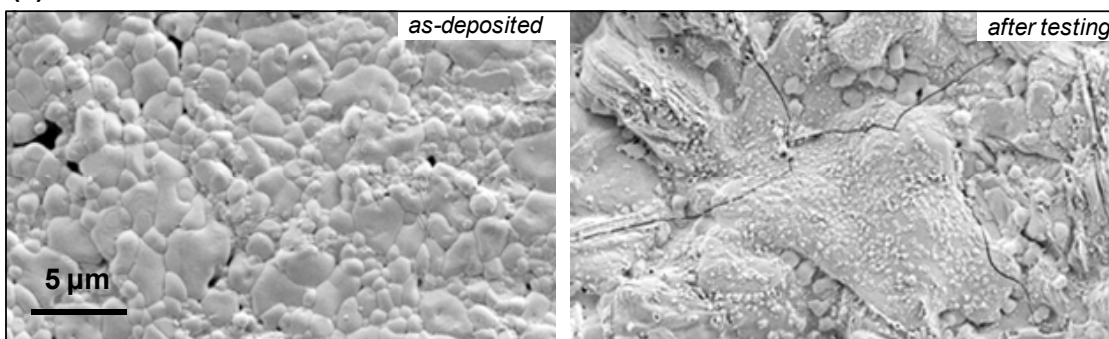
In this section, we discuss attempts to study hydrogen electro-oxidation over sputtered Ni films, fabricated using deposition conditions similar to those used for Pt and Pd. However, films appeared to be unstable after electrochemical characterization. As-deposited Ni films appeared intact, but after electrochemical characterization at 250 °C, 150 and 400 nm thick Ni films aggregated into islands (Figure E.1). In the case of 400 nm films (Figure E.1b), the morphology of what appears to the substrate surface also changed, appearing smoother with poorly defined grain boundaries. Using energy dispersive spectroscopy, we found no significant composition difference between the islands and the smooth matrix, that is, Ni, P, and O were present in both regions, implying that Ni, though not clearly visible, is also present in regions which have morphologies similar to CsH_2PO_4 .

Interestingly, films which were not electrochemically characterized but heat-treated at similar conditions remained intact (Figure E.2). 100 nm films heat-treated at superprotonic conditions, with and without electrochemical testing, yielded completely different results. Films which were only heat-treated, Figure E.2(a,d), displayed characteristics similar to those observed for Pt films after testing. However, films which were electrochemically characterized with a 10 mV perturbation (about 0 V) showed severe degradation. It was not possible to distinguish between film and substrate (Figure E.2b); the surface was comprised of uniformly round grains, significantly larger than those in the starting material (Figure E.2c). This is consistent with the observation that

the films disappeared completely (Figure E.2d) leaving behind a yellowish tint on the CsH_2PO_4 substrate. The substrate itself also appeared to have degraded and was embedded with fibers from carbon paper.

The physical characteristics of the substrate after electrochemical characterization are consistent with dehydration of CsH_2PO_4 , but several repeated and well-controlled experiments (with adequate humidity levels) confirm that $\text{Ni} \mid \text{CsH}_2\text{PO}_4 \mid \text{Ni}$ cells indeed degrade, usually with the film disappearing and the substrate deforming slightly. These observations are highly suggestive of a reaction between CsH_2PO_4 and Ni. It is worthwhile to note that reaction between NiO and CsH_2PO_4 was not observed in even after 48 h in air at superprotonic conditions (Appendix B).

(a) ~150 nm Ni on CDP



(b) ~400 nm Ni on CDP

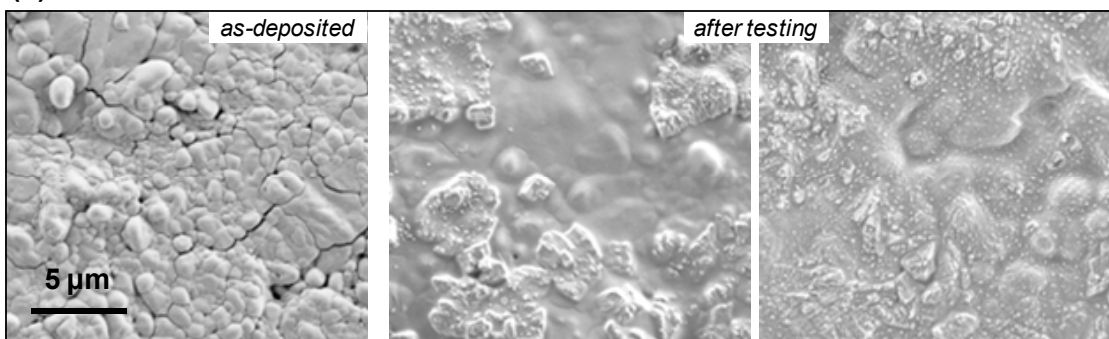


Figure E.1 SEM micrographs of Ni films deposited on top of CsH_2PO_4 , as-deposited and after electrochemical characterization at 235 °C in humidified H_2 gas with ~ 0.4 atm H_2O : (a) 150 nm Ni films (b) 400 nm Ni films.

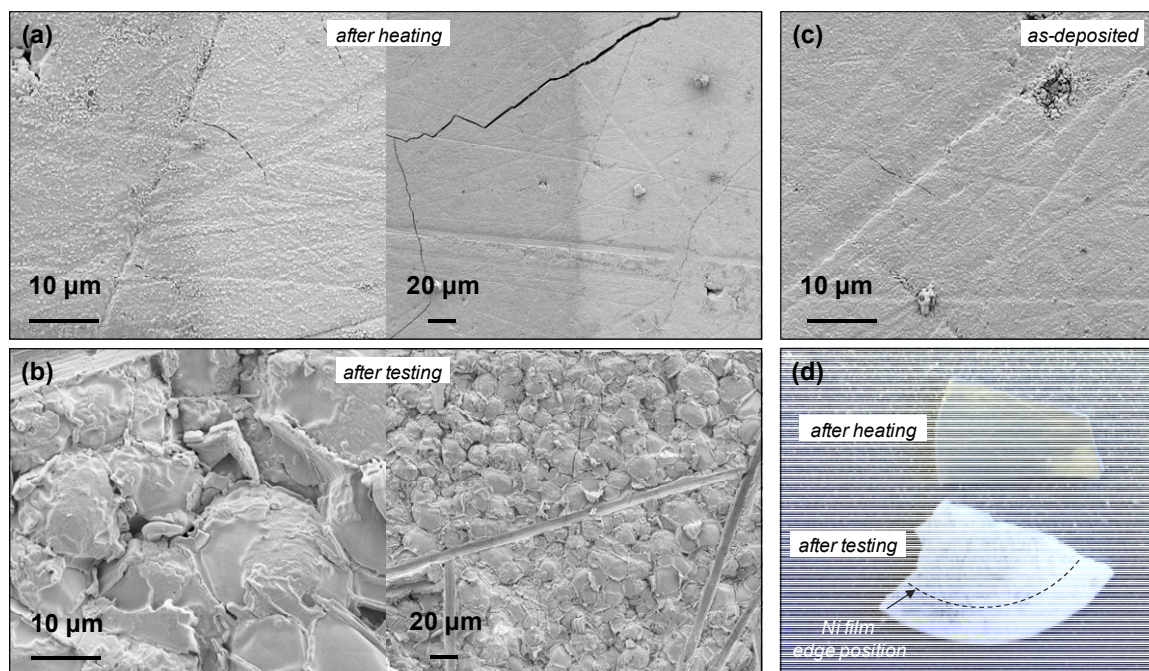


Figure E.2 100 nm Ni films after (a) heat treatment and (b) electrochemical characterization at 250 °C in humidified H_2 gas with ~ 0.5 atm H_2O compared to (c) as-deposited films. Shown in (d) are photographs of the two samples; the dotted line marks the original $\text{Ni-CsH}_2\text{PO}_4$ boundary.

X-ray diffraction patterns corresponding to the samples in Figure E.2(b–c) are shown in Figure E.3. Patterns collected for as-deposited Ni films and after electrochemical characterization contain peaks for CsH_2PO_4 . However, the Ni peak, initially small for as-deposited films, disappears completely after electrochemical characterization, implying that either Ni is no longer crystalline or it has reacted with or dissolved into CsH_2PO_4 . No peaks for NiO were observed before or after electrochemical characterization.

It is worthy to note that as-deposited Ni films obtained by thermal evaporation yielded Ni diffraction peaks with higher relative intensity compared to films obtained by sputter deposition, as shown in Figure E.4 for 400 nm Ni films obtained by both

deposition methods. Thermally evaporated films were stable after heat treatment (not shown), but electrochemical characterization has not yet been carried out.

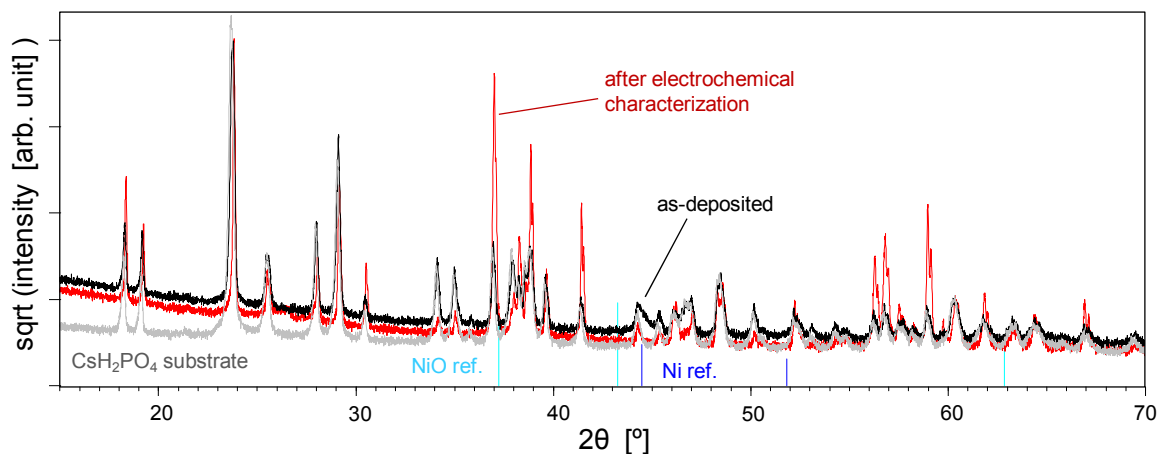


Figure E.3 X-ray diffraction patterns of 100 nm Ni films on top CsH₂PO₄ before and after testing, shown alongside a pattern for CsH₂PO₄ and reference peaks for Ni and NiO. These Ni patterns correspond to the cell shown in Figure E.29(b–c).

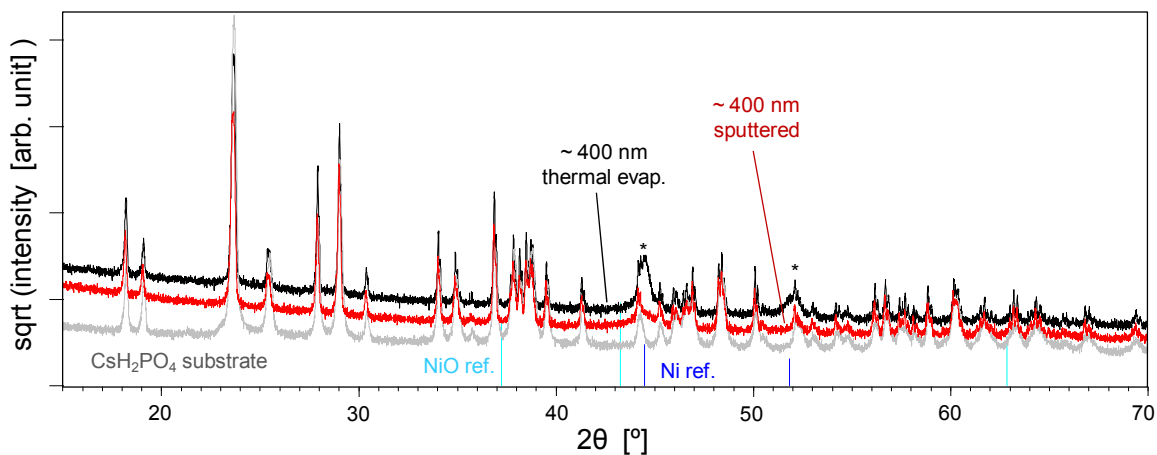


Figure E.4 X-ray diffraction patterns of as-deposited 400 nm Ni films on top CsH₂PO₄ fabricated by thermal evaporation and sputter deposition, alongside pattern for CsH₂PO₄ and reference peaks for Ni and NiO.

Appendix F Pt | CsHSO₄ by Atomic Force Microscopy

F.1 Experimental Details

F.1.1 Instrumentation and Setup

Figure F.1 shows photographs of the main components of the electrochemical AFM setup. The copper hotplate, by design, is electrically insulated from the rest of the sample stage (Figure F.1a), and the temperature is controlled using an external temperature controller (Lakeshore Cryotronics, Inc.). The sample (a CsHSO₄ half-cell, in this photograph) was placed on top of a silver mesh in contact with the copper plate. The silver mesh provided a way to make electrical connection to the counter electrode on the underside of the sample while allowing for gas transport to the counter electrode. Half-cells were clipped onto the stage, as shown, and thermocouples were attached using Kapton tape. In this particular photograph, two thermocouples were present, one attached to the cell surface (T_{surf}) and the other to the hotplate surface (T_{plate}), although the latter was not always used in typical measurements. The sample stage attaches to the microscope under the piezoelectric scanner head (Figure F.1b) and inside the environmental chamber. Gases were fed via flexible plastic tubing and vented into open air at the outlet. The entire assembly was placed into a home-made copper Faraday cage which sat in a vibration isolation chamber (Figure F.1c). Cables exiting this chamber in the photograph were those for electrical measurement (left three cables) and hot stage temperature control (right cable).

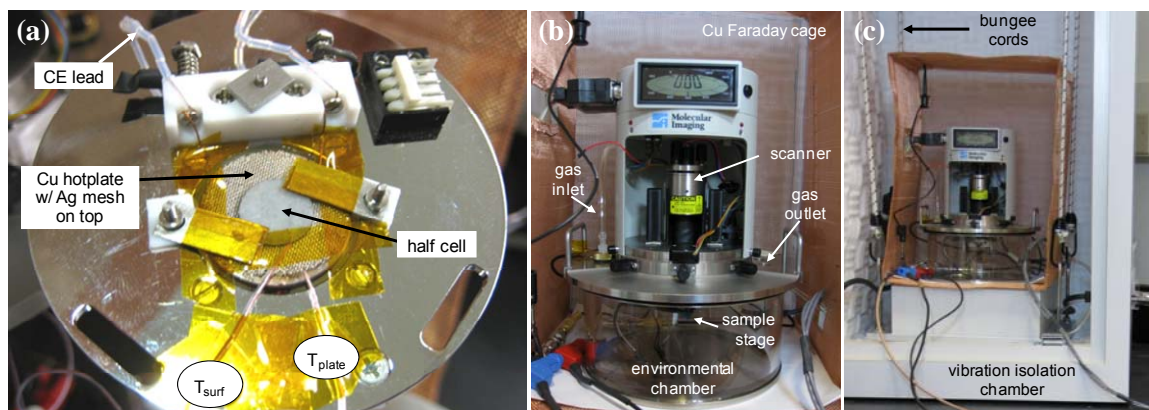


Figure F.1 Photographs of experimental setup for electrochemical AFM: (a) heated sample stage, (b) microscope with environmental chamber, and (c) Faraday cage and vibration isolation unit for noise reduction.

F.1.2 Sample Heating

For imaging at elevated temperatures, heat conductive pastes (often also electrically conducting) pastes are typically used to ensure good thermal contact between the sample and hotplate. In the case of electrochemical AFM measurements, this is not ideal and therefore, we relied on physical contact of the sample and hotplate for heat transfer. To examine how the resulting temperature gradient can influence electrochemical AFM measurements on CsHSO_4 , we constructed a cell similar to the desired AFM configuration except that the top surface was painted with conductive silver paste (Figure F.2); this enabled measurement of the proton conductivity of CsHSO_4 to determine how it varies with the surface and hotplate, both of which are monitored simultaneously (Figure F.1a). As shown in Figure F.3, a relatively large temperature gradient was found to exist across the half-cell, and, moreover, the gradient increases with the set point temperature. For example, to reach the superprotonic transition

temperature of $\sim 141^\circ\text{C}$, a setpoint temperature of $\sim 168^\circ\text{C}$, or a hotplate temperature of $\sim 158^\circ\text{C}$, is required, implying a temperature gradient of $\sim 17^\circ\text{C}$ across the CsHSO_4 disc. However, simultaneous conductivity measurements of the CsHSO_4 sample showed that by a surface temperature of $\sim 135^\circ\text{C}$, the sample had already reached its superprotonic phase. This implies that either the method for measuring the surface temperature is not accurate or, more likely, that the CsHSO_4 surface need not be above the superprotonic temperature as long as the rest of the sample is sufficiently heated (possibly inducing phase transformation across the entire sample).

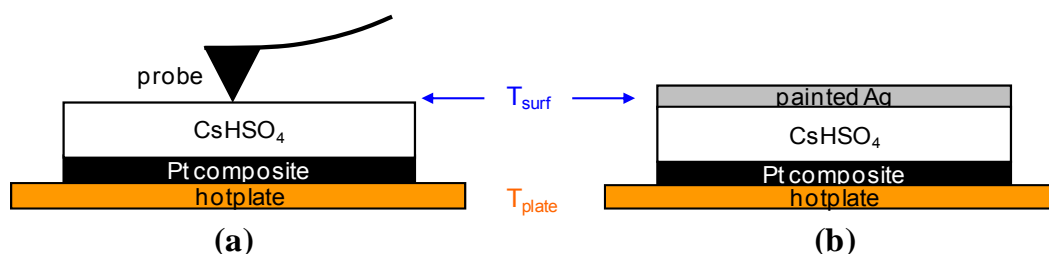


Figure F.2 Schematic of the CsHSO_4 cell configuration: (a) typical half-cell configuration for electrochemical AFM and (b) configuration for CsHSO_4 conductivity measurements and temperature calibration.

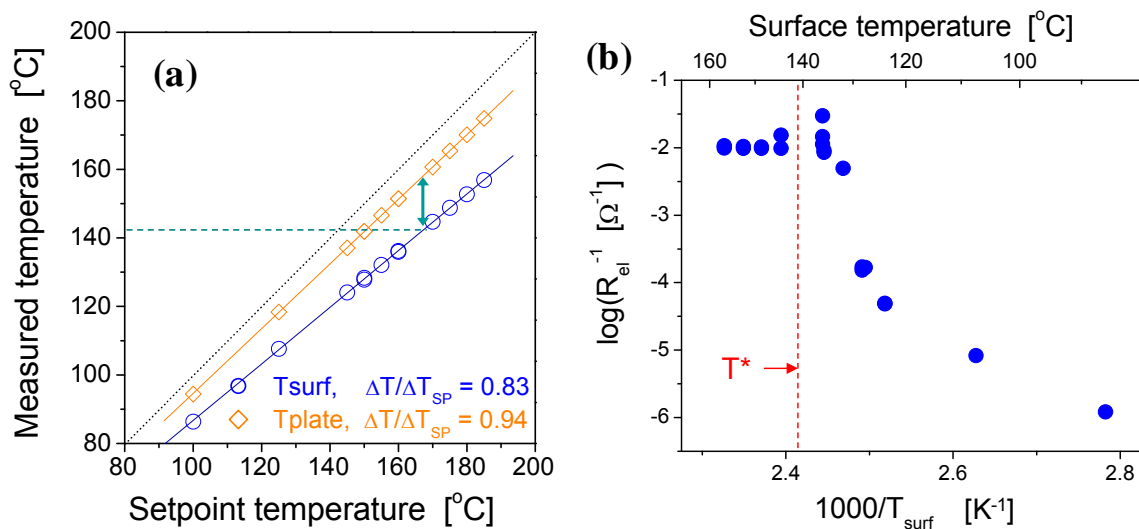


Figure F.3 Analysis of the temperature gradient across CsHSO₄: (a) a plot of the measured temperatures, T_{surf} and T_{plate} against the setpoint temperature. Dotted black line denotes slope of 1, and (b) the inverse resistance for proton conduction in CsHSO₄ as a function of the surface temperature. Dotted line is the reported phase transition temperature of 141 °C.

F.2 Data Analysis

F.2.1 Open- and Short-Circuit Corrections

Unlike conventional electrical measurements, electrochemistry by AFM requires extra consideration because of the extremely low currents that are measured. The most important is the open-circuit correction which is an indication of extraneous, high impedance contributions which are in parallel with the sample of interest during electrochemical measurement. A primary component of the open correction is the stray capacitance, resulting from a dielectric residing between the two electrical cables/leads attached to the sample of interest. Figure F.4 is an illustration of how stray capacitance can influence experimental measurements. Given two parallel RC sub-circuits in series (Figure F.4a), we can visualize how a capacitor, C_s , in parallel with the circuit (Figure F.4b) can affect the resulting impedance response. For arbitrarily selected circuit element

values ($R_1 = R_2 = 100 \text{ G}\Omega$, $C_1 = 1 \text{ pF}$, $C_2 = 10 \text{ pF}$), we generated spectra using various values of stray capacitance (Figure F.4c). From Figure F.4c, it is clear that a stray capacitance comparable to the cell capacitance will result in a masking of the processes. If unaware of the presence of stray capacitance, one would fit the data with two parallel RC sub-circuits (Figure F.4c) thereby obtain errors for the extracted resistor and capacitor values (results not shown). These errors increase with the value of C_S ; in the limit of very high values of C_S , only one arc with a resistance of $2R_1$ would be visible; the capacitance of this arc will correspond to the stray value, masking the true capacitance of the electrical process of interest. On the other hand, for stray capacitance values which are small compared to those for the sample of interest, stray capacitance will not play a significant role in the total impedance response and can therefore be neglected; this is usually the case for conventional measurements.

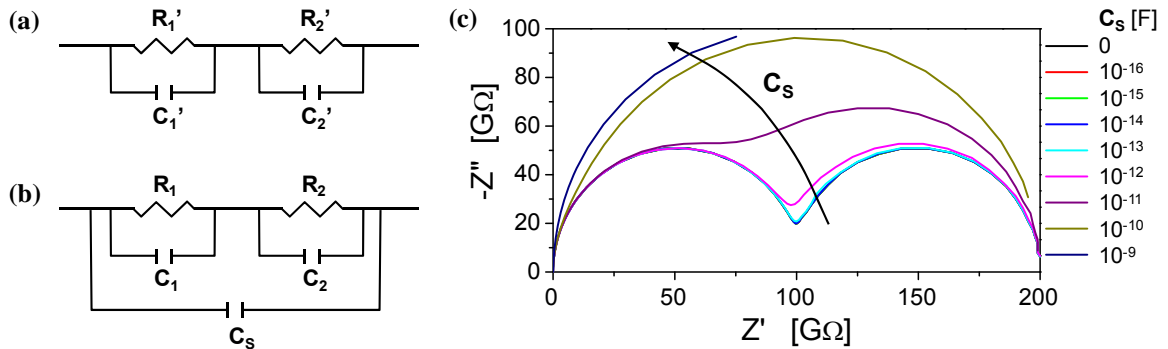


Figure F.4 Illustration of how stray capacitance affects two arbitrary processes: (a) two parallel RC sub-circuits representing the processes of interest, (b) stray capacitance, C_S , in parallel with processes of interest (c) simulation results of the circuit shown in (b) for $R_1 = R_2 = 100 \text{ G}\Omega$, $C_1 = 1$ and $C_2 = 10 \text{ pF}$ and $C_S = 0\text{--}1 \text{ nF}$.

To measure the open correction in the electrochemical AFM system, the probe was withdrawn from the sample surface and the impedance spectrum measured. Although not presented here, the separation distance between the AFM probe and the sample surface did not impact the results of the open-circuit measurement, indicating that the capacitance of air between the probe and sample is negligible compared to contributions from cables and instrumentation. In the electrochemical AFM experimental setup, the stray capacitance was not found to be fixed value. Instead, the open correction measured for the system was found to depend strongly on the internal circuitry of the potentiostat/frequency response analyzer (Figure F.5a); as the current range is varied from 3 pA to 300 mA (where the current range is indicated by its upper current limit), the impedance modulus, $|Z_{stray}|$, decreases. Thus, given that this stray impedance, Z_{stray} , is in parallel with cell impedance, Z_{cell} , (Figure F.5b) measurements performed using a higher current range (of the instrument) will have a greater contribution from spurious effects.

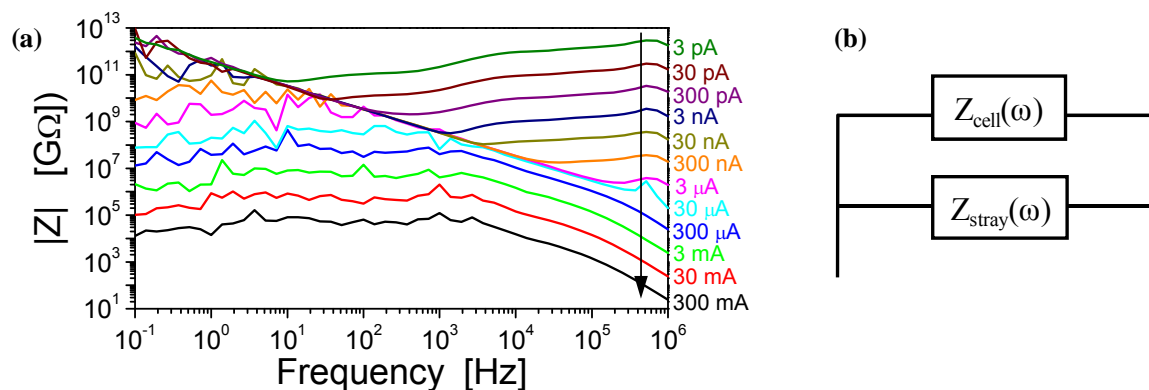


Figure F.5 (a) Bode magnitude plot for open circuit as a function of the current range selected in instrumentation, and (b) a circuit showing how open-circuit resistance (or stray capacitance) affects the cell impedance

To correct for the data collected by AFM, a point-wise open-circuit correction must be applied to the raw data, since a given measurement spans two or three current ranges. To determine the formula for applying the correction, one only needs the expression

$$\frac{1}{Z_{cell}(\omega)} = \frac{1}{Z_{meas}(\omega)} - \frac{1}{Z_{stray}(\omega)} \quad (F.1)$$

where Z_{cell} is the desired, corrected cell impedance, Z_{meas} is the as-measured impedance, and Z_{stray} is the open correction. Only algebraic manipulation of the real and imaginary components is required to compute the stray-corrected cell impedance. This expression is computed at each frequency point; the value of Z_{stray} used at each frequency depends on the specific current range selected by the instrument. Such a point-wise correction was applied to all experimental data collected using the AFM system. An example of an open-circuit correction is shown in Figure F.6 for the Pt | CsHSO₄ system.

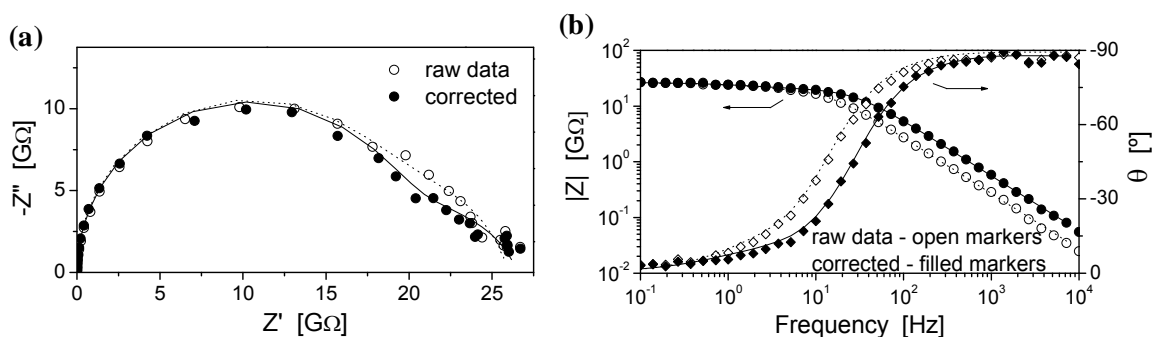


Figure F.6 Representative (a) Nyquist and (b) Bode-Bode plots collected at -1.1 V before and after applying a point-wise open-circuit correction. Data presented are from the Pt | CsHSO₄ system at ~ 150 °C in air, obtained using Probe 6 listed in Table 4.1.

Short corrections are not expected to be as critical for a system which has extremely large impedances. This is confirmed by a measurement of the contact resistance between a Pt-coated AFM probe and Au foil (Figure F.7). The impedance modulus of $5\text{ k}\Omega$ and phase angle of zero across all frequencies indicate a purely resistive response, as expected for a metal-to-metal contact.

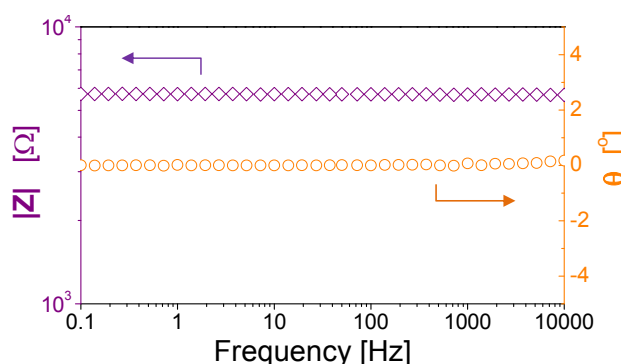


Figure F.7 Representative short-circuit measurement for a Pt-coated AFM probe in contact with a piece of Au foil with a contact force of $\sim 0.06\text{ }\mu\text{N}$. The contact resistance is $5\text{ k}\Omega$ and the phase angle, θ , is zero at all frequencies, consistent with a purely resistive response.

F.2.2 Measurement Stability

Thermal drift is an important consideration when performing AFM measurements, as fluctuations in temperature can affect the piezoelectric response of the AFM scanner which controls the x - y - z position of the probe. Thermal drift at elevated temperatures is more severe than at room or low temperature measurements typical of conventional AFM measurements. Figure F.8 shows an AFM image taken at $\sim 150\text{ }^{\circ}\text{C}$ before and after collecting series of cyclic voltammograms and impedance spectra, over the course of $\sim 5\text{ h}$. By tracking the features of the image, the drift was determined to be 0.1 nm s^{-1} . This drift implies that an electrochemical measurement must be performed

quickly enough to avoid traversing a long distance which can result in a large variation in electrochemical response. For this reason, cyclic voltammetry is preferred for gathering data for quantitative analysis. That is, the portion of data in cyclic voltammograms used for spatial variation analysis, i.e., the return scan of the cathodic branch, takes only ~ 30 s to complete; this corresponds to a drift of ~ 3 nm, sufficiently small given the AFM tip radius of ~ 40 nm.

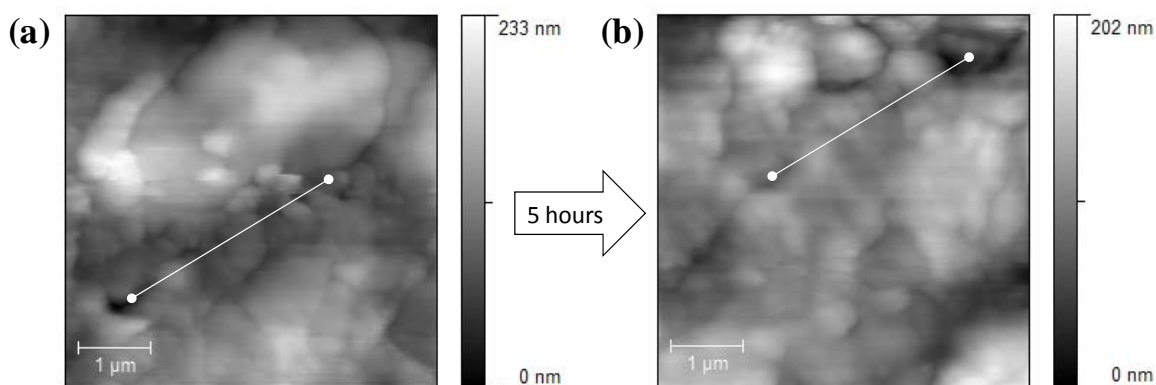


Figure F.8 Topographical AFM image of a CsHSO_4 surface (a) before and (b) after acquisition of spatial variation data. Based on this image, a drift rate of 0.1 nm s^{-1} was estimated.

Because of thermal drift issues, it is important to determine that any features in the impedance spectra are not artifacts of drift. We verified that the appearance of two arcs in the impedance spectra was not due to transient effects; Figure F.9 shows that two spectra collected consecutively, with frequencies swept in opposite directions, yield identical impedance responses.

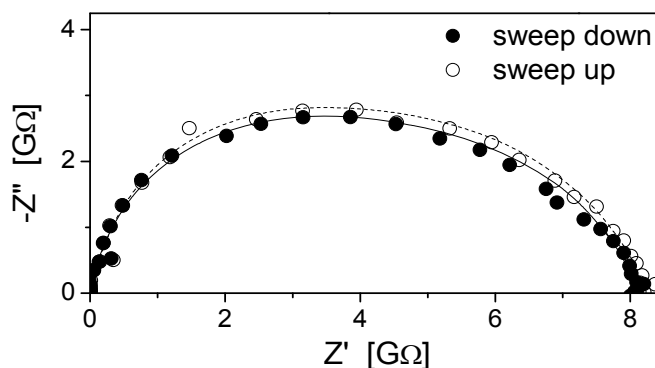


Figure F.9 Two impedance spectra collected consecutively at an applied bias of -1.0 V (using Probe 3 listed in Table 4.1), with the second measured by sweeping the frequency in the opposite direction of the first. The agreement between the two spectra confirms that the shape of the spectra is not a transient artifact. Spectra were acquired at ~ 150 °C in air (~ 0.03 atm H_2O).

F.2.3 Analysis of Cyclic Voltammograms

Raw cyclic voltammetry data were corrected for a non-zero offset current by fitting to a Butler-Volmer expression (Equation 4.5) with an added constant which typically amounted to 10^{-13} A. A consequence of such a correction is the increased scatter that appears at low overpotentials in the Tafel plots (Figure 4.6). For quantitative analysis of oxygen reduction kinetics, capacitive (transient) effects must be minimized, and thus, voltammograms collected at low scan rates are ideal. We verified that a scan rate of 25 mV s^{-1} employed for acquiring cyclic voltammograms for spatial variation studies does not significantly affect the extracted value of α , implying a negligible impact on the conclusions drawn from data presented here. Figure F.10a shows cyclic voltammograms collected at various scan rates, while Figure F.10b shows α values extracted from fitting of the data to Equation 4.6 (specifically, the linear regime of the Tafel plots, between -0.95 and -0.6 V). Extracted α values range from 0.35 at 400 mV s^{-1} to 0.40 at 5 mV s^{-1} ; the deviation in α for the data collected at 25 mV s^{-1} from that at 5 mV s^{-1} , ± 0.01 , is well

within the variation observed spatially (± 0.1 across six different Pt | CsHSO₄ systems. Figure 4.8b).

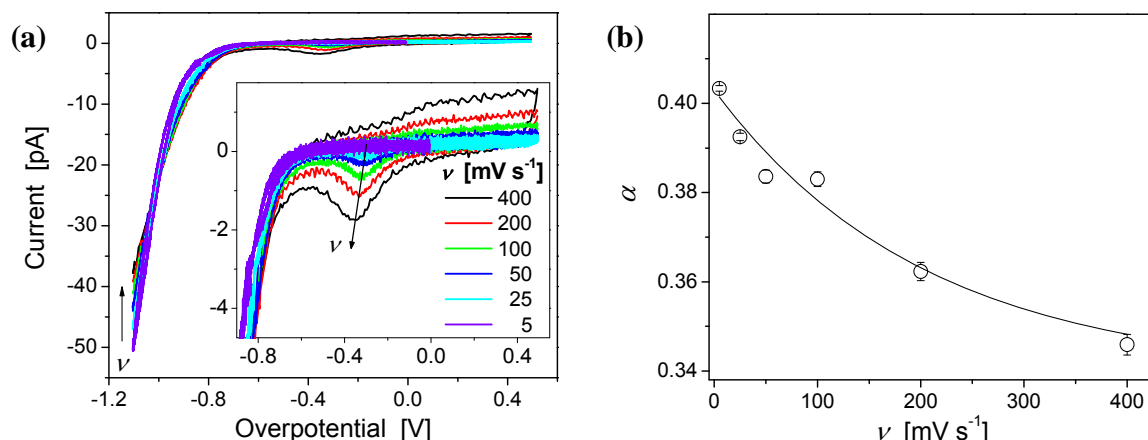


Figure F.10 (a) Cyclic voltammograms for Pt | CsHSO₄ collected at scan rates ranging from 400 to 5 mV s⁻¹ (using Probe 3 listed in Table 4.1), and (b) corresponding exchange coefficients, α , extracted from fitting the return sweep of the cathodic branch (plotted in Tafel form) to Equation 4.6, showing the dependence of α on scan rate.

F.2.4 Effect of Force on Electrochemical Measurements

We confirmed that any variations in the force applied between the Pt probe and the CsHSO₄ surface, determined periodically using force curves, have little effect on the features of the cyclic voltammograms. Figure F.11a is a series of voltammograms collected at a range of forces that is well beyond any force fluctuations observed during electrochemical measurements. Variations in both the oxygen reduction and Pt oxide reduction currents are negligible when the force is doubled, indicating a minimal effect of force on the data presented, and in particular, on the observed spatial variation of electrode kinetics. The agreement between the voltammograms, furthermore, implies that the high-frequency process, which is dominant at high bias, is not a result of contact

resistance at the Pt | CsHSO₄ interface. We also verified that the process of lifting the probe from and re-approaching the CsHSO₄ surface (a procedure required for acquiring electrochemical data at various spatial positions) has a negligible impact on the features of the cyclic voltammogram (Figure F.11b).

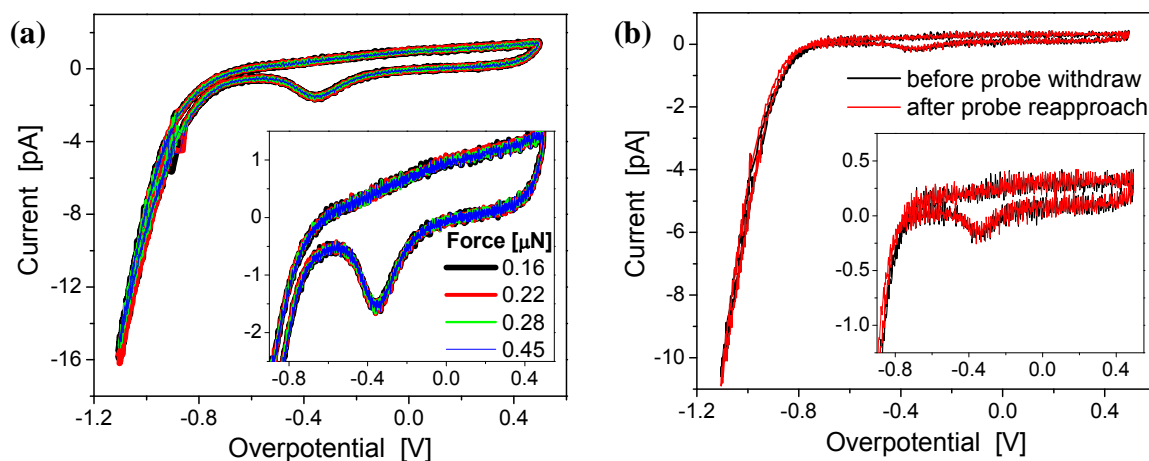


Figure F.11 Cyclic voltammograms for Pt | CsHSO₄ collected at $\sim 150^\circ\text{C}$ in humidified air with $\sim 0.01\text{--}0.03$ atm H₂O (a) at forces, ranging from 0.16 to 0.45 μN , applied between the probe and the CsHSO₄ surface (Probe 6, Table 4.1) and (b) at the same location on the surface, before withdrawing the probe and after reapproaching (Probe 3, Table 4.1).

F.3 Nano-Pt | CsHSO₄ vs. Wire-Pt | CsH₂PO₄

Although it remains inconclusive the source of the correlation between the Butler-Volmer parameters, i_0 and α , there exists some evidence that the activity of the Pt | solid acid interface depends on the morphology of that interface. We compare electrochemical AFM results for the nano-Pt | CsHSO₄ interface with those acquired by Sasaki¹²⁷ for the Pt wire | CsH₂PO₄ system. For the former, the six data sets from Figure 4.9 are collapsed into one line for ease of presentations (Figure F.12a). Data plotted alongside the AFM

results were collected at 235 °C in oxygen with 0.38 atm H₂O for an asymmetric electrode geometry where the working electrode was a 250 μm Pt wire embedded in a CsH₂PO₄ electrolyte, on the opposing side of which is a composite counter electrode (setup described in detail elsewhere³⁶); the results plotted in Figure F.12a were acquired by extracting exchange currents and coefficients for current-voltage curves collected for a single Pt wire | CsH₂PO₄ cell as a function of time (Figure F.12b). The values for both parameters vary with time in such a way so as to yield a correlation between i_0 and α , with a slope comparable to that observed in the nano-Pt | CsHSO₄ system. (The higher currents are due to the larger contact area between the Pt wire and CsH₂PO₄.) The electrochemical response of the Pt | CsH₂PO₄ system appears to be related to changes in the nature of the interface with time (Figure F.12b). However, the source of the agreement between i_0 - α correlations in nanoscale and microscale systems is not immediately obvious and warrants further exploration. Although the proton transport mechanism in CsHSO₄ is similar to that in CsH₂PO₄, microscale measurements of the Pt wire | CsHSO₄ system would enable a direct comparison. It would also be valuable to determine if the i_0 - α correlation can be observed across multiple Pt wire | solid acid systems.

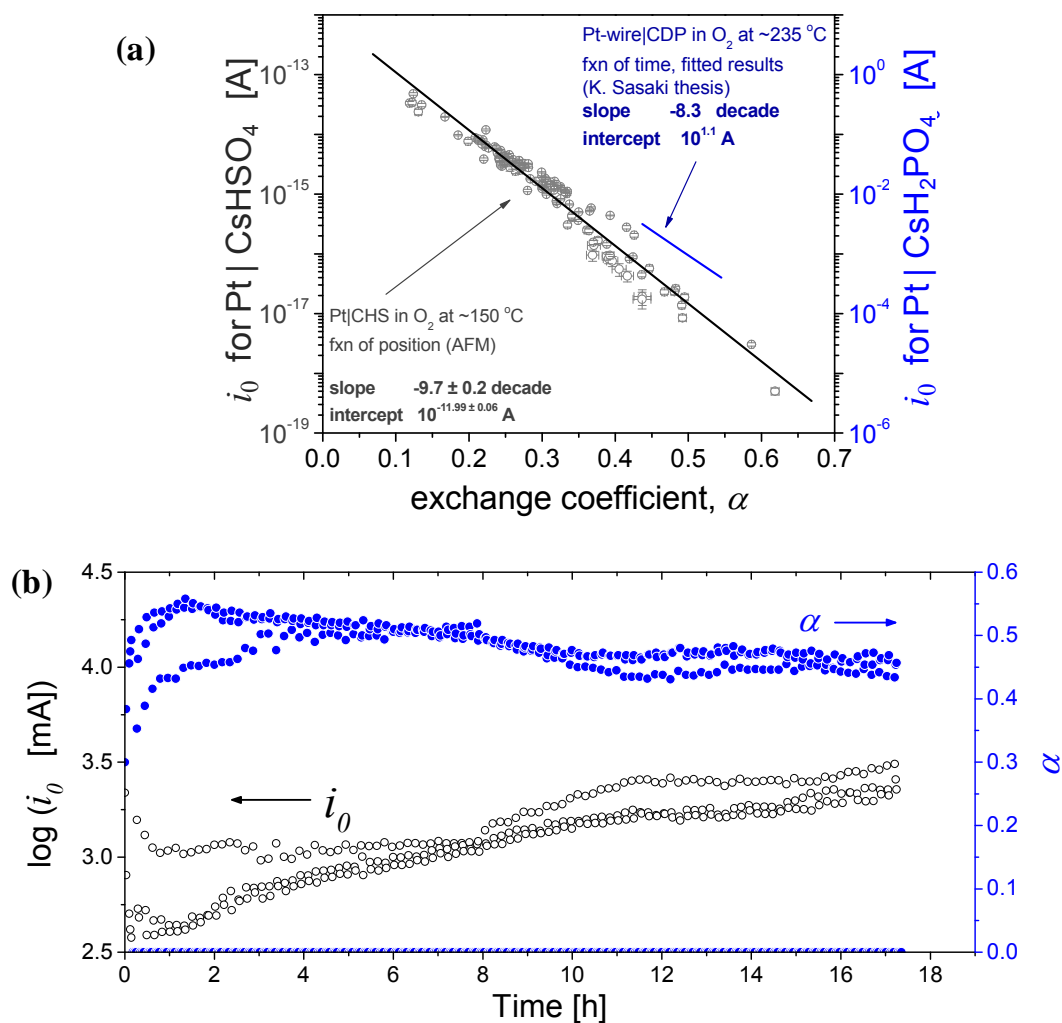


Figure F.12 (a) Plots of exchange current, on a logarithmic scale, as a function of exchange coefficient, comparing the correlation for the Pt | CsHSO₄ interface with that for the Pt | CsH₂PO₄ interface.¹²⁷ (b) For Pt | CsH₂PO₄, values of i_0 and α were extracted from current-voltage data collected as a function of time.

F.4 Platinum Oxide Reduction at Pt | CsHSO₄

In this section, we report some preliminary measurements of the Pt oxide reduction kinetics using the nano Pt | CsHSO₄ system.

F.4.1 Experimental

Pt oxidation measurements were performed under identical conditions to those reported for oxygen electro-reduction studies in Chapter 4. To study Pt oxidation kinetics,

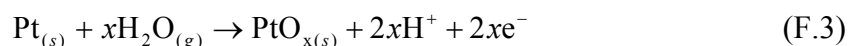
the voltage profile was varied as follows. To examine Pt chemical oxidation behavior, the system was held in air (~ 0.03 atm H_2O) with no voltage applied for times between 0 and 30. After this chemical oxidation step, the voltage was swept from 0 to -1 V at 100 mV s^{-1} in order to measure the Pt oxide reduction peak that was formed. Similarly, to examine Pt electrochemical oxidation behavior, the voltage was swept to 0.5 V at 100 mV s^{-1} at which it was held for times between 0 and 30 min. After each oxidative dwell step, the oxide reduction behavior was examined by sweeping the voltage to from 0.5 to -1 V at 100 mV s^{-1} . Before every chemical or electrochemical oxidation step, the voltage was held at -1 V for 1 min to ensure that the majority of oxides present were removed. It is important to note that, during electrochemical oxidation of Pt at 0.5 V, it is not possible to eliminate contributions from chemical oxidation which may be occurring concurrently.

F.4.2 Results and Discussion

The reduction characteristics of Pt oxides formed by chemical oxidation (Figure F.13a) via,



and electrochemical oxidation (Figure F.13b), via,



are shown in Figure F.13. In the case of chemical oxidation (Figure F.13a), as the oxidation time was increased, the first reduction peak, located at ~ -0.45 V, increased in size between oxidation times of 0 and 5 min, after which the peak size began to decrease. Corresponding to this decrease was the appearance of a second reduction peak at

~ -0.65 V, which increased in size with oxidation time. The onset voltage of the first reduction peak remained relatively constant at ~ -0.2 V despite changes in its size, while the peak voltage shifted to higher overpotentials with oxidation time, particularly at 10 and 30 min. For electrochemical oxidation of Pt (Figure F.13b), a similar behavior was observed, that is, an increase in peak size for oxidation times of 0–5 min, after which the peak decreased in size, concurrent with the appearance of a second reduction peak at larger overpotentials. However, in the case of electrochemical oxidation, the onset voltage occurs at lower overpotentials (below -0.1 V), and the peak position was observed to vary with dwell time more significantly. This may be an indication that electrochemical oxidation of Pt results in the formation of a different form of oxide than that formed by chemical oxidation; this would not be surprising since, based solely on their reactions, one would expect different oxidation pathways. In both cases, the observation of a second reduction peak appearing after long oxidation times suggests that the first reduction peak corresponds to an oxide that is kinetically favored to form, whereas the second reduction peak corresponds to an oxide that is thermodynamically favored. This is consistent with the second reduction peak occurring at larger negative overpotentials which, by definition, implies that the corresponding oxide is thermodynamically more stable than the oxide corresponding to the first reduction peak.

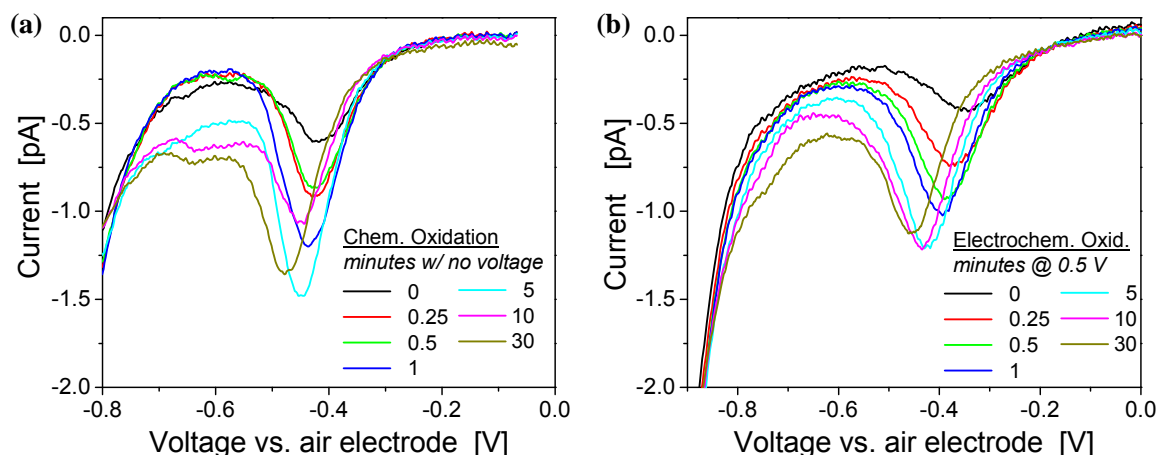


Figure F.13 Pt oxide reduction peaks collected with a 100 mV s^{-1} scan rate at 150°C in synthetic air with $\sim 0.03 \text{ atm H}_2\text{O}$ ($\sim 0.3 \mu\text{N}$ force), after dwelling for various times (a) with no voltage applied, for chemical oxidation of Pt and (b) 0.5 V applied, for electrochemical oxidation of Pt.

A more quantitatively analysis of the first reduction peak (at $\sim -0.45 \text{ V}$) is presented in Figure F.14. The three parameters, peak voltage, current and area, increase quickly with oxidation time for small oxidation times and appear to reach constant values before decreasing after $\sim 5 \text{ min}$, particularly in the case of peak current and area. An increase in peak area means that a larger quantity of material was available for reduction. A plateau of the peak area (amount of oxide formed) with oxidation time is not surprising since as the oxide layer grows thicker, additional oxidation becomes more difficult because of the requirement that oxygen diffuse through the formed oxide layer (or that water, protons and/or electrons be transported through the layer in the case of electrochemical oxidation). A shifting peak voltage while maintaining a relatively constant onset voltage implies that with longer oxidation times, the resulting oxide is kinetically more difficult to reduce.

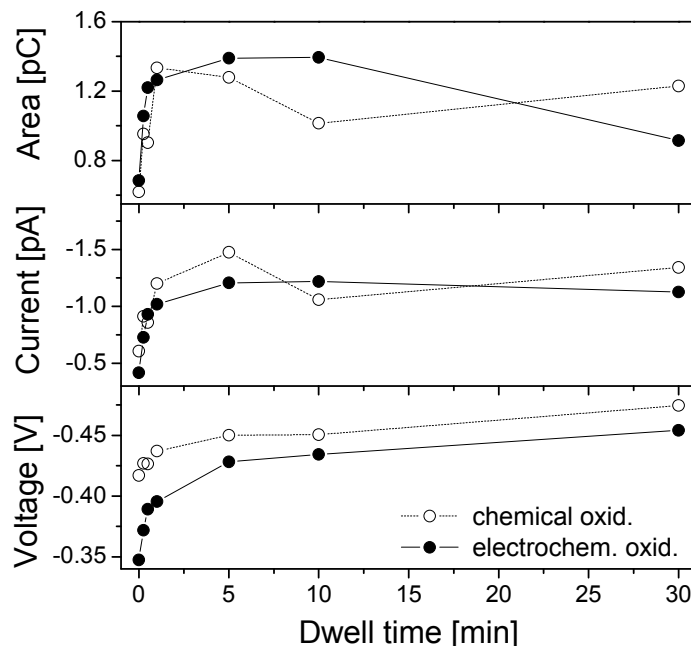


Figure F.14 Peak voltage, current and integrated area for the electrochemical reduction of Pt oxide (Figure F.13) as a function of dwell time at chemically and electrochemically oxidizing conditions.

F.5 Oxygen Electro-Reduction at Pt | Single-crystal CsHSO₄

In this section, we examine the spatial variation of electrocatalysis in the Pt | CsHSO₄ system, in which CsHSO₄ single crystals rather than a polycrystalline discs were employed. Because surface heterogeneities of single crystals are expected to be minimized, we attempt to exploit such a system to confirm the correlation between surface structure and electrochemical activity.

F.5.1 Experimental

Single crystals of CsHSO₄ were grown from a saturated aqueous solution made by dissolution of CsHSO₄ powder in de-ionized water. The resulting solution was filtered through a syringe filter (0.2 μm filter size) to remove dust particles and left, covered, at ambient conditions to allow water evaporation and crystal precipitation. Crystals were

removed from solution and rinsed with water followed immediately by methanol before drying in air.

Select crystals of appropriate dimensions, typically those which were > 5 mm on edge and > 1 mm thick, were sputtered on both faces with 25 nm of platinum (Cressington 208HR, ~ 15 mTorr Ar, 80 mA plasma current). After sputtering and immediately before use in AFM studies, the crystal was fractured laterally, using a razor blade, to generate two CsHSO_4 half-cells. Half-cells fabricated from un-fractured single crystals, pulled directly from solution and sputtered on one face with Pt, were also used for electrochemical AFM measurements.

The single-crystal half-cells were placed on top of a metal mesh which, in turn, sat on top of the AFM hotstage. Electrical connection to the counter electrode was made via this metal mesh (see Section F.1.1). Electrochemical characterization of the crystals via AFM was done so using the same procedures as those employed for polycrystalline samples (Chapter 4).

It is important to note that any residual acid on the single crystal can greatly influence the electrochemical response. Figure F.15 shows cyclic voltammograms collected from a Pt probe in contact with the surface of an un-fractured, as-grown single-crystal surface. Unlike the response for polycrystalline CsHSO_4 samples (Figure F.10a), these voltammograms displayed additional transient features at ~ -0.6 V on the cathodic sweep and at ~ -0.75 and -0.3 V on the return anodic sweep. Although the source of the features has not been determined, the features agree reasonably well with those reported in literature for aqueous acidic electrolyte systems for which peaks associated with hydrogen adsorption and desorption onto Pt are well-known characteristics of the

voltammogram.^{92–96} This observation provides some evidence that such adsorption processes occur only in aqueous/liquid acid systems and that the absence of adsorption features in solid acid systems (Chapter 4) is not solely a consequence of the higher temperatures employed.

The presence of even a small amount of acid causes large variations in the electrochemical response (Figure F.16). Furthermore, once a probe is contaminated with acid, the acid remains at the Pt | CsHSO₄ interface for any subsequent CsHSO₄ samples. To ensure that the electrochemical response examined is that due to the solid acid CsHSO₄ electrolyte rather than residual sulfuric acid, samples (both poly- and single-crystalline) must be rinsed adequately with methanol. Fractured single crystals must be examined visually to ensure that self-enclosed pockets of solution did not contaminate the fractured surface.

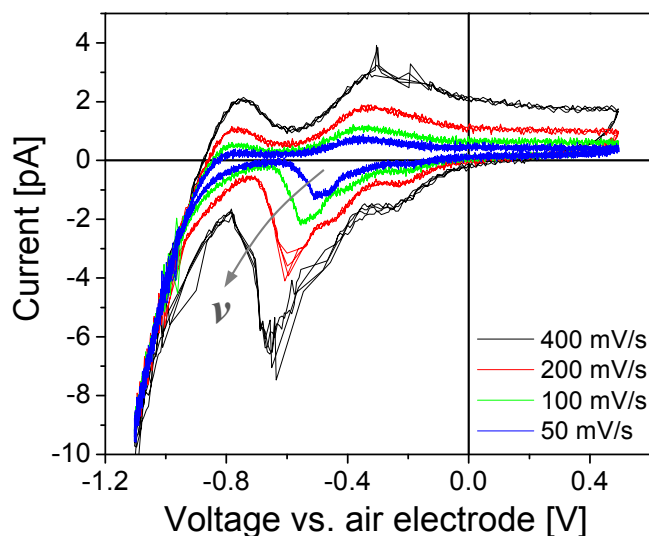


Figure F.15 Cyclic voltammograms for a Pt probe in contact with the surface of an as-grown CsHSO₄ single crystal. Data shown were collected at ~ 150 °C in synthetic air with ~ 0.03 atm H₂O at several different scan rates.

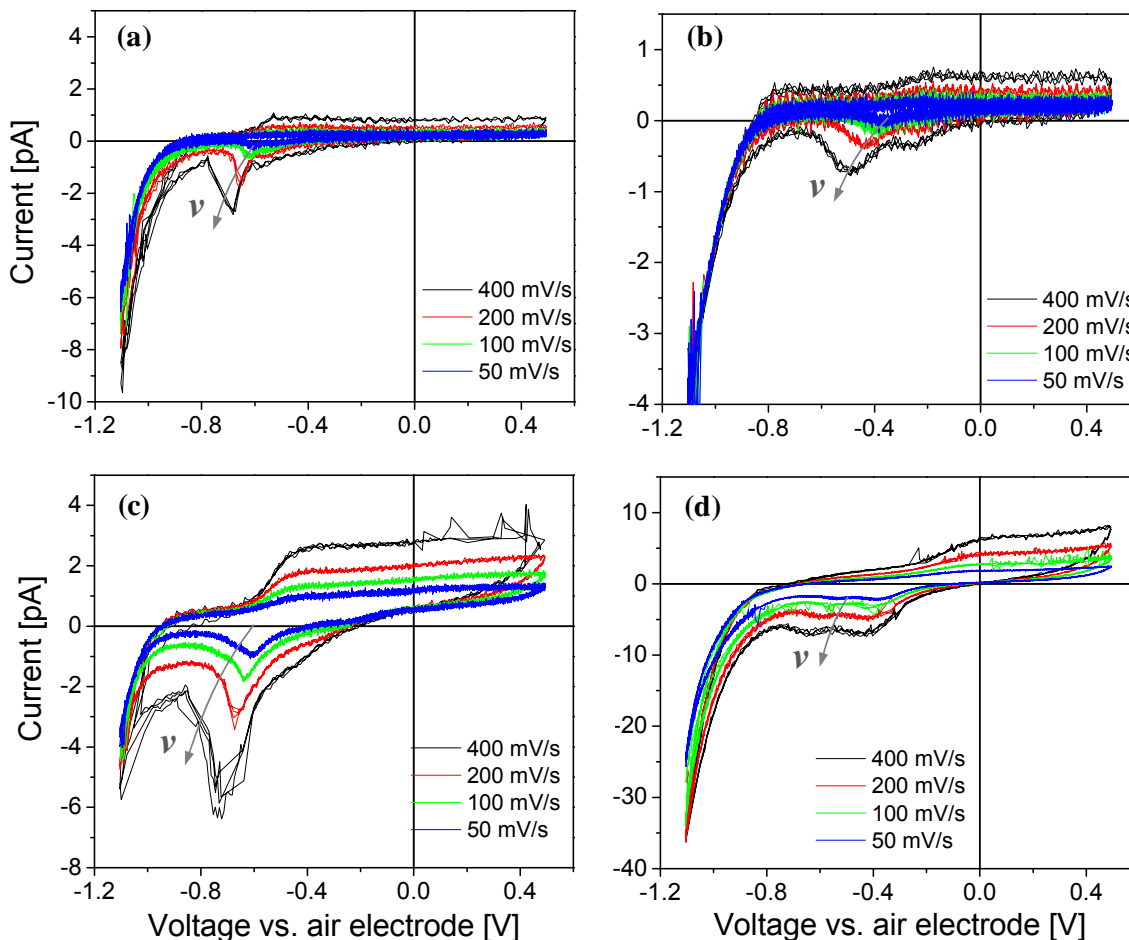


Figure F.16 Cyclic voltammograms for a Pt probe in contact with single-crystal CsHSO_4 , contaminated with acidic solution, showing the variability in the transient response. (a) and (b) correspond to different probes on the same crystal, and voltammograms shown in (c) and (d) were collected from same Pt | CsHSO_4 system but at two different positions on the crystal surface.

F.5.2 Results and Discussion

Figure F.17a shows the cyclic voltammogram for the Pt | CsHSO_4 system in which the single-crystal surface under examination was obtained by fracturing. Like the polycrystalline CsHSO_4 system, the single-crystal response displayed transient features with broad peaks centered at approximately -0.4 V and 0.1 V for cathodic and anodic sweeps of the voltammograms, respectively. These peaks were overlaid with an oxygen

electro-reduction current which reaches ~ 5 pA at -1.1 V. A typical impedance response for this system is shown in Figure F.17b for overpotentials from -1.2 to -0.7 V. For the overpotential range shown, the impedance response was comprised of one arc which varied significantly in size as a function of overpotential. Specifically, the electrode resistance decreased exponentially with overpotential, as indicated by the linear behavior of resistance (on a log scale) when plotted against overpotential (not shown). This behavior is consistent with the DC response, obtained from cyclic voltammetry (25 mV s^{-1} and plotted in Tafel form (Figure F.18a)). A plot of the current, on a logarithmic scale, as a function of overpotential yields a straight line.

Qualitatively, the voltammograms collected for Pt in contact with single-crystal and polycrystalline surfaces are similar; both Pt oxidation and oxide reduction peaks were visible, although their kinetics may differ slightly. However, unlike polycrystalline samples, single-crystal samples display only one impedance arc that is overpotential dependent, indicating that the ohmic response at high frequencies is negligible.

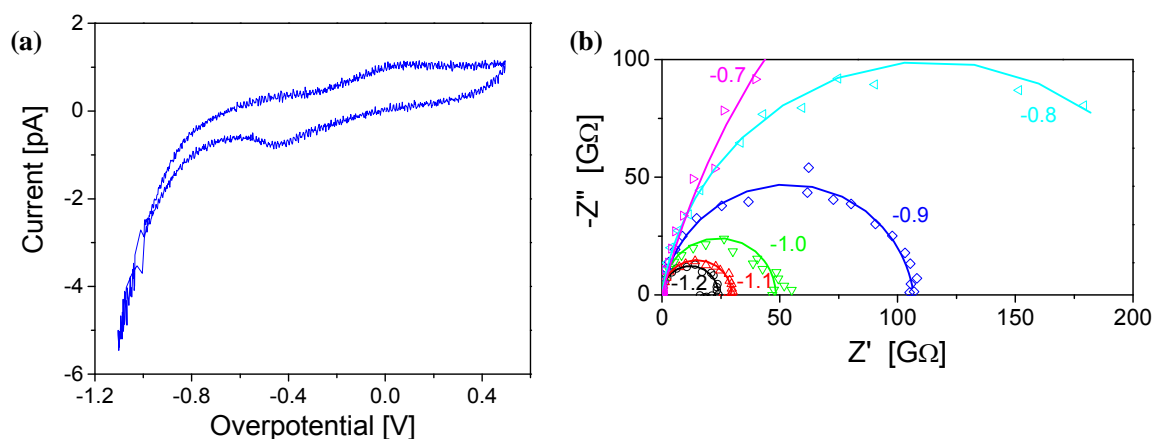


Figure F.17 (a) Cyclic voltammogram for Pt | single-crystal CsHSO_4 collected with a scan rate of 100 mV s^{-1} , and (b) Nyquist spectra for Pt | single-crystal CsHSO_4 collected as a function of overpotential. Lines are fits to a parallel RQ circuit. Data are collected at ~ 150 °C in air with ~ 0.3 atm H_2O .

Extracted α and i_0 values, obtained from the Tafel plots in Figure F.18a and from a second fractured single-crystal sample (not shown), are plotted in Figure F.18b, alongside polycrystalline data. A correlation between the two kinetic parameters exists, and, moreover, the behavior is similar to that observed for polycrystalline CsHSO₄ samples. Specifically, the slopes of α vs. i_0 are similar between the single-crystal and polycrystalline samples. More interestingly, the variability of α and i_0 for the single-crystal samples ($\Delta\alpha \approx 0.15$ and 0.05 for sets 1 and 2, respectively) is similar to that observed for polycrystalline CsHSO₄. This implies that the heterogeneity of electrochemical kinetics across a single-crystal surface (across a comparable sample area of $5\ \mu\text{m} \times 5\ \mu\text{m}$) is not significantly different from that across a polycrystalline surface.

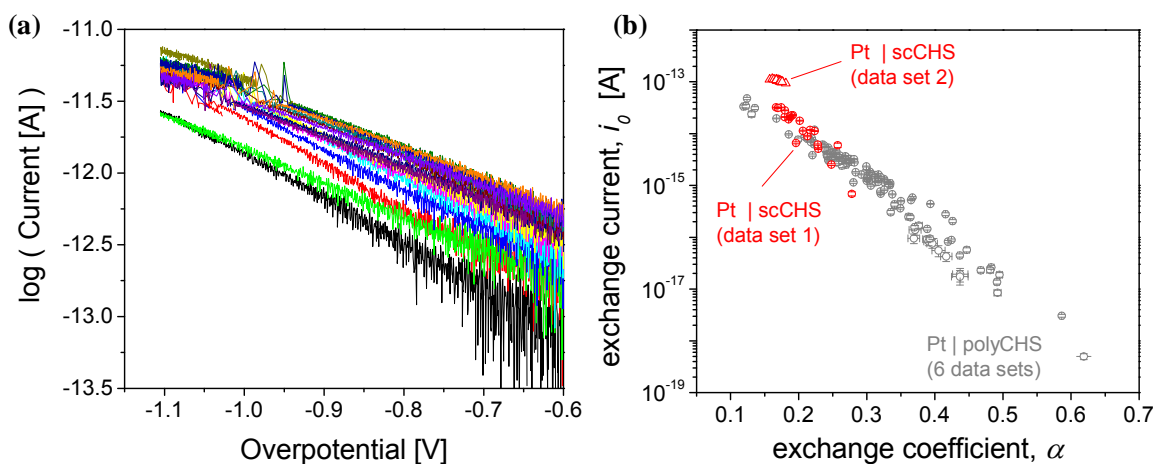


Figure F.18 (a) Tafel plots for the Pt | single-crystal CsHSO₄ interface taken from the return scans of cyclic voltammograms collected at $25\ \text{mV s}^{-1}$ and (b) extracted values of exchange current (log scale) plotted against exchange coefficient for two sets of single-crystal experiments, overlaid with polycrystalline CsHSO₄ data (Figure. 4.9). Data set 1 corresponds to the plots shown in Figure F.17 and Figure F.18a.

A closer examination of the single-crystal surfaces reveal that, although as-fractured surfaces were smooth, they were damaged by the AFM probe during

measurement. An AFM topography image of CsHSO₄ at superprotonic conditions shows indentations on the surface (Figure F.19). Additional investigation revealed that the damage is a consequence of the force applied to the sample by the probe rather than the overpotentials across the Pt | CsHSO₄ interface during electrochemical measurements. Based on this observation and the apparently spatial variation of the electrochemical response (Figure F.18), it is reasonable to conclude that single crystals of CsHSO₄, known to be plastic at superprotonic conditions, are not ideal as smooth substrates, that is, they essentially become polycrystalline samples once the AFM probe makes contact. It should be noted that indentation is not frequently observed in polycrystalline samples due to the roughness of the surface, although it is also likely to occur.

Figure F.20 displays additional images of damaged single-crystal surfaces. Even contact mode AFM probes (with nominal spring constants below 0.1 N m⁻¹) have been observed to indent single crystals of CsHSO₄ (Figure F.20). However, since the actual spring constants of most conventional AFM probes can deviate significantly their nominal values, leading to irreproducible indentation behavior, it is not possible, without well-calibrated AFM probes, to identify the value of force at which CsHSO₄ deforms.

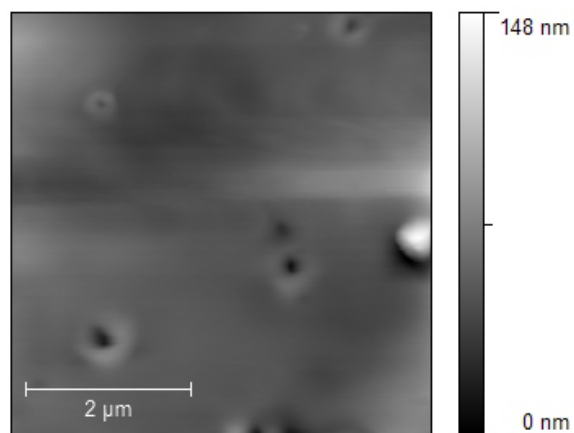


Figure F.19 AFM topography image of a single-crystal CsHSO_4 surface, in situ at 150 °C, after the Pt-coated AFM probe was held various locations on the crystal.

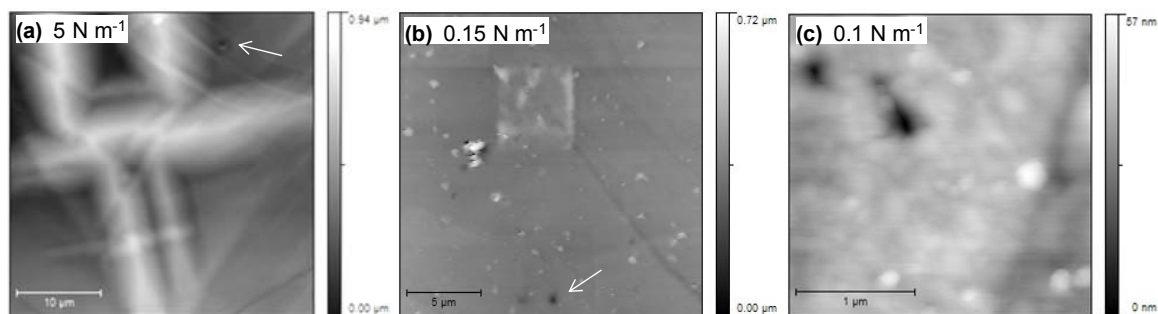


Figure F.20 Additional images of CsHSO_4 single-crystal surfaces showing that even probes with nominally low spring constants can damage the sample. (a) fractured crystal surface, (b) fractured crystal surface for which the square region is a damaged from a prior scan window, and (c) as-grown crystal.

Appendix G Pt | $\text{Ba}_{3-x}\text{K}_x\text{H}_x(\text{PO}_4)_2$ by Atomic Force Microscopy

G.1 Introduction

A series of compounds with the formula $\text{Ba}_{3-x}\text{K}_x\text{H}_x(\text{PO}_4)_2$ for $x \approx 0.5\text{--}1$ have been synthesized²⁴ and shown to crystallize in the trigonal phase. The motivation to synthesize such a compound was based on the structural similarities between the trigonal compound, $\text{Ba}_3(\text{PO}_4)_2$, and superprotonic solid acid compounds with the stoichiometry, $\text{M}_3\text{H}(\text{PO}_4)_2$, such as $\text{Rb}_3\text{H}(\text{SeO}_4)_2$ which is known to undergo a phase transition from monoclinic to trigonal at $\sim 180^\circ\text{C}$. Incorporation of protons into $\text{Ba}_3(\text{PO}_4)_2$ by substitution of Ba^{2+} with K^+ results in trigonal $\text{Ba}_{3-x}\text{K}_x\text{H}_x(\text{PO}_4)_2$ which is stable up to 300°C . Thus, unlike its analogs, $\text{Ba}_{3-x}\text{K}_x\text{H}_x(\text{PO}_4)_2$ does not undergo a phase transformation. $\text{Ba}_{3-x}\text{K}_x\text{H}_x(\text{PO}_4)_2$ possesses the additional advantage of insolubility in water. However, the proton conductivity is two to three orders of magnitude lower than typical solid acid compounds. Specifically, the proton conductivity of $\text{Ba}_{2.2}\text{K}_{0.8}\text{H}_{0.8}(\text{PO}_4)_2$ at 250°C is $2.4 \times 10^{-5} \text{ S cm}^{-1}$, much lower than the value of $2 \times 10^{-2} \text{ S cm}^{-1}$ for CsH_2PO_4 .¹⁰

Although $\text{Ba}_{3-x}\text{K}_x\text{H}_x(\text{PO}_4)_2$ exhibits low proton conductivity, it provides several advantages for exploring the spatial variability of electrocatalysis in solid state systems. Preliminary observation of the morphology of $\text{Ba}_{3-x}\text{K}_x\text{H}_x(\text{PO}_4)_2$ crystallites reveal smooth faceted surfaces, unlike those typical of water-soluble solid acid compounds, and is suggestive of its ideal mechanical properties for use with a AFM probe as the working electrode. As discussed in Chapter 2 and shown in Figure F.19 and Figure F.20 for CsHSO_4 , many of the typical solid acid compounds have unfavorable mechanical

properties, such plastic deformation of the superprotonic phase, for exploring the correlation between surface structure and electrochemical kinetics. In this section, we attempt to use $\text{Ba}_{3-x}\text{K}_x\text{H}_x(\text{PO}_4)_2$ as an electrolyte for studying oxygen electro-reduction kinetics at the $\text{Pt} \mid \text{Ba}_{3-x}\text{K}_x\text{H}_x(\text{PO}_4)_2$ interface.

G.2 Experimental

The synthesis of $\text{Ba}_{3-x}\text{K}_x\text{H}_x(\text{PO}_4)_2$ powder from two aqueous solutions, one of barium acetate and the other containing dipotassium hydrogen phosphate and potassium hydroxide. The general procedure and starting materials are report elsewhere.²⁴ For the $\text{Ba}_{3-x}\text{K}_x\text{H}_x(\text{PO}_4)_2$ powder used in this work, the synthesis temperature was kept at 80 °C and the pH of the solution greater than 13. Powders were characterized with X-ray diffraction and scanning electron microscopy with an energy dispersive spectrometer for composition determination.

Because of the relatively low proton conductivity of $\text{Ba}_{3-x}\text{K}_x\text{H}_x(\text{PO}_4)_2$, the use of half-cells comprised of thick polycrystalline electrolyte membranes (~ 0.5 mm) in conjunction with a nanoscale working electrode, generated currents too low to be measurable. We verified this by fabricating a macroscale cell comprised of polycrystalline $\text{Ba}_{3-x}\text{K}_x\text{H}_x(\text{PO}_4)_2$ electrolyte membrane with a large composite Pt- $\text{Ba}_{3-x}\text{K}_x\text{H}_x(\text{PO}_4)_2$ counter electrode, similar to that for polycrystalline CsHSO_4 half-cells used in Chapter 4. Electrochemical measurements performed on this cell using a Pt-coated probe yielded zero current for all overpotentials (not shown), indicating that ~ 0.5 mm thick $\text{Ba}_{3-x}\text{K}_x\text{H}_x(\text{PO}_4)_2$ electrolytes are too resistive to be useful for electrochemical AFM measurements.

As such, we constructed an electrochemical cell for which the electrolyte membrane is a single micron-sized particle of $\text{Ba}_{3-x}\text{K}_x\text{H}_x(\text{PO}_4)_2$ such that the resistance of the electrolyte is small relative electrocatalysis at the $\text{Pt} | \text{Ba}_{3-x}\text{K}_x\text{H}_x(\text{PO}_4)_2$ interface (Figure G.1). To construct such a geometry, $\text{Ba}_{3-x}\text{K}_x\text{H}_x(\text{PO}_4)_2$ powder was first suspended in methanol by sonication. The suspension was allowed to settle for approximately one hour to remove large aggregates of powders, and the remaining suspension of particles was collected and deposited drop-wise onto a Pt-coated silicon substrate (single crystal, $10 \text{ mm} \times 10 \text{ mm}$ wafer, 50 nm Pt). To evaluate whether the contact at the $\text{Ba}_{3-x}\text{K}_x\text{H}_x(\text{PO}_4)_2 | \text{Pt-coated wafer}$ (i.e., current collector) interface obtained by this method was sufficient so as to not limiting electrochemical currents, the fabrication procedure was modified as follows. The $\text{Ba}_{3-x}\text{K}_x\text{H}_x(\text{PO}_4)_2$ suspension was first dripped onto a bare silicon wafer (Wafer 1), and the resulting wafer was sputtered with 10 nm Pt. This coated substrate was then placed in contact with a second Si substrate (Wafer 2), already pre-coated with Pt, in order to transfer the Pt-coated $\text{Ba}_{3-x}\text{K}_x\text{H}_x(\text{PO}_4)_2$ platelets from Wafer 1. Thus, the $\text{Ba}_{3-x}\text{K}_x\text{H}_x(\text{PO}_4)_2 | \text{Pt}$ contact at the counter electrode was guaranteed by the intimate contact imparted by sputter deposition, while the physical contact between metals, specifically between the platinum films on the $\text{Ba}_{3-x}\text{K}_x\text{H}_x(\text{PO}_4)_2$ and on the Si wafer, is considered adequate for current collection.

For electrochemical AFM measurements, the wafer was placed on an AFM hotstage, and electrical connection was made to the Pt film counter electrode by clipping a small piece of silver mesh onto the top edge of the Pt-coated wafer. Measurements were carried out at temperatures of $175\text{--}220^\circ\text{C}$ under flowing synthetic air with $\sim 0.03 \text{ atm}$ H_2O supplied by flowing the inlet gas through a water bubbler at room temperature. A

potentiostat equipped with a frequency response analyzer and a femtoammeter (ModuLab by Solartron Analytical) was used to perform cyclic voltammetry measurements (100 mV s^{-1} scan rate between -1.1 and 0.6 V).

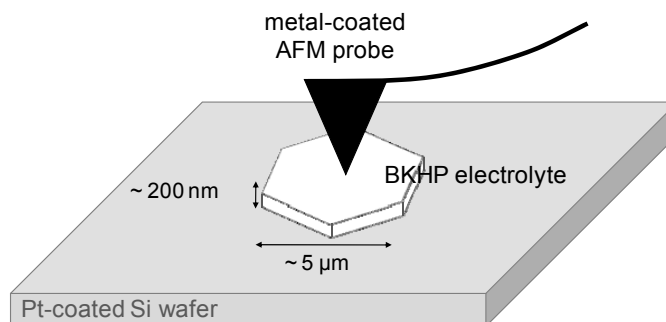


Figure G.1 Schematic of experimental setup for electrochemical AFM measurements of $\text{Ba}_{3-x}\text{K}_x\text{H}_x(\text{PO}_4)_2$ electrolytes. Half-cells are comprised of micron-sized hexagonal platelets of $\text{Ba}_{3-x}\text{K}_x\text{H}_x(\text{PO}_4)_2$ sitting on a Pt counter electrode. The AFM probe serves as a small working electrode that completes the circuit.

G.3 Results and Discussion

G.3.1 $\text{Ba}_{3-x}\text{K}_x\text{H}_x(\text{PO}_4)_2$ Characteristics

The diffraction pattern for the $\text{Ba}_{3-x}\text{K}_x\text{H}_x(\text{PO}_4)_2$ powder (not shown) agrees with the trigonal phase, as reported previously.²⁴ SEM micrographs of the powders (Figure G.2) show a distinct particle microstructure with hexagonal platelets $\sim 5 \mu\text{m}$ wide and $\sim 200 \text{ nm}$ thick. The observation of a hexagonal shape is consistent with the trigonal symmetry of $\text{Ba}_{3-x}\text{K}_x\text{H}_x(\text{PO}_4)_2$. Also visible in the SEM micrograph is the intergrowth of multiple platelets, resulting in aggregates at least several microns in size. Such aggregates, if deposited onto a smooth Si substrate for AFM studies, may cause damage to the probe since the AFM scanner only has a z -range of $\sim 7 \mu\text{m}$. For obtaining a good

distribution of individual, flat electrolyte platelets for electrochemical AFM studies, removal of such aggregates from the suspension done so by settling of the suspension.

The morphology of the powders reveal rather smooth surfaces, notable different from typical solid acid powders, such as those for CsH_2PO_4 , shown in Figure G.2b for comparison. Unlike $\text{Ba}_{3-x}\text{K}_x\text{H}_x(\text{PO}_4)_2$, particles of CsH_2PO_4 are easily agglomerated, with a large range of particle and aggregate sizes. From the energy dispersive spectra, the $\text{Ba}_{3-x}\text{K}_x\text{H}_x(\text{PO}_4)_2$ powders used in these studies were determined to have a potassium content (and therefore proton content) of $x = 0.75$.

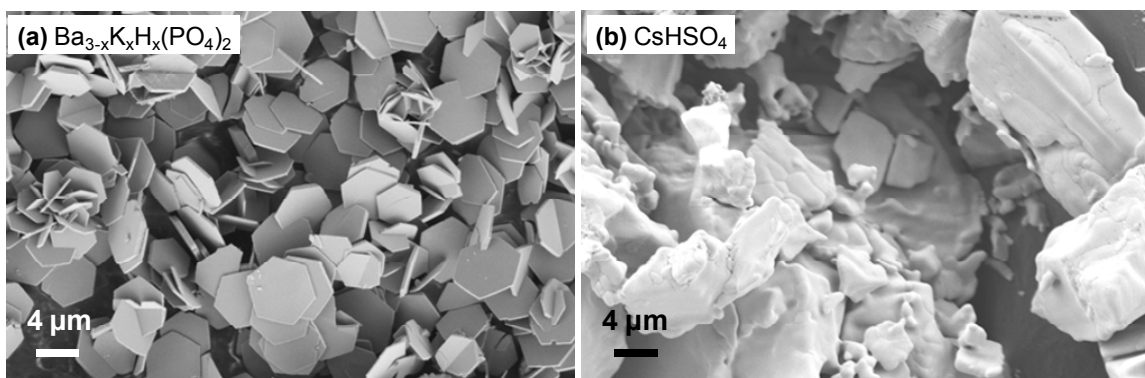


Figure G.2 SEM micrograph of (a) $\text{Ba}_{3-x}\text{K}_x\text{H}_x(\text{PO}_4)_2$ powder ($x = 0.75$) showing typical microstructure obtained for platelet $\text{Ba}_{3-x}\text{K}_x\text{H}_x(\text{PO}_4)_2$ powders and (b) as-synthesized CsHSO_4 powders, for comparison.

G.3.2 Fabrication of Microscale $\text{Ba}_{3-x}\text{K}_x\text{H}_x(\text{PO}_4)_2$ Half-cells

Figure G.3 shows SEM micrographs of $\text{Ba}_{3-x}\text{K}_x\text{H}_x(\text{PO}_4)_2$ particles on top of a Pt-coated Si wafer obtained by dripping of a particle-methanol suspension onto the wafer. The distribution across the entire wafer was non-uniform because of methanol evaporation patterns (not shown). On the scale shown in Figure G.3a, the particles are uniformly distributed. Thus, given a maximum scan range of $35 \times 35 \mu\text{m}^2$ in atomic force

microscope, appropriate regions for AFM studies are available and can be examined by proper alignment of substrate and AFM probe. It should be noted that sample alignment is difficult because the AFM system employed in our studies lacks an optical microscope. Thus, we rely on fabrication techniques to obtain a sufficiently high density of platelets such that $\text{Ba}_{3-x}\text{K}_x\text{H}_x(\text{PO}_4)_2$ substrates can be found during an AFM scan. Figure G.3b is a higher magnification image showing platelets which were lying on the substrate in the preferred orientation. While Figure G.3 reveals several aggregates of platelets, proper processing, i.e., settling of the larger aggregates in the suspension, was determined to minimize the number of aggregates and therefore reduce the likelihood of damaging the AFM tip during electrochemical measurements. Once the concentration of aggregates in the suspension is minimized, the concentration of individual platelets on the surface of the silicon substrate can be increased by repeated addition of solution onto the wafer.

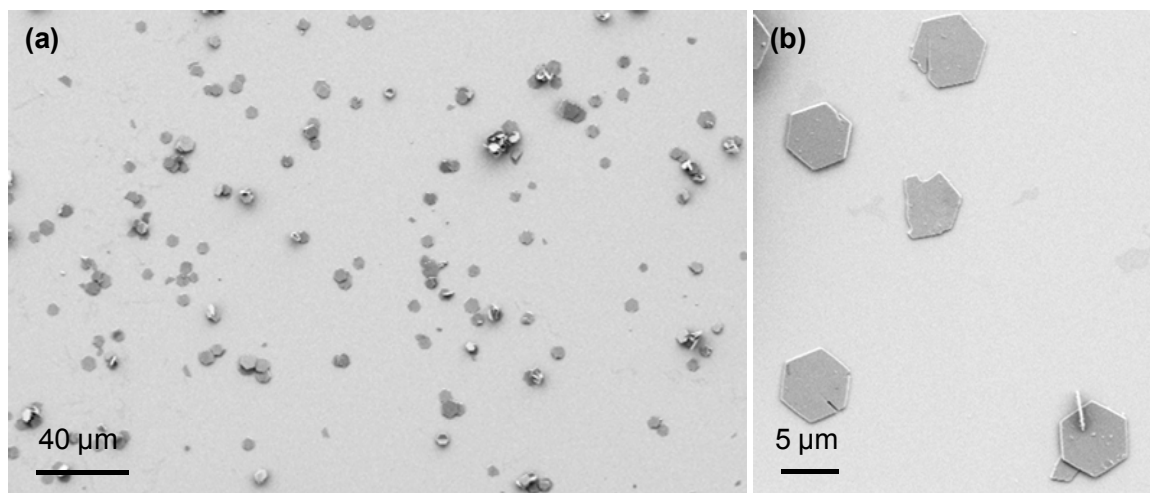


Figure G.3 SEM micrographs of $\text{Ba}_{3-x}\text{K}_x\text{H}_x(\text{PO}_4)_2$ platelets on a Pt-coated Si wafer, obtained by dripping a $\text{Ba}_{3-x}\text{K}_x\text{H}_x(\text{PO}_4)_2$ -methanol suspension. Under an electron beam, $\text{Ba}_{3-x}\text{K}_x\text{H}_x(\text{PO}_4)_2$ platelets appear as darker regions due to its poor electrical conductivity relative to the Pt film.

Figure G.4 shows a series of SEM micrographs of $\text{Ba}_{3-x}\text{K}_x\text{H}_x(\text{PO}_4)_2$ deposited on silicon, used in the wafer-to-wafer transfer process discussed in the experimental section. The top row contains images of a $\text{Ba}_{3-x}\text{K}_x\text{H}_x(\text{PO}_4)_2$ deposited on Wafer 1 (as discussed in the experimental section) after contact was made to Wafer 2, thus depicting missing platelets. The bottom row contains images of Wafer 2 after contact and acquisition of platelets from Wafer 1. Under the electron beam, darker regions are those with relatively poor electronic conductivity compared to brighter regions and corresponds to exposed portions of the Si substrate (Wafer 1, top row) or to uncoated $\text{Ba}_{3-x}\text{K}_x\text{H}_x(\text{PO}_4)_2$ platelets (Wafer 2, bottom row). By examining the two substrates, it is clear that a large fraction of the coated $\text{Ba}_{3-x}\text{K}_x\text{H}_x(\text{PO}_4)_2$ platelets on Wafer 1 were transferred upon contact to Wafer 2. It was also observed that larger aggregates are often fractured into smaller pieces (Figure G.4f) during the transfer step.

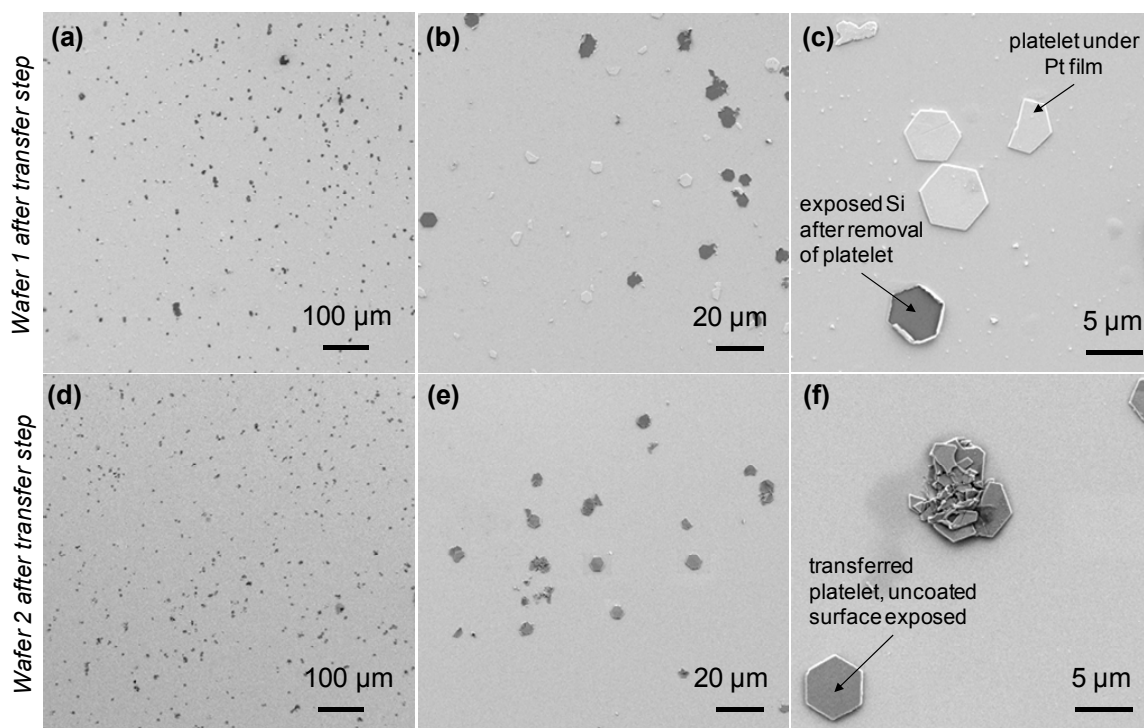


Figure G.4 SEM micrographs of $\text{Ba}_{3-x}\text{K}_x\text{H}_x(\text{PO}_4)_2$ platelets on silicon wafer used for the transfer of Pt-coated $\text{Ba}_{3-x}\text{K}_x\text{H}_x(\text{PO}_4)_2$ platelets from Wafer 1 (top row) to Wafer 2 (bottom row). (a–c) show $\text{Ba}_{3-x}\text{K}_x\text{H}_x(\text{PO}_4)_2$ deposited on a bare silicon substrate (Wafer 1), on top of which is a film of Pt, after contact to Wafer 2. Dark gray hexagonal regions are where $\text{Ba}_{3-x}\text{K}_x\text{H}_x(\text{PO}_4)_2$ platelets were transferred off of the wafer, whereas brighter hexagonal regions are un-transferred platelets, coated with Pt. (d–f) shows the transferred $\text{Ba}_{3-x}\text{K}_x\text{H}_x(\text{PO}_4)_2$ platelets, sitting on a Pt-coated Si wafer (Wafer 2).

G.3.3 Oxygen Electro-reduction at Pt | $\text{Ba}_{3-x}\text{K}_x\text{H}_x(\text{PO}_4)_2$

Figure G.5 shows a topographical image of a $\text{Ba}_{3-x}\text{K}_x\text{H}_x(\text{PO}_4)_2$ platelet (uncoated and deposited directly onto a Pt-coated Si wafer) and the corresponding cyclic voltammograms collected at three different positions on the platelet. Although Figure G.5(b–c) shows voltammograms that are reproducible with cycle and consistent with expectations for the Pt | solid acid interface (see Pt | CsHSO_4), subsequent measurements (Figure G.5d) display a degradation in current followed by a sharp drop during Cycle 4. While the drop in current shown in Figure G.5d is consistent with degradation and wear of the tip, subsequent measurements with the same probe yielded voltammograms that

vary in current, between zero and finite values in a random fashion. Voltammograms collected for the Pt probe in contact with wafer (off of the $\text{Ba}_{3-x}\text{K}_x\text{H}_x(\text{PO}_4)_2$ platelet) also yielded irreproducible results, displaying zero current for the most part with intermittent high currents (consistent with a metal-metal contact).

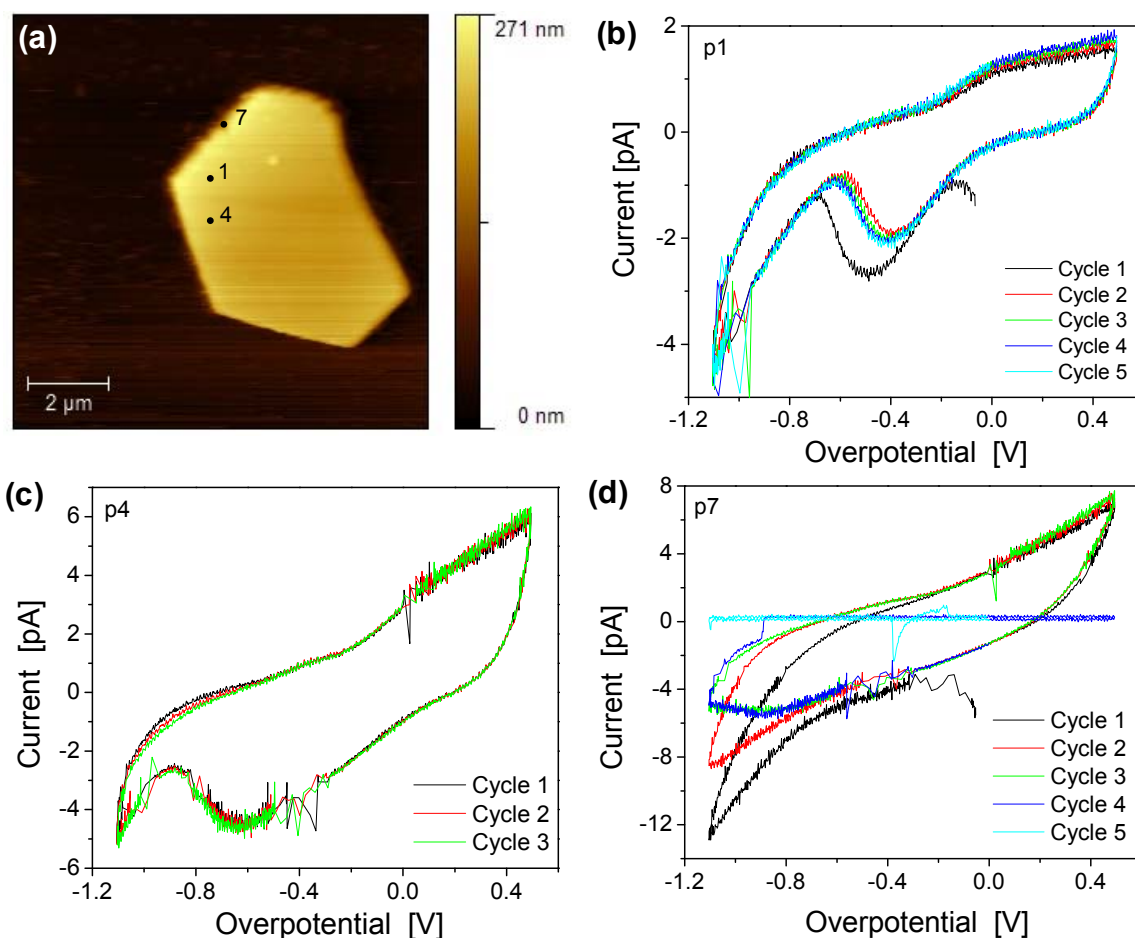


Figure G.5 Electrochemical AFM measurements at Pt | $\text{Ba}_{3-x}\text{K}_x\text{H}_x(\text{PO}_4)_2$: (a) A topographical AFM image of a $\text{Ba}_{3-x}\text{K}_x\text{H}_x(\text{PO}_4)_2$ platelet on a Pt-coated silicon wafer and corresponding cyclic voltammograms measured at positions 1, 4, 7 (b–d) for three or more consecutive cycles at 100 mV s^{-1} . Measurements were performed using a commercial Pt coated AFM probe with a spring constant of $\sim 5 \text{ N m}^{-1}$ at 175°C in air with $\sim 0.03 \text{ atm H}_2\text{O}$. While (b) and (c) show reproducible voltammograms, (c) shows a slow change in the current with cycle number.

To assess whether intermittent current measurements are a result of poor/intermittent contact of $\text{Ba}_{3-x}\text{K}_x\text{H}_x(\text{PO}_4)_2$ platelets with the Pt-coated Si substrate (i.e., counter electrode), a substrate with transferred $\text{Ba}_{3-x}\text{K}_x\text{H}_x(\text{PO}_4)_2$ platelets (i.e., Wafer 2 in Figure G.4(d–f)) was examined. Figure G.6 shows typical results from this type of sample. Similar to the voltammograms in Figure G.5d, the results reveal currents that vary with position on the $\text{Ba}_{3-x}\text{K}_x\text{H}_x(\text{PO}_4)_2$ and with time at the same position. Also evident in these measurements (and in others) is that increasing the temperature from 175 °C (Figure G.5) to 220 °C (Figure G.6) yielded no improvements in the electrochemical response. In addition, the detection of current occurs in a random fashion, indicating the degradation of the probe is not likely the problem, as this would yield currents which decrease with experimental time.

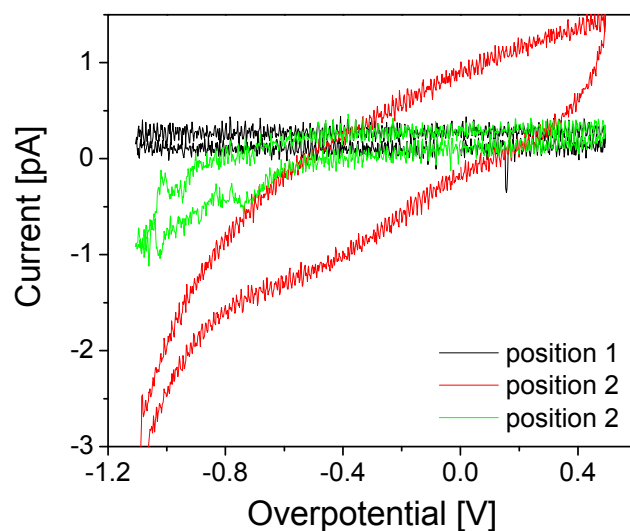


Figure G.6 Cyclic voltammograms collected at 220 °C in synthetic air with ~ 0.03 atm H_2O for two different positions on a $\text{Ba}_{3-x}\text{K}_x\text{H}_x(\text{PO}_4)_2$ platelet, where the counter electrode Pt | $\text{Ba}_{3-x}\text{K}_x\text{H}_x(\text{PO}_4)_2$ interface was comprised of Pt sputtered directly onto $\text{Ba}_{3-x}\text{K}_x\text{H}_x(\text{PO}_4)_2$.

G.3.4 Troubleshooting

A short-circuit measurement was performed on a bare Pt-coated wafer using a used Pt-coated probe, specifically that used to acquire the results presented in Figure G.6. For comparison purposes, similar measurements were carried out using an Au-coated probe (Figure G.7). The short-circuit correction for the Pt | Pt interface is somewhat unexpected. While the currents are sufficiently high, the response is not ohmic as would be expected for a metal-metal contact. On the other hand, the Au-coated probe gives the expected ohmic response, indicating that the source of the non-ohmic response in the case of Pt is the probe rather than the substrate. Possible explanations for the non-ohmic response of Figure G.7a are the formation of an oxide layer or contamination of the Pt probe.

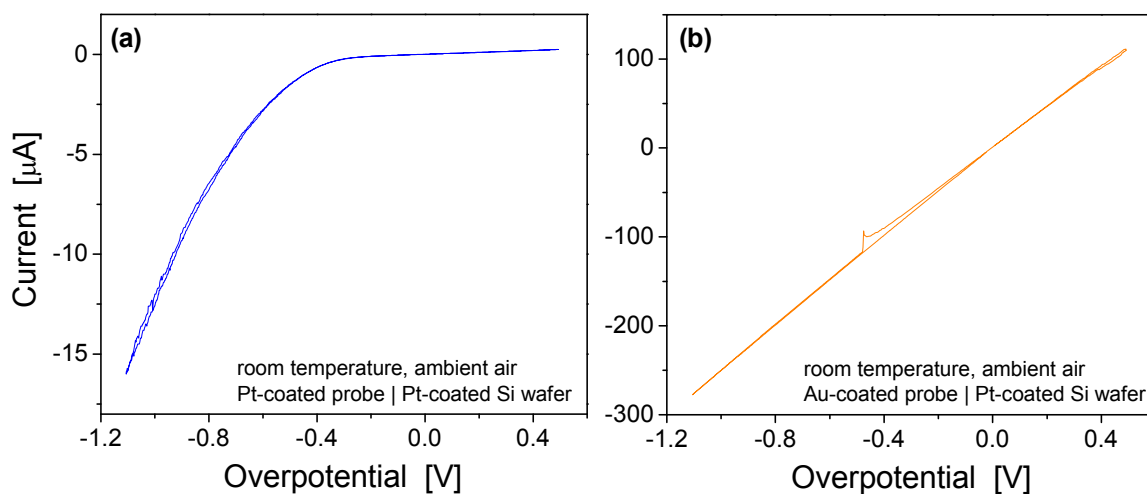


Figure G.7 Short-circuit measurements on Pt-coated silicon wafer at room temperature in ambient air using (a) a used Pt-coated probe from Figure G.5, and (b) a Au-coated probe for comparison.

The effect of residual organics/contaminants, either from the synthesis of $\text{Ba}_{3-x}\text{K}_x\text{H}_x(\text{PO}_4)_2$ or from the suspension in methanol was investigated. Figure G.8 shows Raman spectra collected for $\text{Ba}_{3-x}\text{K}_x\text{H}_x(\text{PO}_4)_2$ platelets on a Si wafer, as-deposited from methanol and after two 15-min intervals of oxygen plasma (100 W, 250 mTorr O_2). The spectra show shifts characteristic of the silicon substrate ($\sim 520 \text{ cm}^{-1}$) as well as for symmetric stretches for PO_4 groups.¹¹³ Additionally, a shift at $\sim 2900 \text{ cm}^{-1}$, attributed to the C-H stretch in organic compounds, indicates the presence of contaminants. However, the removal of such organics by oxygen plasma was not successful despite the relatively high plasma power and duration. Thus, it is unclear what the source of such organics are and its uniformity across the sample. As shown in the spectra, the presence of organics varies with the specific platelet examined. Specifically, after the second interval of plasma treatment (Figure G.8), the C-H stretch was present in the spectrum for one platelet but not another. Thus, without the capability in the AFM system to identify and target a specific platelet particle which we identified (via Raman spectroscopy) to show no organic signatures, it is presently not possible to use oxygen plasma cleaning to our advantage. Not surprisingly, the samples that were treated by oxygen plasma did not yield any improvements in the electrochemical response (not shown).

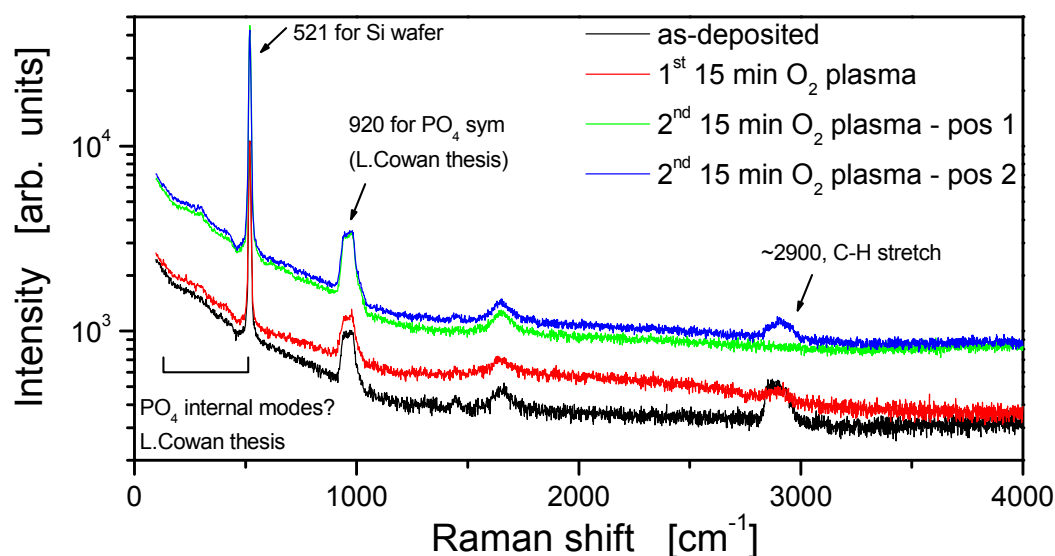


Figure G.8 Raman spectra collected for $\text{Ba}_{3-x}\text{K}_x\text{H}_x(\text{PO}_4)_2$ platelets deposited on bare a Si wafer showing shifts for organic compounds, in addition to those expected for $\text{Ba}_{3-x}\text{K}_x\text{H}_x(\text{PO}_4)_2$ and Si. Spectra were collected for as-deposited $\text{Ba}_{3-x}\text{K}_x\text{H}_x(\text{PO}_4)_2$ and after two 15-min intervals of oxygen plasma treatment, with spectra collected for two different platelets after the second interval of plasma treatment.

G.4 Recommendations for Future Studies

Various attempts to determine the source of intermittent currents measured in electrochemical AFM for the $\text{Pt} | \text{Ba}_{3-x}\text{K}_x\text{H}_x(\text{PO}_4)_2$ interface have been unsuccessful. Based on the observations made for the $\text{Ba}_{3-x}\text{K}_x\text{H}_x(\text{PO}_4)_2$ system thus far, several recommendations are proposed.

- 1) Determine the effect of contaminants from methanol used in the $\text{Ba}_{3-x}\text{K}_x\text{H}_x(\text{PO}_4)_2$ suspension by comparing the voltammograms measured by electrochemical AFM for a bare Pt-coated wafer, and that with methanol deposited on and evaporated from the wafer.

- 2) Employ Raman spectroscopy (or a similar tool) to determine the presence of contaminants in as-synthesized $\text{Ba}_{3-x}\text{K}_x\text{H}_x(\text{PO}_4)_2$ powders and after any subsequent processing steps.
- 3) $\text{Ba}_{3-x}\text{K}_x\text{H}_x(\text{PO}_4)_2$ has a trigonal structure, analogous to $\text{Rb}_3\text{H}(\text{SeO}_4)_2$ which is known to have anisotropic conductivity. By analogy to $\text{Rb}_3\text{H}(\text{SeO}_4)_2$, it is expected that the direction of higher proton conductivity in $\text{Ba}_{3-x}\text{K}_x\text{H}_x(\text{PO}_4)_2$ is in the plane of the platelet (Figure 1.4). Thus, while the platelet morphology of $\text{Ba}_{3-x}\text{K}_x\text{H}_x(\text{PO}_4)_2$ provides geometric advantages for minimizing ohmic losses, it may be worthwhile to consider synthesizing particles with different microstructures.
- 4) Eliminate possible wear on the probe. This can be done by using probes with low force constants, optimizing the deposition of $\text{Ba}_{3-x}\text{K}_x\text{H}_x(\text{PO}_4)_2$ platelets to obtain high densities on the substrate, and/or obtain an AFM with an optical microscope so that specific $\text{Ba}_{3-x}\text{K}_x\text{H}_x(\text{PO}_4)_2$ platelets can be located without repeated topography scans.

Appendix H Pd | CsHSO₄ by Atomic Force Microscopy

The palladium-platinum system has been observed to exhibit promising performance as a cathode for solid acid fuel cells.³ Furthermore, as shown in Appendix D, palladium also displays promising activities for hydrogen electro-oxidation. In this section, we present preliminary results from electrochemical AFM studies of the Pd | CsHSO₄ interface to explore its electrocatalytic behavior compared to that for Pt | CsHSO₄ (Chapter 4). Although there has been evidence that reaction between Pd oxide and CsH₂PO₄ occurs at 240 °C³ (Appendix B), none was detected at 150 °C, that is, at temperatures relevant for the study of CsHSO₄. Therefore, the Pd | CsHSO₄ system may be useful for further exploration of the variability of electrochemical kinetics and the correlation of key kinetic parameters, observed in Chapter 3 for Pt | CsHSO₄.

In order to make a reliable comparison between Pt and Pd, we examine the spatial variation of electrode kinetics at the Pd | CsHSO₄ interface, since it was shown in Chapter 4 that measurements at the nanoscale can vary dramatically across a given CsHSO₄ surface.

H.1 Experimental

Half-cells with Pt-based composite counter electrodes, identical to those used in Chapter 4, were employed for Pd studies. Environmental conditions used and electrochemical measurements performed were also the same. Since Pd-coated probes are not available commercially, bare Si-based probes were sputtered in-house with 15 nm of

Pd. (Cressington 208HR, ~ 15 mTorr Ar, 80 mA plasma current). Table H.1 shows the probes used to collect the data presented in this section. To ensure that the electrochemical response of the metal | CsHSO₄ interface does not vary with the metal film deposition method, Pt was also sputtered onto Si-based probes using the same procedure as was used for Pd. Qualitative agreement of the DC and AC measurements between the sputtered and commercial Pt probes would indicate that Pd studies can be reliably compared to previous results for Pt.

Table H.1 Description of AFM probes employed for comparing Pd | CsHSO₄ and Pt | CsHSO₄.

Probe	Probe coating	Cantilever Type	Nominal spring constant, k [N m ⁻¹]	Metal deposition
1	Platinum	rectangular	5	Commercial, from Chapter 4
2	Platinum	triangular	0.5	Sputtered in-house
3	Palladium	rectangular	5	Sputtered in-house
4	Palladium	triangular	0.5	Sputtered in-house

H.2 Results and Discussion

H.2.1 Oxygen Electro-reduction

Figure H.1a shows a typical cyclic voltammetry response for the nano-Pd | CsHSO₄ system obtained using Probe 3 in Table H.1. The transient effects, most evident at high scan rates, can be readily distinguished from Faradaic currents. Two reduction peaks are visible at ~ -0.4 and -0.7 V (with an onset voltage for the former being ~ -0.3 V), and a smaller, relative broad oxidation peak occurs on the return sweep at ~ -0.4 V. These are overlaid with an oxygen reduction current that increase

dramatically at overpotentials beyond -0.8 V. Impedance spectra collected as a function of overpotential (Figure H.1b) show two convoluted arcs, both of which decrease in size at higher (negative) overpotentials.

From thermodynamic data, the potential for reduction of PdO is -0.36 V at 150 °C in 0.21 atm O_2 , whereas those for Pd(OH) $_2$ and Pd(OH) $_4$ (for which thermodynamic data was available) are -0.21 and -0.11 V. The onset voltage of -0.3 V for the first reduction peak appears to be consistent with reduction of oxidized Pd. However, the identities of the remaining peaks are unclear. We proceed with analysis of oxygen electro-reduction kinetics based on the observation that the oxygen reduction currents are stable over many voltammetry cycles, and thus the processes which generate the unknown transient features do not irreversibly degrade the Pd film or its activity.

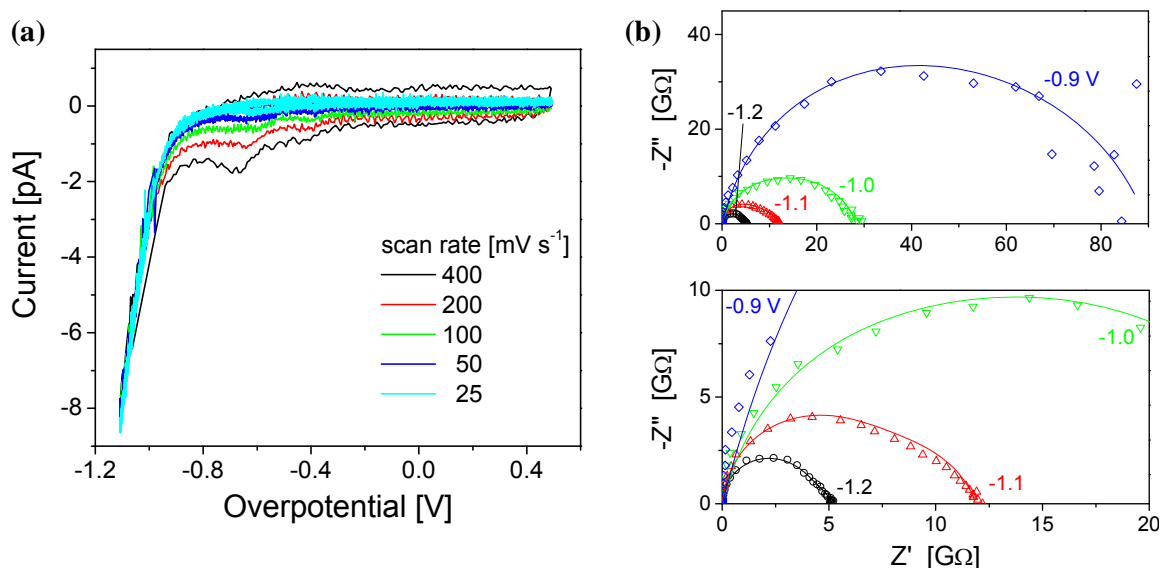


Figure H.1 Electrochemical response of the Pd | CsHSO $_4$ system at ~ 150 °C in air with ~ 0.03 atm H $_2$ O: (a) cyclic voltammograms for Pd | CsHSO $_4$ measured as a function of scan rate and (b) impedance spectra collected as a function of overpotential. (Probe 3 in Table H.1)

The resistances of the high and low-frequency processes, plotted on a semi-logarithmic plot against overpotential (Figure H.2a), fall along lines with finite slopes, indicating that both processes depend exponentially on the overpotential. The resistance of the low-frequency process, R_{LF} , is greater than that for the high-frequency process, R_{HF} , for overpotentials below ~ -1 V and dominates the total resistance at overpotentials below ~ -0.9 V. Because the low-frequency process depends more strongly on overpotential, the total resistance follows R_{LF} at low overpotentials but deviates at high overpotentials due to R_{HF} . This behavior is qualitatively consistent with DC data obtained from cyclic voltammetry, plotted in Tafel form (Figure H.2b).

The behavior of Pd | CsHSO₄ differs slightly from that of Pt | CsHSO₄ presented in Chapter 4. While the low-frequency arc appears to behave similarly, that is, R_{LF} depends exponentially on overpotential, the high-frequency process, in the case of Pd, also depends on overpotential, albeit to a lesser extent. (As shown in Figure H.2a, the low-frequency resistance of Pd spans three orders of magnitude across 500 mV, while the high-frequency resistance spans one order.) One might be tempted to attribute the observed dependence of the high-frequency process to error resulting from fitting the impedance spectra, but direct examination of the impedance response (Figure H.1b) indicates that both arcs are indeed changing with overpotential.

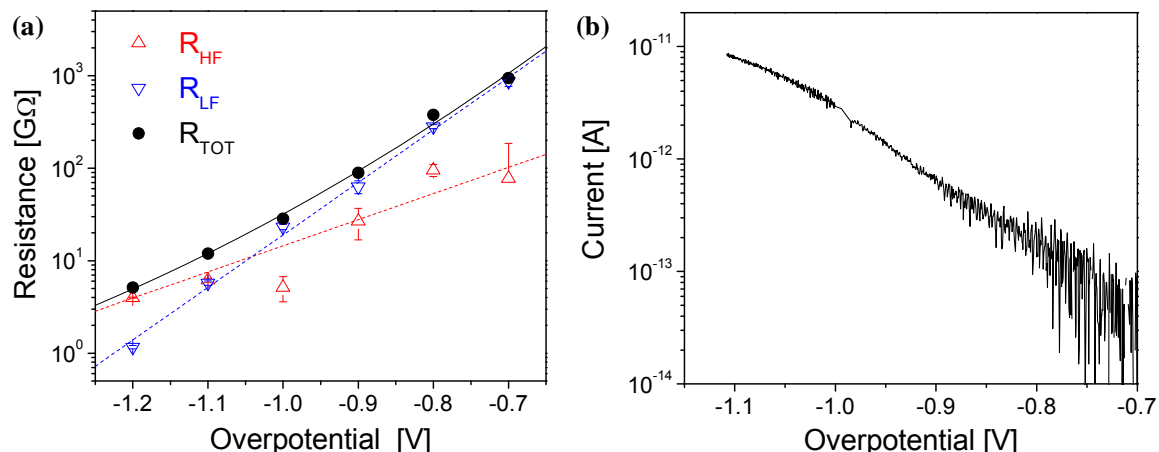


Figure H.2 (a) Resistances of the high-frequency (R_{HF}) and low-frequency (R_{LF}) electrode processes, and their sum, plotted as a function of overpotential. Electrode resistances were extracted from fitting the Nyquist spectra shown in Figure H.1b. (b) Tafel plot for the Pd|CsHSO₄ system acquired from the cathodic branch (return sweep) of a cyclic voltammogram collected at 25 mV s⁻¹.

Tafel plots for the Pd|CsHSO₄ system as a function of position across the CsHSO₄ surface reveal a linear regime at overpotentials below -1 V. At high overpotential, the Tafel plot changes behavior; as the overpotential becomes larger, the slope of Tafel plot increases for some measurements but decreases or remains constant for others. The source of this variation is presently unknown.

Based on results from Figure H.1a and Figure H.2a, we can set the range for Tafel analysis of R_{LF} to be approximately between -1 and -0.7 V, the former being the overpotential beyond which R_{HF} dominates the total response and the latter being the overpotential at which transient effects start to surface. The exchange current, i_0 , and exchange coefficient, α , were extracted by fitting the Tafel equation (Equation 4.6) to the plots in this overpotential window. Despite uncertainties in both the electrochemical response at high overpotential as well as the transient behavior of the Pd|CsHSO₄ system, the extracted Tafel parameters appear to be correlated (Figure H.4). Moreover, the slope of the i_0 - α correlation agrees reasonably well with that for the Pt|CsHSO₄ system

(Chapter 4) and for data collected using Probes 2 and 4 in Table H.1 (raw data not shown).

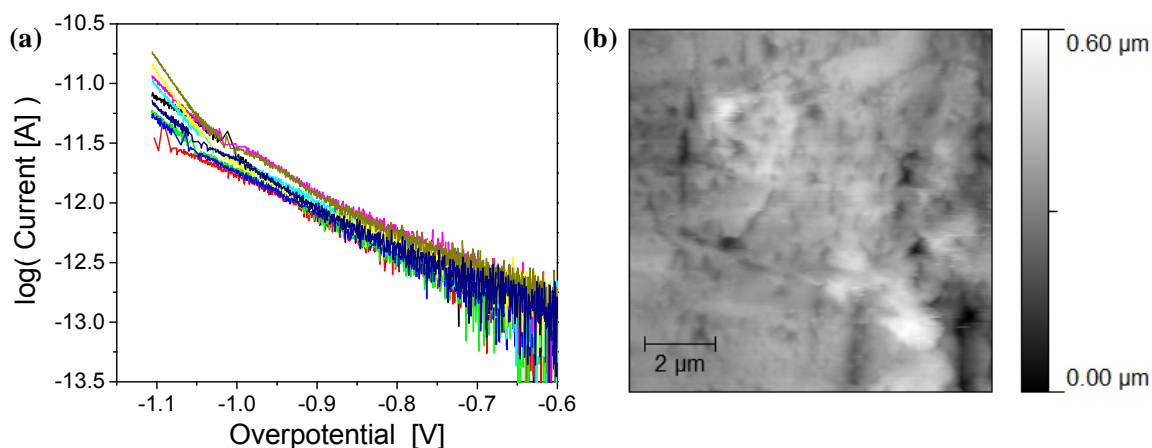


Figure H.3 (a) Select Tafel plots of the cathodic branches (return sweep) of cyclic voltammograms collected at 25 mV s^{-1} at various positions across (b) a $5 \times 5 \text{ } \mu\text{m}^2$ CsHSO_4 surface.

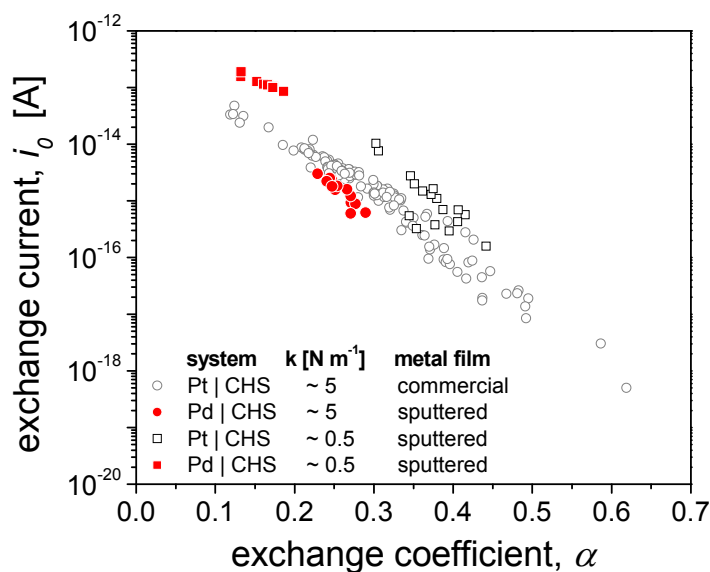


Figure H.4 Exchange current (log scale) plotted against exchange coefficient comparing four metal | CsHSO_4 systems using probes shown in Table H.1. CHS = CsHSO_4

It is interesting to note that the currents for Probes 2 and 4 ($k = 0.5 \text{ N m}^{-1}$) have noticeably higher currents, by approximately half an order of magnitude. This is most

likely due to the higher contact area between the probe and CsHSO_4 (which results in a higher overall current passing through the probe | CsHSO_4 interface). AFM topography images of the surface during testing, Figure H.5(a–b), reveal that these probes can severely damage the surface of the sample. It is unclear why these probes exhibited such high forces on the sample, since their nominal spring constants are low compared to those for Probes 1 and 3. Besides the triangular shape of the cantilevers for Probes 2 and 4, the only other difference is their construction from silicon nitride which is a harder material than silicon.

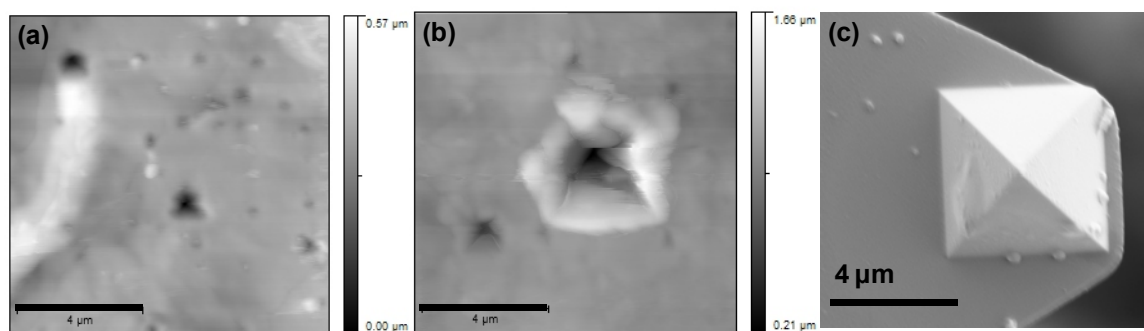


Figure H.5 (a–b) AFM images of a CsHSO_4 polycrystalline sample damaged by AFM probes, (Probes 2 and 4 in Table H.1) and (c) SEM micrograph of a probe for comparison.

H.2.2 Transient Behavior of $\text{Pd} | \text{CsHSO}_4$

We present here the cyclic voltammetry response for the $\text{Pd} | \text{CsHSO}_4$ collected using Probe 4 (Figure H.6). (This data set does not correspond to data shown in Figure H.4.) Due to the large $\text{Pd} | \text{CsHSO}_4$ contact area, high currents were measured, enabling exploration of the transient behavior which would otherwise be difficult to capture for the system shown in Figure H.1a. Clearly visible in the voltammogram are two reduction peaks and two oxidation peaks. The former, with peak positions of ~ -0.3 V and -0.4 to

–0.6 V, are denoted Peaks 1 and 2, respectively, and the latter, with peak positions of –0.35 to –0.4 V and –0.05 to 0.05 (depending on the scan rate), are denoted Peaks 3 and 4, respectively. Oxidation peaks (3 and 4) are notably broader than reduction peaks (1 and 2), indicating slower kinetics. The existence of two peaks is consistent with previous Pd measurements (Figure H.1a), although at lower scan rates, a third reduction feature is visible (denoted with asterisks), with a peak position of –0.5 V at a scan rate of 25 mV s^{–1}.

The relative kinetics of the processes can be determined by the shift in the peak position with scan rate. As the scan rate is increased, the peak position of Peak 1 does not vary significantly whereas that for Peak 2 shifts to higher (negative) overpotentials, indicating that the latter process cannot “keep up” with the high scan rates.

The onset voltage of Peak 1 can be estimated at –0.2 V, notably lower than the value expected for the onset of PdO reduction, –0.36 V, but comparable to that for Pd(OH)₂, –0.21 V.

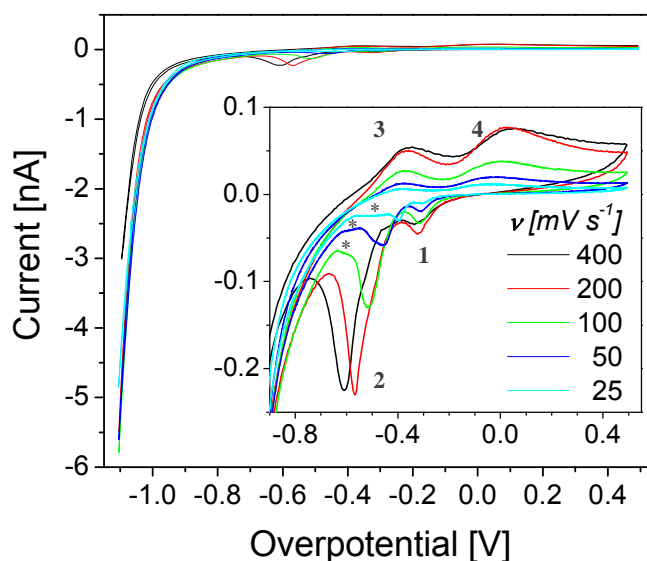


Figure H.6 Cyclic voltammograms for Pd | CsHSO₄, collected at 150 °C in air with ~ 0.03 atm H₂O, showing the transient behavior.

H.2.3 Palladium Oxidation

We examined the reduction behavior of Peaks 1 and 2 as a function of oxidation time in air at applied voltages of 0 V and 0.5 V, conditions that allow for chemical and electrochemical oxidation of Pd, respectively (Figure H.7). In the case of chemical oxidation (dwelling with no voltage applied), the peak positions for both Peaks 1 and 2 shifted to larger overpotentials with dwell time, with the two peaks becoming completely convoluted for a 10 min dwell time (Figure H.7). The steady-state current at -1 V increases with dwell time, with some scatter. In the case of electrochemical oxidation (0.5 V applied voltage), the current-voltage curves are much less noisy, with the current at -1 V clearly increasing with dwell time (Figure H.7b). Peak 1 shrinks with dwell time, disappearing completely after 10 min, while Peak 2 increases, with the peak position shifting to higher overpotentials. The disappearance of Peak 1 and the increase in the area of Peak 2 suggests that electrochemical oxidation favors the formation of species which are subsequently reduced via Peak 2. This is also true in the case of chemical oxidation but to a much lesser extent, as indicated by the presence of Peak 1 even after 5 min dwell time (Figure H.7b). It is important to keep in mind that these peaks might not necessarily correspond to oxides of Pd. For example, solid products which could result from reaction between Pd and CsHSO_4 at oxidative conditions would be electro-reduced once sufficiently negative overpotentials are applied. Another process which could generate transient features in the voltammograms is the insertion of hydrogen into Pd, that is, under reducing currents, protons from CsHSO_4 are reduced by electrons to hydrogen atoms which are then inserted into Pd. This insertion/charging process could surface as a peak in cyclic voltammetry as interstitial sites in Pd are being filled.

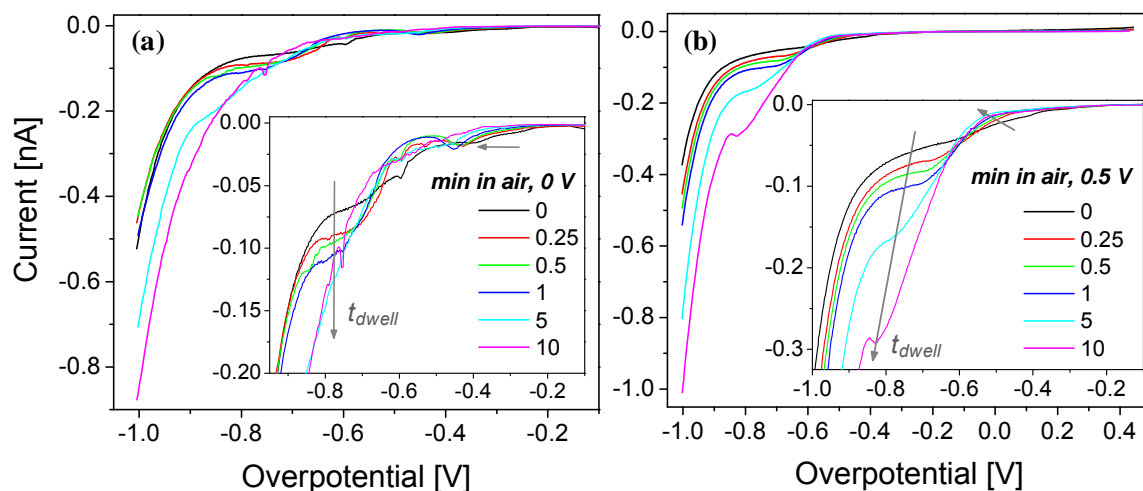


Figure H.7 Behavior of reduction peaks in Pd | CsHSO₄ ($\nu = 100 \text{ mV s}^{-1}$) collected at 150 °C in flowing air with $\sim 0.03 \text{ atm H}_2\text{O}$, after dwelling for various times (a) with no voltage applied, for chemical oxidation of Pd and (b) 0.5 V applied, for electrochemical oxidation of Pd.

H.2.4 Stability of Pd | CsHSO₄

Despite electrochemical characterization of Pd | CsHSO₄ at $\sim 150 \text{ °C}$ for several hours, during which cyclic voltammograms (between -1.1 and 0.5 V) were routinely collected and oxidation tests performed, the steady-state electrochemical currents did not appear to degrade significantly with time. As shown in (Figure H.8a) for data collected at various positions across the CsHSO₄ surface, the current at -1.1 V fluctuated randomly with time (and position) while that at -0.8 V increases slightly with time (and position). The latter can also be seen in Figure H.8b for three select voltammograms collected at arbitrary positions/times; the increase in steady-state current appears to be correlated with the transient features which also increase in size. This behavior generally implies that the contact area has increased. In contrast to the behavior at -1.1 V , the increase in current at -0.8 V with time outweighs any changes in current due to spatial heterogeneity.

The observation that the currents do not degrade significantly is an indication that Pd (oxide) does not react with CsHSO₄ in a way that is detrimental to the oxygen reduction kinetics. Although Pd (presumably the oxide form) was observed to react with CsH₂PO₄ at temperatures near ~ 240 °C, reaction at ~ 150 °C was not observed even after 48 h (Appendix B). This is consistent with, though not necessarily evidence of, the observed stability of the Pd | CsHSO₄ system.

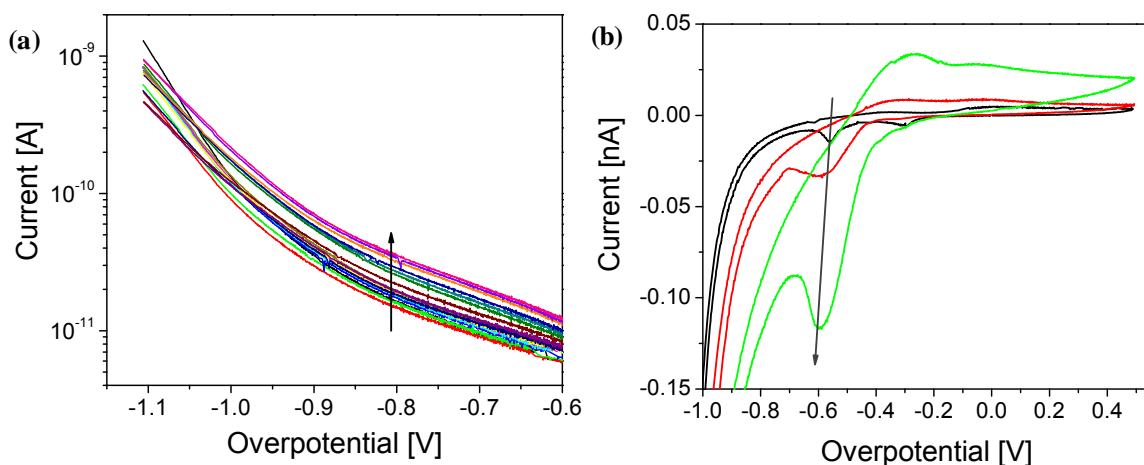


Figure H.8 Spatial variation of Pd | CsHSO₄ at $T = 150$ °C in air with ~ 0.03 atm H₂O: (a) Tafel behavior as a function of position (and time), taken from voltammograms collected at 25 mV s^{-1} and (b) three voltammograms (100 mV s^{-1}) collected at beginning, middle and end of the spatial variation studies in (a).

H.3 Summary

- 1) A correlation of i_0 and α was observed for Pd, using probes similar to those used for the Pt | CsHSO₄ system presented in Chapter 4.
- 2) Despite having nominally low spring constants, triangular-type silicon nitride probes appeared to cause more damage to CsHSO₄ than rectangular-type silicon probes. In general, probes of the same design should be used when comparing different metal coatings.

- 3) Pd | CsHSO₄ displayed two primary transient features for which both the reduction and corresponding oxidation peaks were visible. These peaks may be related to oxide formation but are not necessarily, themselves representative of PdO or related oxides. This is because any charging/discharging process in series with an electrochemical step can manifest itself as a peak in the voltammogram.
- 4) Pd does not appear to react significantly (if at all) with CsHSO₄.
- 5) Across five different Pd | CsHSO₄ (not all presented in this section), we frequently observed an increase in the Tafel slope at high overpotentials. It is unclear whether the intermediate-to-high overpotential regime has some contribution from kinetically slow transient processes, even at a 25 mV s⁻¹, which would generate artifacts in the Tafel plot.

Appendix I Crystallographic Compatibility in $\text{Cs}_{1-x}\text{Rb}_x\text{H}_2\text{PO}_4$

I.1 Visualization of the Cubic-to-Monoclinic Transformation in CsH_2PO_4

The cubic-to-monoclinic transformation for CsH_2PO_4 is depicted in Figure I.1. From examination of the lattice parameters (Table I.1 and Table I.2) and the geometry of the two unit cells, the relationship between the two structures can be determined as follows. A tetragonal cell is constructed by connecting the face diagonals of four adjacent cubic unit cells (Figure I.1a). A shift in this cell in the -3 direction (Figure I.1b), while not necessary for this analysis, aids with visualization of atom movement during the transformation. The tetragonal cell is subsequently stretched unequally along its three axes (not shown) and the Cs atoms shifted to keep two units of CsH_2PO_4 in the cell (Figure I.1c). Finally, the top face is sheared along the c direction to increase the angle β from 90° to 107.7° (Figure I.1d). Appropriate shifts of the atoms result in the final monoclinic structure.

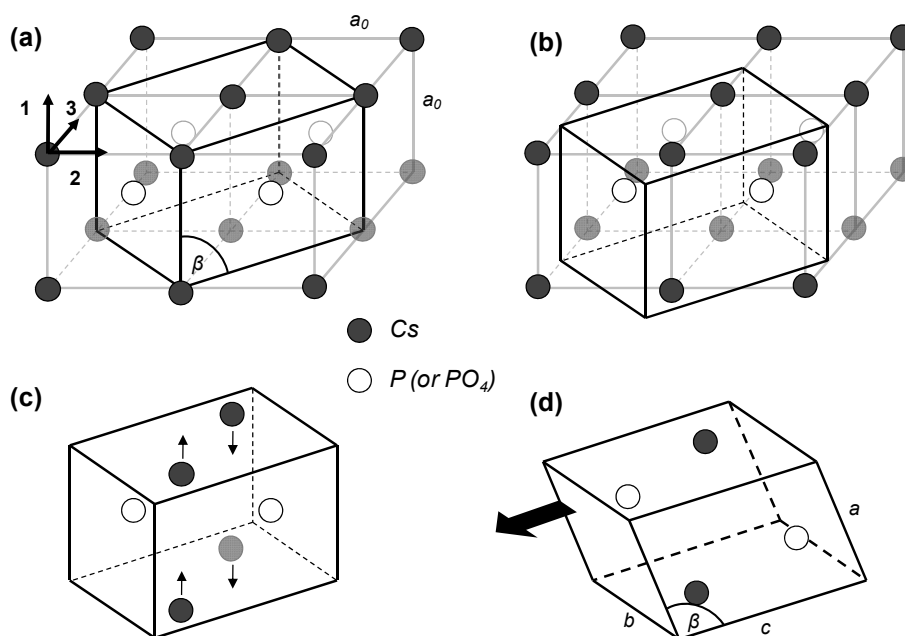


Figure I.1 Visualization of the phase transformation in CsH_2PO_4 with only P and O atoms drawn. The contents of a monoclinic cell can be obtained from (a–b) a shifted tetragonal sub-lattice obtained from four cubic unit cells. (c) The Cs cation is shifted off the bc planes to keep two Cs atoms per lattice, and (c–d) the bc plane is sheared along the c direction to obtain the β angle.

Table I.1 Lattice parameters and atomic positions for the low-temperature monoclinic structure of CsH_2PO_4 .⁶⁸

P2₁/m (#11)					
$a = 4.8788 \text{ \AA}$, $b = 6.3848 \text{ \AA}$, $c = 7.9091 \text{ \AA}$, $\alpha = \gamma = 90^\circ$, $\beta = 107.71^\circ$					
<i>Atom</i>	<i>Multiplicity</i>	<i>Occupancy</i>	<i>x</i>	<i>y</i>	<i>z</i>
Cs	2	1	0.0351(1)	0.25	0.26564(4)
P	2	1	0.5290(3)	0.75	0.2370(2)
O(1)	2	1	0.3883(7)	0.75	0.3912(5)
O(2)	2	1	0.8461(9)	0.75	0.3228(6)
O(3)	4	1	0.4188(7)	0.5528(5)	0.1270(4)
H(1)	1	1	0.195	0.75	0.348
H(2)	1	1	0.5	0.5	0

Table I.2 Lattice parameters and atomic positions for the high-temperature cubic structure of CsH_2PO_4 .¹¹⁷

Pm-3m (#221)					
$a_0 = 4.9549(4) \text{ \AA}$, $\alpha = \beta = \gamma = 90^\circ$					
<i>Atom</i>	<i>Multiplicity</i>	<i>Occupancy</i>	<i>x</i>	<i>y</i>	<i>z</i>
Cs	1	1	0	0	0
P	1	1	0.5	0.5	0.5
O	24	1/6	0.322	0.248	0.5
H	48	1/24	—	—	—

I.2 Calculation of Transformation Matrix

This section follows procedures outlined by Bhattacharya¹¹⁵ and details on how to compute the transformation matrix described by Equation 5.2. For some transformations (including that for CsH_2PO_4), the homogeneous deformation of the lattice vectors to transform between the austenite and martensite phases does not yield a transformation that is symmetric. In this case, the direct mapping of the lattice vectors of the cubic and monoclinic cases is

$$\mathbf{e}_i^m = \mathbf{T}_1 \mathbf{e}_i^a \quad (\text{I.1})$$

where \mathbf{e}_i^a and \mathbf{e}_i^m are given by Equation 5.3 and 5.4, respectively. \mathbf{T}_1 , the homogeneous deformation, can be computed readily by matrix algebra.

$$\mathbf{T}_1 = \begin{pmatrix} \frac{a}{a_0} & \frac{c}{2a_0} \cos \beta & \frac{c}{2a_0} \cos \beta \\ 0 & \frac{c \sin \beta + b}{2a_0 \sqrt{2}} & \frac{c \sin \beta - b}{2a_0 \sqrt{2}} \\ 0 & \frac{c \sin \beta - b}{2a_0 \sqrt{2}} & \frac{c \sin \beta + b}{2a_0 \sqrt{2}} \end{pmatrix} \quad (\text{I.2})$$

By convention, the definition of the transformation matrix should be positive-definite and symmetric, and therefore, the deformation \mathbf{T}_1 is modified to obtain the symmetric, positive-definite matrix \mathbf{U}_1 . To obtain \mathbf{U}_1 , $\mathbf{T}_1 = \mathbf{Q}\mathbf{U}_1$ is decomposed such that \mathbf{Q} is a rotation; because of frame-indifference, a rotation leaves the state of the lattice unchanged. The procedure for computing \mathbf{U}_1 is:

- 1) Find the matrix, $\mathbf{C} = \mathbf{T}_1^T \mathbf{T}_1$. \mathbf{C} is a positive-definite matrix.
- 2) Compute the eigenvalues $\{\gamma_1, \gamma_2, \gamma_3\}$ and the eigenvectors $\{\mathbf{u}_1, \mathbf{u}_2, \mathbf{u}_3\}$ of \mathbf{C} .

- 3) Take the positive root of each eigenvalue, $\mu_i = \sqrt{\gamma_i}$ for $i = 1, 2, 3$. Note γ_i is positive since \mathbf{C} is a positive-definite matrix.
- 4) The Bain matrix, \mathbf{U}_1 , with eigenvalues $\{\mu_1, \mu_2, \mu_3\}$ and eigenvectors $\{\mathbf{u}_1, \mathbf{u}_2, \mathbf{u}_3\}$, is given by:

$$\mathbf{U}_1 = \mu_1 \mathbf{u}_1 \otimes \mathbf{u}_1 + \mu_2 \mathbf{u}_2 \otimes \mathbf{u}_2 + \mu_3 \mathbf{u}_3 \otimes \mathbf{u}_3 \quad (\text{I.3})$$

Once \mathbf{U}_1 is known, all other variants can be obtained by applying the rotations of the cubic austenite lattice to this matrix. Variants, $\mathbf{U}_1, \mathbf{U}_2, \dots, \mathbf{U}_N$ have the form

$$\mathbf{U}_j = \mathbf{R}^T \mathbf{U}_1 \mathbf{R} \quad (\text{I.4})$$

where \mathbf{R} is a rotation in the point group of the austenite. The relative symmetries of the austenite and martensite phases, some rotations of \mathbf{U}_1 will not give a unique variant, and precisely N distinct variants will exist, where N is given in Equation 5.1.

I.3 Calculation of Compatible Variant Pairs: Twinning Modes

In this section, we present a calculation of the twinning modes in CsH_2PO_4 which can occur on cooling from the cubic phase. We assume a simple microstructure comprised of one type of twin, that is, there exists no special microstructures such as twins within twins. To calculate the twinning modes of a given transformation, crystallographically compatible variants are first identified. Figure I.2 shows a schematic diagram of twins formed between a pair of variants \mathbf{U}_j and \mathbf{U}_i . \mathbf{U}_i and \mathbf{U}_j can form a twin if they satisfy the twinning equation

$$\mathbf{Q}\mathbf{U}_i - \mathbf{U}_j = \mathbf{a} \otimes \mathbf{n} \quad (\text{I.5})$$

for some rotation \mathbf{Q} and unit vector \mathbf{n} normal to the twinning interface. The twinning equation is a statement of the kinematic compatibility condition which requires the existence of an invariant plane, described by \mathbf{n} , at the interface between two regions that have undergone continuous deformation.

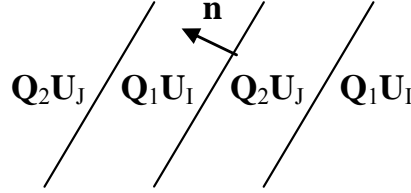


Figure I.2 Parallel twins separating two alternating variants, \mathbf{U}_J and \mathbf{U}_I . \mathbf{Q}_1 and \mathbf{Q}_2 denote rotations.

The twinning equation (I.5) has two solutions if Equation (I.4) is satisfied for some 180° rotation $\mathbf{R} = -\mathbf{I} + 2\mathbf{v} \otimes \mathbf{v}$ about unit vector \mathbf{v} :

$$\mathbf{a} = 2 \left(\frac{\mathbf{U}_j^T \mathbf{v}}{|\mathbf{U}_j^T \mathbf{v}|^2} - \mathbf{U}_j \mathbf{v} \right), \quad \mathbf{n} = \mathbf{v} \quad (\text{I.6})$$

$$\mathbf{a} = \rho \mathbf{U}_j \mathbf{v}, \quad \mathbf{n} = \frac{2}{\rho} \left(\mathbf{v} - \frac{\mathbf{U}_j^T \mathbf{U}_j \mathbf{v}}{|\mathbf{U}_j \mathbf{v}|^2} \right) \quad (\text{I.7})$$

where ρ is non-zero and chosen such that $|\mathbf{n}| = 1$. The solution given by Equation (I.6) describes a Type I twin (i.e., the twinning plan is the plane of symmetry in the austenite), whereas the solution given by Equation (I.7) describes a Type II twin (i.e., the direction of shear is the direction of symmetry in the austenite). In the case where there are two distinct 180° rotations, \mathbf{R}_1 and \mathbf{R}_2 , which satisfy Equation (I.4) for the same variant pair, Equations (I.6) and (I.7) yield two distinct solutions, each of which can be described as

Type I and Type II twins. (Specifically, the Type I solution using \mathbf{R}_1 corresponds to the Type II solution using \mathbf{R}_2 and vice versa.) These are called Compound twins.

If Equation (I.4) cannot be satisfied for a pair of variants and a two-fold rotation, it is necessary to calculate matrix $\mathbf{D} = \mathbf{U}_J^T \mathbf{U}_I^T \mathbf{U}_I \mathbf{U}_J^{-1}$. If \mathbf{D} is the identity matrix, then the twinning equation has no solution. Otherwise, the eigenvalues of \mathbf{D} , $\{\lambda_1, \lambda_2, \lambda_3\}$, corresponding to eigenvectors, $\{\mathbf{e}_1, \mathbf{e}_2, \mathbf{e}_3\}$, must satisfy

$$\lambda_1 \leq 1, \quad \lambda_2 = 1, \quad \lambda_3 \geq 1 \quad (\text{I.8})$$

If Equation (I.8) holds, then the two solutions to the twinning equation are given by

$$\mathbf{a} = \rho \left(\sqrt{\frac{\lambda_3(1-\lambda_1)}{\lambda_3-\lambda_1}} \mathbf{e}_1 + \kappa \sqrt{\frac{\lambda_1(\lambda_3-1)}{\lambda_3-\lambda_1}} \mathbf{e}_3 \right) \quad (\text{I.9})$$

$$\mathbf{n} = \frac{\sqrt{\lambda_3} - \sqrt{\lambda_1}}{\rho \sqrt{\lambda_3 - \lambda_1}} \left(-\sqrt{1-\lambda_1} \mathbf{U}_J^T \mathbf{e}_1 + \kappa \sqrt{\lambda_3-1} \mathbf{U}_J^T \mathbf{e}_3 \right) \quad (\text{I.10})$$

where $\kappa = \pm 1$, and ρ is non-zero and chosen such that $|\mathbf{n}| = 1$. As with Equations (I.6) and (I.7) two solutions (one for $\kappa = 1$ and one for $\kappa = -1$) are expected.

I.4 Calculation of the Austenite-Martensite Interface

Figure I.3 shows a schematic diagram of a simple austenite-martensite interface which is formed between the pure austenite phase and a twinned microstructure of two variants.

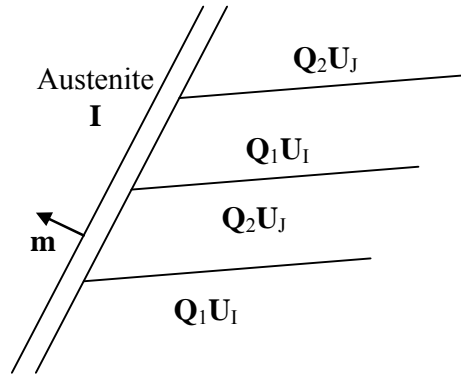


Figure I.3 Schematic of the interface between the austenite and two variants of martensite. \mathbf{m} is the normal vector to the interface.

The interface is defined by the solution to both the twinning equation (I.5) *and* the austenite-martensite interface equation:

$$\mathbf{Q}'(\lambda \mathbf{Q} \mathbf{U}_j + (1 - \lambda) \mathbf{U}_i) = \mathbf{I} + \mathbf{b} \otimes \mathbf{m} \quad (\text{I.11})$$

where λ is some scalar satisfying $0 \leq \lambda \leq 1$ and \mathbf{m} is the unit vector normal to the austenite-martensite interface. Once a solution to Equation (I.5) for matrix \mathbf{U}_i is found — given by either Equations (I.6)–(I.7) and/or (I.9)–(I.10) — the existence of a solution to Equation (I.11) is determined by the values of δ and η .

$$\delta = \mathbf{a} \cdot \mathbf{U}_i (\mathbf{U}_i^2 - \mathbf{I})^{-1} \mathbf{n} \quad \text{and} \quad \eta = \text{tr}(\mathbf{U}_i^2) - \det(\mathbf{U}_i^2) - 2 + \frac{|\mathbf{a}|^2}{2\delta} \quad (\text{I.12})$$

An austenite-martensite interface exists if and only if

$$\delta \leq -2 \quad \text{and} \quad \eta \geq 0 \quad (\text{I.13})$$

If the conditions in Equations (I.13) are satisfied, the interface is described by

$$\mathbf{b} = \rho \left(\sqrt{\frac{\lambda_3(1-\lambda_1)}{\lambda_3-\lambda_1}} \mathbf{e}_1 + \kappa \sqrt{\frac{\lambda_1(\lambda_3-1)}{\lambda_3-\lambda_1}} \mathbf{e}_3 \right) \quad (\text{I.14})$$

$$\mathbf{m} = \frac{\sqrt{\lambda_3} - \sqrt{\lambda_1}}{\rho\sqrt{\lambda_3 - \lambda_1}} \left(-\sqrt{1 - \lambda_1} \mathbf{e}_1 + \kappa \sqrt{\lambda_3 - 1} \mathbf{e}_3 \right) \quad (\text{I.15})$$

where $\kappa = \pm 1$, ρ is chosen such that $|\mathbf{m}| = 1$, and $\lambda_1 \leq \lambda_2 \leq \lambda_3$ are the eigenvalues corresponding to the eigenvectors, $\{\mathbf{e}_1, \mathbf{e}_2, \mathbf{e}_3\}$, of matrix \mathbf{E} defined as

$$\mathbf{E} = (\mathbf{U}_i + \lambda \mathbf{n} \otimes \mathbf{a})(\mathbf{U}_i + \lambda \mathbf{a} \otimes \mathbf{n}) \quad (\text{I.16})$$

and

$$\lambda = \frac{1}{2} \left(1 - \sqrt{1 + \frac{2}{\delta}} \right) \quad (\text{I.17})$$

If $\delta < -2$, another pair of solutions is obtained by replacing λ in Equation (I.16) with $(1 - \lambda)$. For each allowable variant pair, two types of twins can form, each of which has four possible solutions for the austenite-martensite interface. Therefore, there are up to eight solutions expected for a given variant pair.

I.5 Results for CsH_2PO_4

All calculations shown in this section are based on lattice parameters shown in Table I.1 and Table I.2. The twelve variants of martensite, obtained using Equation (I.4) are shown in Table I.3. Each variant was obtained by a rotation of \mathbf{U}_1 by the angle and about the axis indicated. Note that the choice of symmetry operation on \mathbf{U}_1 is not unique, as different rotations applied to \mathbf{U}_1 can yield the same result.

Table I.3 Martensite variants for the cubic-to-monoclinic transition of CsH_2PO_4 and the corresponding rotation angle and axes about which to rotate to obtain \mathbf{U}_2 – \mathbf{U}_{12} from \mathbf{U}_1 .

Variant	Rotation Angle & Axis	Variant	Rotation Angle & Axis
$\mathbf{U}_1 = \begin{pmatrix} \gamma & \varepsilon & \varepsilon \\ \varepsilon & \alpha & \delta \\ \varepsilon & \delta & \alpha \end{pmatrix}$		$\mathbf{U}_7 = \begin{pmatrix} \alpha & -\varepsilon & -\delta \\ -\varepsilon & \gamma & \varepsilon \\ -\delta & \varepsilon & \alpha \end{pmatrix}$	120° (1–11)
$\mathbf{U}_2 = \begin{pmatrix} \gamma & -\varepsilon & -\varepsilon \\ -\varepsilon & \alpha & \delta \\ -\varepsilon & \delta & \alpha \end{pmatrix}$	180° (100)	$\mathbf{U}_8 = \begin{pmatrix} \alpha & \varepsilon & -\delta \\ \varepsilon & \gamma & -\varepsilon \\ -\delta & -\varepsilon & \alpha \end{pmatrix}$	180° (110)
$\mathbf{U}_3 = \begin{pmatrix} \gamma & -\varepsilon & \varepsilon \\ -\varepsilon & \alpha & -\delta \\ \varepsilon & -\delta & \alpha \end{pmatrix}$	180° (010)	$\mathbf{U}_9 = \begin{pmatrix} \alpha & \delta & \varepsilon \\ \delta & \alpha & \varepsilon \\ \varepsilon & \varepsilon & \gamma \end{pmatrix}$	180° (–101)
$\mathbf{U}_4 = \begin{pmatrix} \gamma & \varepsilon & -\varepsilon \\ \varepsilon & \alpha & -\delta \\ -\varepsilon & -\delta & \alpha \end{pmatrix}$	180° (001)	$\mathbf{U}_{10} = \begin{pmatrix} \alpha & \delta & -\varepsilon \\ \delta & \alpha & -\varepsilon \\ -\varepsilon & -\varepsilon & \gamma \end{pmatrix}$	240° (1–11)
$\mathbf{U}_5 = \begin{pmatrix} \alpha & \varepsilon & \delta \\ \varepsilon & \gamma & \varepsilon \\ \delta & \varepsilon & \alpha \end{pmatrix}$	180° (–110)	$\mathbf{U}_{11} = \begin{pmatrix} \alpha & -\delta & \varepsilon \\ -\delta & \alpha & -\varepsilon \\ \varepsilon & -\varepsilon & \gamma \end{pmatrix}$	180° (101)
$\mathbf{U}_6 = \begin{pmatrix} \alpha & -\varepsilon & \delta \\ -\varepsilon & \gamma & -\varepsilon \\ \delta & -\varepsilon & \alpha \end{pmatrix}$	120° (11–1)	$\mathbf{U}_{12} = \begin{pmatrix} \alpha & -\delta & -\varepsilon \\ -\delta & \alpha & \varepsilon \\ -\varepsilon & \varepsilon & \gamma \end{pmatrix}$	240° (11–1)

where

$$\gamma = \frac{a(\sqrt{2}a + c \sin \beta)}{a_0 \sqrt{2a^2 + c^2 + 2\sqrt{2}ac \sin \beta}}$$

$$\varepsilon = \frac{1}{\sqrt{2}a_0} \left(\frac{ac \cos \beta}{\sqrt{2a^2 + c^2 + 2\sqrt{2}ac \sin \beta}} \right)$$

$$\alpha = \frac{1}{2\sqrt{2}a_0} \left(\frac{c(c + \sqrt{2}a \sin \beta)}{\sqrt{2a^2 + c^2 + 2\sqrt{2}ac \sin \beta}} + b \right)$$

$$\delta = \frac{1}{2\sqrt{2}a_0} \left(\frac{c(c + \sqrt{2}a \sin \beta)}{\sqrt{2a^2 + c^2 + 2\sqrt{2}ac \sin \beta}} - b \right)$$

In the case of CsH_2PO_4 , the variant pairs that form twins satisfied Equation (I.4) for a two-fold rotation and, therefore, Equations (I.6)–(I.7) were used to determine the twinning modes. The variant pairs which are not related by a two-fold rotation did not satisfy Equation (I.8), and therefore, do not form twins. The twinning modes are summarized in Table I.4. Compatible variant pairs are denoted by “Y” and incompatible by “N”. The variant pairs $\text{U}_1\text{--U}_2$, $\text{U}_3\text{--U}_4$, $\text{U}_5\text{--U}_6$, $\text{U}_7\text{--U}_8$, $\text{U}_9\text{--U}_{10}$, and $\text{U}_{11}\text{--U}_{12}$ form compound twins, denoted by “C” in the table. An example of the two solutions to the twinning equation (I.5) for the $\text{U}_1\text{--U}_3$ variant pair is

$$\mathbf{a} = (0.4378, -0.0809, -0.3799) \quad \mathbf{n} = (0, 1, 0) \quad (\text{I.18})$$

and

$$\mathbf{a} = (-0.0709, 0.6285, 0.06380) \quad \mathbf{n} = (0.7329, 0, -0.6804) \quad (\text{I.19})$$

Table I.4 Allowed twinning modes of CsH_2PO_4 martensite. Y indicates a pair of variants capable of forming a twin boundary, N indicates that a pair of twins cannot form a twin boundary, and C indicates a compound twin.

Variant	1	2	3	4	5	6	7	8	9	10	11	12
1		C	Y	Y	Y	N	N	Y	Y	N	Y	N
2	C		Y	Y	N	Y	Y	N	N	Y	N	Y
3	Y	Y		C	N	Y	Y	N	Y	N	Y	N
4	Y	Y	C		Y	N	N	Y	N	Y	N	Y
5	Y	N	N	Y		C	Y	Y	Y	N	N	Y
6	N	Y	Y	N	C		Y	Y	N	Y	Y	N
7	N	Y	Y	N	Y	Y		C	Y	N	N	Y
8	Y	N	N	Y	Y	Y	C		N	Y	Y	N
9	Y	N	Y	N	Y	N	Y	N		C	Y	Y
10	N	Y	N	Y	N	Y	N	Y	C		Y	Y
11	Y	N	Y	N	N	Y	N	Y	Y	Y		C
12	N	Y	N	Y	Y	N	Y	N	Y	Y	C	

For each solution to the twinning equation, given by Equations (I.6)–(I.7), we can determine whether the twins can form a compatible interface with the austenite phase, using the criteria stated in Equation (I.13). Table I.5 is a summary of the variant pairs that can form an austenite-martensite interface.

Table I.5 CsH_2PO_4 martensite variant pairs that are capable of forming an interface with the austenite phase: Y indicates that an interface between the austenite phase and the twins of a specified variant pair is possible, N indicates that it is not possible, and “/” indicates that twinning boundaries are not allowed so an interface with the austenite phase is not possible.

Variant	1	2	3	4	5	6	7	8	9	10	11	12
1		N	Y	Y	Y	/	/	N	Y	/	N	/
2	N		Y	Y	/	N	Y	/	/	N	/	Y
3	Y	Y		N	/	Y	N	/	N	/	Y	/
4	Y	Y	N		N	/	/	Y	/	Y	/	N
5	Y	/	/	N		N	Y	Y	Y	/	/	N
6	/	N	Y	/	N		Y	Y	/	N	Y	/
7	/	Y	N	/	Y	Y		N	N	/	/	Y
8	N	/	/	Y	Y	Y	N		/	Y	N	/
9	Y	/	N	/	Y	/	N	/		N	Y	Y
10	/	N	/	Y	/	N	/	Y	N		Y	Y
11	N	/	Y	/	/	Y	/	N	Y	Y		N
12	/	Y	/	N	N	/	Y	/	Y	Y	N	

If a pair of variants can form an interface with the austenite phase, there are up to eight ways such an interface can exist, four for each twin type. In the case of CsH_2PO_4 , Equation (I.13) is never satisfied for both of the twin types. Therefore, if a solution exists, it is described by 4 rather than 8 vector pairs, **b** and **m**. For the \mathbf{U}_1 – \mathbf{U}_3 variant pair, the austenite-martensite interface is described by Equations (I.20)–(I.23). These four solutions correspond to the Type II twin.

$$\mathbf{b} = (0.0667, 0.0778, 0.2028) \quad \mathbf{m} = (-0.9523, 0.3042, 0.0226) \quad (\text{I.20})$$

$$\mathbf{b} = (0.2188, -0.0585, 0.0183) \quad \mathbf{m} = (-0.1874, -0.3811, -0.9053) \quad (\text{I.21})$$

$$\mathbf{b} = (0.2188, 0.0585, 0.0183) \quad \mathbf{m} = (-0.1874, 0.3811, -0.9053) \quad (\text{I.22})$$

$$\mathbf{b} = (0.0667, -0.0778, 0.2028) \quad \mathbf{m} = (-0.9523, -0.3042, 0.0226) \quad (\text{I.23})$$

Although 42 variant pairs can form martensite twins, only 24 can form austenite-martensite interfaces, resulting in a total of 96 solutions. It should be noted that the variant pairs that form compound twins in monoclinic CsH_2PO_4 cannot form an interface with the cubic austenite phase.

Appendix J Microstructure of Solid Acid Compounds: Supplemental

J.1 Additional Images

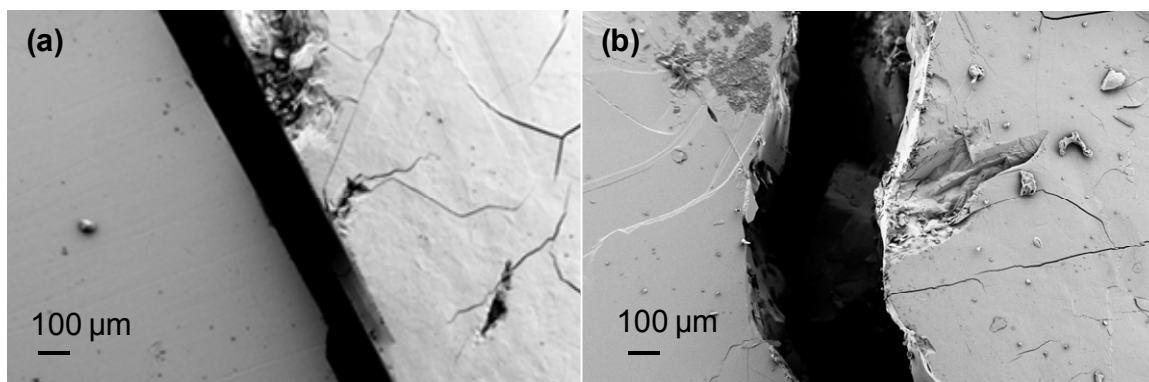


Figure J.1 SEM micrographs of CsH_2PO_4 single crystals, side by side, before and after heat treatment to superprotonic temperatures. Crystal surfaces were prepared by either (a) uni-directional polishing or (b) fracture, then broken in half. For each image, the surfaces on the left and right correspond to two halves of the crystal, before and after heat treatment, respectively.

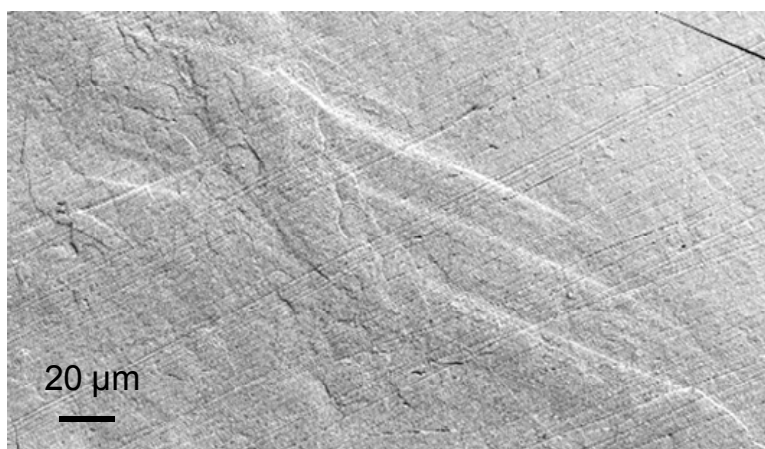


Figure J.2 SEM micrograph of a polished CsH_2PO_4 single-crystal showing features (running from upper-left to lower-right of image) that appear after heating to superprotonic temperatures. Polishing lines run along a different direction (lower-left to upper-right).

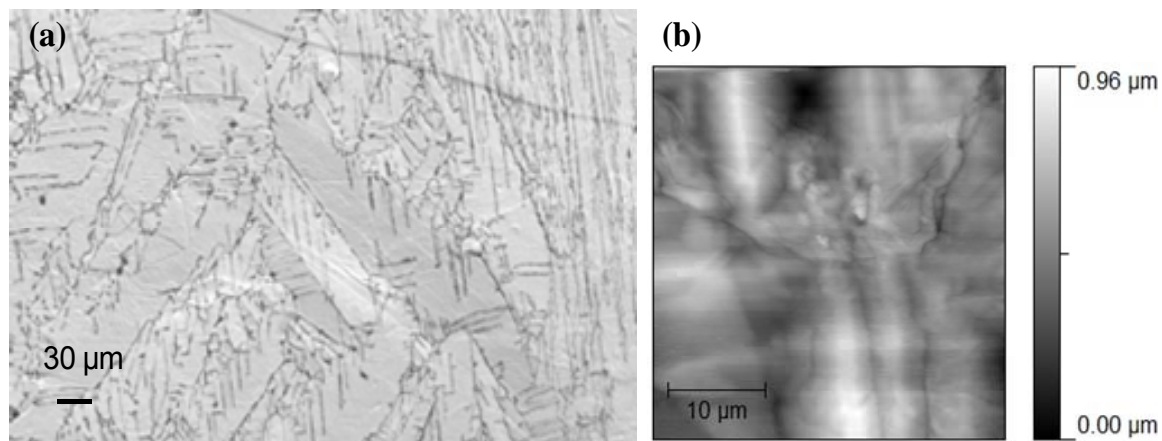


Figure J.3 (a) SEM micrograph of polished CsHSO_4 surface after heating to 155 °C in ambient air, and (b) AFM image of a fractured CsHSO_4 surface at 149 °C. Image was taken after ~ 5 h at superprotonic temperatures and still reveals twinning.

Appendix K Pt | CsH₂PO₄ | Au as a Mixed Potential Hydrogen Sensor

K.1 Introduction

Solid state electrochemical sensors have been developed for the detection of a wide variety of gases, including H₂, CO, NO_x, and hydrocarbons.^{128–129} Potentiometric sensors offer several advantages over amperometric sensors since generated voltages across potentiometric cells are independent of sensor dimensions. Furthermore, potentiometric sensors that are governed by the mixed potential effect^{130–131} can generate a measurable voltage in a single uniform gas, allowing for simpler operation and design. The mixed potential effect has been discussed in literature in the context of both dual chamber and single chamber mode. In the dual chamber mode, evidence of the mixed potential effect was the observation of open-circuit voltages deviating from the computed Nernst voltage^{132–133} while in the single chamber mode, a measurable voltage can be generated when using dissimilar electrodes.^{131, 134–138}

The response behavior of the mixed potential has been shown to depend on the kinetics of the electrochemical reactions at hand, for example, whether the reaction kinetics are limited by charge transfer or mass transport.^{130–131, 139} Consequently, the characteristics of a mixed potential sensor are governed by a large number of parameters including environmental factors such as gas composition and temperature as well as sensor characteristics such as the choice of electrolyte and electrode. What is more, electrode properties such as surface area, microstructure, and activity for the sensing gas

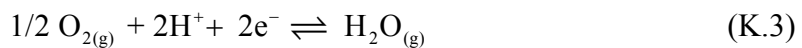
play a significant role in the sensor response. In this work, we demonstrate the mixed potential effect for a sensor based on the solid acid electrolyte, CsH_2PO_4 .

K.2 Mixed Potential Effect

In uniform H_2 - H_2O -Ar atmospheres, H_2 and H_2O can reach equilibrium via the reaction



However, in the presence of an electrode | electrolyte interface, the following reactions can proceed:



with the electrons generated by (K.2) being consumed by (K.3). Graphically, this is depicted by the intersection of the current-voltage curves for (K.2) and (K.3), as shown in Figure K.1a. (Note that Equations (K.2) and (K.3) also apply in H_2 - H_2O -air atmospheres.) At the point of intersection, the reducing and oxidizing currents on a given metal electrode are equal, resulting in what is termed the mixed potential, denoted as E_{Au} and E_{Pt} for Au and Pt metals, respectively. The difference between the mixed potential established at each metal corresponds to the voltage measured across the Pt | electrolyte | Au cell. A change in the gas composition causes a shift in the curves (Figure K.1a) and therefore a change in the voltage measured across the cell. As evident in Figure K.1, the voltage existing across the cell depends on the shape of the current-voltage curves. Therefore, it is common to use metals with sufficiently differing activities

for the electrochemical reactions of interest as this would yield the largest difference in mixed potential across the two metals. It is important to note that, depending on the gas environment, additional reactions can contribute to the mixed potential effect.

Because the mixed potential is established by kinetics, electrode microstructure and geometric factors play a role in the response by changing the net current that can flow at each metal. For example, in Figure K.1b, we schematically show the effect of mass transport limitations (for oxygen gas, in this case). A shift in the current-voltage curves due to a gas composition change results in a different voltage response than in the case of no mass transport limitations (Figure K.1a).

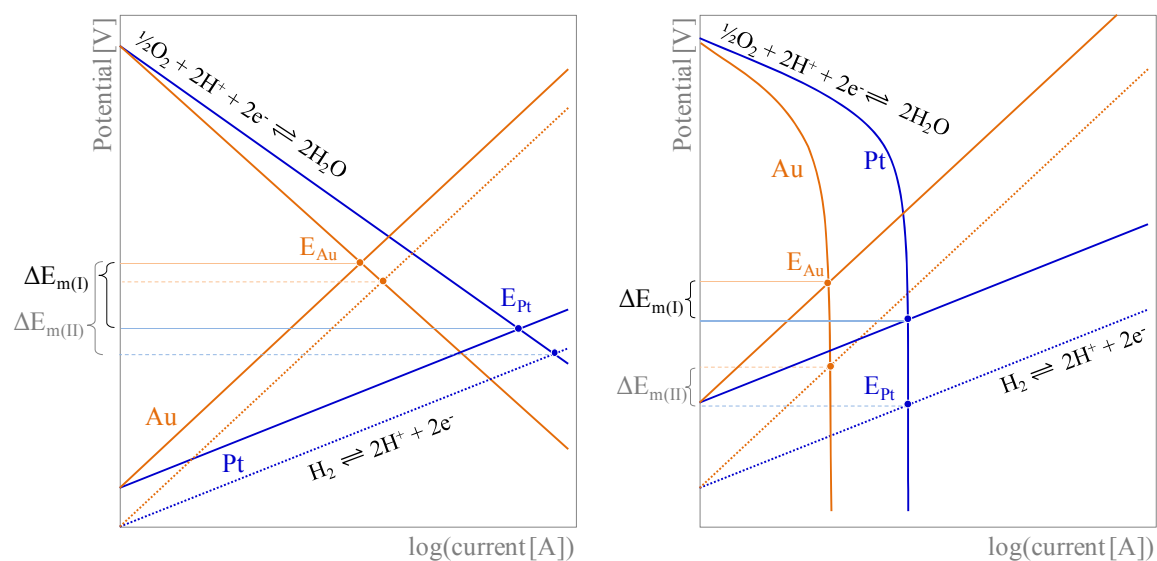


Figure K.1 Schematic polarization curves for determining mixed potentials (a) with and (b) without mass transport limitations. E_{Au} and E_{Pt} denote the mixed potentials established at each metal, and ΔE_{m} corresponds to the voltage measured across the sensor. Subscripts I and II denote before and after a shift in the gas composition (or current-voltage curves).

K.3 Experimental

CsH_2PO_4 powders were prepared from aqueous solutions of Cs_2CO_3 (99.9%, Alfa Aesar, 12887) and H_3PO_4 (85%, Mallinckrodt, 2796). The resulting solution was added to methanol to induce rapid precipitation, and the precipitate was dried at 100 °C. The powder was uni-axially pressed (491 MPa for 20 min) into polycrystalline CsH_2PO_4 discs 9.3 mm in dia. and ~ 1 mm thick. Disc surfaces were mechanically polished (grit size 600) before deposition of Pt and Au films. Sensors were prepared by sputtering Au and Pt films (AJA International) on opposing sides of CsH_2PO_4 discs which were masked at its edges by tape during deposition. The sputtering time was controlled to obtain metal films ~ 75 nm thick.

Electrical contact to the metal films was made by sandwiching the cell between two sheets of Toray carbon paper which, in turn, were mechanically contacted to silver ring current collectors. The response behavior of the sensor was examined at 235 °C under uniform H_2 -Ar- H_2O atmospheres with a total flow rate of 200 mL min^{-1} . The hydrogen partial pressures examined, 0.0005–0.5 atm, were achieved by mixing appropriate flow rates of 100%, 2%, and 0.1% H_2 gas (ultra-high purity grade with Ar balance) via calibrated digital mass flow controllers. A water partial pressure of ~ 0.5 atm was maintained by bubbling inlet H_2 -Ar through a heated water bath and monitored by a humidity sensor (Rotronic Instrument Corp.). The open-circuit voltage of the cell was measured using a Keithley 617 electrometer.

For each composition examined, appropriate flow rates of 100, 2, and/or 1% H_2 in Ar were used. Due to limitations in the reactor design, these gases were not pre-mixed before entering the reactor. Between measurements of the sensor response for each

hydrogen partial pressure (values between 0.001 and 0.5 atm), the gas composition was returned to baseline of 5×10^{-4} atm H₂.

Films before and after sensor characterization were examined by scanning electron microscopy (LEO 1550VP, Carl Zeiss SMT) and X-ray diffraction (Phillips X'Pert Pro). Film characteristics are typical of those reported for Pt thin films (Chapter 3 and Appendix C) and, therefore, are not shown here.

K.4 Results and Discussion

K.4.1 Sensor Response

The response of the Pt | CsH₂PO₄ | Au sensor is shown in Figure K.2 in which each feature corresponds to the change in cell voltage due to a different hydrogen partial pressure, as labeled. The measured voltage is greater at lower partial pressure, with the baseline p_{H_2} of 5×10^{-4} atm H₂ yielding a voltage over -200 mV. At the highest p_{H_2} of 0.5 atm, the open-circuit voltage is approximately -20 mV. Given the cell configuration employed (which the positive lead of the electrometer attached to Pt), the negative voltages measured implies that the mixed potential established at Pt is lower than that at Au.

The lack of reproducibility in the shape of the transient response is likely due to the low gas velocities used, that is, despite the large volumetric flow rate of 200 mL min^{-1} , the gas velocity near the sensor was $\sim 16 \text{ cm min}^{-1}$ due to the large cross-section of the reactor. At low p_{H_2} levels, the response overshoots before reaching to the steady-state value when p_{H_2} is increased from or decreased back to the baseline value. At

high $p\text{H}_2$ levels, the response appears to be more stable, displaying a small overshoot and a gradual increase to the steady-state value when the $p\text{H}_2$ is increased from the baseline value. On return to the baseline value, the voltage decays gradually. There is no apparent correlation between the observed transient behavior and the gas source used (i.e., mixture of 100, 2, and/or 0.1% H_2) to obtain the desired composition. Thus, the most plausible explanation is that compositional variations in the gas stream, due to poorly mixed source gases, cause fluctuations in the measured voltage.

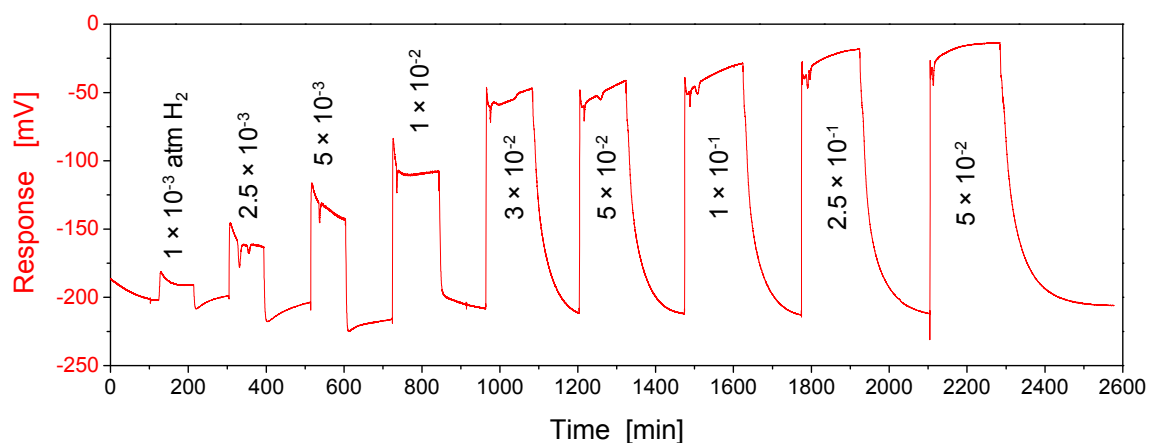


Figure K.2 Plot of measured open-circuit voltage (response) as a function of time for a $\text{Pt} \mid \text{CsH}_2\text{PO}_4 \mid \text{Au}$ sensor at 235°C in $\text{H}_2\text{-H}_2\text{O-Ar}$ atmospheres with $0.5\text{ atm H}_2\text{O}$ and various hydrogen partial pressures (as labeled). The baseline composition was arbitrarily set to $5 \times 10^{-4}\text{ atm H}_2$.

Steady-state values of the response, estimated by extrapolation from Figure K.2, are plotted in Figure K.3. The response, as indicated previously, ranges between -200 mV and -20 mV for hydrogen partial pressures spanning three orders of magnitude ($0.0005\text{--}0.5\text{ atm } p\text{H}_2$). There appears to be two distinct regimes; the slope of the plot is $\sim 75\text{ mV dec}^{-1}$ for $p\text{H}_2 < 0.01\text{ atm}$ and $\sim 23\text{ mV dec}^{-1}$ for $p\text{H}_2 > 0.01\text{ atm}$, indicating a higher sensitivity to gas compositions at lower hydrogen partial pressures.

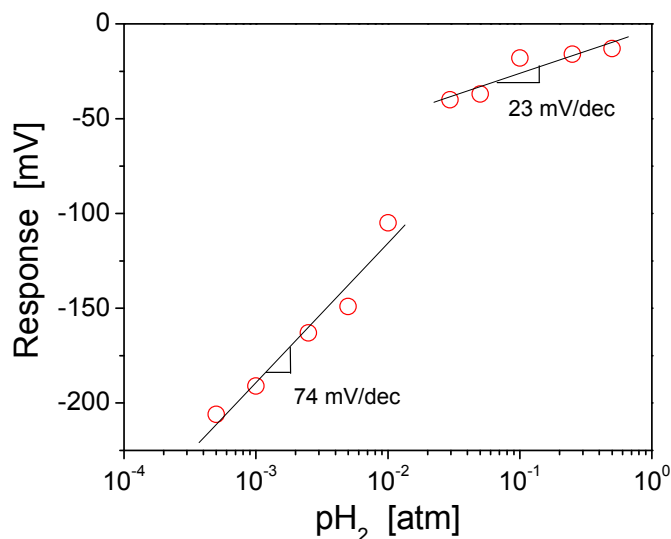


Figure K.3 Mixed potential response of Pt | CsH₂PO₄ | Au sensor for various hydrogen partial pressures at 235 °C in H₂-H₂O-Ar atmospheres with 0.5 atm H₂O. This plot corresponds to data shown in Figure K.2.

An abrupt change in the measured voltage (plotted against composition) is commonly attributed to mass transport limitations.¹³⁰ Depicted in Figure K.4 is the case in which both oxygen reduction and hydrogen oxidation are limited by mass transport, the former being true for all compositions and the latter when low hydrogen partial pressures are employed. At relatively high $p\text{H}_2$, the limiting current is higher and, therefore, the mixed potential occurs outside of the mass transport limited regime for hydrogen oxidation. However, as $p\text{H}_2$ is lowered, a sudden jump in the mixed potential occurs, as depicted between E_{m2} and E_{m3} , with the latter potential lying within the mass-transport limited regime.

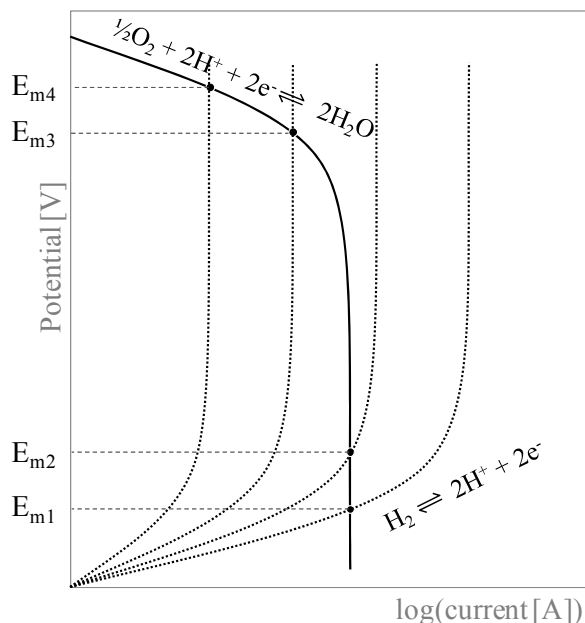


Figure K.4 Schematic showing how mass transport limitations can result in a large change in the mixed potential for a small change the gas composition. E_{m1} – E_{m4} indicate the mixed potentials established on a metal as the p_{H_2} gas composition is varied.

Additional tests reveal large variations in the response. Shown in Figure K.5 are data for two additional cells, plotted alongside data from Figure K.3 (denoted as HS-CDP07). Figure K.5 shows that not only do different samples yield drastically different responses, but even a given cell, tested on two different days (HS-CDP07, expt 1 vs. expt 2), yields significantly different results. Figure K.6 is a voltage-time plot corresponding to HS-CDP09 (Figure K.5). Immediately clear are differences in the transient behavior compared to that in Figure K.2; the steady-state values are attained relatively quickly, indicating faster response times. Furthermore, the measured voltages are close to zero (–1 mV) for a large range of partial pressures.

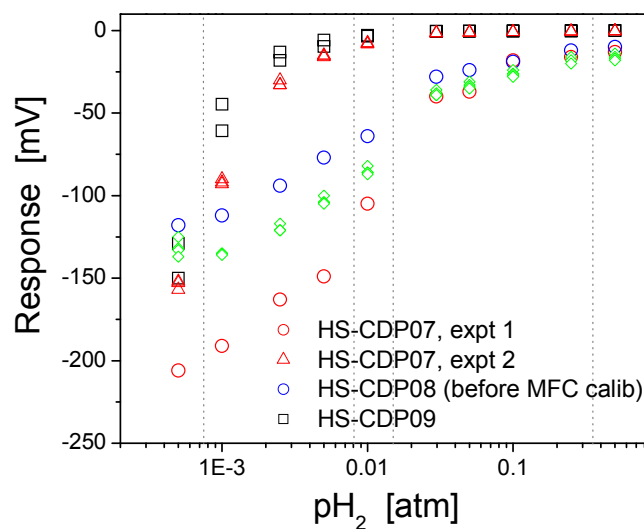


Figure K.5 Mixed potential response of various Pt | CsH₂PO₄ | Au sensors for varying hydrogen partial pressures at 235 °C in H₂-H₂O-Ar atmospheres with 0.5 atm H₂O. Dotted lines indicates a change the gas source used to obtained the desired partial pressure.

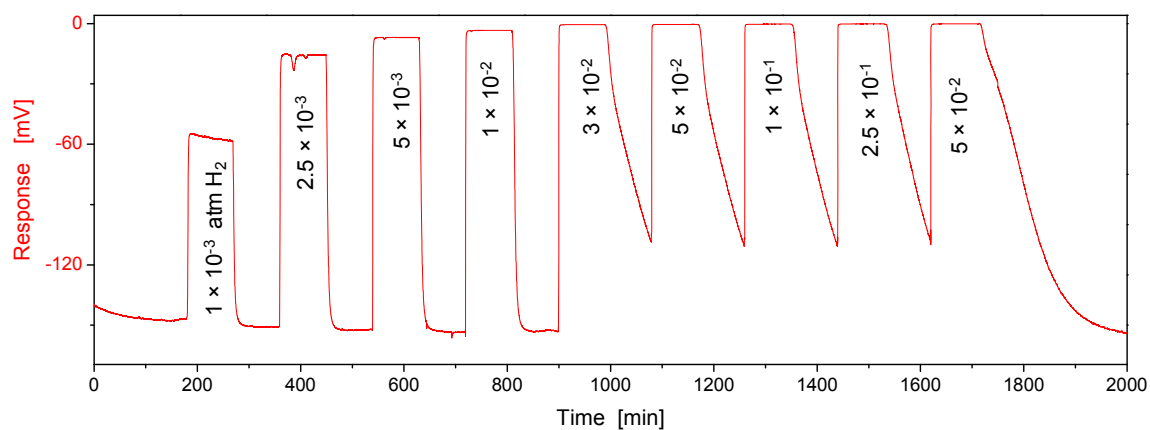


Figure K.6 Plot of measured open circuit voltage (response) as a function of time for a Pt | CsH₂PO₄ | Au sensor (HS-CDP09 in Figure K.5) at 235 °C in H₂-H₂O-Ar atmospheres with 0.5 atm H₂O and various hydrogen partial pressures (as noted). The baseline composition was set to 5 × 10⁻⁴ atm H₂.

K.4.2 Variability in the Sensor Response

Poor mixing of gases (due to low gas velocities), while expected to influence the transient response, should not cause irreproducibilities in the steady-state voltage across the cell. The observed variability in the Pt | CsH₂PO₄ | Au sensor response is most likely due to microstructural variations in the films which can influence both response time and the mixed potential.

Mass transport effects may also play a role. The gas atmosphere contains high hydrogen and water contents and therefore an extremely low oxygen concentration (significantly lower than the lowest $p\text{H}_2$ used in this study). Thus, small fluctuations in $p\text{O}_2$, due to leaks and/or changes in the H₂ and H₂O content, may influence the value of the mixed potential. Moreover, the low $p\text{O}_2$ levels in the system mean that O₂ is mass transport limited and the reaction shown in (K.3) lies far to the left. It should be noted that although the gas flow rate is kept constant for the data presented in this work, observation of changes in the sensor response with gas flow rate (not shown) indicates that mass transport limitations play a role. The water partial pressure changes by a maximum amount of 0.03 atm when the gas composition is changed (most notable when the gas atmosphere is switched from the low- $p\text{H}_2$ baseline composition to a high $p\text{H}_2$ composition) due to variations in the amount of water vapor that Ar and H₂ gases collect during passage through the water bubbler. For $p\text{H}_2\text{O}$ fluctuations about a set point value of 0.5 atm used in this study, the sensitivity to water vapor content was negligible.

K.5 Summary and Recommendations

We have established that, at temperatures relevant for solid acid electrolytes, the mixed potential effect can be observed. In inert environments, larger voltages (approximately -200 mV) were measured at lower hydrogen partial pressures. The sensor response appeared to be irreproducible across samples and even within the same sample; this is attributed to microstructure variations.

Future studies should be carried out with small reactors with low cross-sectional area. Given the results of Chapter 3, metal films need not be 75 nm. Improved response times may result from thinner (~ 10 nm) films for which the equilibration of hydrogen within the film is minimized. Also, it is possible to use particulate electrodes, for example, carbon powder, rather than the relatively expensive Au as the relatively inert electrode.

It is important to note that sensing of H_2 in air is more practical as this is most likely the environment in which a sensor would operate. In this case, for safety reasons, it is necessary to keep the hydrogen partial pressures relatively low. Measurements in a balance of air are expected to yield a different sensor response from those in inert atmospheres due to the significantly higher oxygen content compared to that established by H_2 - H_2O mixtures. Furthermore, the higher oxygen content may lead to more reproducible sensor responses. Note that for operation in air, it is necessary to consider additional reactions that may contribute to the mixed potential. For example, it has been suggested that the electrochemical oxidation of metal (for example, Pt via the reaction, $Pt_{(s)} + H_2O_{(g)} \rightleftharpoons PtO_{(s)} + 2H^+ + 2e^-$) can participate in establishing the mixed potential.

References

1. Boysen, D. A.; Uda, T.; Chisholm, C. R. I.; Haile, S. M. High-Performance Solid Acid Fuel Cells through Humidity Stabilization. *Science* **2004**, *303*, 68–70.
2. Successful Delivery of First 1.4 kW Solid Acid Fuel Cell Stack by Norwegian-Californian Partnership. http://www.safcell-inc.com/_press/20110223-Milestone%203%20PR.pdf.
3. Chisholm, C. R. I.; Boysen, D. A.; Papandrew, A. B.; Zecevic, S.; Cha, S.; Sasaki, K. A.; Varga, A.; Giapis, K. P.; Haile, S. M., From Laboratory Breakthrough to Technological Realization: The Development Path for Solid Acid Fuel Cells. *Electrochem Soc Interface* 2009, pp 53–59.
4. Carrette, L., Friedrich, K.A., Stimming, U. Fuel Cells; Principles, Types, Fuels, and Applications. *ChemPhysChem* **2000**, *1*, 162–193.
5. Larminie, J.; Dicks, A., *Fuel Cell Systems Explained*. 2nd ed.; J. Wiley: Chichester ; New York, 2003; p xxii, 406 p.
6. Baranov, A. I.; Shuvalov, L. A.; Shchagina, N. M. Superior Conductivity and Phase Transitions in CsHSO₄ and CsHSeO₄ Crystals. *JETP Letters* **1982**, *36*, 459–462.
7. Pawlowski, A.; Pawlaczyk, C. Electric-Conductivity and Capacity Studies of Rb₃H(SeO₄)₂ Single-Crystal near the High-Temperature Phase-Transition. *Ferroelectrics* **1988**, *81*, 1165–1170.
8. Ramasastry, C.; Ramaiah, K. S. Electrical-Conduction in Na₃H(SO₄)₂ and (NH₄)₃H(SO₄)₂ Crystals. *J Mater Sci* **1981**, *16*, 2011–2016.
9. Chisholm, C. R. I.; Haile, S. M. Superprotonic Behavior of Cs₂(HSO₄)(H₂PO₄) – a New Solid Acid in the CsHSO₄-CsH₂PO₄ System. *Solid State Ionics* **2000**, *136*, 229–241.
10. Haile, S. M.; Chisholm, C. R. I.; Sasaki, K.; Boysen, D. A.; Uda, T. Solid Acid Proton Conductors: From Laboratory Curiosities to Fuel Cell Electrolytes. *Faraday Discuss* **2007**, *134*, 17–39.
11. Chisholm, C. R. I.; Merle, R. B.; Boysen, D. A.; Haile, S. M. Superprotonic Phase Transition in CsH(PO₃H). *Chem Mater* **2002**, *14*, 3889–3893.
12. Haile, S. M.; Boysen, D. A.; Chisholm, C. R. I.; Merle, R. B. Solid Acids as Fuel Cell Electrolytes. *Nature* **2001**, *410*, 910–913.
13. Haile, S. M. Materials for Fuel Cells. *Materials Today* **2003**, 24–29.
14. Uda, T.; Boysen, D. A.; Chisholm, C. R. I.; Haile, S. M. Alcohol Fuel Cells at Optimal Temperatures. *Electrochem Solid-State Lett* **2006**, *9*, A261–A264.

15. Taninouchi, Y. K.; Uda, T.; Awakura, Y.; Ikeda, A.; Haile, S. M. Dehydration Behavior of the Superprotonic Conductor CsH_2PO_4 at Moderate Temperatures: 230 to 260 Degrees C. *J Mater Chem* **2007**, *17*, 3182–3189.
16. Taninouchi, Y.; Uda, T.; Awakura, Y. Dehydration of CsH_2PO_4 at Temperatures Higher Than 260 Degrees C and the Ionic Conductivity of Liquid Product. *Solid State Ionics* **2008**, *178*, 1648–1653.
17. Urusovskaya, A. A.; Kirpichnikova, L. F. Specific Features of Plastic Deformation in CsHSO_4 Crystals. *Crystallogr Rep* **1998**, *43*, 307–310.
18. Kirpichnikova, L. F.; Urusovskaya, A. A.; Mozgovoi, V. I. Superplasticity of CsHSO_4 Crystals in the Superionic Phase. *JETP Letters* **1995**, *62*, 638–641.
19. Kislitsyn, M. N. Materials Chemistry of Superprotonic Solid Acids. California Institute of Technology, Pasadena, 2009.
20. Sasaki, K. A. Electrochemical Characterization of Solid Acid Fuel Cell Electrodes. California Institute of Technology, Pasadena, 2010.
21. Merle, R. B.; Chisholm, C. R. I.; Boysen, D. A.; Haile, S. M. Instability of Sulfate and Selenate Solid Acids in Fuel Cell Environments. *Energy Fuels* **2003**, *17*, 210–215.
22. Zhou, W. H.; Bondarenko, A. S.; Boukamp, B. A.; Bouwmeester, H. J. M. Superprotonic Conductivity in $\text{MH}(\text{PO}_3\text{H})$ ($\text{M} = \text{Li}^+, \text{Na}^+, \text{K}^+, \text{Rb}^+, \text{Cs}^+, \text{NH}_4^+$). *Solid State Ionics* **2008**, *179*, 380–384.
23. Bondarenko, A. S.; Zhou, W. H.; Bouwmeester, H. J. M. Superprotonic $\text{KH}(\text{PO}_3\text{H})\text{-SiO}_2$ Composite Electrolyte for Intermediate Temperature Fuel Cells. *J Power Sources* **2009**, *194*, 843–846.
24. Chisholm, C. R. I.; Toberer, E. S.; Louie, M. W.; Haile, S. M. Engineering the Next Generation of Solid State Proton Conductors: Synthesis and Properties of $\text{Ba}_{3-x}\text{K}_x\text{H}_x(\text{PO}_4)_2$. *Chem Mater* **2010**, *22*, 1186–1194.
25. Uda, T.; Haile, S. M. Thin-Membrane Solid-Acid Fuel Cell. *Electrochem Solid-State Lett* **2005**, *8*, A245–A246.
26. Costamagna, P.; Srinivasan, S. Quantum Jumps in the PEMFC Science and Technology from the 1960s to the Year 2000 Part I. Fundamental Scientific Aspects. *J Power Sources* **2001**, *102*, 242–252.
27. Varga, A.; Brunelli, N. A.; Louie, M. W.; Giapis, K. P.; Haile, S. M. Composite Nanostructured Solid-Acid Fuel-Cell Electrodes Via Electrospray Deposition. *J Mater Chem* **2010**, *20*, 6309–6315.

28. Papandrew, A. B.; Chisholm, C. R. I.; Elgammal, R. A.; Ozer, M. M.; Zecevic, S. K. Advanced Electrodes for Solid Acid Fuel Cells by Platinum Deposition on CsH_2PO_4 . *Chem Mater* **2011**, *23*, 1659–1667.
29. Appleby, A. J. Electrocatalysis and Fuel Cells. *Catal Rev Sci Eng* **1970**, *4*, 221.
30. Adler, S. B. Factors Governing Oxygen Reduction in Solid Oxide Fuel Cell Cathodes. *Chem Rev* **2004**, *104*, 4791–4843.
31. Fukai, Y., *The Metal-Hydrogen System: Basic Bulk Properties*. 2nd ed.; Springer: 2005; p 497.
32. Jiang, S. P.; Love, J. G.; Badwal, S. P. S. Electrochemical Techniques in Studies of Solid Ionic Conductors. *Key Engineering Materials* **1997**, *125–126*, 81–132.
33. Orazem, M. E.; Tribollet, B., *Electrochemical Impedance Spectroscopy*. Wiley-Interscience: New Jersey, 2008; p 560.
34. Barsoukov, E.; Macdonald, J. R., *Impedance Spectroscopy : Theory, Experiment, and Applications*. 2nd ed.; John Wiley: Hoboken, N.J., 2005; p xvii, 595 p.
35. Jiang, S. P.; Love, J. G.; Badwal, S. P. S., Electrochemical Techniques in Studies of Solid Ionic Conductors. In *Electrical Properties of Oxide Materials*, Nowotny, J.; Sorrell, C. C., Eds. Trans Tech Publications: Zurich, Switzerland 1997; Vol. 125–126, pp 81–132.
36. Sasaki, K. A.; Hao, Y.; Haile, S. M. Geometrically Asymmetric Electrodes for Probing Electrochemical Reaction Kinetics: A Case Study of Hydrogen at the Pt- CsH_2PO_4 Interface. *PCCP* **2009**, *11*, 8349–8357.
37. O'Hayre, R.; Prinz, F. B. The Air/Platinum/Nafion Triple-Phase Boundary: Characteristics, Scaling, and Implications for Fuel Cells. *J Electrochem Soc* **2004**, *151*, A756–A762.
38. Bieberle, A.; Meier, L. P.; Gauckler, L. J. The Electrochemistry of Ni Pattern Anodes Used as Solid Oxide Fuel Cell Model Electrodes. *J Electrochem Soc* **2001**, *148*, A646–A656.
39. Jiang, S. P.; Chan, S. H. A Review of Anode Materials Development in Solid Oxide Fuel Cells. *J Mater Sci* **2004**, *39*, 4405–4439.
40. Adler, S. B. Factors Governing Oxygen Reduction in Solid Oxide Fuel Cell Cathodes. *Chem Rev* **2004**, *104*, 4791–4843.
41. Bard, A. J.; Faulkner, L. R., *Electrochemical Methods: Fundamentals and Applications*. 2nd ed.; John Wiley & Sons: New York, 2000; p xxi, 831 p.
42. Materialschemist View of Cantilever in Atomic Force Microscope. [http://commons.wikimedia.org/wiki/File:AFM_\(used\)_cantilever_in_Scanning_Electron_Microscope,_magnification_1000x.GIF](http://commons.wikimedia.org/wiki/File:AFM_(used)_cantilever_in_Scanning_Electron_Microscope,_magnification_1000x.GIF) (accessed April 19, 2011).

43. Bonnell, D., *Scanning Probe Microscopy and Spectroscopy: Theory, Techniques, and Applications*. 2nd ed.; Wiley-VCH: 2000.
44. Adler, S. B. Reference Electrode Placement in Thin Solid Electrolytes. *J Electrochem Soc* **2002**, *149*, E166–E172.
45. Rutman, J.; Riess, I. Placement of Reference Electrode in Solid Electrolyte Cells. *Electrochim Acta* **2007**, *52*, 6073–6083.
46. Mizusaki, J.; Tagawa, H.; Saito, T.; Yamamura, T.; Kamitani, K.; Hirano, K.; Ehara, S.; Takagi, T.; Hikita, T.; Ippommatsu, M.; Nakagawa, S.; Hashimoto, K. Kinetic Studies of the Reaction at the Nickel Pattern Electrode on YSZ in H₂-H₂O Atmospheres. *Solid State Ionics* **1994**, *70–71*, 52–58.
47. Radhakrishnan, R.; Virkar, A. V.; Singhal, S. C. Estimation of Charge-Transfer Resistivity of Pt Cathode on YSZ Electrolyte Using Patterned Electrodes. *J Electrochem Soc* **2005**, *152*, A927–A936.
48. Sukeshini, A. M.; Habibzadeh, B.; Becker, B. P.; Stoltz, C. A.; Eichhorn, B. W.; Jackson, G. S. Electrochemical Oxidation of H₂, CO, and CO/H₂ Mixtures on Patterned Ni Anodes on YSZ Electrolytes. *J Electrochem Soc* **2006**, *153*, A705–A715.
49. Bieberle, A.; Gauckler, L. J. Reaction Mechanism of Ni Pattern Anodes for Solid Oxide Fuel Cells. *Solid State Ionics* **2000**, *135*, 337–345.
50. Chueh, W. C.; Haile, S. M. Electrochemical Studies of Capacitance in Cerium Oxide Thin Films and Its Relationship to Anionic and Electronic Defect Densities. *PCCP* **2009**, *11*, 8144–8148.
51. Beckel, D.; Bieberle-Hutter, A.; Harvey, A.; Infortuna, A.; Muecke, U. P.; Prestat, M.; Rupp, J. L. M.; Gauckler, L. J. Thin Films for Micro Solid Oxide Fuel Cells. *J Power Sources* **2007**, *173*, 325–345.
52. Baumann, F. S.; Maier, J.; Fleig, J. The Polarization Resistance of Mixed Conducting SOFC Cathodes: A Comparative Study Using Thin Film Model Electrodes. *Solid State Ionics* **2008**, *179*, 1198–1204.
53. Fleig, J. Microelectrodes in Solid State Ionics. *Solid State Ionics* **2003**, *161*, 279–289.
54. Koep, E.; Mebane, D. S.; Das, R.; Compson, C.; Liu, M. L. Characteristic Thickness for a Dense La_{0.8}Sr_{0.2}MnO₃ Electrode. *Electrochem Solid-State Lett* **2005**, *8*, A592–A595.
55. la O', G. J.; Shao-Horn, Y. Oxygen Surface Exchange Kinetics on Sr-Substituted Lanthanum Manganite and Ferrite Thin-Film Microelectrodes. *J Electrochem Soc* **2009**, *156*, B816–B824.
56. Uda, T.; Boysen, D. A.; Haile, S. M. Thermodynamic, Thermomechanical, and Electrochemical Evaluation of CsHSO₄. *Solid State Ionics* **2005**, *176*, 127–133.

57. Uda, T.; Chisholm, C. R. I.; Haile, S. M., Private Communication.
58. Louie, M. W.; Sasaki, K.; Haile, S. M. Towards Understanding Electrocatalysis in CsH_2PO_4 -Based Fuel Cells: Platinum and Palladium Thin Film Electrodes. *ECS Trans* **2008**, *13*, 57–62.
59. Baumann, F. S.; Fleig, J.; Habermeier, H. U.; Maier, J. Impedance Spectroscopic Study on Well-Defined $(\text{La,Sr})(\text{Co,Fe})\text{O}_{3-\delta}$ Model Electrodes. *Solid State Ionics* **2006**, *177*, 1071–1081.
60. Jung, W.; Tuller, H. L. Investigation of Cathode Behavior of Model Thin-Film $\text{SrTi}_{1-x}\text{Fe}_x\text{O}_{3-\delta}$ ($x = 0.35$ and 0.5) Mixed Ionic-Electronic Conducting Electrodes. *J Electrochem Soc* **2008**, *155*, B1194–B1201.
61. Mizusaki, J.; Amano, K.; Yamauchi, S.; Fueki, K. Electrode-Reaction at $\text{Pt}, \text{O}_2(\text{g})/\text{Stabilized Zirconia Interfaces}$.2. Electrochemical Measurements and Analysis. *Solid State Ionics* **1987**, *22*, 323–330.
62. Schmidt, M. S.; Hansen, K. V.; Norrman, K.; Mogensen, M. Effects of Trace Elements at the Ni/scYSZ Interface in a Model Solid Oxide Fuel Cell Anode. *Solid State Ionics* **2008**, *179*, 1436–1441.
63. Fultz, B.; Howe, J. M., *Transmission Electron Microscopy and Diffractometry of Materials*. 2nd ed.; Springer: 2005; p 770.
64. Rasband, W. S. Imagej. <http://imagej.nih.gov/ij/>.
65. Louie, M. W.; Kislitsyn, M.; Bhattacharya, K.; Haile, S. M. Phase Transformation and Hysteresis Behavior in $\text{Cs}_{1-x}\text{Rb}_x\text{H}_2\text{PO}_4$. *Solid State Ionics* **2010**, *181*, 173–179.
66. Ikeda, A.; Haile, S. M. *Solid State Ionics*, submitted **2011**.
67. Swanson, H. E.; Tatge, E. Standard X-Ray Diffraction Powder Patterns I. *National Bureau of Standards (U.S.), Circular* **1953**, *539*, 1–95.
68. Preisinger, A.; Mereiter, K.; Bronowska, W. The Phase Transition of CsH_2PO_4 (CDP) at 505K. *Mater Sci Forum* **1994**, *166*, 511–516.
69. Kreuer, K. D. Fast Proton Transport in Solids. *J Mol Struct* **1988**, *177*, 265–276.
70. Ebisuzaki, Y.; Kass, W. J.; Okeeffe, M. Solubility and Diffusion of Hydrogen and Deuterium in Platinum. *J Chem Phys* **1968**, *49*, 3329
71. Katsuta, H.; Mclellan, R. B. Diffusivity Permeability and Solubility of Hydrogen in Platinum. *J Phys Chem Solids* **1979**, *40*, 697–699.
72. Sakamoto, Y.; Kamohara, H. Diffusivity and Solubility of Hydrogen in Platinum Determined by the Electrochemical Permeation Method. *J Jpn Inst Met* **1981**, *45*, 797–802.

73. Gileadi, E.; Fullenwi.Ma; Bockris, J. O. M. Permeation of Electrolytic Hydrogen through Platinum. *J Electrochem Soc* **1966**, *113*, 926–930.
74. Hertz, J. L.; Tuller, H. L. Electrochemical Characterization of Thin Films for a Micro-Solid Oxide Fuel Cell. *J Electroceram* **2004**, *13*, 663–668.
75. Radhakrishnan, R.; Virkar, A. V.; Singhal, S. C. Estimation of Charge-Transfer Resistivity of $\text{La}_{0.8}\text{Sr}_{0.2}\text{MnO}_3$ Cathode on $\text{Y}_{0.16}\text{Zr}_{0.84}\text{O}_2$ Electrolyte Using Patterned Electrodes. *J Electrochem Soc* **2005**, *152*, A210–A218.
76. Atkinson, A.; Barnett, S.; Gorte, R. J.; Irvine, J. T. S.; McEvoy, A. J.; Mogensen, M.; Singhal, S. C.; Vohs, J. Advanced Anodes for High-Temperature Fuel Cells. *Nature* **2004**, *3*, 17–27.
77. Litster, S.; McLean, G. PEM Fuel Cell Electrodes. *J Power Sources* **2004**, *130*, 61–76.
78. O'Hayre, R.; Lee, M.; Prinz, F. B. Ionic and Electronic Impedance Imaging Using Atomic Force Microscopy. *J Appl Phys* **2004**, *95*, 8382–8392.
79. Bussian, D. A.; O'Dea, J. R.; Metiu, H.; Buratto, S. K. Nanoscale Current Imaging of the Conducting Channels in Proton Exchange Membrane Fuel Cells. *Nano Lett* **2007**, *7*, 227–232.
80. Aleksandrova, E.; Hiesgen, R.; Friedrich, K. A.; Roduner, E. Electrochemical Atomic Force Microscopy Study of Proton Conductivity in a Nafion Membrane. *PCCP* **2007**, *9*, 2735–2743.
81. Takimoto, N.; Ohira, A.; Takeoka, Y.; Rikukawa, M. Surface Morphology and Proton Conduction Imaging of Nafion Membrane. *Chem Lett* **2008**, *37*, 164–165.
82. Layson, A.; Gadad, S.; Teeters, D. Resistance Measurements at the Nanoscale: Scanning Probe AC Impedance Spectroscopy. *Electrochimica Acta* **2003**, *48*, 2207–2213.
83. Vels Hansen, K.; Jacobsen, T.; Norgaard, A.-M.; Ohmer, N.; Mogensen, M. Scanning Probe Microscopy at 650 °C in Air. *Electrochem Solid-State Lett* **2009**, *12*, B144–B145.
84. Loster, M.; Friedrich, K. A.; Scherson, D. A. Assembly and Electrochemical Characterization of Nanometer-Scale Electrode|Solid Electrolyte Interfaces. *J Phys Chem B* **2006**, *110*, 18081–18087.
85. O'Hayre, R.; Feng, G.; Nix, W. D.; Prinz, F. B. Quantitative Impedance Measurement Using Atomic Force Microscopy. *J Appl Phys* **2004**, *96*, 3540–3549.
86. Norby, T.; Friesel, M.; Mellander, B. E. Proton and Deuteron Conductivity in CsHSO_4 and CsDSO_4 by in Situ Isotopic Exchange. *Solid State Ionics* **1995**, *77*, 105–110.
87. *HSC Chemistry*. Outokumpu Research Oy: 1974–2002.
88. Birss, V. I.; Chang, M.; Segal, J. Platinum Oxide Film Formation-Reduction: An In-situ Mass Measurement Study. *J Electroanal Chem* **1993**, *355*, 181–191.

89. Hsueh, K.-L.; Gonzalez, E. R.; Srinivasan, S. Effects of Phosphoric Acid Concentration on Oxygen Reduction Kinetics at Platinum. *J Electrochem Soc* **1984**, *131*, 823–828.
90. Tammeveski, K.; Tenno, T.; Claret, J.; Ferrater, C. Electrochemical Reduction of Oxygen on Thin-Film Pt Electrodes in 0.1 M KOH. *Electrochim Acta* **1997**, *42*, 893–897.
91. Paik, C. H.; Jarvi, T. D.; O'Grady, W. E. Extent of PEMFC Cathode Surface Oxidation by Oxygen and Water Measured by Cv. *Electrochem Solid-State Lett* **2004**, *7*, A82–A84.
92. Xu, H.; Kunz, R.; Fenton, J. M. Investigation of Platinum Oxidation in PEM Fuel Cells at Various Relative Humidities. *Electrochem Solid-State Lett* **2007**, *10*, B1–B5.
93. Zhai, Y.; Zhang, H.; Xing, D.; Shao, Z.-G. The Stability of Pt/C Catalyst in H₃PO₄/PBI PEMFC During High Temperature Life Test. *J Power Sources* **2007**, *164*, 126–133.
94. Song, Y.; Fenton, J. M.; Kunz, H. R.; Bonville, L. J.; Williams, M. V. High-Performance PEMFCs at Elevated Temperatures Using Nafion 112 Membranes. *J Electrochem Soc* **2005**, *152*, A539–A544.
95. Kwon, K.; Park, J. O.; Yoo, D. Y.; Yi, J. S. Phosphoric Acid Distribution in the Membrane Electrode Assembly of High Temperature Proton Exchange Membrane Fuel Cells. *Electrochim Acta* **2009**, *54*, 6570–6575.
96. Aragane, J.; Urushibata, H.; Murahashi, T. Evaluation of an Effective Platinum Metal Surface Area in a Phosphoric Acid Fuel Cell. *J Electrochem Soc* **1994**, *141*, 1804–1808.
97. Fouda-Onana, F.; Bah, S.; Savadogo, O. Palladium-Copper Alloys as Catalysts for the Oxygen Reduction Reaction in an Acidic Media I: Correlation between the ORR Kinetic Parameters and Intrinsic Physical Properties of the Alloys. *J Electroanal Chem* **2009**, *636*, 1–9.
98. Kumar, S.; Zou, S. Electrooxidation of CO on Uniform Arrays of Au Nanoparticles: Effects of Particle Size and Interparticle Spacing. *Langmuir* **2009**, *25*, 574–581.
99. Murthi, V. S.; Urian, R. C.; Mukerjee, S. Oxygen Reduction Kinetics in Low and Medium Temperature Acid Environment: Correlation of Water Activation and Surface Properties in Supported Pt and Pt Alloy Electrocatalysts. *J Phys Chem B* **2004**, *108*, 11011–11023.
100. Parthasarathy, A.; Srinivasan, S.; Appleby, A. J.; Martin, C. R. Temperature Dependence of the Electrode Kinetics of Oxygen Reduction at the Platinum/Nafion Interface – a Microelectrode Investigation. *J Electrochem Soc* **1992**, *139*, 2530–2537.
101. Remita, H.; Siril, P. F.; Mbomekalle, I.-M.; Keita, B.; Nadj, L. Activity Evaluation of Carbon Paste Electrodes Loaded with Pt Nanoparticles Prepared in Different Radiolytic Conditions. *J Solid State Electrochem* **2006**, *10*, 506–511.

102. Takasu, Y.; Ohashi, N.; Zhang, X.-G.; Murakami, Y.; Minagawa, H.; Sato, S.; Yahikozawa, K. Size Effects of Platinum Particles on the Electroreduction of Oxygen. *Electrochim Acta* **1996**, *41*, 2595–2600.
103. Tilak, B. V.; Chen, C.-P.; Birss, V. I.; Wang, J. Capacitive and Kinetic Characteristics of Ru-Ti Oxides Electrodes: Influence of Variation in the Ru Content. *Can J Chem* **1997**, *75*, 1773–1782.
104. Uchida, H.; Yoshida, M.; Watanabe, M. Effects of Ionic Conductivities of Zirconia Electrolytes on Polarization Properties of Platinum Anodes in Solid Oxide Fuel Cells. *J Phys Chem* **1995**, *99*, 3282–3287.
105. Chisholm, C. R. I.; Haile, S. M. High-Temperature Phase Transitions in $\text{K}_3\text{H}(\text{SO}_4)_2$. *Solid State Ionics* **2001**, *145*, 179–184.
106. Chisholm, C. R. I.; Haile, S. M. Entropy Evaluation of the Superprotonic Phase of CsHSO_4 : Pauling's Ice Rules Adjusted for Systems Containing Disordered Hydrogen-Bonded Tetrahedra. *Chem Mater* **2007**, *19*, 270–279.
107. Chisholm, C. R. I.; Haile, S. M. Structure and Thermal Behavior of the New Superprotonic Conductor $\text{Cs}_2(\text{HSO}_4)(\text{H}_2\text{PO}_4)$. *Acta Crystallogr B* **1999**, *55*, 937–946.
108. Pawlowski, A.; Szczesniak, L.; Polomska, M.; Hilczer, B.; Kirpichnikova, L. Pretransitional Effects at the Superionic Phase Transition of $\text{Rb}_3\text{H}(\text{SeO}_4)_2$ Protonic Conductor. *Solid State Ionics* **2003**, *157*, 203–208.
109. Merinov, B. V.; Haile, S. M.; Bismayer, U. Crystal Structure of the "Intermediate" Phase of the Protonic Conductor $\text{Rb}_3\text{H}(\text{SeO}_4)_2$. *Solid State Ionics* **2002**, *146*, 355–365.
110. Cui, J.; Chu, Y. S.; Famodu, O. O.; Furuya, Y.; Hattrick-Simpers, J.; James, R. D.; Ludwig, A.; Thienhaus, S.; Wuttig, M.; Zhang, Z. Y.; Takeuchi, I. Combinatorial Search of Thermoelastic Shape-Memory Alloys with Extremely Small Hysteresis Width. *Nat Mater* **2006**, *5*, 286–290.
111. Zhang, Z. Y.; James, R. D.; Muller, S. Energy Barriers and Hysteresis in Martensitic Phase Transformations. *Acta Mater* **2009**, *57*, 4332–4352.
112. Zarnetta, R.; Takahashi, R.; Young, M. L.; Savan, A.; Furuya, Y.; Thienhaus, S.; Maass, B.; Rahim, M.; Frenzel, J.; Brunken, H.; Chu, Y. S.; Srivastava, V.; James, R. D.; Takeuchi, I.; Eggeler, G.; Ludwig, A. Identification of Quaternary Shape Memory Alloys with Near-zero Thermal Hysteresis and Unprecedented Functional Stability. *Adv Funct Mater* **2010**, *20*, 1917–1923.
113. Cowan, L. A. Superprotonic Solid Acid Phase Transitions and Stability. California Institute of Technology, Pasadena, 2007.
114. Martsinkevich, V. V.; Ponomareva, V. G.; Drebuschak, T. N.; Lavrova, G. V.; Shatskaya, S. S. Structure of $\text{Cs}_{1-x}\text{Rb}_x\text{H}_2\text{PO}_4$ Solid Solutions. *Inorg Mater* **2010**, *46*, 765–769.

115. Bhattacharya, K., *Microstructure of Martensite: Why It Forms and How It Gives Rise to the Shape-Memory Effect*. Oxford University Press: 2003.
116. Uesu, Y.; Kobayashi, J. Crystal-Structure and Ferroelectricity of Cesium Dihydrogen Phosphate CsH_2PO_4 . *Phys Status Solidi A* **1976**, *34*, 475–481.
117. Yamada, K., Sagara, T., Yamane, Y., Ohki, H., Okuda, T. Superprotonic Conductor CsH_2PO_4 Studied by ^1H , ^{31}P NMR and X-Ray Diffraction. *Solid State Ionics* **2004**, *175*, 557–562.
118. Preisinger, A., Mereiter, K., Bronowska, W. The Phase Transition of CsH_2PO_4 (CDP) at 505K. *Mat Sci Forum* **1994**, *166*, 511–516.
119. Bronowska, W. High-Temperature Phenomena in RbD_2PO_4 and CsH_2PO_4 Polymeric Transformations or Polymorphic Phase Transitions? *Mater Sci-Poland* **2006**, *24*, 229–236.
120. Romain, F.; Novak, A. Raman-Study of the High-Temperature Phase-Transition in CsH_2PO_4 . *J Mol Struct* **1991**, *263*, 69–74.
121. Otomo, J.; Minagawa, N.; Wen, C. J.; Eguchi, K.; Takahashi, H. Protonic Conduction of CsH_2PO_4 and Its Composite with Silica in Dry and Humid Atmospheres. *Solid State Ionics* **2003**, *156*, 357–369.
122. Boysen, D. A.; Haile, S. M.; Liu, H. J.; Secco, R. A. High-Temperature Behavior of CsH_2PO_4 under Both Ambient and High Pressure Conditions. *Chem Mater* **2003**, *15*, 727–736.
123. Franceschetti, D. R.; Macdonald, J. R. Interpretation of Finite-Length-Warburg-Type Impedances in Supported and Unsupported Electrochemical Cells with Kinetically Reversible Electrodes. *J Electrochem Soc* **1991**, *138*, 1368–1371.
124. Ikeda, A., Private Communication. 2011.
125. Antolini, E. Palladium in Fuel Cell Catalysis. *Energy Environ Sci* **2009**, *2*, 915–931.
126. Wipf, H. Diffusion of Hydrogen in Metals. *Top Appl Phys* **1997**, *73*, 51–91.
127. Sasaki, K.; Haile, S. M., Private Communication.
128. Pasierb, P.; Rekas, M. Solid-State Potentiometric Gas Sensors-Current Status and Future Trends. *J Solid State Electrochem* **2009**, *13*, 3–25.
129. Korotcenkov, G.; Do Han, S.; Stetter, J. R. Review of Electrochemical Hydrogen Sensors. *Chem Rev* **2009**, *109*, 1402–1433.
130. Siebert, E.; Rosini, S.; Bouchet, R.; Vitter, G. Mixed Potential Type Hydrogen Sensor. *Ionics* **2003**, *9*, 168–175.
131. Garzon, F. H.; Mukundan, R.; Brosha, E. L. Solid-State Mixed Potential Gas Sensors: Theory. Experiments and Challenges. *Solid State Ionics* **2000**, *136*, 633–638.

132. Miura, N.; Lu, G. Y.; Yamazoe, N. Progress in Mixed-Potential Type Devices Based on Solid Electrolyte for Sensing Redox Gases. *Solid State Ionics* **2000**, *136*, 533–542.
133. Rosini, S.; Siebert, E. Electrochemical Sensors for Detection of Hydrogen in Air: Model of the Non-Nemstian Potentiometric Response of Platinum Gas Diffusion Electrodes. *Electrochim Acta* **2005**, *50*, 2943–2953.
134. Moseley, P.; Williams, D. Sensing Reducing Gases. *Nature* **1990**, *346*, 23–23.
135. Dyer, C. K. A Novel Thin-Film Electrochemical Device for Energy-Conversion. *Nature* **1990**, *343*, 547–548.
136. Tomita, A.; Namekata, Y.; Nagao, M.; Hibino, T. Room-Temperature Hydrogen Sensors Based on an In³⁺-Doped SnP₂O₇ Proton Conductor. *J Electrochem Soc* **2007**, *154*, J172–J176.
137. Lu, G. Y.; Miura, N.; Yamazoe, N. Mixed Potential Hydrogen Sensor Combining Oxide Ion Conductor with Oxide Electrode. *J Electrochem Soc* **1996**, *143*, L154–L155.
138. Miura, N.; Ono, M.; Shimano, K.; Yamazoe, N. A Compact Solid-State Amperometric Sensor for Detection of NO₂ in Ppb Range. *Sens Actuators B* **1998**, *49*, 101–109.
139. Fergus, J. W. Solid Electrolyte Based Sensors for the Measurement of CO and Hydrocarbon Gases. *Sens Actuators B* **2007**, *122*, 683–693.